Temporal Networks : from network theory to brain science

Nicola Pedreschi

Aix*Marseille université
Socialement engagée

THÈSE DE DOCTORAT

Soutenue à Aix-Marseille Université

Nicola Pedreschi

Temporal Networks : from network theory to brain science

Discipline
PHYSIQUE ET SCIENCES DE LA MATIERE

Specialité
Physique Théorique et Mathématique

École doctorale
ED 352

Laboratoire/Partenaires de recherche
CPT
INS
APHM

Composition du jury

Rémi Monasson LPT, ENS	Rapporteur
Olaf Sporns Indiana University Network science Institute, USA	Rapporteur
Sophie Achard INRIA	Examinatrice
Rosa Cossart INMED	Examinatrice
Alain Barrat CPT	Directeur de thèse
Demian Battaglia INS	Co-Directeur de thèse

CPT Centre de Physique Théorique
Aix*Marseille université Initiative d'excellence
Commission européenne
Région Provence Alpes Côte d'Azur
Institut de Neurosciences des Systèmes

Résumé

Au cours des dernières décennies, la science des réseaux est devenue un cadre fondamental pour dévoiler les principes d'organisation des systèmes complexes. Dans les neurosciences, les approches théoriques des réseaux ont été utilisées de manière intensive pour découvrir les propriétés inhérentes des réseaux cérébraux. Dans le cerveau, en effet, les systèmes en réseau s'étendent sur différentes échelles spatiales, puisque les nœuds d'un réseau peuvent représenter des neurones individuels, des populations de neurones ou à la plus grande échelle des zones cérébrales. En outre, les arêtes des systèmes en réseau du cerveau peuvent représenter différents types de connexions entre les nœuds : on peut, par exemple, choisir d'étudier les propriétés des connexions physiques entre les nœuds d'un réseau cérébral, à n'importe quelle échelle, et analyser ainsi la *Connectivité structurelle* (CS) de ce système ; ou, au contraire, on peut s'intéresser à la capture des interdépendances statistiques entre l'activité de chaque paire de nœuds, ce qui donne lieu à la *Connectivité fonctionnelle* (CF) des réseaux cérébraux. (CF) des réseaux cérébraux. Si la CS correspond au tissu de connexions anatomiques reliant entre eux les neurones, les populations neuronales ou les aires cérébrales, selon l'échelle d'observation, la CF représente au contraire le sous-produit observable de la communication entre ces entités élémentaires (nœuds) se déployant au-dessus de la CS et donnant naissance aux représentations neuronales et, finalement, à la cognition. La recherche des propriétés de réseau de la CS a révélé une organisation globale en petit monde des réseaux cérébraux, à différentes échelles spatiales, ce qui correspond à équilibrer le coût de câblage d'un tel réseau en faveur d'un schéma opérationnel dans lequel les niveaux inférieurs de traitement de l'information peuvent être distribués localement, et leurs produits combinés par une intégration généralisée à un niveau supérieur. Les études de la FC ont en effet montré comment les principes d'organisation des réseaux fonctionnels semblent confirmer la validité d'un tel schéma, avec la réserve que le taux de changement de la CF, et donc la reconfiguration variable dans le temps des connexions fonctionnelles entre les nœuds, semble être intrinsèquement lié, par exemple pour les réseaux cérébraux à grande échelle, aux échelles de temps comportementales.

Mon travail de thèse s'inscrit dans l'optique selon laquelle le lien entre la structure et la fonction doit être étudié au niveau de la dynamique, et l'analyse des flux résolus dans le temps des CF se traduit intuitivement par un cadre de type *réseau temporel*. L'étude des réseaux temporels représente aujourd'hui l'une des disciplines de pointe de la science des réseaux et vise à découvrir les propriétés sous-jacentes d'un système complexe en réseau évoluant dans le temps. Cet objectif est atteint en suivant la *temporalité*, c'est-à-dire l'ordre temporel ou la *simultanéité*, des connexions dans

un système, ce qui permet d'identifier, par exemple, des structures temporelles pertinentes dont l'existence, ou *fonction*, peut être liée à des moments d'intérêt spécifiques de l'évolution du système ou à des processus se déroulant au-dessus de sa structure en réseau variable dans le temps. Les réseaux temporels sont omniprésents et s'étendent à différentes échelles et contextes, depuis les infrastructures de transport jusqu'aux réseaux de différents types d'interactions sociales entre personnes ou animaux, en passant par les interactions entre protéines dans les cellules, entre autres.

Dans mon travail, et dans cette thèse, je me concentre sur l'analyse des réseaux temporels du cerveau à différentes échelles spatiales. Cependant, alors que la majeure partie de mon travail de thèse consistait à concevoir des approches de réseaux temporels pour analyser la connectivité fonctionnelle résolue dans le temps à la micro- et macro-échelle dans le cerveau, je me suis également intéressé, avec mes superviseurs, à soulever certaines questions fondamentales concernant l'étude des réseaux temporels en général. Cette ligne de recherche a conduit à la définition d'une nouvelle structure qui peut être détectée dans les réseaux variant dans le temps.

Le plan de ce manuscrit est le suivant :

— Dans le chapitre 1, je présente les notions et concepts de base de la science des réseaux qui sont les plus pertinents pour mon travail. Je décris ensuite comment ces concepts doivent être repensés et adaptés pour convenir à l'analyse des réseaux temporels, en accordant une attention particulière aux définitions qui sont les plus importantes pour mon travail original.

— Le chapitre 2 représente un résumé des principaux résultats de l'utilisation de la science des réseaux pour étudier les systèmes en réseau dans le cerveau. Je présente ici les propriétés des réseaux cérébraux structurels et fonctionnels, et je souligne comment mon travail va dans le sens de la découverte du lien manquant entre ces deux dimensions de la connectivité, à travers la dynamique. Je présente également et passe brièvement en revue deux systèmes cérébraux spécifiques qui font l'objet de mes recherches : l'hippocampe, à l'échelle micro, et le système du langage, à l'échelle macro. Je décris aussi brièvement une condition pathologique spécifique, l'épilepsie, car une partie de mon travail vise à décrire les changements majeurs qui se produisent dans la connectivité des réseaux cérébraux épileptiques.

— Dans le chapitre 3, je présente mon premier projet de recherche. Ici, je montre comment les séquences d'activation d'assemblées cellulaires transitoires à l'échelle micro, dans la formation hippocampique de rats anesthésiés, peuvent être traduites dans un formalisme de réseau temporel. Ici, j'extrais la CF résolue dans le temps d'un réseau de neurones en mesurant la quantité d'informations partagées entre leurs rythmes de décharge. Je décris ensuite les différents états méta-stables (*états du réseau*) de ces neurones partageant l'information en termes de recrutement variable dans le temps dans les différentes couches d'une organisation globale persistante cœur-périphérie du réseau, et en termes de taux

de changement, la *liquidité*, de leurs connexions fonctionnelles. Je caractérise ensuite les comportements typiques des nœuds de ces réseaux fonctionnels au sein des états du réseau au moyen de mesures de la théorie des réseaux, montrant ainsi comment, dans le cadre de cette vision théorique de l'information et des réseaux des assemblées de cellules, une variété de comportements neuronaux de type hub apparaît. En outre, je décris comment la proéminence d'un nœud par rapport aux autres dans un réseau change, également de manière drastique, d'un état du réseau à l'autre, et n'est pas liée de manière significative à la localisation anatomique ou aux propriétés physiologiques des cellules.

— Dans le chapitre 4, je décris une deuxième étude dans laquelle je m'attaque à l'analyse des réseaux cérébraux à macro-échelle variant dans le temps. Je présente ici une nouvelle approche pour étudier l'apparition, et peut-être les mécanismes sous-jacents, de l'aphasie comme symptôme post-crise chez les patients épileptiques humains. J'extrais un CF résolu dans le temps comme un réseau multicouche variant dans le temps dont les liens dans les différentes couches représentent l'activité cohérente en phase dans différentes bandes de fréquence des signaux enregistrés par des électrodes intracrâniennes implantées chez des patients épileptiques pharmaco-résistants. J'étudie le recrutement ou le rejet dynamique de nœuds dans ou hors de différentes communautés au sein de chaque couche en extrayant un flux de matrices "*module allegiance*" à fenêtre temporelle. En récupérant des états méta-stables discrets d'allégeance aux modules, je montre comment ils se rapportent aux différentes périodes d'un enregistrement, en identifiant notamment deux états qui se rapportent le plus aux symptômes de troubles du langage évalués par les médecins pendant la récupération des patients après une crise. Je décris également comment les relations entre la dynamique de la communauté des nœuds dans différentes couches, c'est-à-dire les bandes de fréquence (de delta, 1-4Hz, à$gamma$, 20 − 40Hz), sont également affectées par la crise et spécule sur les implications sur le système du langage. Je discute donc de la façon dont cette recherche en cours pourrait éventuellement évaluer l'implication du système du langage dans une réorganisation multifréquence de la dynamique de la CF. Je décris en fait comment cela pourrait conduire à une communication désordonnée induite par la crise entre les zones cérébrales liées au langage, donnant ainsi lieu à l'aphasie comme un effet de déconnexion fonctionnelle transitoire. Cette étude permet d'introduire une nouvelle façon de comparer non seulement les réseaux instantanés, mais aussi les propriétés du *flux de réseau* à différents moments, ce qui peut avoir une application générale dans les études de réseau temporel au-delà du problème spécifique.

— Dans le chapitre 5, j'étudie la relation entre la simultanéité des connexions dans un réseau temporel général et l'existence de structures pertinentes. En particulier, je me concentre sur la question fondamentale de savoir comment discerner si les nœuds importants, *prominents*, d'un réseau temporel interagissent entre

eux, donnant lieu à des structures *cohésives* temporelles. À cet égard, je présente une nouvelle définition du *rich club temporel* comme une structure impliquant les nœuds les plus connectés dans un réseau variant dans le temps, qui reste plus stable sur un certain laps de temps que ce qui est attendu si les connexions étaient établies au hasard. J'étudie la temporalité pure d'une telle structure, en soulignant comment les clubs riches temporels peuvent apparaître de manière transitoire même dans des réseaux où un rich club statique ne peut être retrouvé, et comment différents rich clubs temporels peuvent être liés à différents moments d'intérêt de l'évolution du réseau dynamique. En outre, j'étudie le rôle de cette structure dans les processus de propagation sur les réseaux temporels, en dévoilant comment un groupe temporellement cohésif de nœuds importants peut favoriser la propagation d'un pathogène dans un réseau de contacts sociaux.

Je conclus ce manuscrit par le chapitre 6, où je discute de la signification de mes résultats, en précisant où se situe mon travail dans le cadre plus large de la neuroscience des réseaux et dans le domaine encore plus large des réseaux temporels. Mots

clés : systèmes complexes, réseaux temporels, neurosciences des réseaux

Abstract

Network science is a fundamental framework to unveil the organizational principles of complex systems. In neuroscience network theoretic approaches have been used to uncover inherent properties of brain networks. In the brain networked systems span across different spatial scales: nodes in a network can represent individual neurons, populations of neurons up to brain areas. In my thesis I study the dynamic reconfiguration of the Functional Connectivity (FC) of brain networks, translating the time-varying FC into a temporal network framework. The study of temporal networks (TNs) uncovers the underlying properties of a complex networked system evolving in time by keeping track of the time-ordering or the simultaneity of connections. In this work I analyze brain TNs at different spatial scales. I show how sequences of activation of transient cell assemblies at the micro-scale can be translated into a TN formalism. Extracting the time resolved FC of a network of neurons by measuring the amount of shared information between their firing patters, I capture the different meta-stable states of a TN of neurons in terms of the dynamic recruitment into the layers of an overall persistent core-periphery organization, and in terms of the liquidity of the FC. I characterise typical behaviors of nodes in this functional TN within states by means of network theoretic measures, showing how a variety of hub-like neuronal behaviors arise and that the prominence of a node in a network changes from a network state to the other, and is not significantly related to the anatomy or physiology of cells. At the macro-scale, I present a novel approach to study the arising of aphasia as a post-seizure symptom in human epileptic patients. I extract a multi-layer, time varying FC whose edges in each layer represent the synchronous activity in a different frequency band of pairs of SEEG signals. I study the dynamic reconfiguration of communities of nodes within each layer by extracting a stream of time-windowed module allegiance (MA) matrices. Finding discrete states of MA, I show how they relate to the different periods of a recording, in particular identifying two states that most relate to the language impairments. I describe how the relations between the community dynamics in different layers are affected by the seizure. I therefore describe how this ongoing research could assess the involvement of the language system in a multi-frequency dynamic re-organization of FC, giving rise to aphasia as product of post-ictal disordered communication among language brain areas. Lastly, I investigate the relation between the simultaneity of connections in a TN and the existence of relevant structures. In particular, I describe how important nodes in a TN interact with each other forming simultaneously connected structures, contributing to the novel definition of the temporal rich club (TRC): a temporally cohesive structure involving the most connected nodes in a time-varying network, that remains more stable over a certain time-span than expected from chance. I show how TRCs can transiently

arise even in networks where a static rich club is not present and that different TRCs can relate to different moments of interest of the network's evolution. Furthermore, I investigate the role of TRC in spreading processes on TNs, such as diffusion of information in a network of interacting neurons (or social contacts), unveiling how a TRC can foster the spreading. This thesis thus provides evidence that temporal network approaches can shed light on the roles of different neurons or brain areas in the communication dynamics in brain networks and on how different regimes of the dynamic reconfiguration of FC relate to cognitive dysfunctions. My work also introduces the novel definition of the temporal rich club, thus contributing to the growing repertoire of methods and tools to analyze and describe temporal networks in general.

Keywords: complex systems, temporal networks, network neuroscience

Acknowledgements

I would like to thank my two supervisors, my mentors, Alain Barrat and Demian Battaglia. In these past three years they have guided me with keen attention on balancing advice and trust. I feel grateful to have had the chance to work alongside these two remarkable scientists, who have inevitably set a probably unreachable standard in what I think a researcher should be. I thank the whole Doc2AMU programme, the coordinator Mossadek Talby and the project manager Sarah Ethier-Sawyer for their support, along with all of the other Doc2AMU doctorates and students that have shared this adventure with me. In these last three years I've worked scattered around this beautiful new city, Marseille, yet, everywhere I was, I felt at home. At CPT, I found some wonderful colleagues, with whom I felt at ease from the very first moment, almost as it had been years that we worked together. At INS, I found yet another family: even though I'm sure most of the people there are still convinced that my main vocation is to make coffee for everybody, everyone was always willing to help, whether discussing about work or featuring in a science-related video. I have shared this time of my life with so many people, and groups of people, that have turned me into the person I am today: there's no need for me to list your names as, I hope, you know how grateful I am that our paths have crossed. Lastly, I would like to thank my parents and my sister, for their unconditional support and love. A final mention goes to my grandmother Leda: not only trying to convince you that what I do is of any use represents the biggest intellectual challenge that I have ever faced, but your wits, humour and kindness have always inspired me to give everything I can for my work, without taking myself too seriously.

This project has received funding from the European Union's Horizon 2020 research and innovation programme under the Marie Skłodowska-Curie grant agreement No713750. Also, it has been carried out with the financial support of the Regional Council of Provence- Alpes-Côte d'Azur and with the financial support of the A*MIDEX (n° ANR- 11-IDEX-0001-02), funded by the Investissements d'Avenir project funded by the French Government, managed by the French National Research Agency (ANR).

Contents

List of Figures

Introduction

In the last decades network science has become a fundamental framework to unveil the organizational principles of complex systems. In neuroscience, network theoretic approaches have been used intensively to uncover inherent properties of brain networks. In the brain, in fact, networked systems span across different spatial scales, since nodes in a network can represent individual neurons, populations of neurons or coarse-grained brain areas at the largest scale. Furthermore, the edges in brain networked systems can represent different types of connections among nodes: one can, for instance, choose to study the network properties of the physical connections among nodes in a brain network, at any scale, thus analyzing the *Structural Connectivity* (SC) of such system; or, instead, one can be interested in capturing the statistical interdependencies between the activity of each pair of nodes, thus giving rise to the *Functional Connectivity* (FC) of brain networks. If SC corresponds to the fabric of anatomical connections linking together neurons, neuronal populations or brain areas, depending on the scale of observation, the FC represents instead the observable byproduct of the communication between those elementary entities (nodes) unfolding on top of the SC and giving rise to neural representations and, ultimately, cognition. The search for network properties of SC has unveiled an overall small-world organization of brain networks, at different spatial scales, aimed at balancing the wiring cost of such network in favour of an operational scheme in which lower levels of information processing can be locally distributed, and its products combined by higher level, widespread integration. FC studies have indeed shown how the organizational principles of functional networks seem to confirm the validity of such scheme, with the caveat that the rate of change of the FC, and thus the time-varying reconfiguration of functional connections among nodes, seems to be inherently related, for instance for large-scale brain networks, to behavioral time scales.

My PhD work is in line with the view in which the link between structure and function should be investigated at the level of dynamics, and the analysis of time-resolved streams of FCs intuitively translates into a *temporal network* framework. The study of temporal networks represents nowadays one of the forefront disciplines of network science and it is aimed at uncovering the underlying properties of a complex networked system evolving in time. This is achieved by keeping track of the *temporality*, i.e., the time-ordering or the *simultaneity*, of connections in a system, allowing to identify, for instance, relevant temporal structures whose existence, or *function*, can be related to specific moments of interest of the system's evolution or to processes unfolding on top of its time-varying networked fabric. Temporal networks are ubiquitous and span across different scales and contexts, from transportation infrastructure, to networks of

different kinds of social interactions among people or animals, to protein interactions in cells, among others.

In my work, and in this thesis, I focus on the analysis of brain temporal networks at different spatial scales. However, while most of my PhD work consisted in devising temporal networks approaches to analyse time-resolved functional connectivity at the micro- and macro-scale in the brain, I was also interested, together with my supervisors, in raising some fundamental questions regarding the study of temporal networks in general. This line of research lead to the definition of a novel structure that can be detected in time-varying networks.

The outline of this manuscript is the following:

— In Chapter 1, I introduce the basic notions and concepts of network science that are most relevant for my work. I therefore describe how these concepts need to be re-conceived and adapted in order to suit the analysis of temporal networks, giving particular attention to the definitions that are most important for my original work.

— Chapter 2 represents a summary of the main results of the use of network science to study networked systems in the brain. I present here the network properties of structural and functional brain networks, and stress how my work goes in the direction of uncovering the missing link between these two dimensions of connectivity, through dynamics. I also introduce and briefly review two specific brain systems that are the object of my research: the hippocampus, at the micro-scale, and the language system, at the macro-scale. I also briefly describe a specific pathological condition, epilepsy, as part of my work aims at describing the major changes that occur in the connectivity of epileptic brain networks.

— In Chapter 3, I present my first research project, which resulted in a published article [143]. Here, I show how the sequences of activation of transient cell assemblies at the micro-scale, in the hippocampal formation of anesthetized rats, can be translated into a temporal network formalism. Here, I extract the time resolved FC of a network of neurons by measuring the amount of *shared* information between their firing patters. I then capture the different meta-stable states (*network states*) of these information-sharing neurons in terms of the time-varying recruitment into the different layers of an overall persistent core-periphery organization of the network, and in terms of the rate of change, the *liquidity*, of their functional connections. I then characterise typical behaviors of nodes in this functional networks within the network states by means of network theoretic measures, showing therefore how, within these information- and network-theoretic view of cell assemblies, a variety of hub-like neuronal behaviors arise. Furthermore, I describe how the prominence of a node over the others in a network changes, also drastically, from a network state to the other, and it is not significantly related to the anatomical localization or physiological

properties of cells.

— In Chapter 4, I describe a second study in which I tackle the analysis of macro-scale time-varying brain networks. I present here a novel approach to study the arising, and possibly the underlying mechanisms, of aphasia as a post-seizure symptom in human epileptic patients. I extract a time-resolved FC as a multi-layer, time varying network whose edges in different layers represent the phase-coherent activity in different frequency bands of each pair of signals recorded from intra-cranial electrodes implanted in pharmaco-resistant epileptic patients. I study the dynamic recruitment or dismissal of nodes into or out of different communities within each layer by extracting a stream of time-windowed *module allegiance* matrices. Retrieving discrete meta-stable states of module allegiance, I show how they relate to the different periods of a recording, in particular identifying two states that most relate to the language impairment symptoms assessed by physicians during the patients recovery after a seizure. I further describe how the relations between the community dynamics of nodes in different layers, i.e., frequency bands (from delta, $1-4$Hz, to gamma, $20-40$Hz), are also affected by the seizure and speculate on the implications on the language system. I therefore discuss how this ongoing research could possibly assess the involvement of the language system in a multi-frequency re-organization of the dynamics of the FC, describing how this could lead to a seizure-induced disordered communication between language-related brain areas, thus giving rise to aphasia as a transient functional disconnection effect. This study provides the opportunity to introduce a novel way to compare not only individual temporal network instant frames, but also the properties of *network flow* at different moments, which may have general application in temporal network studies beyond the specific problem. The manuscript of a research article describing this study in detail is under preparation.

— In Chapter 5, I investigate the relation between the simultaneity of connections in a general temporal network and the existence of relevant structures. In particular, I focus on the fundamental question of how to discern whether *prominent*, important nodes in a temporal network do interact with each other giving rise to temporally *cohesive* structures. In this regard, I present the novel definition of the *temporal rich club* as a structure involving the most connected nodes in a time-varying network, that remains more stable over a certain time-span than what expected from chance. I study the pure temporality of such structure, highlighting how temporal rich clubs can transiently arise even in networks where a static rich club cannot be retrieved as well as how different temporal rich clubs can be related to different moments of interest of the evolution of the dynamic network. Furthermore, I investigate the role of such structure in spreading processes on temporal networks, unveiling how a temporally cohesive group of important nodes can foster the spread of a pathogen in a network of social contacts. The work presented in this chapter is described in detail in a

manuscript [142] that is currently under submission for publication.

I conclude this thesis manuscript with Chapter 6, where I discuss the significance of my findings, specifying where my work stands in the broader picture of network neuroscience and in the even broader field of temporal networks.

1. Network Science: From static to dynamic networks

In this chapter I introduce the basic concepts of graph theory originally developed to study static networks and present how the same definitions, along with new specific ideas, have been further generalised to networks that change over time, i.e., temporal networks. In particular I focus on concepts, measures and tools used in the analysis of static and dynamic networks that lie at the core of my research, which I describe in detail in chapters 3 to 5.

1.1. Static Networks

1.1.1. Basic Concepts

A *network* $G(V,E)$, or a *graph* as it is referred to in the mathematical literature, is composed of a set of *nodes*, or *vertices*, $V = 1,\ldots,N$ (where N is the number of nodes in the graph) and of a set of *links*, or *edges*, $E = (i,j) \forall i,j \in V$. We denote as L the total number of edges, i.e., the size of E. Ideally, any system composed of interacting agents can be represented as a network [58, 135]. This sort of systems are omnipresent and can be found at the most disparate spatial scales and in different contexts. Examples range from gene regulatory networks, metabolic networks, networks of cells and neurons, up to larger scale networks such as networks of social interactions between animals or humans or other connections between and amongst individuals, logistic and transportation infrastructures, the Internet or the World Wide Web.

Unweighted, undirected networks The simplest representation of a system as a network is that of *unweighted, undirected* graphs. An unweighted, undirected network is defined by its adjacency matrix A whose matrix element $A(i,j) = 1$ if nodes i and j are connected and 0 otherwise. The adjacency matrix of unweighted, undirected networks is symmetric, i.e., $A(i,j) = A(j,i)$. A basic property of a node in a network is its *degree*, namely the number k_i of edges connected to a vertex i and defined as $k_i = \sum_{j \neq i} A(i,j)$ (Figure 1.1).

Directed networks The adjacency matrix of directed graphs is asymmetric, i.e., $A(i,j)$ and $A(j,i)$ can be different, which allows to represent the direction of edges connecting each pair of nodes. Thus the matrix element $A(i,j) = 1$ indicates the presence of an edge *from* node i *to* node j. Therefore, each vertex i has an *out*-degree

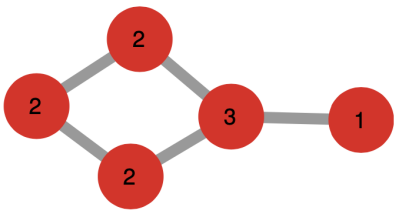

Figure 1.1. – Sketch of a graph where the numbers at the center of nodes' markers represent their degree.

$k^i_{out} = \sum_{j\neq i} A(i,j)$ and an *in*-degree $k^i_{in} = \sum_{j\neq i} A(j,i)$ (Figure 1.2). Communication networks, such as email exchange networks, networks of citations in scientific papers or of telephone calls are examples of directed graphs, since the connection between two vertices has a clear direction in those cases.

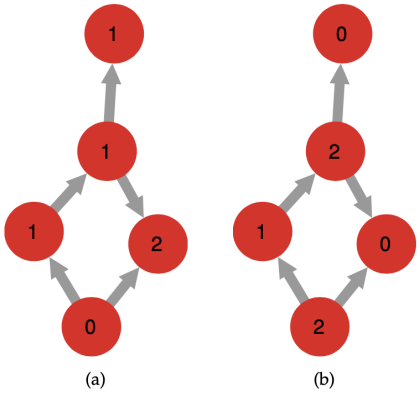

Figure 1.2. – Sketches of the same graph where the figures on nodes' markers indicate their in-degree (left) and out-degree (right).

Weighted networks In order to capture higher degrees of complexity of the system under study and to represent it as a network, a *weight* w_{ij} can be assigned to each edge (i,j). The intuitive generalization of the degree of a node to weighted, undirected graphs is therefore a node's *strength* $s_i = \sum_{j\neq i} w_{ij}$ (Figure 1.3), whereas for weighted, directed graphs each node i has an *out*-strength and an *in*-strength. Weighted graphs take into account the diversity of the intensity of interactions between vertices [15, 136], which is characteristic of real networks. Real world examples of weighted graphs are transportation networks (directed or undirected) where the weight of edges connecting vertices can represent the traffic volumes between two locations (railway stations, airports, cities, etc.) as well as functional brain networks, where the weight of an edge represents, for instance, the amount of shared information between neurons or brain areas.

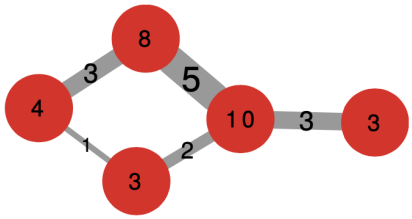

Figure 1.3. – Numbers drawn on edges correspond to their weight, whereas numbers on nodes indicate their strength.

Statistical properties of graphs The degree of a node is an individual property, whereas the average degree $\langle k \rangle = \frac{\sum_{i \in V} k_i}{N}$ of a network informs about the overall structure, yet it only represent a single bit of data. Investigating the whole *degree distribution* can shed light on key properties of a network. When looking at the degree distributions of real world networks, a pattern that is commonly found is that the majority of nodes have low degree, whereas a decreasing number of nodes display much higher values, up to a small minority of nodes having maximal values of degree. The degree values of real networks, in fact, often span over several orders of magnitude (Figure 1.4). This is the case for power grids, transportation networks, synapses in the brain as well as internal cell interactions. This is due to the fact that most real world networks maintain a similar organization at many different scales. This property of networks is referred to as *scale-free* organization, and is synthesised in the fact that the degree distribution of such networks is well approximated by a scale free distribution:

$$p(k) \sim k^{-\alpha}$$

where α is the exponent.

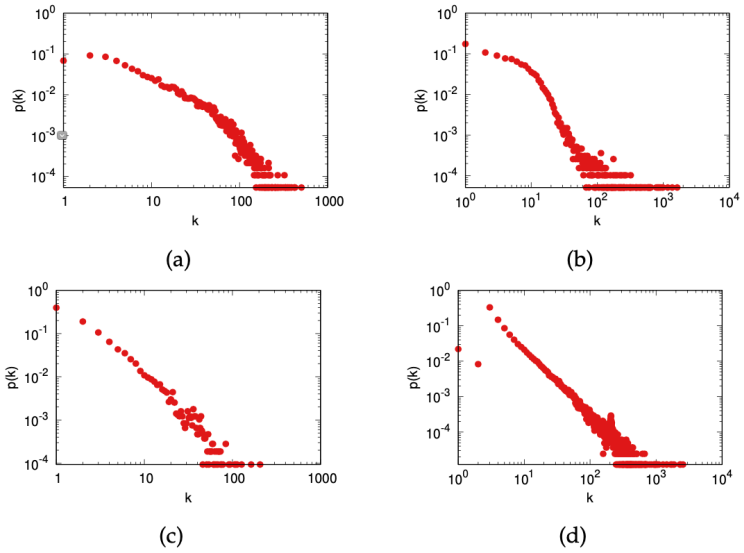

Figure 1.4. – Examples of degree distributions of real networks: (a) coauthorship in scientific publication; (b) coappearance of characters in the same comic book; (c) interactions of trust between PGP users; (d) connections through the Slashdot platform. Adapted from [49].

Paths and Distances In networks the physical distance between two vertices is replaced by *path length*: a *path* is a route running over the edges in a network, and its *length* is merely the number of edges the path is composed by. The shortest path between i and j is often referred to as the distance between nodes i and j, d_{ij}. Shortest paths do not contain loops or intersect themselves. In undirected graphs $d_{ij} = d_{ji}$, whereas in directed graphs d_{ij} and d_{ji} can differ. The largest shortest path d_{max} in a network is referred to as the *network diameter*, and corresponds to the maximal distance between two nodes in the network, whereas the average path length $\langle d \rangle$ is the average distance between nodes in a network, and for undirected networks it is defined as

$$\langle d \rangle = \frac{1}{N(N-1)} \sum_{i,j=1,\dots,N,\, j \neq i} d_{ij}$$

1.1.2. Random graphs and Null Models

The ultimate task of network science is to use a networked representation to gain insights into real world systems. As previously shown, many real networks are not well described by a regular lattice, but can instead have broad degree distributions as well as local fluctuations in the density of connections. However there are some regularities and symmetries that one can measure: in order to discern whether the result of a measurement is or not something that could have emerged by chance, one needs to compare the measurement on empirical data to a *random null model*. The

theory of random graphs, in which edges are distributed randomly, or following some simple rules, among the pairs of nodes finds massive use in this sense. This modeling procedure allows both to explain the origins of arising properties of real networks, as well as to compare measurements computed on real data to the same measurements on synthetic random networks [12, 49].

Data randomization An intuitive strategy to discern whether measurements computed on the original data deviate from what could be observed by chance is to perform randomization procedures on the data itself, and then compare the measure on the original data with that obtained for its randomized (reshuffled) version. Depending on the measure one wishes to compute, there is a variety of choices that one can make in order to preserve some key properties of the original data throughout the randomization procedure. We will see in the next sections and chapters some specific choices of preserving or breaking symmetries in the original data in order to test the significance of measurements.

Random Graphs Another possibility is to compare the measurements computed on empirical data to models of random graphs that have, for instance, the same size, i.e., number of nodes, of the original network. Random graph studies can be split into two main categories of random graphs: $G_{N,p}$ and $G_{N,L}$ models (defined in the works of [74] and [61], respectively). The difference lies in the choice of the quantities that one chooses to preserve in the random generation of the graph: in $G_{N,p}$ one defines the probability p that an edge is assigned to a pair of the vertices, while $G_{N,L}$ allows to fix the number of edges in the final network L. The $G_{N,p}$ model is particularly convenient to compute some statistical properties of random graph such as the degree distribution. The degree distribution of the $G_{N,p}$ model is a binomial distribution:

$$p_k = \binom{N-1}{k} p^k (1-p)^{N-1-k}.$$

We note that for $L << \frac{N(N-1)}{2}$ and $\langle k \rangle << N$ p_k becomes a Poisson distribution:

$$p_k = e^{-\langle k \rangle} \frac{\langle k \rangle^k}{k!}.$$

As previously discussed, real world networks have a tendency to have fat tailed degree distributions, with few nodes of high degree, and most of nodes with low degree and therefore deviate from the Poisson degree distribution of randomly generated networks.

1.1.3. Structures in networks

Real networks are typically made of interconnected subgraphs, i.e., subsets of vertices and edges of the overall network, of higher density of connections within them,

and more loosely connected to the rest of the network.

Clustering coefficient A nodal property that captures whether a node is bound to nodes that tend to densely interconnect with each other is the local *clustering coefficient*

$$C_i = \frac{2L_i}{k_i(k_i-1)}$$

where L_i is the number of edges between the nodes connected to node i (i's first-neighbours, or neighbours), and $C_i \in [0,1]$. Together with other node-wise parameters the local clustering coefficient can be of crucial help to understand the function of a node in a network: groups of nodes with high clustering coefficient can form *modules* and *communities* and other dense structures, whereas, for instance, nodes with lower clustering coefficient can represent the bridging connection between two dense clusters.

K-cores The decomposition of large complex networks into their highly interconnected parts helps to describe and investigate the complex topologies of real world networks. One of the first approaches in this spirit is the $k-$*core* decomposition of networks [6, 57]. A $k-$core is obtained by first removing from the network all vertices with degree lower than k, and, from the rest of vertices, removing those vertices whose degree dropped to values lower than k after the first step. The result is, when it exists, the $k-$core, i.e., the maximal subgraph of the original network composed of vertices of degree at least equal to k. Therefore, networks are organized as an ensemble of successively nested $k-$cores of increasing k (Figure 1.5). Such decomposition therefore allows to disentangle the hierarchical structure of complex networks.

Communities Other structures that shape the meso-scale organization of a network are its communities. The role of network communities and their interplay and mutual relations have in fact been of keen interest in many fields, from sociology [64], to medicine and biology [81] among others. Intuitively, a *community* is a group of nodes that have higher likelihood of connecting to one another than with nodes belonging to other communities (an example of easy to spot communities in a network can be found in Figure 1.6). The definition of a community is based on several specific notions:

— the *internal* and *external* degrees k_i^{int} and k_i^{ext} of a node i in a community, where the former refers to the number of edges connecting i to nodes in the same community and the latter to the number of edges linking i to nodes of other communities;

— the *intra-* and *inter-* cluster densities $\delta_{int}(C)$ and $\delta_{ext}(C)$ of a community C as the ratio between the existing internal (external) edges of C and the number of all possible internal (external) edges:

$$\delta_{int} = \frac{\#\ \ internal\ \ \ edges\ \ \ of\ \ \ C}{n_c(n_c-1)/2}, \tag{1.1}$$

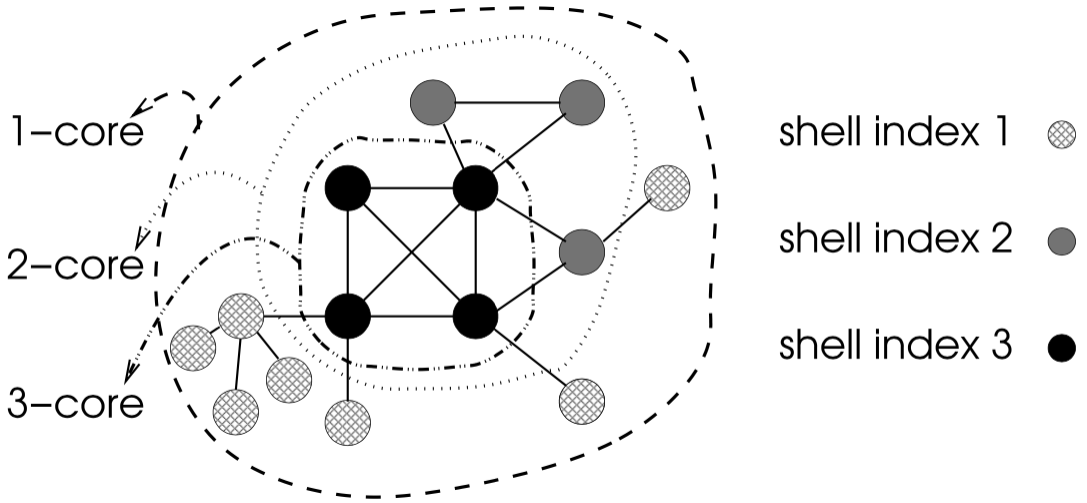

Figure 1.5. – Sketch of the $k-$core decomposition, adapted from [6]. Each closed line contains the nodes belonging to a given $k-$core, and different types of nodes correspond to different $k-$shells: a vertex has *shell index* k if it belongs to the $k-$core but not to the $(k+1)-$core and, therefore a $k-$*shell* S^k is composed by all the vertices of shell index k.

$$\delta_{ext} = \frac{\#\quad external\quad edges\quad of\quad C}{n_c(n_c-1)/2}, \tag{1.2}$$

where n_c is the number of nodes in C.

For C to be a community, δ_{int} is expected to be significantly higher than the density of the whole network, while δ_{ext} has to be much smaller. Another property of a community is its *connectedness*: for C to be a community there must a be a path between each pair of its nodes, that only runs through nodes included in C [64].

Modularity The pattern of connections amongst nodes that wire a random network are expected to be uniform, thus in random networks the presence of locally denser structures, communities, is not expected. Therefore by comparing the edge density of a community with the edge density of the same nodes obtained by a random null model one can determine whether the original community actually corresponds to a denser subgraph, or to a random local fluctuation in the edge density emerged by chance. In order to measure the quality of a partition into communities of a network the concept of *modularity* was introduced in terms of systematic deviations from random wiring of a network [29, 76]. Given a network of N nodes, L edges and a partition of the network into n_c communities, where each community $c = 1,\ldots,n_c$ has N_c nodes and L_c edges, if L_c is larger than the expected number of edges between the N_c vertices given the degree distribution of the network, than the subgraph C_c is really a community. The quality function that measures the deviation of the network's original adjacency matrix A_{ij} from the expected number of links if the network is

randomly generated p_{ij} is the *modularity* Q, defined as

$$Q = \frac{1}{2L} \sum_{(i,j) \in C_c} \left(A_{ij} - p_{ij} \right)$$

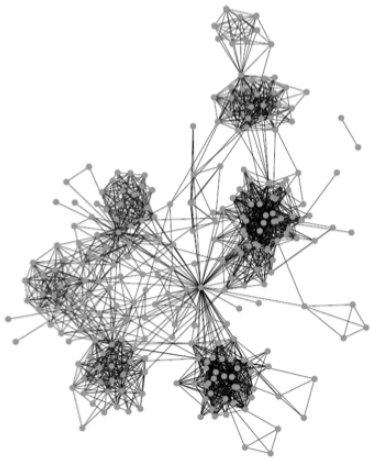

Figure 1.6. – Visualization of a network with community structure. In particular, this picture represents the network of Facebook friendships of a user [50].

1.1.4. Core-periphery and Rich Club

Some large scale networks have a common topology: a very densely connected set of core nodes, and a bunch of peripheral nodes linked only to few neighbors. What is surprising is that in many real networks the cores are denser than one would anticipate from the degree distribution of the network. This meso-scale organization of networks has been investigated in two main approaches, that resulted in two different definitions: *core-periphery* [53, 87], and *rich club* [48, 138], the latter focusing only on the role of core nodes.

Core-periphery

Two main approaches dominate the literature of methods to retrieve core-periphery structure in networks. The first is the *discrete model*, in which all nodes are divided into two groups: nodes with high degree of interconnectedness are considered core nodes while the others, remaining nodes, are the only sparsely connected periphery. Furthermore most peripheral nodes are more likely to be connected to core nodes than to the rest of the periphery, very much like the routes of public transportation in cities. In the discrete model such binary classification is achieved by maximizing the quantity $\sum_{uv} A_{uv}\Delta_{uv}$ where A is the adjacency matrix and Δ a matrix whose entry uv is equal to 1 if both of nodes u and v is in the core, 0 otherwise. The procedure to retrieve the optimal core-periphery partition for the network consists in maximizing $\sum_{uv} A_{uv}\Delta_{uv}$ by tuning Δ, as the adjacency matrix is fixed.

The second approach is the so called *continuous model*, where the restriction to two classes into which separate nodes is lost. In the continuous model rather than enforcing two classes of nodes, a *coreness* value is assigned to each node. In the simplest implementation of the model the quantity to be optimised is still $\sum_{uv} A_{uv}\Delta_{uv}$, yet Δ here is defined as $\Delta_{uv} = c_u c_v$, where c_u is the coreness of node u. For instance nodes in the blue circle in Figure 1.7 (right) have a value of coreness equal to 1, the nodes in the violet circle have coreness equal to 0.5 and those in the green outer circle, the periphery, have 0 coreness. The repertoire of methods to establish and assign the c_u values dives into more complex approaches, one of which we will describe in depth in the next chapters.

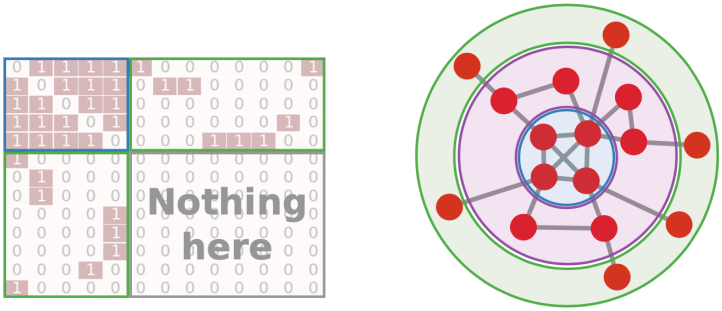

Figure 1.7. – **Discrete and Continuous models of core-periphery:** (left) the adjacency matrix of a toy model unweighted, undirected graph in the Discrete Model; in the top left diagonal block we can clearly see the core nodes being densely interconnected, whereas the peripheral nodes share only sparse connections with the core nodes (out of diagonal blocks), while they are not connected with each other. (right) a toy example of the continuous model where each concentric shell corresponds to layers of nodes with the same coreness values, radially decreasing from the center to the circumference. Adapted from [49].

The Rich Club phenomenon

For a static network the *rich club* coefficient is defined as the density of edges in the subset $S_{>k}$ of the $N_{>k}$ nodes with degree larger than k ([48, 179]):

$$\phi(k) = \frac{2E_{>k}}{N_{>k}(N_{>k}-1)}$$

where $E_{>k}$ is the number of edges connecting the $N_{>k}$ nodes. An increasing $\phi(k)$ indicates that nodes of larger degree tend to form increasingly connected groups of nodes ("rich club effect").

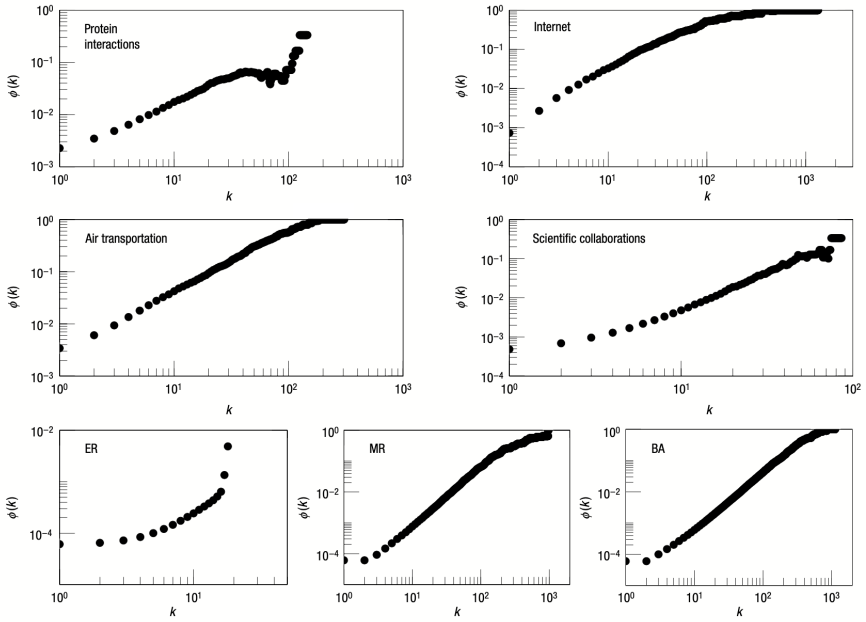

Figure 1.8. – **Rich-club ordering $\phi(k)$ for real networks**: rich-club coefficient $\phi(k)$ for four real world networks: a proteins interaction network, the internet, an air transportation network and a scientific collaboration network. The three plots on the bottom correspond to the distribution of $\phi(k)$ in three synthetic random networks: an Erdös-Rényi graph (ER), a graph generated with the Molloy-Reed algorithm with degree distribution $P(k) \sim k^{-3}$ (power law distributed degree), and the Barabasi-Albert model of preferential attachment producing a scale-free graph with power-law degree sequence with exponent $\gamma = 3$. Adapted from [48].

However, such effect can be present even in random networks [48], so that the rich club ordering is detected by comparing $\phi(k)$ with the value obtained for a random network with the same degree sequence as the original one, $\phi_{ran}(k)$, i.e., by studying the ratio

$$\rho(k) = \frac{\phi(k)}{\phi_{ran}(k)}$$

$\rho(k) > 1$ indicates indeed that the nodes with degree larger than k are more connected than by chance.

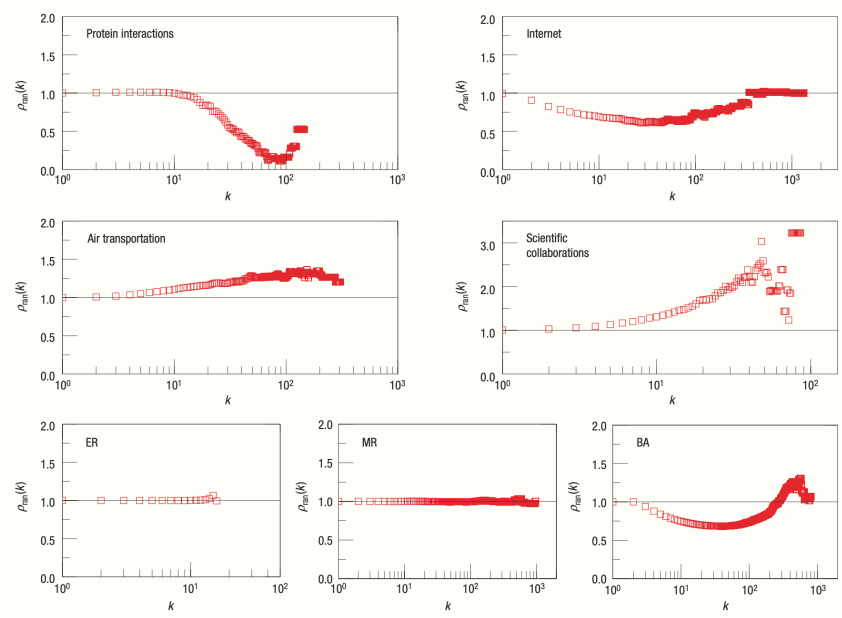

Figure 1.9. – $\rho(k)$: comparison of $\phi(k)$ of the original network and the null hypothesis ϕ_{ran}. $\rho(k) = \phi(k)/\phi_{ran}(k)$ is plotted as a function of k and compared to the baseline value 1.The protein interaction network and the internet map lack a rich club, whereas such a structure is present for the air transportation network and even more so for the scientific collaboration network. We note how the ER and MR random networks do not display any rich club whereas the BA network shows a mixed behaviour with high values of $\rho(k)$ for very high values of k. Adapted from [48].

1.1.5. Multilayer networks

In many real world systems agents that can be represented as nodes in a network, can display interactions of different types with each other. For instance, in social networks one can categorize edges based on the nature of the interaction that they represent. The natural result is the representation of a social system as multiple social networks using different types of interactions among the same set of individuals. The representation of a system that displays multiple kinds of interactions among the same agents as a network with multiple *layers*, with each of the layers corresponding to a different type of interaction, is referred to as a *multilayer network* [101]. In Figure 1.10.a-b are presented two equivalent representations of a multilayer network of participation to conferences of the same researchers: in 1.10.a the color of the layer corresponds to a specific conference, edges (solid black lines) in the three layers in the left column correspond to direct interactions ("talked to each other") between the nodes (researchers) at the corresponding conference (layer), whereas the edges connecting nodes on in the multilayer network on the right represent co-location interactions ("attended the same talk") between nodes. The dotted lines connect each node to its own copy in a different layer. Another way that is often used to visually

represent multilayer networks is shown in Figure 1.10.b, where the color of an edge corresponds to the conference where that interaction happened, and the line-styles of edges capture the different types of interactions

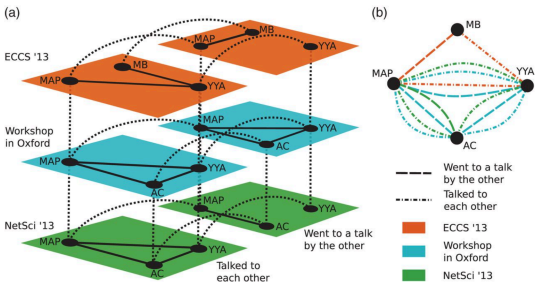

Figure 1.10. – Two visualizations of the same multilayer network: a) each node represents a researcher, the color of horizontal layers indicates a conference they attended, the two columns stand for two different kinds of interactions ("talked to each other", left, "went to a talk together", right); b) nodes represent researchers and the color and line-styles represent the multiple kind of interaction. Adapted from [101].

The simplest way to define the equivalent of the adjacency matrices for multilayer networks is in its tensor representation: a multilayer network of N nodes and d layers can be described through the tensor $A_{ij\alpha\beta}$ where $i, j = 1,\ldots,N$ are the vertices i and j while $\alpha,\beta = 1,\ldots,d$ are the layer indices. Such mathematical definition of multilayer graphs allowed to generalise the concepts of degree, centrality, underlying structures such as motifs and cliques to this class of networks, which is briefly introduced here, and further described in Chapter 2, as part of the work presented in this thesis focuses on a specific use of multilayer networks (see Chapter 4).

1.2. Temporal Networks

The evolution over time of a networked system can be described, in discrete time, as a series of instantaneous snapshots (static graphs) of the nodes and edges that interact at the specific corresponding time. This representation enables to capture the formation and disappearance over time of the edges connecting the different nodes in the network. Temporal, or time-varying, networks span from social systems, such as networks of person-to-person communication (emails, mobile phone messages and calls), co-location and face-to-face interactions, to molecular interaction networks in cells, infrastructural networks and, as we will see in detail in the following chapters, to networks in the brain.

1.2.1. Definition

We note that there exist two formal definitions of temporal networks [90]. Each of the two definitions can be used to represent ideally any time-evolving networked system, yet, depending on the system under study, one definition might be more suitable than the other. An *instant-event temporal network* $G(V,E)$ is defined by a set of nodes $V = \{1,\dots,N\}$ and a set of instant-events $E = \{e_1, e_2, \dots, e_E\}$, where each event $e_q = (i_q, j_q, t_q)$ describes an interaction between nodes i_q and j_q at time t_q. In the second definition of temporal network one takes into account also the duration of events and the temporal network $G(V,E)$ is therefore defined by the set of vertices $\mathcal{V}$ and by its set of events E where each event is now defined as $e_q = (i_q, j_q, t_q, \tau_q)$ and corresponds to the interaction between i_q and j_q that first happens at t_q and that lasts τ_q. In the work presented in the following chapters we will always use the first definition and refer to the instant-events $e_q = (i_q, j_q, t_q)$ as *temporal edges*.

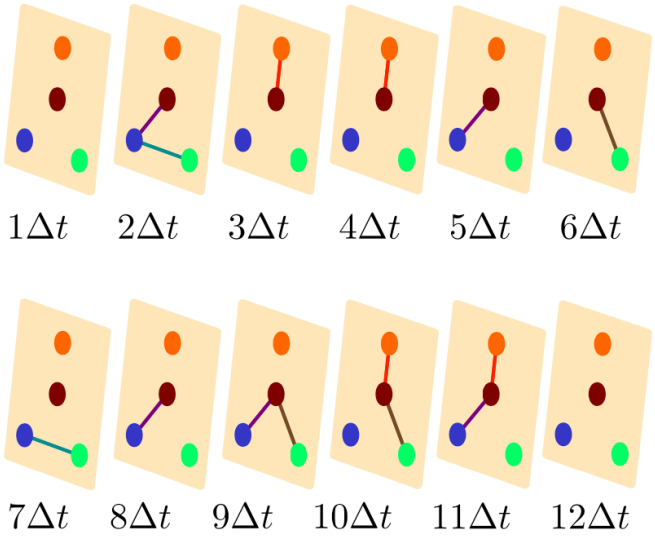

Figure 1.11. – **Snapshot-graph sequence:** visual representation of a temporal network as a series of instantaneous snapshots of the network at different multiples of the time-resolution Δt of the time-evolving networked system.

In terms of visual representation of a temporal network, there are two main existing approaches: the representation of a time-varying graph as a sequence of snapshots of the network is probably the most intuitive (Figure 1.11), and is called *snapshot-graph sequence*; however a second, more "edge-centric" representation exists, which is referred to as *link-timeline* network, and corresponds to diagrams such as the one described in Figure 1.12.A snapshot-graph sequence $G_T(T, \mathbf{G})$ represents a temporal network using a sequence of times $T = (t_1, t_2, \dots, t_T)$ and a sequence of graph snapshots $\mathbf{G} = (G_1, G_2, \dots, G_T)$ where the instantaneous graph G_q at time t_q is defined by the set of temporal edges present at the corresponding time. This representation makes

it easy to handle networks with a fixed time resolution Δt so that $t = \Delta t, 2\Delta t, \ldots, T$, as shown in Figure 1.11, and represents the approach that was favoured during the studies reported in this manuscript.

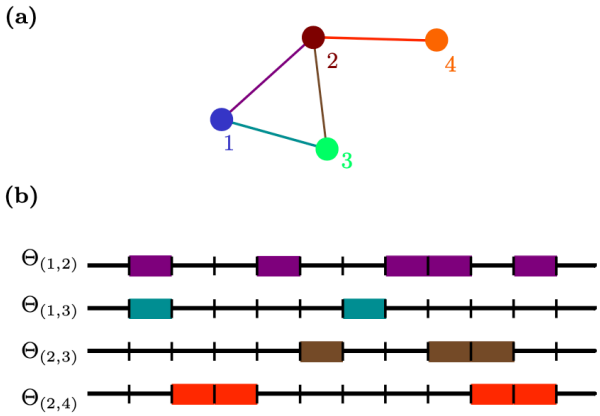

Figure 1.12. – **Link-timeline network:** a) a toy example of a graph in which each edge is highlighted in a different color; b) the link-time representation of the time-evolution of the network: each of the horizontal lines corresponds to a specific edge in the graph depicted in a), a block colored with the color of an edge indicates that the corresponding edge is present at that time.

Aggregated Networks

A first approach to study the properties of a temporal network is to analyse the relative time-*aggregated* network. An aggregated network is a static network $G = (V, E)$ with set of nodes V and set of edges E, in which an edge is drawn between two nodes i and j if they have at least shared one temporal edge, with a weight w_{ij} given by the number of temporal edges between i and j that occurred within the time period $[1, T]$ of the temporal aggregation. The degree k of a node in G is thus the number of distinct other nodes with which it has interacted at least once in $[1, T]$, and its strength s the total number of temporal edges it has participated to. As we will see in detail in Chapter 5, aggregated networks can be important to discern, for instance, groups or nodes that were frequently connected throughout the evolution of the temporal network, yet it yields no information on whether these connections ever happened *simultaneously*.

1.2.2. Time respecting paths and simultaneity

When the time dimension is included in the network representation, many of the definitions and measures used to described static graphs need rethinking or revising. A clear example can be found in the concept of *paths* in a temporal network. Paths

connecting nodes represent the routes along which the dynamics of any process taking place on top of the network can unfold. In a temporal graph paths need therefore to respect the time ordering of the temporal edges that form them, hence the definition of *time-respecting paths* as sequences of contacts (temporal edges) with non decreasing time. A time respecting path is therefore not only defined by the origin vertex i and the destination vertex j but also by the times t of the start of the path and that of its end t'. Since in different moments of the evolution a time-respecting path from i to j following the same edges might reappear, and even other time-respecting paths linking the two nodes yet following different routes could appear, time respecting paths are usually defined within some observation window $t \in [t_0, T]$. The set of nodes that can be reached by time respecting paths within a specific window from a node i is called the *set of influence* of i. The importance of time-respecting paths becomes evident in the application of temporal networks to the study of disease spreading: a time respecting path from an infected individual i to a susceptible one j can correspond to the series of temporal edges that a disease could be transmitted through to reach and infect j.
In the same spirit of the definition of time respecting paths, the structures that form the meso-scale fabric of temporal networks also depend on the co-occurrence, the *simultaneity*, or concurrency [122] of the edges connecting the vertices, as we will see in the following sections.

1.2.3. Temporal structures 1: $(k-\Delta)-$cores

The definition of structures traditionally retrieved and analysed in static networks need therefore to be revised in order to take into account the time dimension. In [68], the authors present a novel approach to perform the equivalent of a $k-$core decomposition on a static graph for a time varying network, introducing $(k,\Delta)-$*cores*, or *span cores*. In order to do so it is first necessary to introduce the concept of *temporal degree* d^i_Δ of a node i over a time interval Δ, as the number of other nodes to which i is constantly connected during the time interval. As Δ increases it is thus non-increasing. In other terms, d^i_Δ therefore represents the number of temporal edges connected to i that exist in *all timestamps* of the interval Δ. A $(k,\Delta)-$core is defined as a maximal set of vertices $C_{k,\Delta}$ such that $d^u_\Delta \geq k \forall\, u \in C_{k,\Delta}$. A span-core is therefore a set of vertices that defines a *cohesive* subgraph, where the *cohesion* property lies in the conditions on the two parameters k and Δ: vertices in the subgraph must have at least k temporal edges that last throughout the whole temporal span of duration Δ. The search for span-cores in temporal networks can give an idea of whether cohesive groups of nodes indeed exist in the system under study and also raise questions such as "what is the span-core of largest k and Δ"? Such structures are called *maximal* span-cores. These structures can impact the spreading processes on a temporal network [44]: the removal from the network of nodes involved in these highly cohesive structures can be an effective counter-measure against the spreading.

1.2.4. Randomized reference models for temporal networks

Ever since the birth of the theory of temporal networks, researchers have been interested in devising models that can explain a specific property of time-varying graphs or serve to produce synthetic temporal networks with desired, tunable characteristics that can therefore be used in computational experiments of dynamic processes. However, since the focus of this manuscript lies in the retrieval of meaningful structures, their mutual relations and their role with respect to the dynamical regimes that the networked system undergoes, in this section we introduce and discuss another class of null models for temporal networks, *randomized reference networks*, where the empirical network serves as input and randomization procedures remove some specific correlations.
A wide range of randomization procedures exist for temporal networks [70, 89]. Here, my focus is on the simultaneity and stability of interactions, which define the existence of temporally cohesive structures. As simultaneous interactions can occur simply by chance in periods of larger activity, I will consider some randomization procedures that preserve the temporal activity timeline, i.e., the number of temporal edges at each time step. Moreover, in order to investigate the role of temporality, one needs to consider procedures that keep either the whole structure of the aggregated network G, or at least the aggregated degree of each node. Following these motivations, here I describe three ways to randomize temporal networks among the methods described in [70], which are of great relevance for my work (see Chapter 5).

— *Timestamps shuffling*: this reshuffling procedure, denoted $P[w,t]$ in [70], randomly permutes the timestamps t_q of all temporal edges while keeping the nodes indices i_q and j_q fixed. This randomization therefore conserves the overall activity timeline of the network as well as the structure and weights of the edges in the aggregated graph G;
— *Event shuffling, or Topology-constrained snapshot shuffling*, denoted $P[\mathscr{L}, p(t,\tau)]$ in [70]: this procedure shuffles the contacts between existing links while keeping the contacts' starting time and duration, thus preserving contact duration statistics, global activity timeline and structure of the aggregated network.
— *Degree-constrained link shuffling*, denoted $P(k, p_{\mathscr{L}}(\Theta))$ in [70]: it permutes the edges in the aggregated graph and associated timelines between all node pairs (i,j) while keeping the aggregate degree k of each node fixed. It preserves the global activity timeline and the aggregated degree of each node, as well as the distribution of edge weights, but randomizes the structure of the aggregated network.

1.2.5. Temporal structures 2: temporal communities

A vast literature was developed to investigate the meso-scale structure and organization of time-varying networks. We saw how the $(k-\Delta)-$cores represent a first approach to uncover some hidden, cohesive structures in a temporal network. The search for *communities* in a temporal network represents an even more challenging

task: already in static graphs the very definition of a community as a densely interconnected subgraph, less connected to the rest of the network (possibly made of other dense subgraphs) is somewhat intuitive, yet, loose and generic. In temporal networks one needs to take into account the ongoing disappearance and reappearance of nodes and edges (Figure 1.13) the stability over time of the connections that make a community, as well as the nodes that are included/excluded into of out of the community throughout the network's evolution. These questions along with others, regarding also the *function* of communities with respect to either processes happening on the network as well as the process that the temporal network represents, have been asked and, as of now, only partially answered to by researchers [22, 72, 132, 153].

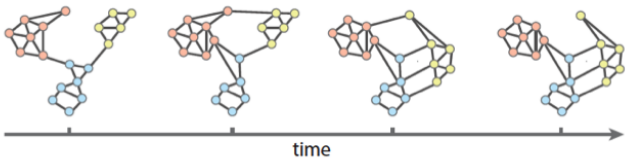

Figure 1.13. – **Communities in time:** visualization of a time series corresponding to the evolution in time of the community structure of a network. The network represented is a graph of brain connections [19]. We see how, from a time-frame to the next, some links vanish and others are formed: the shape and size of the different communities change and the network topology evolves.

Multislice Modularity Several approaches have been developed to detect the presence of densely interconnected communities in temporal networks. Here we focus on the approaches that generalise the concept of *modularity* to multi-layer and, thus, time-varying networks. The usual procedure for establishing a quality function, the modularity Q, as a direct count of intra-community edges (or edge weights) minus that expected at random fails to provide any information regarding the inter-layer couplings in multi-layer networks, and, as a consequence, in a temporal network, too, when the latter is interpreted as a multi-layer network in which each layer corresponds to the network at a specific time (snapshot-sequence temporal networks). In this representation, inter-layer couplings can be assigned between each node i at time t and the same node at the adjacent times $t-\Delta t$ and $t+\Delta t$, for instance, when node i has an instantaneous degree different from 0 in all three snapshots. In this setup, the quality function that is maximized in order to retrieve the optimal community partition of the temporal network is the *multislice* modularity $Q_{multislice}$ [132], defined as:

$$Q_{multislice} = \frac{1}{2\mu}\sum_{ijr}\left\{\left(A_{ijs}-\gamma_s\frac{k_{is}k_{js}}{2m_s}\right)\delta_{sr}+\delta_{ij}Cjsr\right\}\delta(g_{is},g_{jr})$$

where A_{ijs} is the multislice adjacency tensor, where i and j are vertex indices and s is the slice index (so the time index in temporal networks). The quantity μ corresponds to the sum over the degrees of all nodes in all slices, thus $\mu = \sum_{is} k_{is}$, and C_{jsr} is the interslice coupling matrix, thus informing on the existence or the weight of the inter-slice edge between copies of a node j in slices s and r. The multislice modularity $Q_{multislice}$, once maximized, thus ensures to retrieve the optimal partition of the temporal networks into communities that span over time intervals of varying length, simultaneously detecting communities across the whole time-evolution of a temporal network. The disadvantages of methods based on the optimization of this quality function lie in the complexity of existing algorithms, that therefore tend to perform poorly on temporal networks with a large set of nodes and large time duration.

Node dynamics across instantaneous communities An alternative approach, which will be further explained in the following chapters, which can be useful when dealing with large temporal networks, is to investigate the mutual relations among nodes with respect to their instantaneous (static, computed at each time stamp) community memberships. In other words, when it is computationally expensive to retrieve purely temporal communities in a dynamic network, one can retrieve the instantaneous partition of the network on each of its snapshots and then compute, within a desired time window, the probability of each pair of nodes to be found in the same community at the same time. The result, when the instantaneous community partitions are detected through modularity based approaches, is, for each time window w, the so called *module-allegiance*, or *association* matrix [22] T^w_{ij}, whose matrix element corresponds to the probability

$$T^w_{ij} = \sum_{t \in w} \frac{\delta(c^i(t), c^j(t))}{|w|},$$

where $c^i(t)$ and $c^j(t)$ are the communities of nodes i and j at time t, respectively, and $|w|$ is the length of the time window w.

1.3. Spreading Processes on networks

With *spreading processes* we refer to a whole variety of phenomena in which something, like a pathogen, a virus, but also an information, news (true or fake), as well as ideas, can spread through the nodes in a network following the fabric of its connections [16].
The vulnerability of our socio-econommic system to the danger of epidemics has become ever more evident in these last years. However the modeling of epidemic spreading on networks relies on a vast literature that preceded the COVID-19 pandemic. Although my thesis does not dwell directly on spreading processes, we will use them as a tool to characterize some network structures (Chapter 5). Therefore, here I provide a brief introduction to the basic concepts and models aimed at describing

how the spread of a disease unfolds onto a network.

SI model

In the *SI model* S represents the set of sane individuals that are therefore *susceptible* to the pathogen, i.e., they can be infected, whereas I corresponds to the set of infected individuals that can therefore transmit the pathogen to the susceptible ones. This model allows only one possible state transition for each individual: from susceptible to infected. The basic assumption in the traditional *SI* model is the so called *homogeneous mixing*: each susceptible individual has the same probability to come in contact with an infected person. Once an S individual comes in contact with an I individual, the transition probability of S into I (probability of contracting the pathogen) is one of the parameters of the model, β. Therefore, denoting $S(t)$ and $I(t)$ the time-varying numbers of susceptible individuals and infected individuals, respectively, the average number of new infections is:

$$\frac{dI(t)}{dt} = \beta\langle k\rangle \frac{S(t)I(t)}{N}$$

Where $N = S + I$ is the number of vertices in the network and $\langle k\rangle$ the average degree. Simplifying the equation defining $i(t) = I(t)/N$ and $s(t) = S(t)/N$ and solving the differential equation we obtain for the fraction of infected nodes:

$$i = \frac{1_0 e^{\beta\langle k\rangle t}}{1 - i_0 + i_0 e^{\beta\langle k\rangle t}}$$

where i_0 is the initial average number of infected individuals $i_0 = i(t = 0)$. When i is small, the solution of its differential equation is well approximated by an exponential $i(t) \approx i_0 e^{\beta\langle k\rangle t}$. This solution suggests how the time scale $\tau = \frac{1}{\beta\langle k\rangle}$ of the prevalence of infected individuals is inversely proportional to the infection rate β: the larger the infection rate, the faster the spreading. In this model the epidemic always spreads to eventually infect the whole population, and only stops when the network becomes saturated by infected individuals and there are no more susceptible vertices to infect: therefore when $i \to 1$.

SIS model

The *Susceptible-Infected-Susceptible* adds a fundamental change to the previous model: a susceptible individual, once infected, can overcome the pathogen, recover, and become susceptible again. Therefore in this model there are two possible state transitions: $S \to I$ and $I \to S$. The $S \to I$ transition happens with rate β upon contact as in the SI model, while the transition $I \to S$ is spontaneous and occurs with fixed rate μ. The differential equation for the fraction of infected nodes in the network thus becomes:

$$\frac{di(t)}{dt} = \beta\langle k\rangle i(t)\big(1 - i(t)\big) - \mu i(t),$$

which, neglecting the i^2 term, becomes the linear equation:

$$\frac{di(t)}{dt} = -\mu i(t) + \beta\langle k\rangle i(t),$$

with solution

$$i(t) \sim i_0 e^{-t/\tau},$$

where $\frac{1}{\tau} = \beta\langle k\rangle - \mu$. This is a relevant difference in comparison to the SI model. In fact, the time-scale of the spreading depends both on the spreading rate β and on the recovery rate μ: if the recovery rate is large enough than the epidemic will not spread across the whole population, instead it will eventually die out, since individuals will recover more quickly than the rate with which they can be infected. This leads to the definition of the *epidemic threshold*:

$$\frac{1}{\tau} = \mu(R_0 - 1) \geq 0, \tag{1.3}$$

where $R_0 = \beta\langle k\rangle/\mu$ is the reproductive rate of the SIS model, which has to be larger than 1 for the spreading to occur. This allows, for instance, if the recovery rate of a specific disease is known, to define the critical value of the infection rate β_c which would cause the spreading of the infection: $\beta_c = \mu/\langle k\rangle$.

In these two sections however, we introduced the SI and SIS models under the assumption of homogeneous mixing: each individual in the network has approximately the same number of edges $k \approx \langle k\rangle$. Such property, as seen in other sections, is not common in real networks that, for example, can have fat-tailed degree distributions. Refined approaches taking into account the heterogeneity of degrees, such as heterogeneous mean-field approaches [60, 77], find the epidemic threshold as the condition:

$$\frac{\beta}{\mu} = \frac{\langle k\rangle}{\langle k^2\rangle - \langle k\rangle}. \tag{1.4}$$

This implies, for example, that networks with fat-tailed degree distributions, where $\langle k^2\rangle \to \infty$ in the limit of infinite size of the network, yield a null epidemic threshold. We can intuitively explain this by the fact that in power-law degree-distributed networks once a hub node has become infected it can spread the pathogen to many other nodes, and, in particular, more likely to other hub nodes, thus making the spreading faster. The study of spreading processes, described by means of the SI and the SIS models, has been extended to temporal networks, in order to investigate the relation between the time-varying fabric of connections in the network and the diffusion of a pathogen unfolding on top of it [90, 122]. In this context we therefore have two intertwined time-scales: the time-scale of the spreading process and that of the evolution of the network. When the two time scales differ significantly, it is possible to distinguish two limiting regimes: one in which the network evolves on a much slower time-scale and can therefore be regarded as static w.r.t. the spreading; a second in which the evolution of the network is so rapid that only its time-averaged properties are relevant for the spreading dynamics. Several approaches have been put forward to study the

case in which the two time-scales are similar, and thus the evolution of the network affects the spreading from a time-stamp to the next [96, 98]. A unifying framework to compute the epidemic threshold in temporal networks is presented in [169], an approach that we will use in Chapter 5 to evaluate the effect of a specific structure in temporal networks.

2. Network Neuroscience: From neurons to networks in the brain

In this chapter I introduce and review the three main definitions of networks, or *connectivity*, in systems neuroscience: *structural*, *functional* and *effective* connectivity. I will focus in the following sections on the different nature of interactions that each of these classes of networks corresponds to, and will present some examples, stressing the ubiquity of such networks at virtually all spatial scales in the nervous systems. I will summarize some of the main findings in term of network-theoretic properties of structural and functional networks, dwelling on the complex relationship between these two layers of connectivity in brain networks. I will discuss how the missing link, allowing to bridge structure and function within the same bigger picture, is dynamics. This leads to the introduction of *dynamic Functional Connectivity* and the following need to represent and analyse time-varying functional networks as temporal networks. I will stress some key properties of brain temporal networks that represent the foundation of my own work, described later in chapters 3, 4 and 5. In the last two sections I will briefly introduce the notion of *cell assembly*, a concept that is intertwined with transient, time-varying micro-scale functional networks, dedicating particular attention to their presence and role in the hippocampus; then I will review the main implications of a particular condition, epilepsy, on micro and macro-scale brain functional networks. All together, this introductive chapter reviews the main concepts and ideas underlying my work in network-neuroscience.

2.1. Brain connectivity

With *connectivity* we refer to patterns of connections among elementary entities in the brain, such as individual neurons at the micro-scale, neuronal populations or assemblies at the meso-scale up to brain regions at the macro-scale, depending on the scale of the observation. Connectivity in the brain, i.e., brain networks, can be divided into three main classes depending on what the edges in this networks represent:

Structural Connectivity represents the physical, anatomical connections linking together neurons, populations of neurons and brain areas.

Functional Connectivity corresponds to brain networks whose edges represent statistical inter-dependencies between the *activities* of pairs of nodes.

Effective Connectivity where edges of these directed networks correspond to *causal* relationships. I will disambiguate in the following sections how networks falling into this class can be obtained through model-based (that in a way can be seen as a synthesis of structural and functional connectivity) and data-driven methods.

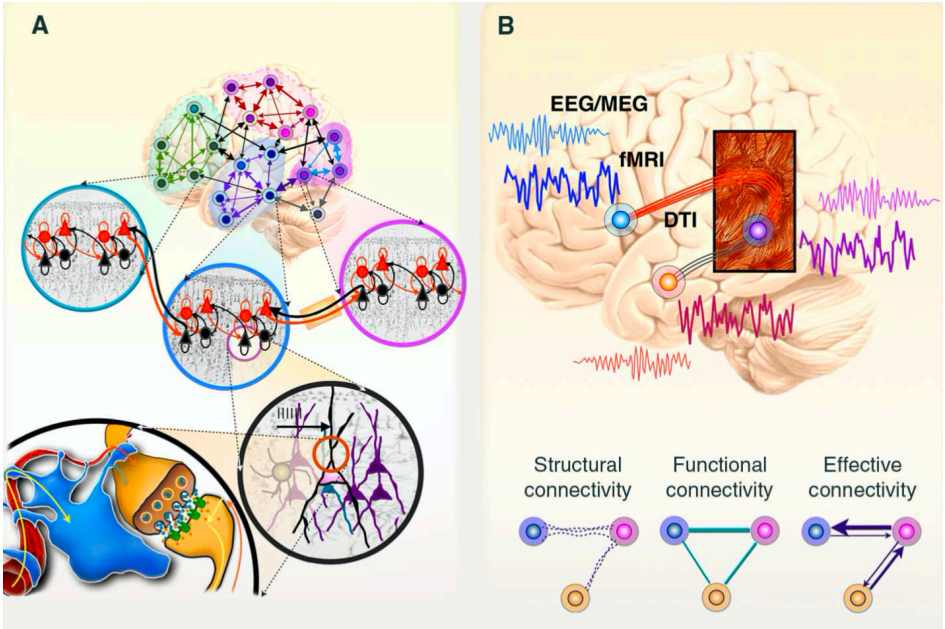

Figure 2.1. – A) schematic representation of the multiscale organization of brain networks: macro-scale networks are composed of nodes that represent themselves coarse-grained entities, and zooming into the brain we can find finer grained meso and micro-scale networks. B) schematic representation of the different recorded signals that can lead to extract structural (through diffusion tensor imaging, DTI) and functional (for instance by means of functional magnetic resonance imaging, fMRI, or electro and magneto encephalography, EEG and MEG, respectively) networks and the three kinds of connectivity that can be extracted from these signals: structural, functional and effective connectivity (bottom). Adapted from [140]

.

2.1.1. Structural connectivity

In neuroscience, with structural connectivity we refer to the description of anatomical connections physically existing between network nodes. Thus, the edges connecting the elementary agents of a nervous system are encoded in the *structural*

connectivity matrix SC, i.e., an adjacency matrix A_{ij} that usually corresponds to a weighted, directed graph. In more evolved nervous systems, structural networks can be found at several spatial scales (Figure 2.1.A), thus edges and nodes in the graph can represent different entities at different scales: from synaptic connections linking together individual neurons at the microscale, to networks of populations of neurons at the mesocale, up to separate brain regions connected by inter-regional fiber pathways at the macroscale. At all these scales, one usually refers to the network of all structural connections between probed network nodes as *connectome* [160]. In order to extract the connectome at each of these scales one has to overcome some challenges that also depend on the scale of observation. Such challenges are related to two aspects of the anatomy of the brain:

1. the connectome is not a static entity, rather it is an ever-evolving re-wiring of the anatomical links between nodes, with time scales that also depend on the spatial scale of observation, i.e., faster dynamics at the micro-scale. This represents the biggest obstacle when studying the micro-circuitry at the smallest spatial scale in the brain;
2. the unit elements that can be represented as nodes in a structural network are harder to delineate as the spatial-scale of observation widens: while neurons are relatively easy to identify and well defined, in larger scale networks brain areas and neural populations are less clearly demarcated.

Therefore different techniques are needed to properly extract SC information at different scales, such as: semi-automated collation of hundreds of electron microscopy pictures to track cellular and axonal sections contours and perform 3D cell reconstructions [31]; injections of tracers to track selective connectivity preferences within brain regions [8], systems of few regions [13], or even entire cortex [116]; magnetic resonance imaging (MRI) techniques, such as Diffusion Tensor Imaging (DTI), able to visualize and track bundles of white-matter fibers crossing long distances between separated regions [79] (Figure 2.1.B).

Network Properties of SC

Studies of SC in neuroscience have involved intensive use of graph theoretical tools in the effort to search for general organizational principles in terms of network topography or wiring optimisation, as well as to identify underlying structures. Here are some formative examples of graph theoretical properties of structural brain networks at different scales.

When used to investigate the network properties of the microcircuitry of the brain, these approaches showed, for instance, that pyramidal neurons in the somato-sensory cortex of rats have a complex topological organization [145]: they are not arranged randomly, nor in a regular lattice, but as small-world networks without hubs. In fact, when computing the distance-dependent connection probability (accounted for as a measure of structural connectivity) between each pair of neurons, the assessment of the significance of sub-networks including 3 to 8 neurons in the empirical data

with respect to a null model, revealed the presence of over-represented connectivity patterns made of neighboring neurons (synaptic edges of length $50\mu m$), where no neuron had significantly larger degree compared to the others. Interestingly, when gradually taking into account spatially longer connections, the most densely connected groups, clusters, of neurons involved cells separated by mean distances of $100–125\mu m$ [118, 145]. In this scenario, a general tendency of pairs of neurons to connect to each other more likely if both are already connected to a common neuron was revealed, in analogy with the mutual acquaintance rule observed in some social systems [97], but without the typical hub-like behavior. A similar architecture, characterised by a globally sparse, yet, locally clustered brain connectivity with few long-range edges that ensure short paths of communication between virtually any pair of nodes, has been found in large-scale structural networks, such as, for instance, the macaque visual cortex and the cat cortex [23]. Here, however, hub nodes have indeed been identified as hub regions connected to denser local clusters of nodes and other hub nodes involved in other clusters. Such universal property of brain structural connectivity has been associated to the need, at any scale in the brain, to minimize the wiring cost of its physical connections while preserving the complexity of the dynamics of information flow [37].

Network theoretic measures in micro and macro-scale structural networks revealed the presence of relevant network structures. For instance a rich club architecture was found in a variety of SCs, ranging from the neuronal connectome of nematode worm *C. elegans* [167] (Figure 2.2), to the large scale human connectome [79, 85].

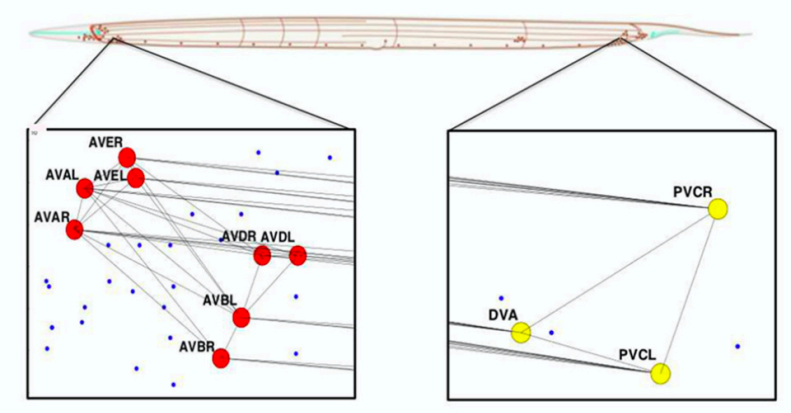

Figure 2.2. – Rich club of the C. Elegans' connectome shown in the context of the full body. Nodes are only located in the head (red) and tail (yellow) and the edges represent synaptic connections among neurons. Adapted from [167]

.

Altogether these studies highlight the tendency of highly connected nodes, repre-

senting *hubs* of the networked fabric of the structural connectivity, to be more densely connected to each other than what expected solely from their degree. Brain areas that are part of the rich club of the human connectome (Figure 2.3) are suggested to be communication hubs which, instead of operating individually, act as a strongly interlinked collective [85]: a possible interpretation is that such dense structure of prominent nodes ensures the resilience of the flow of information in case of malfunction of an individual hub.

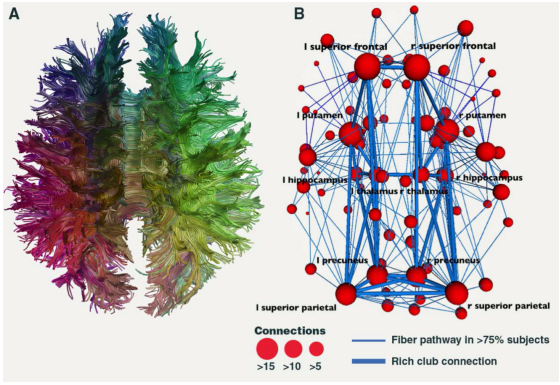

Figure 2.3. – A) reconstruction of the human connectome with DTI and the relative rich club organization in B). Adapted from [85].

In summary, the structural connectivity at the micro, meso and macro-scale in the brain seems to be characterised by the existence of local clusters, or communities of nodes, where nodes are densely interconnected within the same clusters. Studies like [85, 167] stress that clusters are connected to each other through fewer prominent, highly connected nodes, i.e. true *connecting hubs*: such important elements are densely connected to each other through the relatively few long range structural links, forming a collective, hierarchically prominent structure which is resilient against the failure or malfunction of individual hubs.

2.1.2. Functional Connectivity

We have seen how brain network nodes, neurons, populations of neurons or brain regions, are wired together. Information, some sort of coded messages, can travel along those physical connections. All information processing related to our perception, cognition and behaviour is believed to originate and arise from the very microscopic mutual exchange of *spikes* (propagating pulses of electric depolarization of the cell membrane, able to elicit neurotransmitter release at synaptic terminals) between pairs of neurons with connected synapses. Spatiotemporal patterns of spikes represent those coded messages: spike-encoded information can thus be copied, transferred, stored and merged between components linked by the SC. These computational operations are distributed along the structural connections and ultimately underlie functions and behaviours, thus they can be interpreted as giving rise to another kind

of networks, in which the edges represent the amount of statistical inter-dependency of the activities of two vertices: *Functional Connectivity* (FC).

Some functional metrics used to extract FC define the interaction between nodes as the "synchrony" of the fluctuations and modulations of node activities. For instance, measuring the linear covariance between the fluctuations in activity of brain regions during functional MRI (Figure 2.4) by means of Pearson's and Spearman's rank *correlation coefficients* (CC), represents a common way to extract the FC. As an extension of linear CC, *mutual information* (MI) provides a more general measure of the dependence between signals, capturing in principle also nonlinear relations, as I will describe in detail in the following sections.

Since neural activity is known to oscillate simultaneously at different frequency bands [38, 174] analyses of FC of synchronization are often conducted in the spectral domain. Measures that generalize linear correlation from the time to the spectral domain of more complex oscillating signals, such as those produced by coarse grained neural populations, use the notions of coherence or of phase synchronization [152, 171] and phase-locking value [106]. While, at the micro-scale, individual neurons are not necessarily oscillating and can keep firing in irregular manner, neuronal populations can collectively oscillate, due to the fluctuating interplay between excitatory and inhibitory currents [36]. The *communication through coherence* [66] hypothesis suggests that these collective oscillations cause periodic fluctuations in the excitability of neurons in coarse grained populations: thus structurally connected neural populations can communicate, i.e., be *functionally* linked, only if their local activity fluctuations are aligned in phase.

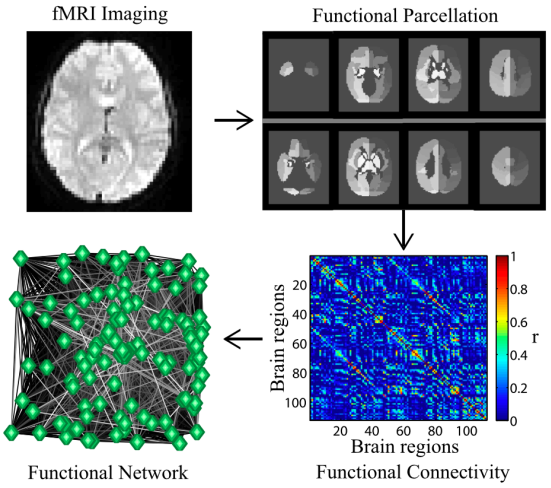

Figure 2.4. – Raw fMRI data (Upper Left) from a subject's brain; signals originate from cortical structures, which constitute the network's nodes (Upper Right). The functional connectivity, constituting the network edges, between two cortical structures is given in this case by a Pearson correlation between the mean regional activity signals (Lower Right). The resulting N × N correlation matrix represents a subject-specific weighted functional brain network (Lower Left). Adapted from [20].

In general, once a measure to evaluate the FC has been chosen, an FC matrix is extracted from data: FC corresponds to yet another adjacency matrix, where the matrix element FC_{ij} reflects the amount of *functional* interaction between nodes at the relative scale of observation. If the chosen measure is symmetric, then the resulting FC corresponds to an undirected network. I will now focus now solely on undirected FCs, while leaving the description and discussion of directed FC measures to the next section.

Network analysis of functional networks

Network-theoretic analyses of brain functional networks have highlighted some key properties of FC that partly reflect the organizational principles observed in structural connectivity. For instance, in [4] graph theoretic analysis of functional networks, extracted from resting-state fMRI recordings of human healthy patients, revealed the presence of a small-world topology. Such property was reflected in a global sparsity of the network, with more densely connected local subgraphs - where information outgoing from one node can reach another node in a subgraph through a short path - and few long range edges linking hub nodes (Figure 2.5). These hub brain regions where defined by their high level of connectedness, representing the few nodes with higher degree in the degree distribution of the overall graph. This topological organization of the network was reported to enhance the resilience of the system to *targeted attack*, which was evaluated by gradually eliminating each hub node, and all

of its connections, from the graph and measuring the size and average path length of the largest cluster in the remaining network. This procedure was repeated on a scale-free random network and the comparison between the analyses carried out on empirical and synthetic networks highlighted the tendency of brain functional networks to preserve higher largest-cluster size and relative lower average path length for larger portions of removed hub nodes.

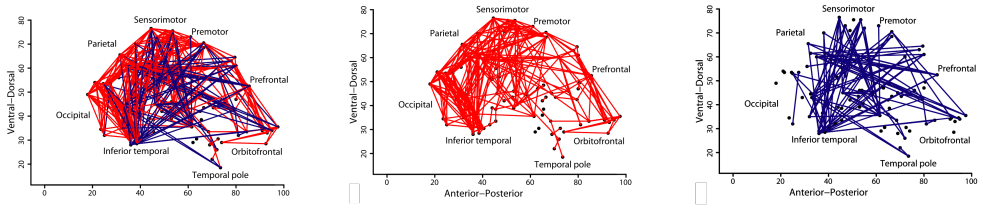

Figure 2.5. – Anatomical map of a small-world human brain functional network. Left, Four hundred five undirected edges, 10% of the possible inter-regional connections, are shown in a sagittal view of the right side of the brain. Edges representing connections between nodes separated by a small distance (< 7.5 cm) are red; edges representing connections between nodes separated by large distance (> 7.5 cm) are blue. Center, Short-distance connections are shown separately in red. Right, Long-distance connections, thus linking members of the rich-club, are shown separately in blue. Adapted from [4].

Furthermore, the small-worldness of brain networks was shown to play a central role in terms of network efficiency and cost [2]. The *global* efficiency E_{global} of a network is defined in terms of the minimum path length between any pair of nodes L_{ij} in the network, and is a measure of the efficiency of information transfer along the edges of a network:

$$E_{global} = \frac{1}{N(N-1)} \sum_{i \neq j} \frac{1}{L_{ij}},$$

whereas the *nodal* and *local* efficiency are defined defined as:

$$E_{nodal}(i) = \frac{1}{N} \sum_{j} \frac{1}{L_{ij}},$$

$$E_{loacl} = \frac{1}{N_{G_i}(N_{G_i}-1)} \sum_{j,k \in G_i} \frac{1}{L_{jk}}.$$

Global and local efficiencies were measured as a function of variable wiring cost, or density, of the network $0.01 \leq K \leq 0.5$, where K represents the fraction of all $N(N-1)/2$ possible edges in a (undirected) graph. The efficiency curves (Figure 2.6) of the brain networks were compared to the same curves evaluated for a regular lattice and for a random network: brain networks had global efficiency greater than the lattice but lower than the random graph, and local efficiency greater than random but smaller than lattice. The functional brain networks extracted from fMRI recordings [2] came from two cohorts of patients, one constituted by young patients, and the second group made of older members, and comparison of the local and global efficiencies for the two groups revealed significant differences, with an overall reduction of efficiency associated to aging.

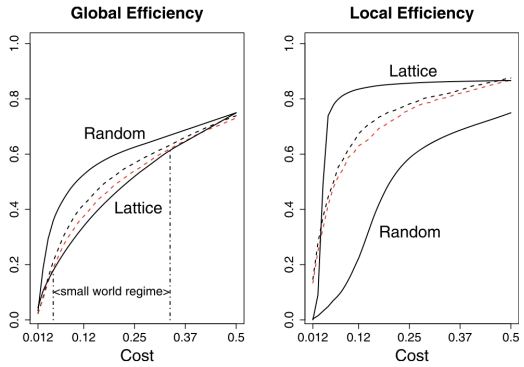

Figure 2.6. – Global and local efficiency (y-axis) as a function of cost (or density of the network, x-axis) for a random graph, a regular lattice, and brain networks. For all networks, global and local efficiency increase with cost; the random graph has greater global efficiency than the lattice; the lattice has greater local efficiency than the random graph. On average young brain networks (black broken lines) and old brain networks (red broken lines) have efficiency curves located between the limiting cases of random and lattice topology. Adapted from [2].

The local modular structure that was found in human connectomes was also observed in large scale brain functional networks [3], with node hubs playing a key role in intra-community connections. Interestingly, when comparing global network measures (small-worldness, high clustering and global efficiency, modularity) of the FC of healthy controls and comatose patients, no significant differences where found. This suggested that global functional network properties are homeostatically conserved even under very severe clinical conditions. However, the finer grained analysis of these networks highlighted a large decrease, in functional networks of comatose patients, of the degree of nodes that represented hub regions in the healthy volunteers. Conversely, peripheral nodes in the healthy FC became hub regions in patients. Furthermore a higher variability of the modular structure of the network was observed across patients.

2.1.3. Directed Functional connectivity and Effective Connectivity

Other measures of FC go beyond synchrony or correlation, in the attempt to reflect causal influence. Unlike correlation, which is symmetric and thus give rise to undirected functional networks, measures of causal interdependence between time-series of neural activity give rise to directed networks. An intuitive way to account for the direction of interaction can be to assess the temporal precedence of the "causing" on the "caused" fluctuation. This can be achieved for instance by using lagged cross-correlation or mutual information rather than zero-lag correlation [108], since the effect cannot precede the cause. In a model-free approach, causality can be captured by showing that consideration of the past activity of a putative causal source region improves the prediction of the future activity of a target region, as in Granger Causality analyses of neural time-series [35, 78].

While undirected (linear correlation, coherence) and directed (Granger Causality) measures of FC are pure measurements of statistical interdependencies performed on time series, with *Effective Connectivity* we refer to the parameter of a model aiming at explaining such dependencies. In the framework of *Dynamic Causal Modeling* [67], for instance, effective connectivity plays the role of a parameter in a model that describes the motion, or flow, of neuronal or physiological states: such parameter controls how the state of a certain brain area, influences the motion or flow of another brain area. In this framework different models describing the dynamics can be compared and selected by fitting the synthetic functional networks they give rise to, to the empirical ones that they to reproduce. In this optimization procedure, the resulting set of model parameters that describe the *causal* (thus, in an interventional sense) edges among nodes corresponds to the effective connectivity.

2.2. Bridging Structure and Function: dynamics

The definitions of SC and FC presented in the previous sections could be seen as independent: one can in fact extract the FC by means of the analyses of multivariate neuronal activity time series, at any spatial scale, without any previous knowledge about the morphology and the SC of the neural system under study. Such interpretation does not allow to unravel the connection between the physical wiring linking the anatomical parts of the brain that then act as computational units, interacting by means of exchange and processing of information, whose correlated or synchronous activities in turn give rise to functional networks. Another approach tends to consider SC as the primary explanation for the routing of information in brain networks: in this view, which target should receive the information conveyed by neural activity, or where information should be "pulled" from, thus mechanisms that should be reflected by the FC, are entirely determined by the SC. Indeed SC and FC are very similar, e.g. in terms of network properties: small-worldness, high-clustering, high efficency, fat tailed degree distributions. However, the rate of change of the FC on behavioral time

scales is faster when compared to physiological processes reshaping and rewiring SC, at least at the meso and macro-scale, which suggests that FC cannot correspond to a passive mirror of the underlying SC. A promising view proposes that the FC is in fact the measurable product of underlying collective dynamics. In this theoretical setup [24, 26] alternative regimes of system dynamics, or *states* within the *dynome* [103] (i.e., the dynamical repertoire [73]) of a system would give rise to alternative configurations of the FC on top of a constant underlying SC, phenomena that is referred to as *functional multiplicity*. Analogously, systems with different anatomical connections, i.e., different SC, can nevertheless display equivalent dynamical regimes [115] giving rise to similar FC (*structural degeneracy*). In other words if SC represents the physical pathways along which the communication of information among nodes can happen, FC represents the observable that can serve as proxy for the communication between nodes: yet the real underlying communication dynamics unfolding on top of the SC and giving rise to a whole repertoire of FCs remains unknown, as of now, and represents the key aspect capable of linking structure and function together (Figure 2.7).

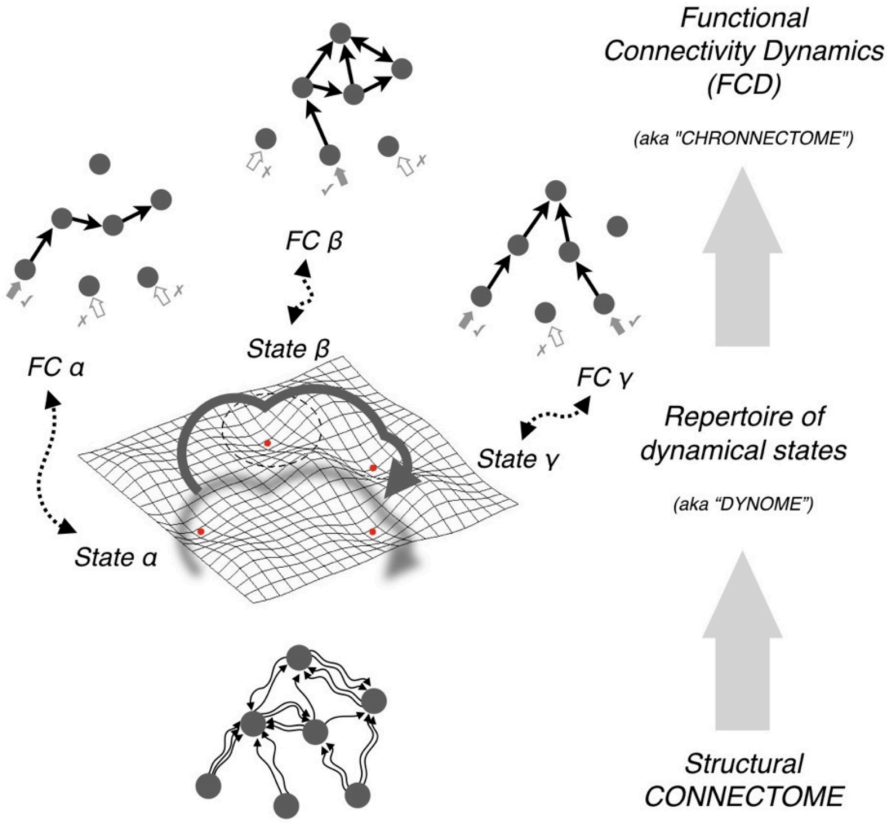

Figure 2.7. – The SC of a neuronal circuit shapes but does not fully determine neural dynamics. The set of possible dynamical states compatible with a given connectome constitutes its associated "dynome", or internal repertoire of available dynamical modes. Every dynamical state implements a different way of exchanging information between network units, leading to alternative functional connectivities. Eventually, as a result of the stochastic sampling of the dynome, switching transitions between these many possible functional connectivity (FC) networks occur giving rise to non trivial functional connectivity dynamics (FCD), also referred to as the "chronnectome". Adapted from [26].

In the attempt of unveiling this hidden relation, computational simulations of virtual brain models that take into account the empirical SC, but also non linear dynamics close to critical transitions [54, 93], come to the similar conclusion that a whole state-space of configurations of functional connectivity can arise from the same structural connectivity pattern. Virtual brain models tuned to regimes maximizing the degeneracy of their *dynome*, sampled via a noise-driven exploration, also succeed in reproducing qualitatively the switching *chronnectome* observed in resting state fMRI [80] (Figure 2.7). In these studies, large-scale brain networks are described as systems driven away from dynamical equilibrium by noise, and the following exploration of the state space results in the transient manifestations of different configurations of the FC.

This perspective has inspired practical, potentially clinically-useful applications of the links existing between SC and FC via dynamics. For instance an effective method to fill the gaps in both structural and functional information about clinical patients (affected by Alzheimer' disease) relies on the possibility to infer virtual SC from empirically extracted FC, and vice versa [9] (Figure 2.8).

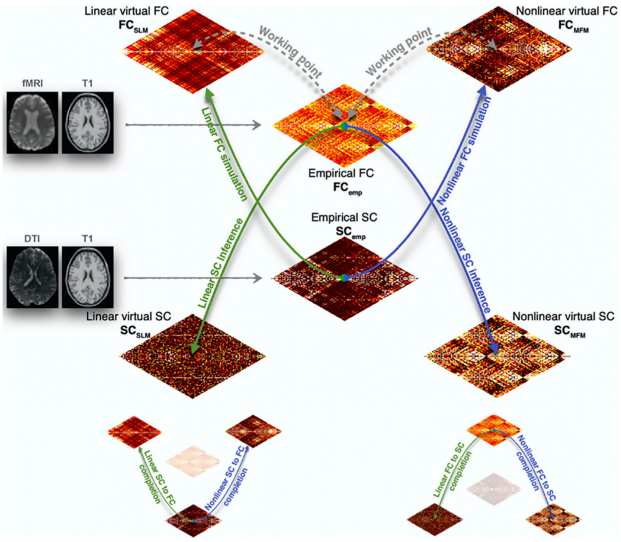

Figure 2.8. – Schematic representation of how the process of inferring *virtual* FC from empirical SC, or virtual SC from empirical FC in order to complete neuroimaging data of patients. Adapted from [9].

2.2.1. Dynamical Functional Connectivity

If it is dynamics that gives rise to the repertoire of FC that a neural system can *visit* throughout its time evolution (Figure 2.7), then it is intuitive to describe the FC as a temporal, rather than static, network. In fact the time resolved analysis of multivariate time series of general activity of nodes in a neural system, by means of a sliding time window in which to compute such measures, gave rise to the concept of *dynamic Functional Connectivity*, dFC. The time-varying nature of the FC can in fact be captured, for instance, by measuring the correlation between each pair of simulated resting-state BOLD signals [80] within a time-interval that is then shifted forward in time. The result is an FC matrix for each time-window, and thus a stream of FCs for the whole simulated recording (Figure 2.9): this representation is intuitively translatable into a snapshot-sequence temporal network (see Chapter 1).

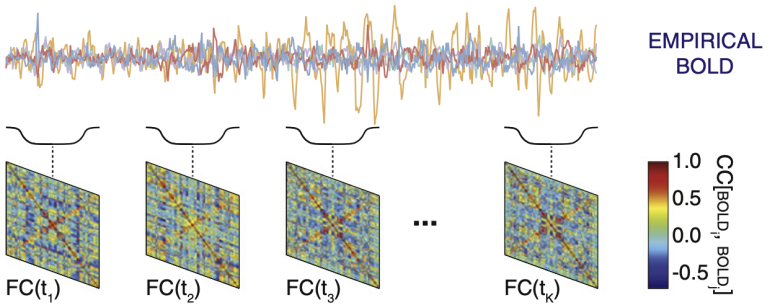

Figure 2.9. – FC networks extracted from empirical resting state BOLD signals in a time-windowed approach evolve over time. Adapted from [80].

In order to assess the variability of FCs within the overall stream of time-resolved functional networks, one can measure the correlation (or similarity, along with a whole repertoire of measures of distances between matrices) between every pair of FC matrices (instant snapshots in the temporal network): the result is a correlation matrix $CC\big(FC(t_1), FC(t2)\big)$, whose axis both represent time windows, and where each matrix element expresses the correlation between the FCs extracted in windows t_1 and t_2, respectively, that is referred to as *dynamic Functional Connectivity* (dFC) matrix (Figure 2.10).

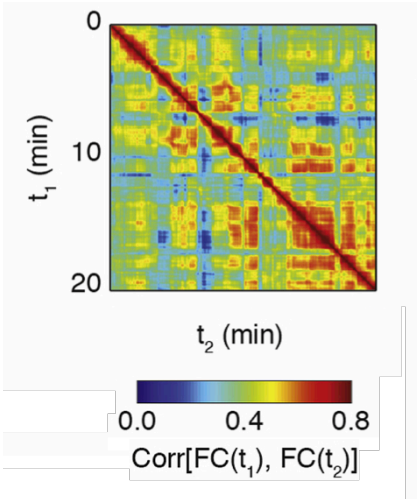

Figure 2.10. – An example of dFC matrix extracted from fMRI recordings of human patients. The matrix element $dFC(t_1, t_2)$ corresponds to the linear correlation $Corr[FC(t_1), FC(t_2)]$ between the FCs at times t_1 and t_2,respectively (color-bar in the figure). Blocks colored in more intense red correspond to different epochs of highly correlated FC matrices: FC states. Adapted from [25].

The presence of diagonal and out-of-diagonal blocks in the dFC suggests the existence of highly correlated instant FC matrices, i.e., clusters of time-windows where the

functional connectivity varies only slightly and most of the functional edges persist: these blocks represent FC states whose duration exceeds the length of the time window used to evaluate instant FCs, and the presence of out-of-diagonal blocks in the dFC shows the possibility of these states to reoccur throughout the whole evolution of the system (Figure 2.10). In Figure 2.11 we clearly see how state α is constrained in a small block on the top left corner, it is then followed by a period of rapidly changing FCs where no state can be retrieved, until a second state, state β, highlights a longer stream of auto-correlated FCs, which then disappears only to be followed by the reappearance of state α.

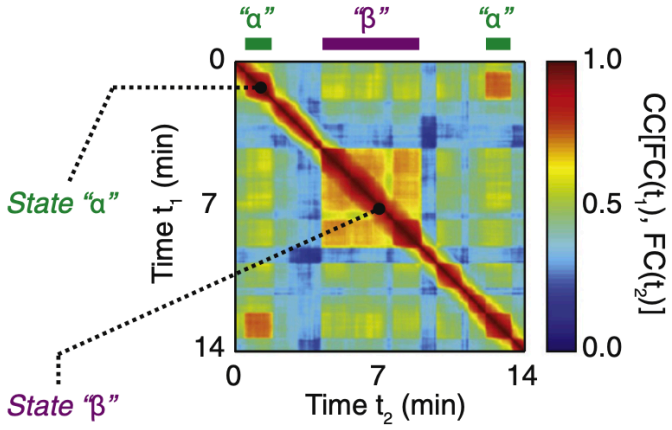

Figure 2.11. – A dFC matrix, where blocks correspond to two different states, α and β: the presence of an out of diagonal block suggests how the first and third diagonal blocks actually correspond to the same "state" of functional connectivity. Adapted from [80].

This property of dFC has attracted a vast literature to develop methods and tools capable of detecting and characterising the different functional states. Time resolved streams of FCs and dFC matrices have been therefore extracted from empirical recordings, too. Importantly, techniques aimed at identifying the different functional states that occur and reoccur within the evolution of brain networks, allowed to find properties and organizational principles of variably stable or frequent configurations of the FC that can be related to clinical conditions as well as behaviour and cognition. In fact, the overall stream of FC matrices, as well as state-wise properties of connectivity, can be studied by means of temporal network analysis methods. Even by measuring instantaneous network measures, such as the global network strength (referred to as connectivity strength) or the clustering coefficient, and comparing the time-series of these values computed for schizophrenia patients and for controls showed significant differences between the two cohorts [41].

Other dFC studies focused on shifts in modularity and module/community alle-

giance (see Chapter 1 for definition). For instance, the study carried on in [20] shows how modular structure of functional brain networks would change dynamically during learning of motor tasks, and that characteristics of such dynamics would be associated with learning success. Here authors construct a weighted temporal network by computing the temporal correlations between activity in each pair of brain regions, in fMRI recordings. Then, time series of instant modularity are computed to unveil a segregation of the network into local communities that is more significant than what expected in a random network of the same size. The community organization of the functional network is shown to reconfigure over time: re-adapting the modularity-based community detection method originally devised for generalised multi-layer networks (see Chapter 1, Figure 2.12.A) by considering each time window as a different layer of the network, temporal communities are identified across the time-span of the recording. The dynamic re-configuration of the modular structure of the functional temporal network is investigated both in terms of time-varying size and number of local communities as well as focusing on the recruitment/dismissal of nodes into/out of the different modules that appear, persist and possibly vanish over time. By introducing the notion of *flexibility* of a node as a measure of how many different temporal communities a node becomes part of during a period of time, results show how some brain regions exhibit the tendency to persist in the same community (low-flexibility nodes), while others switch communities with high frequencies (high-flexibility nodes). The global flexibility of a network is defined as the mean flexibility of all nodes in the network. The modulation of flexibility in relation to the different phases of learning is evident not only at group level but also at the individual level: while the modulation of flexibility by learning is found across all subjects in the study, the variation of flexibility across different subjects is larger than that found across different sessions of each of the individual subjects.

A similar study aims at unveiling the role of the flexibility of the modular structure of large scale brain networks in relation to working-memory [34]. This study shows how different configurations of the modular organization characterise different periods of the temporal network (transient functional states) relate to different tasks and, consequently, network flexibility is shown to be modulated by the working-memory tasks (Figure 2.12.B-C). In order to investigate the mutual relations of modules of brain areas in relation to the reconfiguration of the temporal network triggered by tasks, the concept of module-module *integration* is introduced and defined as the average over the elements of the allegiance matrix that link nodes belonging to two different temporal communities. Such analysis shows how the higher values of integration are displayed in frontal brain areas, with respect to non frontal ones, during task, and similar values are instead found at baseline for frontal and occipital-parietal regions.

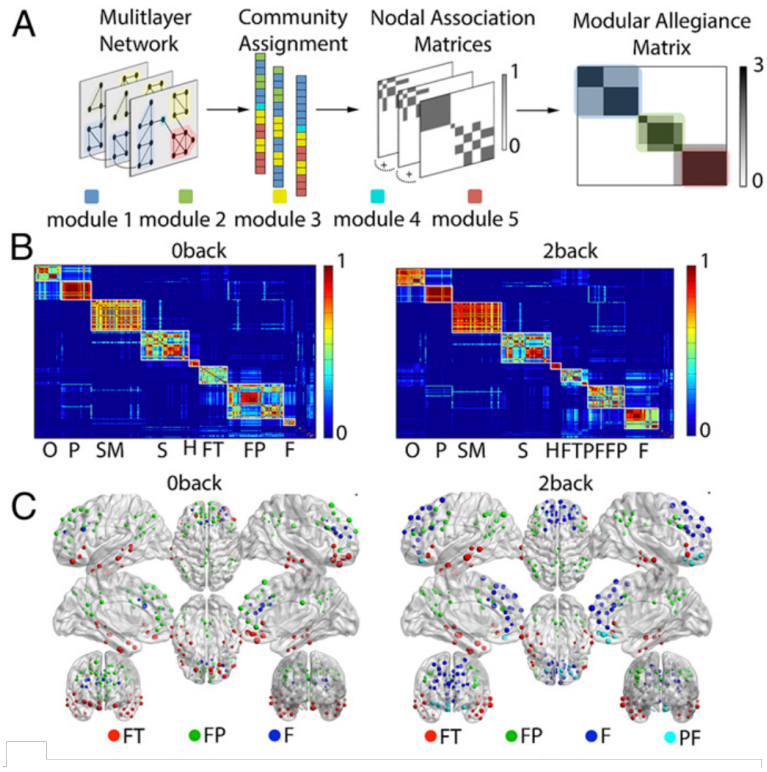

Figure 2.12. – Evolving network organization. A) Modular allegiance matrix obtained from the community assignment of nodes on each instantaneous snapshot of the network. B) The modular allegiance matrices for the baseline condition (0-back, Left) and task (2-back, Right). The letter beneath the block diagonal elements indicates the network module identified in the consensus partition: F, frontal; FP, frontal-parietal; FT, frontotemporal; H, hippocampal; O, occipital; P, parietal; PF, right prefrontal; S, subcortical; SM, somatomotor. C) A mapping of the frontal modules obtained in B to their brain coordinates for the baseline (Left) and task condition (Right). Adapted from [34].

While these studies, among others, show how the dynamic reorganization of functional connectivity can be characterised by metastable states corresponding to relatively long-lasting periods of similar network configurations, that have clear relations with cognitive tasks, there are concerns on whether discrete connectivity states in resting-state dFC exist and can be extracted. A different approach to tackle resting-state dFC avoids to segment in a sequence of sharp switching transitions between FC states, but instead attempts to describe it as a flow across continuously morphing connectivity configurations, as presented in [25]. In this viewpoint, FC networks are collapsed into points in the configuration space (the ensemble of FC realizations) that the system explores in a stochastic trajectory that describes its dynamics. In order to characterise the "randomness", or rather the type of stochastic walk best describing the dFC, the authors define the *dFC-speed* $V_{dFC_\tau}(t)$, i.e. the rate of change of the FC

from a window to the next:

$$V_{dFC_\tau}(t) = 1 - corr[FC(t), FC(t+\tau)]$$

where τ corresponds to the length of the time window used to compute FCs, so the smallest possible time interval separating two non overlapping windows. Such quantity is therefore interpreted as measure of the *distance* in the FC space travelled by the system between consecutive windows. Analyses of the distributions of $V_{dFC_\tau}(t)$ were shown to be non Gaussian and generally fat tailed: reconfigurations of FC from a window to the next corresponding to distances that are anomalously small (thus, associated to low dFC speed) or large (high dFC speed) are observed with anomalous large frequency. Furthermore, when visualizing the trajectories in FC space by means of t-Stochastic Neighborhood Embedding (t-sne, [170]), such paths are characterised by smooth segments of small, locally concentrated steps (dFC speed slows down), associated to blocks in the dFC: authors refer to blocks in the dFC as "knots", stressing how they correspond to phases where FCs are highly correlated and where therefore where small distances are travelled from a window to the other. Knots are interrupted by quick jumps of large size (dFC speeds up), that the authors refer to as dFC leaps. Such properties may also reflect the existence of a multiplicity of FC states, each of those corresponding to dFC knots, that the system explores locally with slower dFC (smaller steps), only to "accelerate" (larger jumps) when switching from a state (a cluster of FCs) to another. In order to test the non triviality of these properties the stochastic trajectories associated to empirical dFCs where compared to trivial null models. The two null models used for the validation of results corresponded to the null hypothesis of the system fluctuating around an underlying *order*, thus implying the stationarity of the FC, and the null hypothesis of a *random* exploration of the FC space. The latter null model was implemented by randomly reshuffling the sequences of instantaneous FCs in time, deleting the existence of knots and leaps in the original dFC matrix, that might indeed correspond to stable clusters of FC. The *ordered* null hypothesis was tested by generating a phase-randomized version of the original stream of FC, a method that does not fully suppress the knots and leaps of the original dFC. The comparison of the dFC speed analysis performed on the original data and on the surrogate dFC highlighted how the trajectories of empirical FC streams deviate both from *order* and from *randomness*, given the significant difference of the distributions of dFC speed in the three scenarios, in particular when FCs where computed within longer time windows (Figure 2.13).

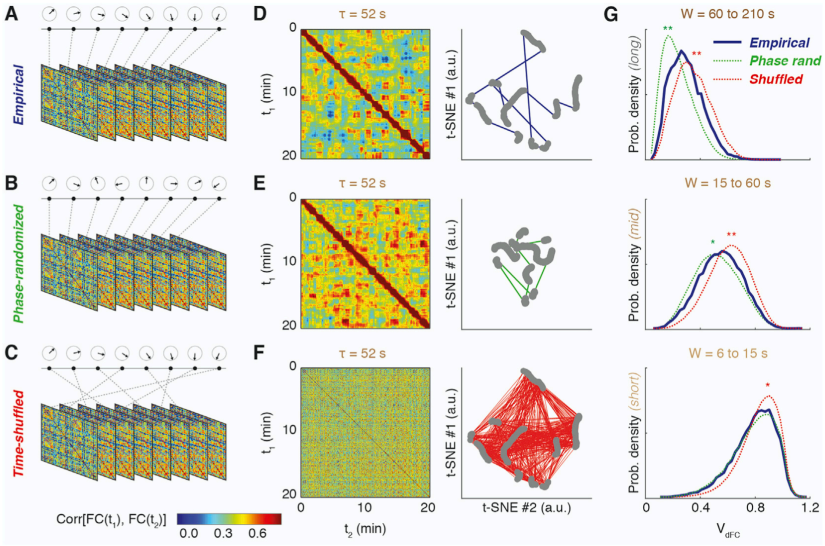

Figure 2.13. – Streams of windows of FC for empirical data (A), and the two random models (B,C). D,E,F) dFC matrices of empirical data and of the two random models and corresponding visualization of the trajectories in the FC space. G) distributions of V_{dFC} for different lengths of the time-window τ used to measure the FC. Adapted from [25].

Even though the slowing down of the system in the proximity of knots (not observed in the random null hypothesis), with faster speeds in between knots (lower speed values for cross-knot jumps in the ordered null model) does not represent per se the proof of the existence of FC clusters in resting state networks, variations of dFC speed have been shown to correlate with states of cognitive dysfunction, such as, for instance, sleep deprivation [112]. Studies such as this suggest how not just correlated states of correlated FC and the relative network properties could represent clinical biomarkers, capable to distinguish healthy controls from patients, but how even the very *style* with which a dynamic neural system explores the space of possible FC configurations could represent an inherent property of brain networks.

2.3. Cell assemblies and connectivity in the hippocampus

2.3.1. Cell assemblies

In their earliest definition [1, 84], the term *cell assembly* was used to refer to a network of neurons that co-activated in a coherent manner, repeatedly, in correspondence of a specific mental process. This view suggests therefore the role of cell assemblies as fundamental units of information processing in the brain. The original concept

of cell assembly was inherently bound to structure, rather than function, and to the concept of synaptic plasticity: a phenomenon occurring at the micro-scale in brains, for which pairs of neighboring neurons with a tendency to fire spikes in a coordinated manner also tend to strengthen their synaptic connections. Such tendency was first referred to as Hebbian plasticity [84], and later updated into spike-time-dependent plasticity (STDP). However, even in this view where structure plays a central role, it is not anymore the spiking of independent neurons that encode information, but rather the coordinated firing of many neurons which expand combinatorially the coding space, something needed to solve the "binding problem" (how to put things together in a joint representation, i.e., passing from many parallel independent representations to a unique representation of this parallel parts). In this sense, cell assemblies represent units of fundamental information processing in the brain, and neuronal representations, or computations, are the result of a dynamic *integration* within cell assemblies of the information conveyed by the individual firing cells [171].

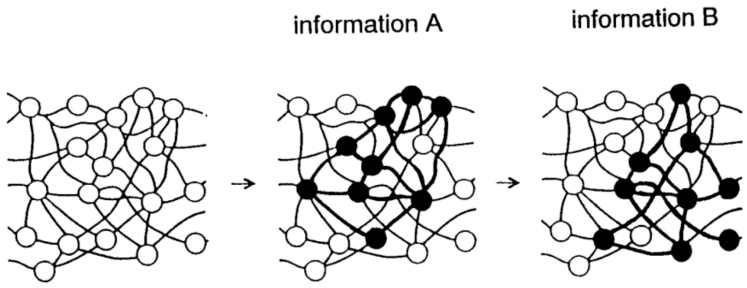

Figure 2.14. – Schematic representation of how different transiently active cell assemblies might encode and integrate different information. Adapted from[154].

A variety of approaches to appraise and detect assemblies exist. In [127], for instance, cell assemblies are defined as flexible groups of co-firing neurons that cannot be simply explained by the independent firing properties of isolated neurons. Interestingly, an intrinsic dynamic occurrence and re-occurrence of cell assemblies is found to happen during baseline activity, at random time intervals, while some cell assemblies are revealed to be "locked" in time to visual stimuli, thus suggesting their direct involvement in a specific information processing operation. Another approach highlights how *Synfire chains*, i.e., timed repetitions of spike sequences [1], are a plausible circuit mechanism to get assemblies [95, 114, 173]. This method naturally refers to the idea of STDP, plasticity driven by exact timing sequences more than just synchrony as in the original idea of Hebb.

Another strategy to identify cell assemblies is through statistical analyses of the structure of the partition function of the collective firing distribution. In this view, a way to capture patterns of activity of neural populations, accounting for the pairwise correlations between pairs of neurons but using very little information regarding the structure, is that of *Maximum Entropy* models [124, 131, 155]. These models,

as shown for instance in the seminal work [155], can reproduce the emergence of collective synchronous activity (assemblies) of individual neurons found in empirical neuronal networks though a general intuitive framework. The activity of individual neurons are measured in the real data (simultaneous single unit recordings in the salamander retina during visual stimulus) and binarised within small discrete time intervals $\Delta\tau$: the activity σ_i of neuron i is $+1$ if the neuron produces a spike within $\Delta\tau$, and -1 otherwise. Then linear correlations between the firing patterns of neurons are computed, showing an abundance of weak pairwise correlations and a probability of observing synchronous spikes from two neurons i and j that is almost equal to the product of the spiking probabilities (time averages of σ_i and σ_j) of the two individual neurons (Figure 2.15).

The maximum entropy distribution of the pairwise correlations is thus taken as the most consistent with the measured correlations, not implicitly assuming unmeasured higher-order interactions or correlations:

$$P(\sigma_1,\sigma_2,\ldots,\sigma_N) = \frac{1}{Z} exp\left[\sum_i h_i\sigma_i \sum_{i\neq j} J_{ij}\sigma_i\sigma_j\right] \tag{2.1}$$

where h_i and J_{ij} have to be chosen so that the averages $\langle\sigma_i\rangle$, $\langle\sigma_i\sigma_j\rangle$ in this distribution agree with experiment; the partition function Z is a normalization factor. We note how equation 2.1 corresponds to an Ising model where σ_i are the spins, h_i the external magnetic field and J_{ij} the exchange interactions.

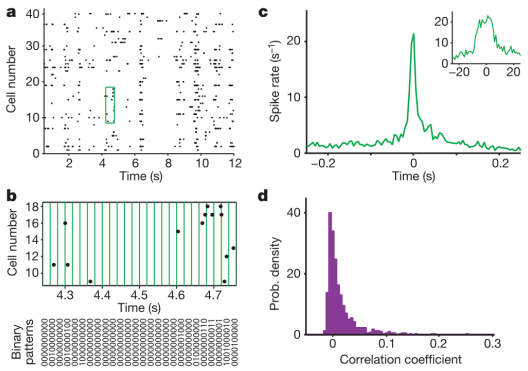

Figure 2.15. – a) A segment of the simultaneous responses of 40 retinal ganglion cells in the salamander to a natural movie clip. Each dot represents the time of an action potential. b) Discretization of population spike trains into a binary pattern is shown for the green boxed area in a. Every string (bottom panel) describes the activity pattern of the cells at a given time point. c) Example cross-correlogram between two neurons with strong correlations; the average firing rate of one cell is plotted relative to the time at which the other cell spikes. Inset shows the same cross-correlogram on an expanded time scale. d) Histogram of correlation coefficients for all pairs of 40 cells from a. Adapted from [155].

In another interpretation, a cell assembly might represent a transient functional network allowing the sharing of information among its cell members: this is the perspective presented by colleagues in [46], described in detail in the following sections, that inspired my own work, presented in Chapter 3.

2.3.2. In the hippocampus

The hippocampus is a part of the brain involved both in the consolidation of episodic or semantic memory (especially in humans) and in spatial navigation (in rodents). Both episodic (or semantic) memory and spatial navigation require in fact some kind of *temporal coding*, i.e., *stored* information on the time-ordered relationships between events (words/concepts) or locations [38]. In fact, both of these operations require the integration of information of a spatio-temporal context. Importantly, cell assemblies seem to play a central role in these functions: in the hippocampus, information regarding the current location is encoded in the maximum firing activity of a neural population of *place cells*, i.e., a maximally active cell assembly [38, 173]. Sequences of cell assemblies thus correspond to sequential changes in the environment (space) due to spatial navigation (in rats). The time-order of the sequence is encoded in the sequence of assemblies of co-firing *place cells* in relation to a specific frequency-band of global oscillations of activity in the hippocampus, the theta cycle [40]. For instance, in [173], authors show how recurring cell activation sequences (cell assemblies, in the syn-fire chains interpretation) in the CA1 region of awake mice can be interpreted as a population-level code integrating spatiotemporal information even in the absence of external constraints (mice allowed to self-regulate their motion). Remarkably, using two-photon calcium imaging to capture population dynamics and single cell behaviour, a distance unit is represented and encoded in the re-occurring sequences. In another study [163], authors use a maximum entropy approach to infer the functional connectivity from the spiking activity of simultaneously recorded neurons in prefrontal cortex (PFC) of rats in a memory consolidation experiment. The recordings of tens of neurons in the PFC where divided into three epochs: a task epoch in which the rat had to learn a specific rule, and two Sleep epochs, one before (Sleep Pre) and one after (Sleep Post) the Task epoch. Comparison of the functional interactions between neurons in the two sleep epochs revealed groups of cells that were significantly more functionally linked (*potentiated* functional couplings) in the Sleep Post w.r.t. the Sleep Pre epoch. The neurons recruited into these groups where shown to co-activate strongly during during Task and Sleep Post, more than in the preceding sleep epochs, thus suggesting how they could represent cell assemblies involved in the consolidation of experience-related memory.

In therms of network properties of cell assemblies, graph-theory based analysis of the functional connectivity of neuronal populations in the developing brains in rat and mice through calcium imaging, unveiled the existence of an overall scale-free topology of the networks, with highly connected hub neurons whose activity was shown to trigger the activation of specific cell assemblies [32]. These highly connected neurons, with respect to a majority of neurons with few connections, were denoted

as *operational* hubs given their ability to orchestrate the synchrony of sub-sets of the rest of the nodes of the graph, thus originating the formation of temporally coherent cell assemblies [51].

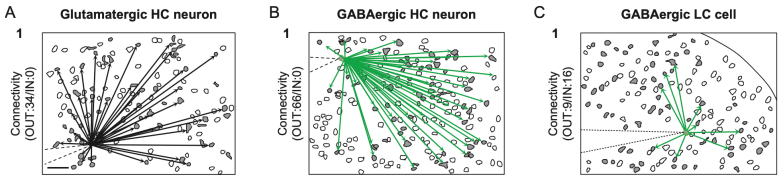

Figure 2.16. – The large neighborhoods of different hub neurons. Adapted from [129].

Operational hubs in developing hippocampal networks were shown to belong to a mixed population of two physiologically specific sets of neurons: glutamatergic pyramidal neurons and GABAergic cells. These studies thus suggest how the prominent role of these neurons seemed to be an inherent elitist characteristics deriving from individuals' firing and morphology properties, almost like an aristocratic "birth-right" privilege inherited from predecessors [129] (Figure 2.16). Furthermore, the tendency of these neurons to become hubs and integrate specific circuit positions was shown to relate not only to where [130] but also to when they are born in the embryo. In particular, GABA cells born the earliest in the development of the hippocampus were shown to be the ones operating as hubs driving the activation of assemblies, and to maintain this function throughout their lifetime [30].

2.3.3. Computing Hubs in the Hippocampus and Cortex

Other works have shown how the functional relationships, extracted by means of information theoretic measures and interpreted as fundamental information processing operations, between neurons in the hippocampus and entorhinal cortex in rats highlight instead the rise of a more "democratic" distribution of *computationally* important roles among nodes within the sequences of active cell assemblies [46]. In this work, colleagues in the lab have recorded simultaneously firing neurons in the CA1 region of the hippocampus and in the medial entorinal cortex (mEC) during anesthesia, and medial prefrontal cortex (mPC) during natural sleep (Figure 2.17.A). LFP potential were used to extract the different global oscillatory states, identifying epochs dominated by slow (SO) or theta oscillations (THE) in anesthesia, and two states corresponding to REM and nonREM during sleep. By binning a the firing patterns of individual neurons, the activity of each neuron has been encoded in binary vectors. This discrete representation of the spike trains of each neuron has allowed the measurement of fundamental information-theoretic quantities, al based on the notion of *time lagged Mutual Information*. The two main information-theoretic features that were therefore computed in a time-windowed fashion, in order to capture the time varying nature of communication of information in this system, where *information sharing* and *information storage*. The *shared* information $I_{shared}(j \rightarrow i)$ between each

pair of neurons $(i,j)_{i,j=1,\dots,N}$ was quantified by the mutual information encoded in each pair of firing patterns $MI[i(t), j(t-\lambda)]$, and defined as:

$$I_{shared}(j \rightarrow i, t) = \sum_{\lambda} MI[i(t), j(t-\lambda)] \tag{2.2}$$

$$I_{shared}(i \rightarrow j, t) = \sum_{\lambda} MI[j(t), i(t-\lambda)] \tag{2.3}$$

where the time-lag λ varies in the range $0 \leq \lambda \leq 0.5T^{\theta}$, T^{θ} being the phase of the theta (THE) cycle. Here it is evident how this setup can naturally translate into a temporal network analysis of the sharing of information among neurons, which is the inspiration and motivation behind part of my work (see Chapter 3). Information sharing can be seen as a generalized form of cross-correlation where the time-lagged mutual information capture all types of linear and nonlinear correlations. Analogously, one can evaluate a generalized auto-correlation functional, known under the name of active information storage [110]. In [46], colleagues evaluated active information storage of a given neuron, within a given time-window as:

$$I_{storage}(i, t) = \sum_{\lambda} MI[i(t), i(t-\lambda)] \tag{2.4}$$

where the time-lag λ varies once again in the range $0 \leq \lambda \leq 0.5T^{\theta}$. In this work, therefore, the notion of assembly was generalised, specifying different *flavours* that it can assume: there can be firing assemblies (the closest to the classical definition), but also computing assemblies such as storage and sharing assemblies. Each time window could be represented as a set of four $N-$dimensional (N being the number of recorded neurons) *feature* vectors, one for each feature: the two information-theoretic measures of shared and stored information (computing assemblies) of each neuron within each window, the global oscillatory state as well as the firing rate (firing assemblies) of individual neurons within the relative window (Figure 2.17.B).

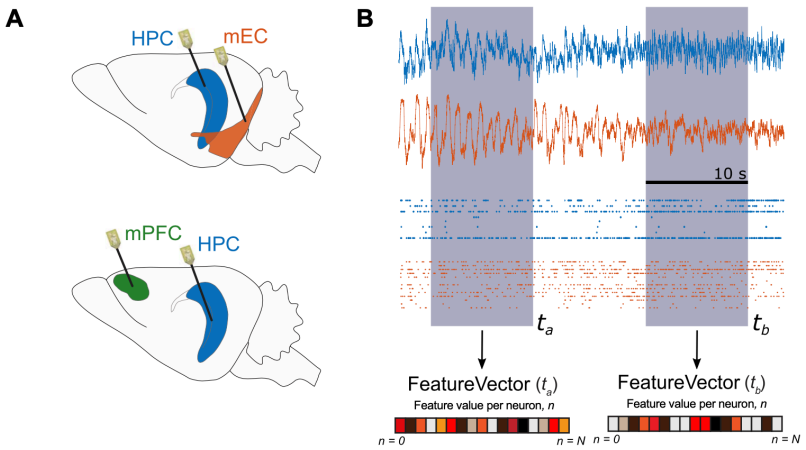

Figure 2.17. – A) schematic representation of the recording sites. B) LFP and single units recordings in the HPC (blue) and mEC (orange); the shaded area corresponds to two different time widows used to compute the information-theoretic features: one feature vector of length N is extracted for each feature within a window. Adapted from [46].

K-means clustering of the time-series of feature vectors allowed to extract epochs of correlated time windows, i.e., states sequences, one for each feature (Figure 2.18). The comparison of the information storage and sharing states with the global oscillatory states showed how both processes where dynamic within the same global state. However, storage and information storing states, or sub-states, were shown to be global-state dependent, with many sharing and storage states occurring preferentially during one of the two global oscillatory states. Importantly, the storage performed by an individual neuron as well as its participation in the sharing of information could vary significantly in time, without comparable changes in its firing rate.

Furthermore, within each time window, hub neurons were defined as neurons behaving in the top 5% of the related feature-vector: reoccurring feature states are therefore characterised by the same hub cells (Figure 2.18).

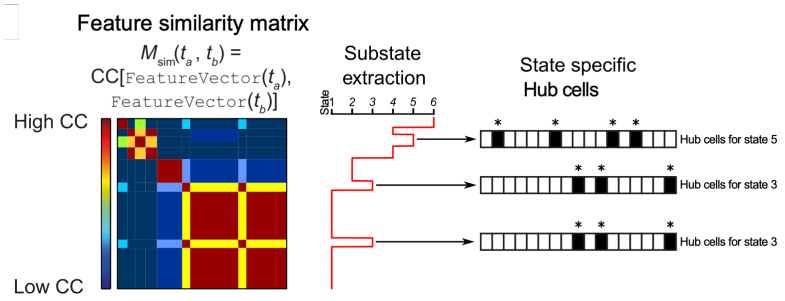

Figure 2.18. – Toy example of a block-wise feature similarity matrix and the corresponding sub-states; each sub-state is characterised by different hub cells. Adapted from [46].

In line with the idea that hub cells are responsible for the recruitment of other cells into a transiently active cell assembly, sharing cell assemblies were defined in this work as the set of neurons that within a time window had non-zero values of shared information with a hub neuron. In network-theoretic terms, info-sharing cell assemblies were represented here as the neighborhood in the information sharing network of prominent hubs. The analysis of the time evolution of the strength (sum over weighted edges of information sharing) showed how such quantity was preserved throughout a global state and across sharing states, yet the set of neurons comprised in the cell assembly would vary substantially, as depicted in the cartoon in Figure 2.19, from a sharing state to another and even more so when compared to the strength within the same sub-state. Defining the *liquidity* of the set of members of cell assembly as well as that of the strength of its connections as the variability of these properties within a sub-state of a cell assembly with a quantity ranging from 0 (low liquidity) to 1 (completely random liquidity), allowed to show how cell assemblies are characterised by a higher liquidity of the set of neurons that form them compared to the liquidity of the strengths of their edges.

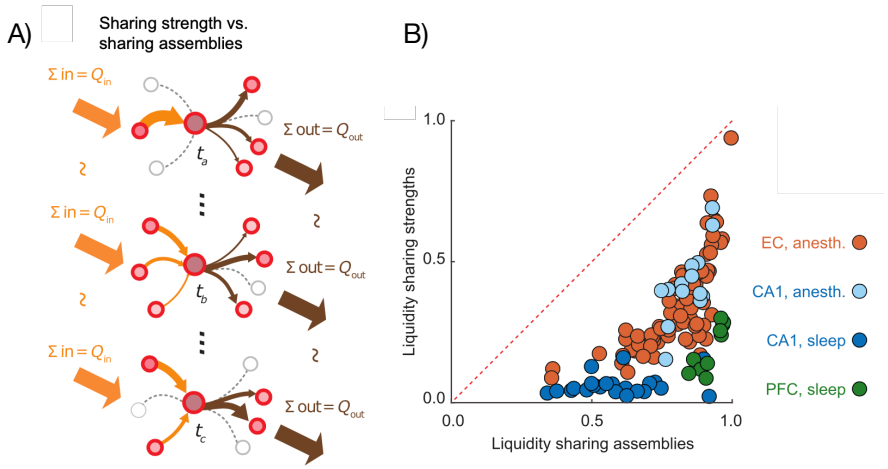

Figure 2.19. – A) schematic representation of the neighborhoods of the same hub cell at different times. B) Scatterplot of the liquidity of the strengths of the edges connecting a cell assembly versus the liquidity of the set of nodes that are part of it. Adapted from [46].

Furthermore, keeping track of what neurons resulted to be hub cells within each storage or sharing state showed that while a minority (by definition) of neurons are considered hubs within an individual state, a vast number of cells act as hubs in at least one state (Figure 2.20). Importantly the distribution of hub neurons across the different areas of the HPC and mEC did not show any significant over concentration of computational hubs related to the underlying anatomy. Together, these results suggested how a neuron might have a central role in a sub-state specific computational operation not necessarily by "birth-right", but rather depending on the very fundamental processing operation being carried out by the cell assembly in which it is recruited. This study thus shows how the distributed processing of information could resemble more a *democratic* than an elitist system.

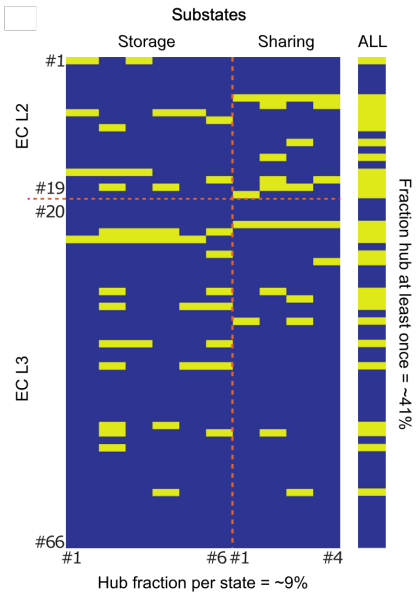

Figure 2.20. – Hub cells in each substate are highlighted in yellow. The column on the right is a vector of length N, i.e., the size of the network, and it's ith element is yellow if the corresponding node i has been a hub cell in at least one sub-state. Adapted from [46].

In Chapter 3 I will describe how information sharing between firing neurons can be represented as a temporal network with key topological and dynamical properties that can also help shed light, in a different perspective, on the computational roles that a neuron can have. In particular, I will reveal a variety of important computational behaviors, different ways to be a computational hub, that a neuron can display within discrete states of the evolution of the network.

2.4. Epilepsy

2.4.1. Temporal lobe epilepsy

Epilepsy is a chronic neuro-physiological disorder characterized by the occurrence and re-occurrence of seizures, defined as transient signs of abnormal excessive and sychronous neural activity. Temporal Lobe Epilepsy (TLE) is the most frequent form of *partial* epilepsy, thus affecting only part of the brain. In TLE seizures are related to hyperexcitability of cortical areas. These synchronised brain networks form the *Epileptogenic Zone* (EZ) [17, 18]. We refer to the condition where seizures remain persistent even after pharmaceutical treatment as pharmaco-resistent epilepsy. The main treatment procedure in this unfortunate case is of surgical nature: physicians proceed to remove the EZ with the highest possible accuracy. In order for such delicate treatment to be successful the EZ must be localised with the best available accuracy and the functional implications of the removal of the brain areas included in the EZ

need to be assessed: the goal is in fact to reach a favorable gain in treatment of the epilepsy with respect to the functional alterations due to the surgical intervention. A first assessment of the areas involved in the EZ is achieved by non invasive techniques, such as DTI and other structural imaging to reveal the presence of lesions as well as methods such as cortical EEG and fMRI to estimate the networked focuses of abnormal neural activity. A second definition and location of the EZ is then achieved through stereo electroencephalography (SEEG). Such method consists in the placement of typically $8-15$ intracerebral electrodes in specific brain structures that are believed to be involved in the onset (origin) or propagation of seizures. SEEG therefore allows the simultaneous recording of EEG signals from different brain areas and constituted the fundamental tool to conceptualise the EZ also as an epileptogenic network, more than a single problematic brain area, or focus [18]. SEEG measurements have, for instance, allowed to describe a common pattern of onset of a seizure in terms of frequency content of the recorded signals: the low voltage fast-discharge (LFD) consists in a flattening of signals corresponding to increase of the high frequencies and a decrease in low frequencies of signals coming from SEEG recording sites. The definition of the *epileptogenicity index* has a measure quantifying the involvement in the LFD of each recording site has beacome a reference method to rank the corresponding brain areas as part of the EZ. Time series of signals recorded through SEEG methods can be used to measure the functional connectivity between each pair of brain areas. As seen in the previous chapters, a variety of metrics and tools can be employed to measure the functional connectivity from multivariate time series. FC definitions not only span from linear to non linear correlations among signals, but can be defined in the time, frequency or wavelet domain (in the latter, time can be expressed as a function of frequency) [105]. Network-theoretic studies of the FC of epileptic brain networks recorderd through SEEG, showed that usually a phase of hyper connectivity, in terms of global and node-wise strength of connections, precedes LFD in partial epilepsy [11, 52], and proved to be useful in further characterizing epileptogenic networks. In terms of network properties, it was shown that functional networks of epileptic brains recorded through fMRI interestingly display no differences when compared to control in terms of global efficiency, local efficiency of modulartiy, yet the epileptic networks undergo massive reorganizations in terms of functional hubness of brain areas [150]: most hub-like regions in controls are the most decreased in patients while the least hub-like regions are the most enhanced. Another general effect of epilepsy on brain functional networks is that it somehow favours structure and function to be more similar. This was shown, for instance, by means of comparing network measure values, along with the rich-club organization, of FC (extracted from resting-state fMRI) and SC (dMRI) for controls and patients suffering from TLE [176].

Surprisingly the functional network metrics of epileptic patients were more similar to the structural ones with respect to control. Altered activity and, therefore, functional connectivity is reported to be shown even in between seizures, where epileptic brain networks display recurrent inter-ictal spikes of hyper excitability [107].

2.4.2. Epilepsy and a specific functional system: language

Depending on what brain areas are involved in the EZ and affected by the recurrent seizures and abnormal inter-ictal activity, symptoms of epileptic human patients can vary drastically. In my work (see Chapter 4) I focus on pharmaco-resistant epileptic patients suffering from aphasia, a form of language impairment. For this reason I briefly introduce in this section some key concepts that constitute important background to my research.

Language system

Brain areas in the cortex relevant for language include Broca's area in the inferior frontal gyrus (IFG), Wernicke's area in the superior temporal gyrus (STG), as well as parts of the middle temporal gyrus (MTG) and the inferior parietal and angular gyrus in the parietal lobe (Figure 2.21). One of the main models for language suggests the existence of two separate networks of brain regions, highlighted both by structure and by function: a dorsal network involved in the acoustic-phonological translation including posterior temporal regions, the inferior parietal region and the inferior frontal operculum (FOP); a second ventral network, including the lateral temporal lobe, the IFG and the pars orbitalis, is responsible for the processing of lexicon and semantics [65, 86].

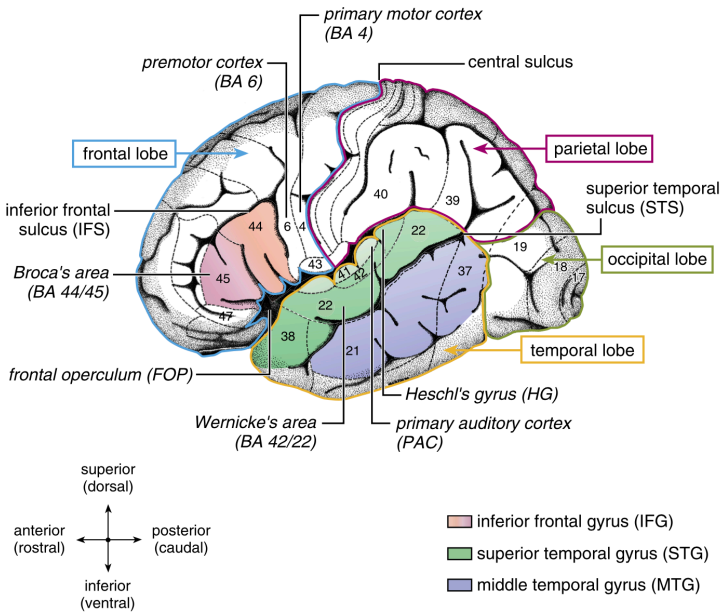

Figure 2.21. – Anatomical and cytoarchitectonic details of the left hemisphere. The different lobes (frontal, temporal, parietal, occipital) are marked by colored borders. Major language relevant gyri (IFG, STG, MTG) are color coded. Adapted from [65].

The frequencies of the oscillating signals recorded in language-associated brain

areas also seem to play a fundamental role in language processing. In fact spectral analysis of SEEG recordings of human patients responding to spoken words. Different frequencies (delta-1 – 3 Hz, theta 4 – 8 Hz, and low 25 – 35 and high 50 – 150 Hz gamma) oscillations seem to be engaged in the multi-time scale properties of speech and language processing. In this hypothesis, these frequency bands provide a link between neurophysiology, neural computation, acoustics and psycholinguistics [14, 75], with higher frequencies associated to simpler processing operations as the decoding of individual sounds, and lower frequencies associated to higher order functions such as the integration of syllables and, possibly, the processing of semantics [125] (Figure 2.22).

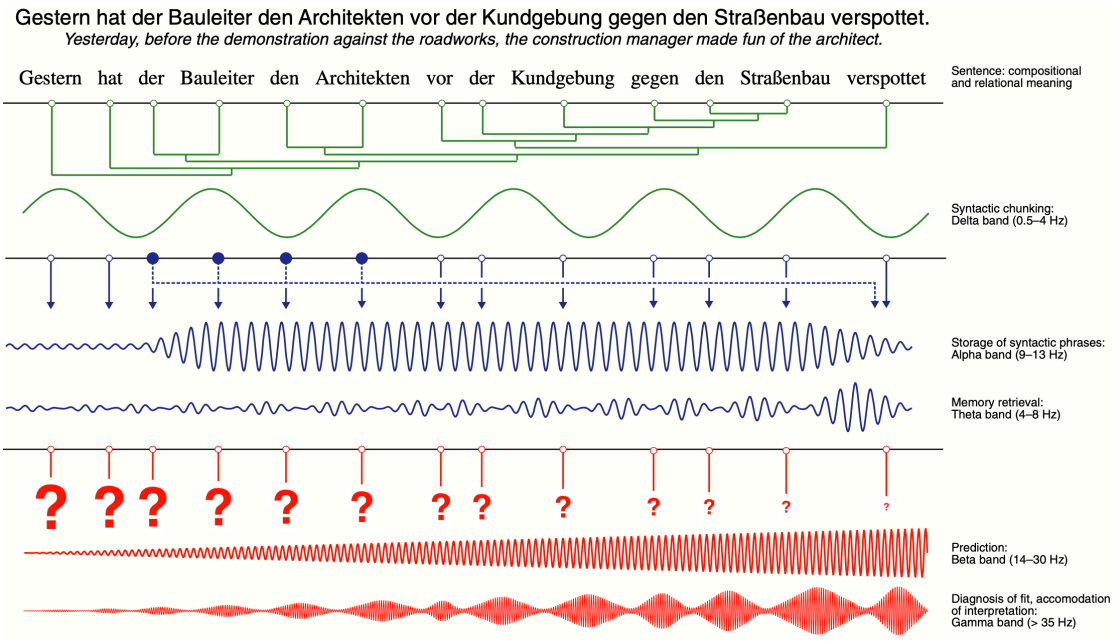

Figure 2.22. – Neural oscillations in language comprehension; green: chunking of words into syntactic phrases is subserved by delta-band cycles; blue: phrases are stored in working memory (solid circles) with the help of alpha-band oscillations; alpha-band amplitude increases during the storage of the subject and object, until these can be linked to the main verb; stored information is retrieved from working memory and long-term memory for integration into the ongoing sentence-level representation, with the support of theta-band oscillations; red: beta-band oscillations are involved in the prediction of upcoming words from the prior cumulative semantic interpretation; gamma-band oscillations assist diagnosis of lexical-semantic contextual fit of incoming words. Adapted from [125].

Post ictal Aphasia

When a seizure involves the language system, the modification of the synchronous relations of the brain areas involved causes a functional disorganization of the network

which, in turn, causes language impairment during the seizure and the return to full recovery. The patients, in fact, gradually resume the state preceding the seizure, with varying recovery times across subjects. These symptoms are thus interestingly reversible and inherently related to functional connectivity. Such symptoms are identified as reduction of speech flow and increase of rhythmic versus illustrative gestures in patients, which can be tested and evaluated in real time by physicians during the seizure and before full recovery [62] (see Chapter 4 for further details).

2.4.2.1. Dynamic reconfiguration of language during TLE

A study that represents an important inspiration for part of my work (see Chapter 4), particularly for the temporal network methods employed, is [83]. In this work the language network of a cohort of patients suffering from TLE and a control group are evaluated by means of fMRI during a language-related taks and at rest. The functional connectivity is measured as the coherence between the BOLD time series of ROIs in the $0.05 - 0.1$ Hz frequency band, with a sliding time-window approach that results in a snapshot-sequence temporal network: one for each condition, task or rest. Furthermore, the brain areas in the network were assigned to four sub-systems: left and right frontal sub-systems (orbital inferior frontal gyrus, inferior frontal gyrus, middle frontal gyrus), and two left and right temporal sub-systems (anterior temporal lobe, middle-anterior temporal lobe, middle-posterior temporal lobe, posterior temporal lobe, angular gyrus). On each dynamic network, dynamic community detection was performed by means of a multilayer modularity-based algorithm (see Chapter 1), which allowed to compute the module allegiance of the different brain regions (Chapter 1), computing the *flexibility* and *promiscuity* of nodes in the temporal network in terms of frequency with which a region changes assigned community and the fraction of the overall number of communities of which a region has been part of at least once, respectively. By comparing these measures computed on real data to random null models that would assume the stationarity in time of the adjacency matrix or the stability of connections within sub-systems, randomizing edges between different subsystems, the authors found an overall dynamic organization of the language network, where left-frontal regions, having lower flexibility, formed a dynamic core, and right-frontal and left-temporal regions showed the highest values in flexibility, thus giving rise to a dynamic periphery.

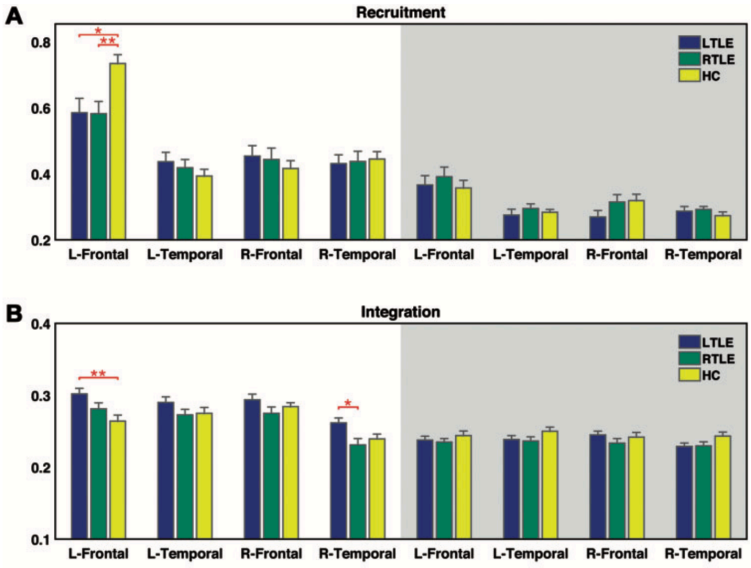

Figure 2.23. – Recruitment (A) and integration (B) estimated during task (white background) and resting conditions (grey background). Asterisk indicates pairwise group differences, $*P \leq 0.05$, $**P \leq 0.01$, all Bonferroni corrected. Error bars reflect standard error (SE). LTLE = left TLE; RTLE = right TLE; HC = healthy control. Adapted from [83].

The dynamic structure of the language system was observed during the expressive language task in TLE patients as well as in control. Defining the level of *integration* of a brain area of the system as a high density of edges with areas from other sub-systems, and *recruitment* as the density of connections with areas in the same subsystem, higher levels of integration where displayed during task compared to rest in healthy controls in left frontal and temporal and right frontal sub-systems. Interestingly the comparison of TLE patients to control highlighted differences in terms of integration and recruitment of sub-systems, as well as significant differences in terms of flexibility of individual brain regions. These findings therefore suggest how the dynamic reconfiguration of language-related functional networks is modified during expressive language task in TLE patients, a result that seem to reinforce the need for temporal network analysis of functional brain networks to unveil, possibly, the mechanisms underlying loss of language capabilities in epileptic patients (Figure 2.23).

2.4.3. Epilepsy at the microscale

At the microscale, calcium imaging of neuronal networks of chronically epileptic mice showed how inter-ictal events are related to the synchronous activity of cell assemblies, yet the recurrent patterns of activation have extreme variability compared to control [134]. Here GABAergic cells still play a central operational role, driving the activation of transiently synchronous assemblies in correspondence of inter-ictal spikes, yet different inter-ictal spikes are shown to involve different groups of GABAergic neurons. A more variable network dynamics in epilepsy with respect to control was

also observed in [133]. Here spatially localized functional clusters (3 or more neurons) of synchronously active cells are observed during *network* events, i.e., statistically significant synchronous network-level activity, in both control and epilepsy. Epileptic networks displayed more clusters than control (Figure 2.24). Furthermore, the large scale network events are characterised by the co-activation of sub-sets of these clusters, in both conditions. However, the more frequent, w.r.t control, network events in epilepsy, related to inter-ictal spikes, showed higher variability in the recruitment of different clusters: different spikes correspond to different patterns of active clusters.

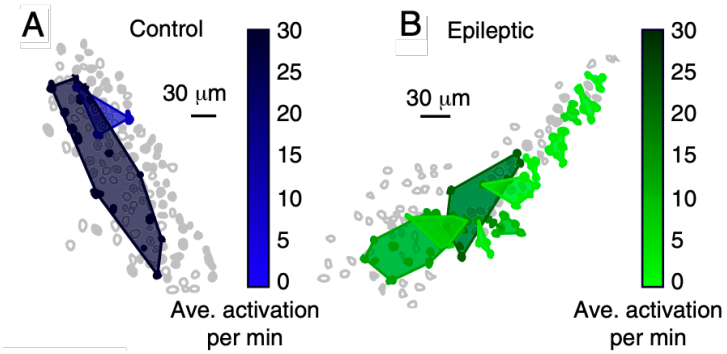

Figure 2.24. – Examples of the spatial mapping of clusters from a control slice (A) and an epileptic slice (B). The shade of the cluster indicates the average frequency of calcium activation for neurons within the cluster. The darker shades indicate clusters with more activity. Adapted from [133].

Such increased variability, or *complexity*, of network dynamics at the micro scale was also investigated by colleagues in [45]. Here, comparing the dynamics of firing, storage and sharing cell assemblies in the HPC and mEC in control and in epileptic rats, revealed a distruption of the internal composition of sub-states, as well as their temporal organization, in epilepsy. In particular, the global oscillatory state-specificity of firing and information sharing and storage sub-states is lost in epilepsy, and *computing* hubs are more numerous yet less sub-state specific.

3. Temporal networks in the brain: Dynamic core periphery structure in cell assemblies

In this chapter I present the work that I carried out, together with my colleagues, and that lead to the published article [143]. This study aims at investigating the relation between the transient activation of cell assemblies (see Chapter 2) to different, distributed information processing operations [45, 46] that can be analysed in term of the ongoing reconfiguration of a temporal network.

3.1. Cell assemblies as information sharing networks

In this work we use the simultaneous single-unit recordings in the mEC and in the HPC of anesthetized rats originally published in [148] and further study in [46] (18 recordings for 16 rats, details of anatomical locations and numbers of cells included can be found in Figure 3.1). In particular we use the information sharing (see Chapter 2, eq. 2.2 for formal definition), i.e., the time-lagged mutual information $I_{shared}(i \rightarrow j)$ between each pair of firing patterns of neurons (i, j) within a 10s time window, as a measure of functional interaction between the two nodes in a time-varying *information sharing* network. The time-window is then shifted by 1 second to extract the information sharing network at the next time-step, assuring a 90% overlap with the previous time-window for the computation of the information theoretic measures.

In Figure 3.2.B, is represented the temporal network construction procedure. Based on the data segments in each of three windows centered at times t_a, t_b and t_c, we extract a $N \times N$ matrix for each time window, where N is the number of neurons and in which the element (i, j) corresponds to the shared information between nodes i and j. Each such matrix, in network terms, is interpreted as the *adjacency matrix* of a weighted graph G of N nodes.

This procedure thus maps each multi-channel recording of length T seconds to a time series of T network representations, obtaining finally a temporal network of information sharing among neurons, formed by the temporal succession of these T network snapshots. Cartoon representations of the temporal network snapshots $G(t_a)$, $G(t_b)$ and $G(t_c)$ in the three highlighted time windows are shown in Figure 3.2.C. Some actual network frames of a specific recording, together with a diagram describing emergence and disappearance of links (*edge activity plot*) can be seen in Figure 3.3.

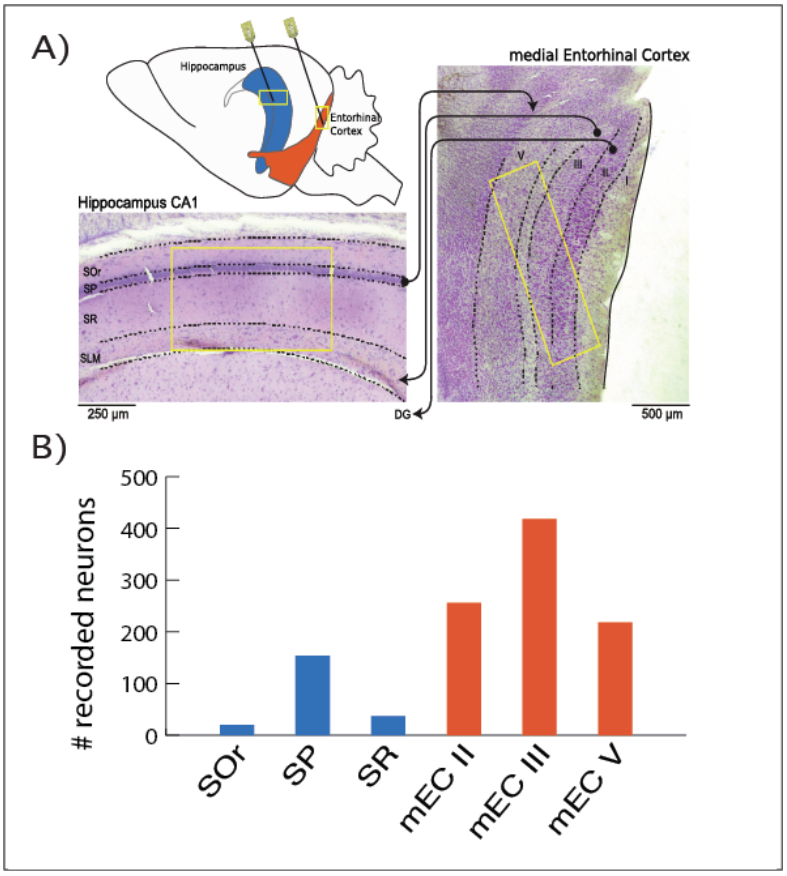

Figure 3.1. – **A)** Simultaneous mEC/CA1 recording setup. **B)** Number of neurons recorded for each layer of each region: a majority of recorded neurons were located in the medial Entorhinal Cortex layers.

On the top of Figure 3.2.B we also present the characteristic switching between global oscillatory states observed in our recordings. Analysis of the local field potentials recorded simultaneously to single unit activity allowed identifying a spontaneous stochastic-like alternation between epochs belonging to a first SO global state (light blue color) spectrally dominated by < 1 Hz oscillations and epochs in a second THE global state, characterized by the presence of high power in a $4-8$ Hz spectral band. In the following we will relate the temporal network reconfiguration dynamics to these global oscillatory state transitions.

3.1.1. Network feature vectors

We carried on our study by analyzing in parallel the evolution of the weighted temporal network structure and of the corresponding unweighted temporal network. To this aim we defined for each time window a binarized version of the network snapshot, whose adjacency matrix is only composed of zeros and ones: the adjacency matrix element is 0 (no link is present in the unweighted network) when two nodes are

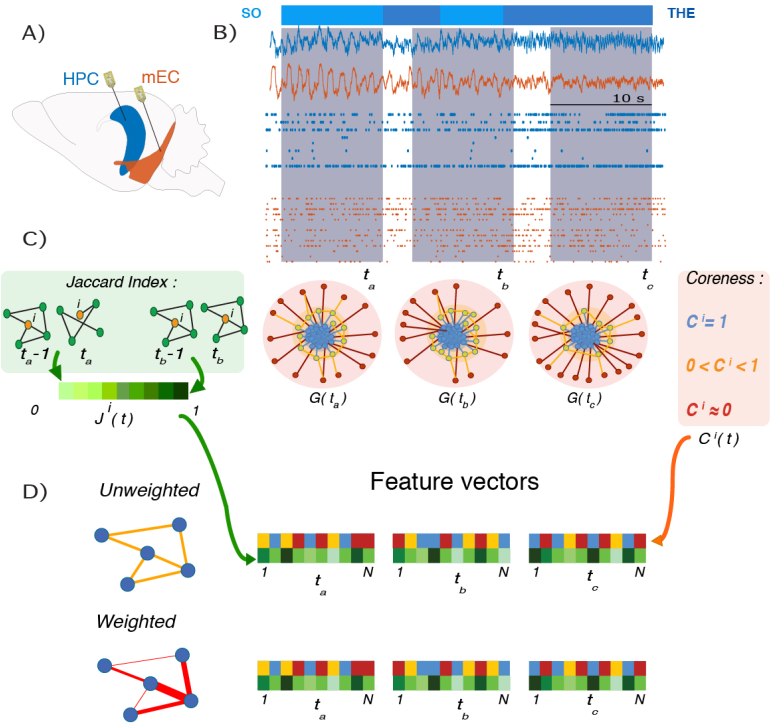

Figure 3.2. – **Recordings and feature vectors. A)** Approximate recording locations in mEC (orange) and CA1 (blue) during anesthesia. **B)** An example of LFP signal recorded by the channels in CA1 and in mEC; below the LFPs are two examples of single unit activity from the same recording. The horizontal bar above the recordings represents the Global Oscillations states: in light blue the *Slow Oscillations* and in darker blue the *Theta Oscillations*. **C)** Illustrative sketches of the two features computed for each node at each time-frame. **D)** Instantaneous feature vectors of the coreness and liquidity values of all neurons (yellow, blue and red for coreness and green for liquidity).

not connected (the shared information between them is zero), and it is equal to 1 when they are (the shared information is nonzero). By comparing weighted and unweighted analyses we could assess whether the network changes involve actual evolution of the structures of the links or rather correspond only to weight modulations on a stable link structure. To quantify the dynamics of the network, we focused on two main aspects —translated into corresponding temporal network features in both weighted and unweighted versions—, aiming at answering two different questions. First: are the connections of the network stable in time, or rapidly changing? Second: does the network have a clear and specific structural organization, and if so, is it persistent in time or unstable and only transient?

In order to answer the first question, we quantified, for each neuron i, how much its neighborhood changed between successive time windows [71, 128, 161, 169]. To this aim we computed for each i and at each time t the *cosine similarity* $\Theta^i(t)$ between the neighborhoods of i (the sub-graphs composed only by the edges involving i) at time

$t-1$ and at time t:

$$\Theta^i(t) \equiv \frac{\sum_j w_{ij}(t-1)\, w_{ij}(t)}{\sqrt{\sum_j w_{ij}(t-1)^2}\sqrt{\sum_j w_{ij}(t)^2}} \tag{3.1}$$

where $w_{ij}(t)$ is the weight of the link between nodes i and j at time t. To analyze the unweighted temporal networks, we instead used the *Jaccard index* $J^i(t)$ between these successive neighborhoods:

$$J^i(t) \equiv \frac{|\nu^i(t-1) \cap \nu^i(t)|}{|\nu^i(t-1) \cup \nu^i(t)|} \quad , \quad J^i(t) \in [0,1] \tag{3.2}$$

where $\nu^i(t-1)$ and $\nu^i(t)$ are the neighborhoods of node i at times $t-1$ and t, respectively. $J^i(t) = 0$ when $\nu^i(t-1)$ and $\nu^i(t)$ are two disjoint sets of nodes, while $J^i(t) = 1$ when the two sets are identical.

Values of these quantities close or equal to 1 suggest that the node has not changed neighbors in successive time windows: hence its neighborhood shows low *liquidity* (elsewhere, it would be said that the node shows high "loyalty" [169]). On the contrary, values close or equal to 0 mean that the neuron has completely changed neighbors between subsequent times: its neighborhood is highly liquid. At each time t, the set of cosine similarity values $\Theta^i(t),\ i \in [1,N]$ and the Jaccard index values $J^i(t),\ i \in [1,N]$ (for the unweighted case) form the time-dependent feature vectors $\Theta(t)$ and $\mathbf{J}(t)$, each of dimension N (Figure 3.2.D).

In order to answer the second question and probe for the presence of specific network architectures, we considered the *core-periphery* organization of the graph. This way of characterizing the information sharing network snapshots was suggested to us by the visual inspection of their spatial embeddings, some of which are represented in Figure 3.3. We thus computed the *coreness coefficient* $C^i(t)$ of each node i in each snapshot t, using the definition of coreness (a kind of continuous coreness - Chapter 1 -, the method is introduced in [56]). In a static, unweighted, undirected network, the coreness C^i of node $i \in [1,N]$ is a real number between 0 and 1, interpreted as follows: when $C^i \sim 1$ the node belongs to the *core* of the network, i.e., a set of tightly connected nodes; when $C^i \simeq 0$ the node belongs instead to the network's *periphery*, i.e., is only loosely linked to the rest of the network; if $C^i = 0$ the node is actually disconnected, i.e., its degree (number of neighbors) is $k^i = 0$. We thus obtain a time dependent vector $\mathbf{C}(t)$ of dimension N by computing at each time t the coreness $C^i(t)$ for each node $i \in [1,N]$ in the network of time-window t. The computation of coreness coefficient can also be performed for weighted networks [56], possibly yielding, however, values larger than 1. Therefore, we normalize the whole time series of vectors of weighted coreness coefficients by the maximum observed value in order to obtain a time series of vectors $\{\mathbf{C}_w(t) | t \in [0,T]\}$ (with $\mathbf{C}_w(t) = \{C^i_w(t), i \in [1,N]\}$) with the same range of values for the unweighted and weighted coreness features (Figure 3.2.D).

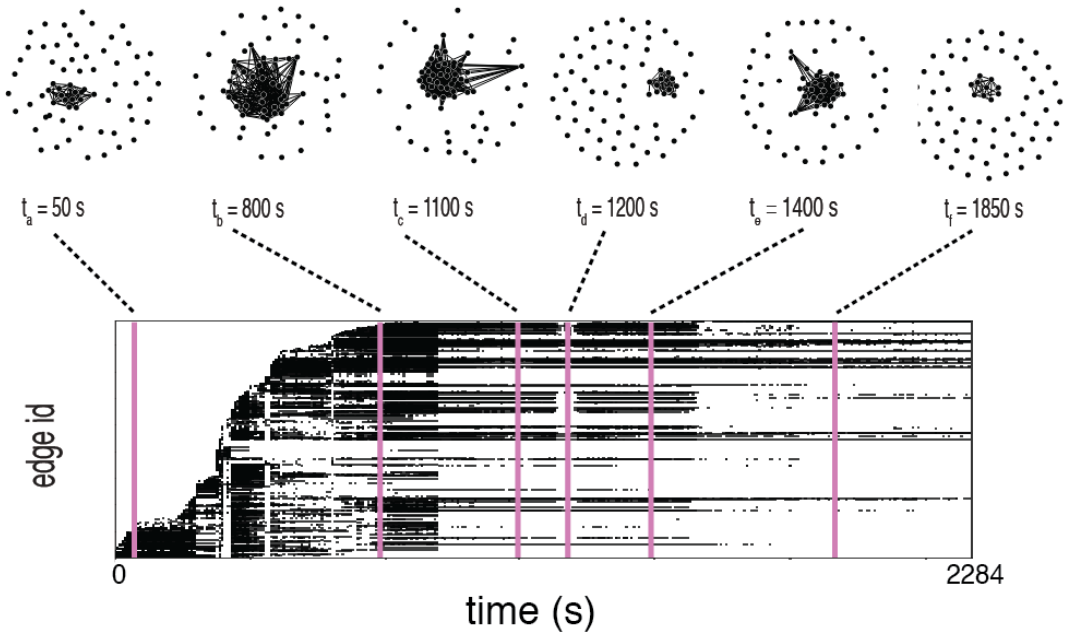

Figure 3.3. – **Temporal network visualization.** In this figure we represent the evolution of the information sharing temporal network computed for one of the recordings, using the visualization toolbox TACOMA (`http://tacoma.benmaier.org/about.html`). The six networks on the top plots represent six snapshots of the network's evolution at the corresponding times. The bottom panel displays the temporal network's *edge activity plot*: each row of the plot represents the activity of one edge of the network, i.e., a black dot on a row means that the corresponding edge on the vertical axis is active. The edges are ordered on the vertical axis by increasing value of their *first activation time*.

3.2. Info sharing networks have a soft core-periphery architecture

In order to investigate the core-periphery organization of the information sharing networks, we looked at the distributions of the instantaneous coreness values $C^i(t)$ over all neurons and time-frames. A weighted coreness distribution from a representative recording is shown in Figure 3.4.A (see Figure 3.6 for equivalent unweighted coreness analyses). Figure 3.4.B moreover displays instantaneous distributions of the weighted coreness, for the same recording and for several time frames. We found that, within each time frame, a majority of neurons had low coreness values, i.e., they were peripheral nodes in the instantaneous sharing network (red color in the cartoons of Figure 3.4.A), while fewer neurons had high coreness values. Interestingly, in most recordings there was not a sharp separation between core and periphery. On the

contrary, we generically observed the presence of a smooth distribution spanning all possible coreness values. The transition between core and periphery was thus smooth, without gaps but with neurons displaying gradually less tight links with the core, without yet being fully peripheral. We note that such smooth distributions are actually encountered in many systems [56], a strict distinction between a very central core and a very loose periphery being only a schematic idealized vision and real networks displaying typically hierarchies of scales and local connectivities.

The analyses of Figure 3.4.A and 3.4.B indicate that at any time-frame the sharing network has a soft core-periphery architecture, but does not inform us about how individual neurons evolve in time within this architecture. In order to follow dynamic changes in the coreness of individual neurons, we studied the time-evolution of this feature for each neuron of each recording.

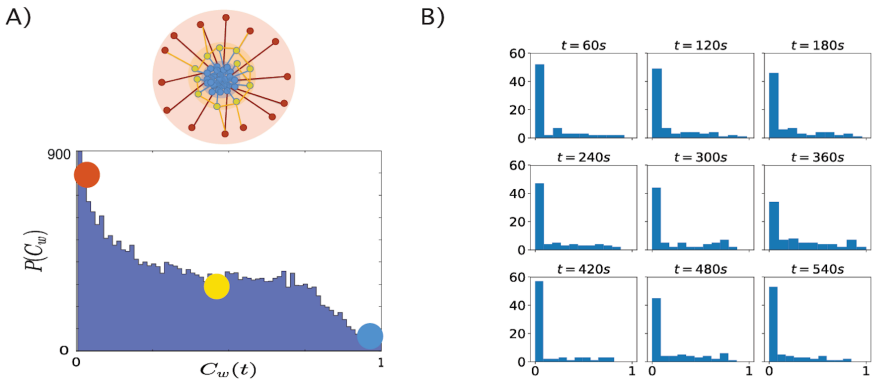

Figure 3.4. – **Dynamic Core-Periphery structure 1. A)** Top: Cartoon representing the *core-periphery* organization of the network with *core* nodes colored in blue and *peripheral* nodes in red; Bottom: histogram of the values of the instantaneous weighted coreness $C^i(t)$ of each neuron at each time of a recording. **B)** Histograms of instantaneous weighted coreness values of the neurons in several individual time-frames (every 60 seconds).

In Figure 3.5.A we plot the coreness $C^i_w(t)$ vs time, for each node $i \in [1, N]$ of a representative recording. The two highlighted lines in the figure represent the coreness evolution of two particular nodes. In light green, we show the instantaneous coreness of the node with maximum average coreness $\langle C^i_w(t)\rangle_T$ (averaged over the recording length T). The figure shows clearly that this neuron's instantaneous coreness is always large: the corresponding neuron is persistently part of the network's core throughout the whole recording. This contrasts with the purple line, which displays the instantaneous coreness of the neuron with largest coreness standard deviation ($\sigma(\langle C^i_w(t)\rangle_T)$): the curve fluctuates from high to low coreness values, indicating that the corresponding neuron switches several times between central core positions in the network and more peripheral ones. The contrast between these two behaviors is highlighted in the cartoon at the bottom of Figure 3.5.A.

The continuous range of observed instantaneous coreness values and the fluctuations in individual coreness values indicate that the set of most central neurons changes in time. We thus examined whether some regions were contributing more than others to this core. To this aim, we define the core, at each time-frame, as the set of neurons whose instantaneous coreness lies above the 95th percentile of the distribution (in histograms such as those in Figure 3.4.B). In Figure 3.5.B we then plot the *core filling factors* of the CA1 and mEC layers (top and center plots, respectively). We define the core filling factor of each region as the percentage of the overall number of neurons of the recording located in that region that belong to the core. We plot the time-evolution core filling factors separately for neurons located in different hippocampal CA1 layers (light and dark blue lines, top panel) and for neurons in different medial entorhinal cortex (mEC) layers (red, orange and yellow lines, center panel). The figure illustrates thet the core-filling factors vary substantially along time. In the example shown here (corresponding to the same recording as in Figure 3.5.A), the core-filling factor of CA1 Stratum Pyramidale (SP) neurons belonging to the core increases from ~ 2% to near 7% during the recording.

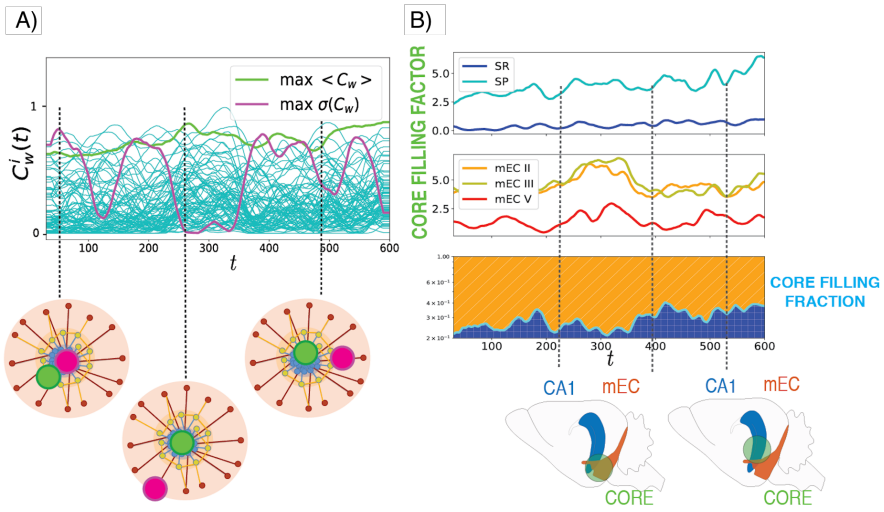

Figure 3.5. – **Dynamic Core-Periphery structure 2.** **A)** Plot of the temporal evolution of the weighted coreness $C_w^i(t)$ of each node i in a specific recording: the red line highlights the evolution of the coreness of the node with highest average coreness $\langle C_w(t)\rangle_{max}$; the orange line corresponds to the node whose coreness fluctuates the most (node of maximum variance of $C_w^i(t)$). **B)** Plots of the *core-filling factor* (top and center panels) and of the *core-filling fraction* (bottom) of the different layers of *hippocampus* (HPC) and medial *entorhinal cortex* (mEC).

The results of Figure 3.5.B indicate that the core is not restricted to neurons belonging to a specific region, but is generally composed of both neurons belonging to EC and neurons belonging to CA1. We remind indeed that our networks are networks of functional connectivity and do not have to reflect necessarily the underlying anatomical connectivity (for which it would be unlikely that our recordings pick up

mono-synaptically connected cells between different regions). However, the participation of CA1 and EC neurons to the core is changing through time and, as a result, the core is sometimes "more on the EC side" or "more on the CA1 side" (see lower cartoons in Figure 3.5.B). To visualize the relative fractions of core neurons belonging to the two different regions, we computed and show in the bottom panel of Figure 3.5.B the normalized *core filling regional fractions*: the fraction of core nodes belonging either to EC (orange) or CA1 (blue) – the sum of these two fractions adding up to 1. The orange and blue bands change thickness along time, reflecting in this recording a progressive shift from a low to a higher involvement of CA1 neurons in the core. This variation of the multi-regional core composition may reflect changes in the way the different regions control information integrative processes.

In Figure 3.6.A we plot the overall distribution of coreness values C_{unw} computed for the same recording whose weighted analysis is depicted in Figures 3.4 and 3.5, while in Figure 3.6.B and C we display the core-filling factor analysis and the instantaneous coreness values sampled at different time-stamps of the same unweighted temporal network. The results of the analysis of the unweighted network follow in all aspects what resulted from that of the weighted version of the network. In Figure 3.6.D we plot the overall distributions of weighted (red) and unweighted (yellow) coreness values for all recordings. We note how the weighted coreness has a tendency to highlight bigger differences in the counts of low versus high values of coreness with respect to the unweighted case. However, the general trend of a majority of low coreness values is found in all recordings.

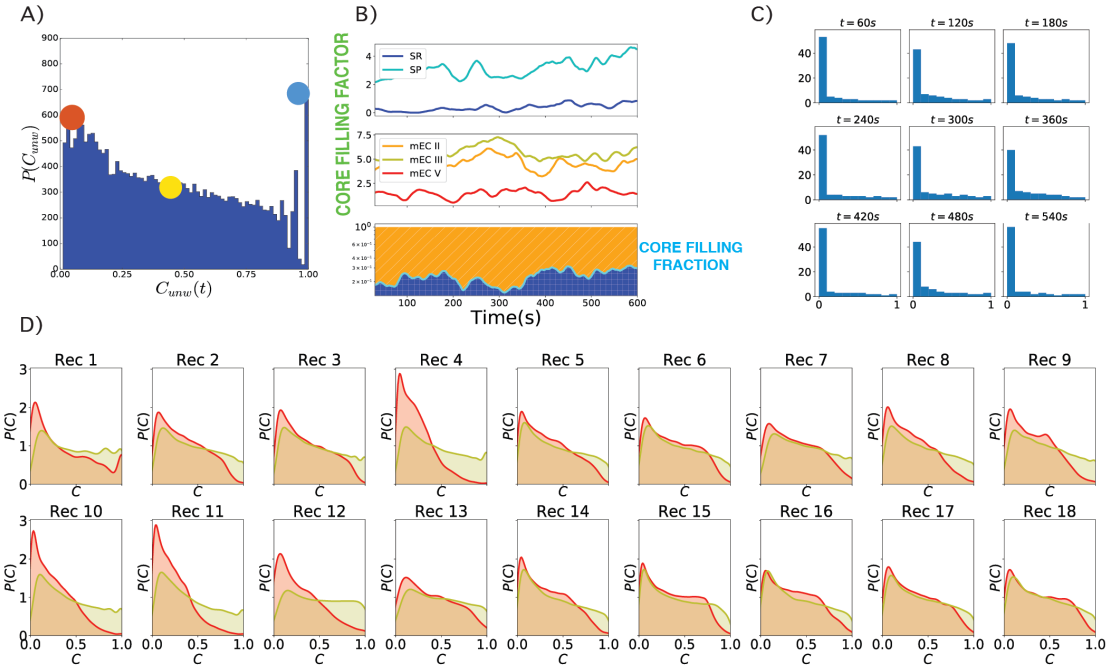

Figure 3.6. – **A)** Histogram of the instantaneous unweighted coreness of all neurons in all time-steps for the same recording as in Figures 3.4 and 3.5 (unweighted analogous of Figure 3.4.A). **B)** Unweighted core-filling factors and core-filling fractions of the same recording as in Figure 3.5. **C)** Histograms of instantaneous unweighted coreness values for 9 different time-steps of the network's evolution. **D)** Density plots of the values of instantaneous weighted (red) and unweighted (yellow) coreness of all neurons at all times, separately for each recording.

3.2.1. Comparison with random null models and randomized references

We are interested in seeing whether the dynamic core periphery structure that we found is not something that could have emerged simply by chance. For this reason, we compare the results obtained in the empirical data to those achieved by repeating the presented analysis on three different null models obtained by different randomization procedures of the original networks:

— A) Random null model: temporal network obtained by generating at each time step t an Erdös-Rényi random graph with the same number of nodes and edges as the original data.

— B) Degree preserving null model: temporal network generated by randomizing at each time t the edges of the original network at the corresponding time, preserving the degree (number of connections) of each node. To this aim we use the method of [120].

— C) Neighborhood preserving null model: a temporal network whose adjacency

matrix at time t is obtained by a systematic reshuffling of the weights of the experimental data temporal network: this preserves the neighborhood (set of neighbours) of each node at each time. This randomization procedure leaves therefore the unweighted structure unchanged.

In Figures 3.7, 3.8 and 3.9 we plot the analysis depicted in Figures 3.4, 3.5 repeated for the three randomized versions of the data. In Figure 3.7 the instantaneous coreness values of nodes of the instant ER model display a noisy dynamics (left, above) around small values, and their distributions for the total recording (left, below) and at different times (right) are peaked around low coreness values, with no high coreness values. For the degree-preserving randomization, in Figure 3.8, the plot of instantaneous coreness reveals patterns, for the nodes of maximum and most fluctuating coreness, that somehow resemble those shown in Figure 3.5, however the coreness values are much lower than those measured for the experimental data. This is reflected in the overall distribution of coreness values and the distributions sampled at specific time stamps, once more peaked around low values and no high values of coreness. We find analogous results for the neighborhood preserving null model (Figure 3.9): even though the instantaneous coreness plot shows different patterns for different nodes, as in the case of Figure 3.5, the values of weighted coreness are sensibly lower.

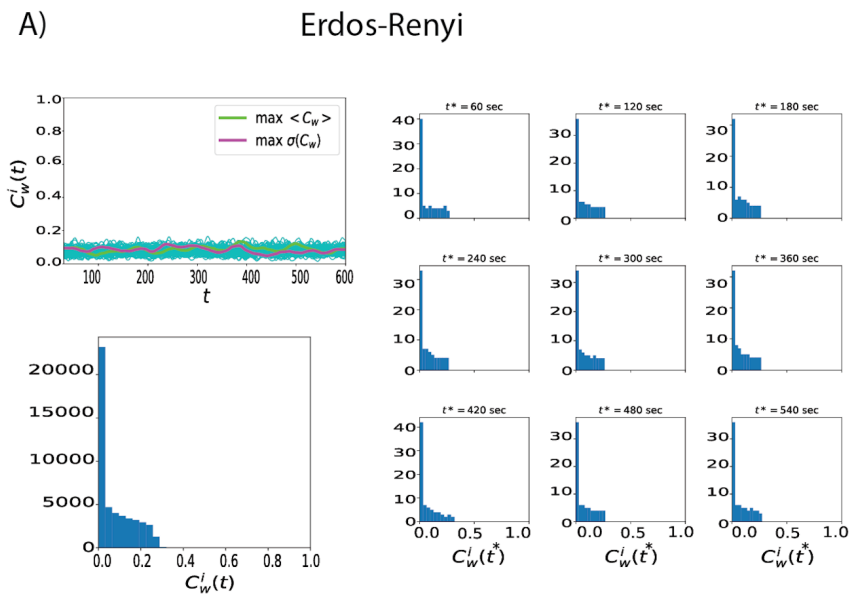

Figure 3.7. – Here we analyze the time series of weighted instantaneous coreness of nodes and the distribution of these values for the first null model, defined as a temporal network with at time t an Erdös-Rényi graph with the same number of nodes and edges as the experimental data at the same time t.

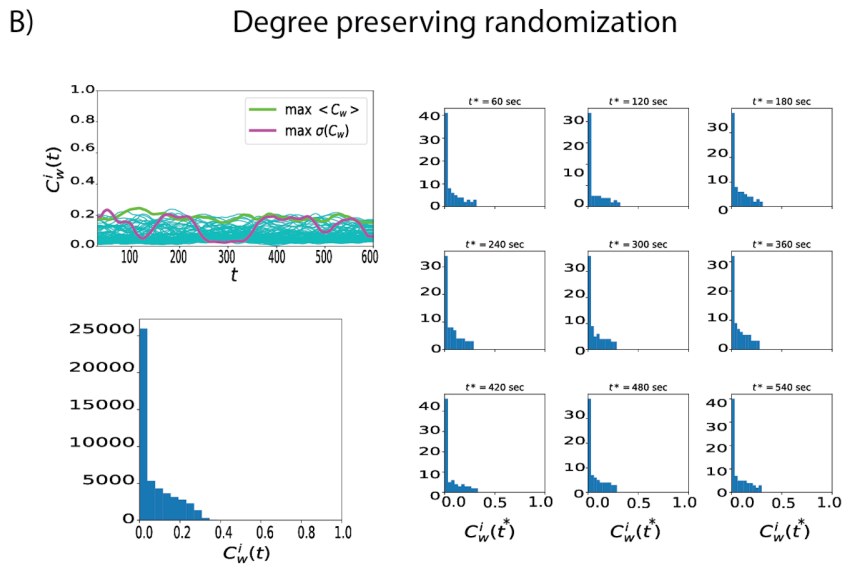

Figure 3.8. – The second null model is obtained by a randomization of the links at each time t, which preserves each node's degree [120].

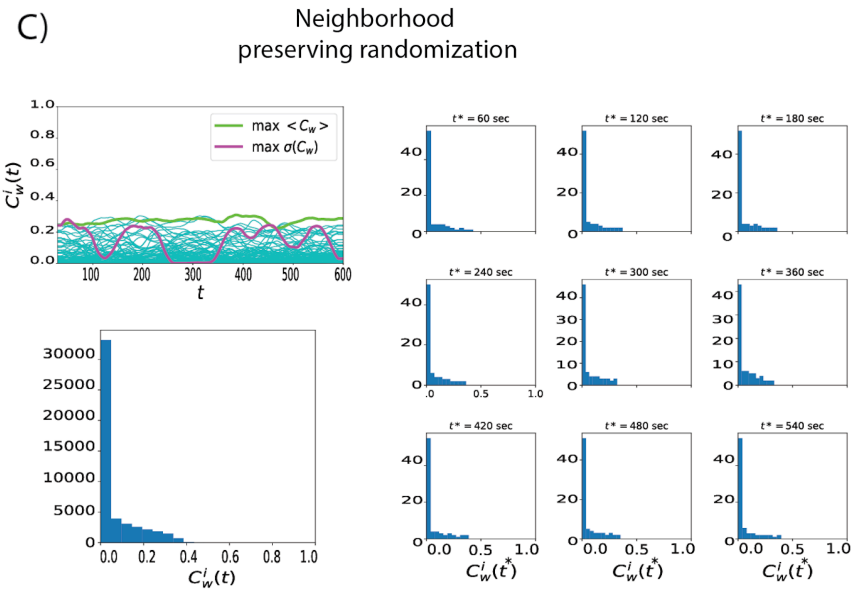

Figure 3.9. – The third null model corresponds to a randomization of the weights of the network's edges at each time, preserving the neighborhood (list of neighbors) of each node at each time.

3.3. Network states

As previously mentioned and summarized in Figure 3.2.C, for each recording and each time window t, we computed for each neuron $i \in [1, N]$ several temporal network properties, tracking notably the "liquidity" of its neighborhood (Jaccard index and cosine similarity) and its position within the core-periphery architecture (weighted and unweighted instantaneous coreness values). To investigate how these properties change dynamically at the global network level, we computed for each of these four quantities the correlation between their values at different times, obtaining four correlation matrices of size $T \times T$. For instance, the element (t, t') of the unweighted liquidity correlation matrix is given by the Pearson correlation between the N values of the Jaccard coefficient computed at t $\{J^i(t),\ i \in [1, N]\}$ and the N values computed at t' $\{J^i(t'),\ i \in [1, N]\}$. In Figure 3.10, we show these four correlation matrices for a representative recording, two for the unweighted features (above, Jaccard index and unweighted coreness), and two for the weighted ones (below, cosine similarity and weighted coreness).

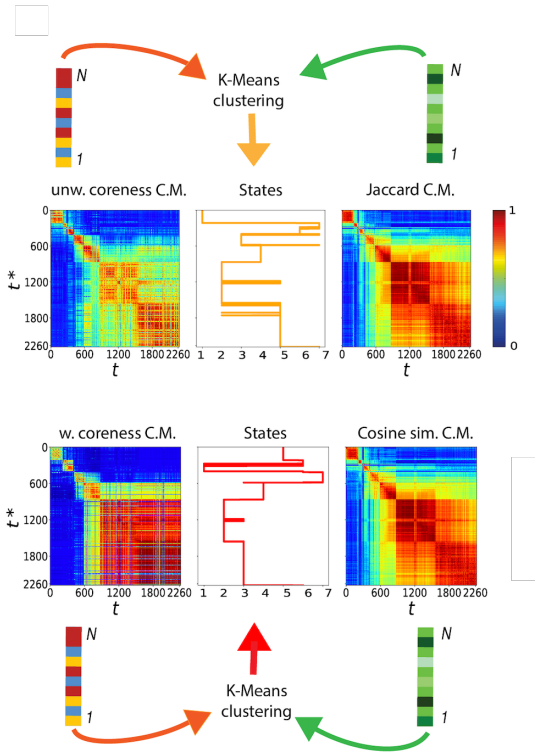

Figure 3.10. – **Liquidity and coreness network-states.** For each recording, the feature vectors of liquidity and coreness described in Figure 3.2D are combined at each time. K-means clustering of these vectors yields for each recording a sequence of *network states* visited by the network. On both sides of the network state sequences are the correlation matrices (C.M.) of the various feature vectors.

The block-wise structure of these correlation matrices suggests the existence of

epochs in time where neurons' feature values are strongly correlated (red blocks on the diagonal). In the case of Figure 3.10, mostly diagonal blocks are observed, with low correlation values outside the blocks, meaning that the network configurations are similar during each epoch but very different in different epochs. In other cases, we sometimes observe as well off-diagonal blocks, indicating that the network might return to a configuration close to one previously observed (we show an example of this behavior in Figure 3.11, as well as an example in which only one epoch is observed). Each block on the diagonal (epoch in which the node properties are strongly correlated) can be interpreted as a network connectivity configuration associated to specific liquidity and coreness assignments of the various neurons. We call *network states* these configurations.

To quantitatively extract such discrete network states, we use the time-series of the feature vectors $\Theta(t)$, $\mathbf{J}(t)$, $\mathbf{C}_w(t)$ and $\mathbf{C}(t)$.We concatenate these vectors two by two at each time, obtaining two $2N$-dimensional feature vectors: the first one contains at each time the values of the unweighted liquidity and coreness of all nodes ($\{\mathbf{J}(t), \mathbf{C}(t)\}$), and the second one contains the corresponding weighted values ($\{\Theta(t), \mathbf{C}_w(t)\}$). We then perform in each case (weighted and unweighted) an unsupervised clustering of these T $2N$-dimensional feature vectors. As a result of this clustering procedure, as shown in Figure 3.10, we obtain a sequence of states (temporal clusters of the feature vectors) that the network finds itself in at different times (yellow state spectrum for the unweighted case, red for the weighted case). In addition, we plot the weighted and unweighted networks states extracted in other recordings, with interesting different patterns, in Figure 3.11.

We compared the network states spectra found for the weighted and unweighted case by computing the mutual information between the two sequences of states for each recording, normalized by the largest entropy among the entropies of the two distinct sequences. Such relative mutual information is bounded in the unit interval and quantifies the fraction of information that a state sequence carries about the other (reaching the unit value when the two state sequences are identical, and being zero if the two sequences are statistically independent). We compute this quantity for each recording and display the distribution of values obtained as a light green boxplot on the left of Figure 3.12.A. This boxplot shows that the mutual information values between the weighted and unweighted network states sequences of a recording are concentrated around a median approaching 0.8. Therefore, the spectra of network states extracted by the weighted and unweighted analyses are generally matching well, indicating the robustness of their extraction procedure. Most importantly, the high degree of matching between weighted and unweighted analyses confirms that network state changes correspond to actual connectivity re-organizations (as revealed by unweighted analyses) and not just to weight modulations on top of a fixed connectivity.

As previously discussed, the system undergoes switching between two possible global brain states during the anesthesia recordings: these global states are associated to different oscillatory patterns, dominated by either Theta (THE) or slow (SO) oscillations. We studied therefore what is the relation occurring between changes in the network state and global oscillatory state switching. To this aim, we computed

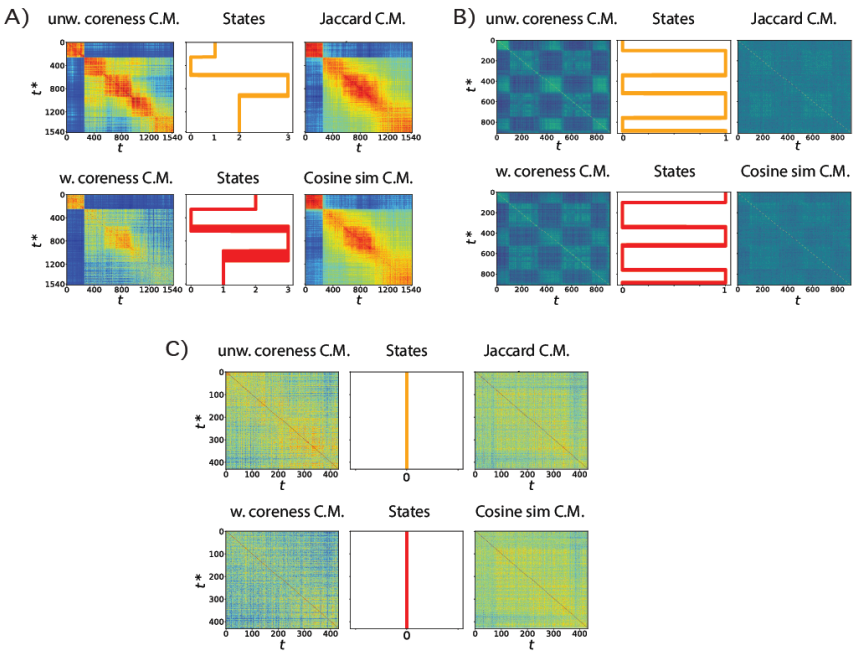

Figure 3.11. – Recordings with different types of feature vectors correlation matrices and network states spectra. In each case, we show as in Figure 3.10.A. the temporal sequence of network states extracted by the unsupervised clustering of feature vectors, with on both sides the correlation matrices. Top plots correspond to unweighted features, bottom plots to weighted features. **A)** Case with diagonal blocks in the correlation matrices, with no off-diagonal blocks. The sequence of network states is in agreement with this structure, i.e. the network visits each network state only once. **B)** Case with chess-board-like correlation matrices. As seen from the network-state-spectra this recording is indeed in periodic oscillation between two states. **C)** Case in which no state can be clearly identified: this recording can be interpreted as in an extremely liquid single state, where both the core-periphery organization of the network and the neighborhoods of neurons change continuously with no clear temporal structure.

the normalized mutual information between network state sequences (weighted or unweighted) and global state sequences. The distributions of the values obtained are shown as boxplots on the right of Figure 3.12.A, for both weighted (red) and unweighted (yellow) network states sequences. In both cases, we detect positive, although low, values of the relative mutual information with global oscillatory states, with a median value close to ~ 0.3. This indicates that some coordination between global oscillatory state and network state switching exists but that oscillatory state switching does not well explain network state switching. A very simple reason for this poor correlation is that, while there are just two main global oscillatory states (see

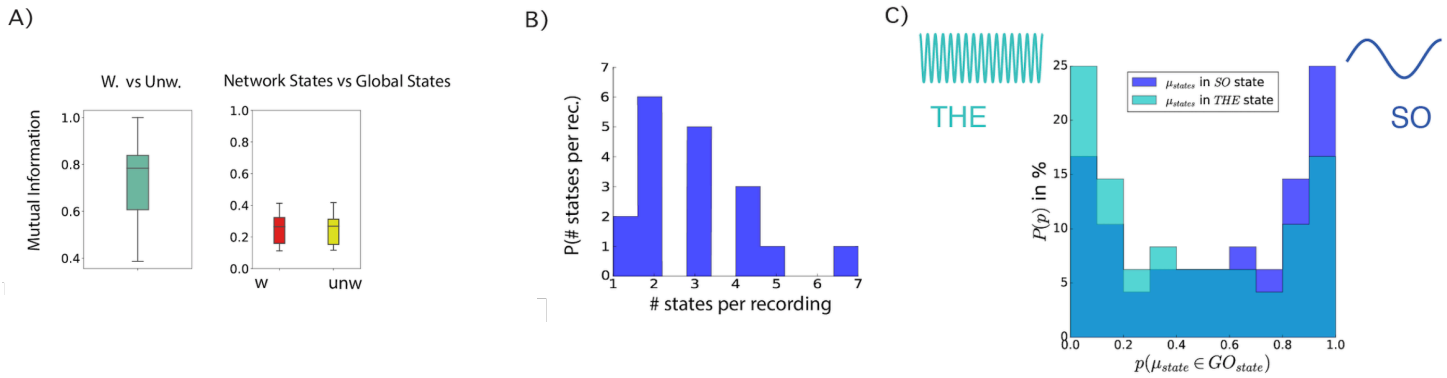

Figure 3.12. – **Liquidity and coreness network-states. A)** Left panel: Distribution of the values of the mutual information between the weighted and unweighted network states spectra of all recordings. Right panel: distribution of the values of mutual information between the weighted network states spectrum and the global oscillating states spectrum (red boxplot) for all recordings (yellow boxplot: same for the unweighted network states spectra). **B)** Statistics of the number of network states in the different recordings. In many recordings this number is larger than 2, and it can reach values as large as 7. **C)** Histograms showing the percentage of *states* having probability p to occur during a specific *Global Oscillations state*, *slow* (blue) or *theta* (light blue).

however section 3.6), the number of network states is not a priori limited. In fact, the statistics of the number of network states in the different recordings, shown in Figure 3.12.B, indicates that in many recordings we could extract at least three network states and sometimes up to seven. Therefore, network state switching can occur within each oscillatory global state.

Nevertheless, it is possible that each given network state would tend to occur mostly within one specific global oscillatory state. To check whether this is the case, we computed for each network state the fraction of times that this state occurred during THE or SO epochs. We show in Figure 3.12.C the histograms of these time fractions, measured over the set of all network states. The light blue histogram corresponds to the fractions of time a network state manifested itself during the THE state (the dark blue histogram gives the same information but for the SO state). Both histograms are markedly bimodal, indicating that a majority of states occur a large fraction of times during either the THE or the SO states, but not in both. In other words, network states are to a large degree oscillatory state specific. Therefore, the global oscillatory states do not fully determine the observed coreness and liquidity configurations (there may be several network states for each of the oscillatory states) but most network states can be observed only during one specific global oscillatory state and not during the other.

3.4. Connectivity profiles and styles

The network-states as defined in the previous section therefore represents epochs of dynamic reconfiguration of the functional connections among pairs of neurons (liquidity) and of the core-periphery organization of the network. In order to shed light on the dynamics unfolding *within* each network state, we investigate and characterize the temporal network properties at the level of single neurons within each of the detected network states. To do so, we computed, for each node and in each state, a set of dynamical features averaged over all time frames assigned to the specifically considered state. We focus here on the weighted features, since the weighted and unweighted analysis provide similar results. The state-specific *connectivity profile* of a given neuron i in a given state included first:

— its state-averaged weighted coreness value;
— its state-averaged cosine similarity value.

Note that analogous time-resolved features were already used for network state extraction, but that we consider here state-averaged values. We also computed four additional network state specific features, defined as follows for each node $i \in [1, N]$ in a state h spanning the set of times T^h (see explanatory cartoons in Figure 3.13):

— the state-averaged strength $\langle s^i(t)\rangle_{t\in T^h} \equiv \langle \sum_j w_{ij}(t)\rangle_{t\in T^h}$, hence the state-averaged total instantaneous weight of the connections of i;
— the activation number n_a^i: it is the number of times that the strength of node i changes from 0 to a non-zero value within the state, hence it gives the number of time that i changes its connectivity from being isolated to being connected to at least one another neuron;
— the total connectivity time τ^i: it is the number of time frames within T_h in which i is connected to at least one another neuron;
— the Fano factor $\Phi^i \equiv \frac{\sigma(\langle \Delta t^i\rangle_h)}{\langle \Delta t^i\rangle_h}$: each of the n_a^i periods in which i is connected to at least another neuron has a certain duration Δt^i (the sum of these durations is τ^i), and Φ^i, the ratio of the variance and the average of the different connectivity durations of i over the state h, quantifies whether these durations are of similar value or very diverse.

Each neuron's temporal properties within a given state are thus summarized by the values of these overall six features, which define the neuron's state-specific connectivity profile as a six-dimensional vector. Normalizing all the features to have values between 0 and 1, connectivity profiles can be visually represented as radar plots (Figure 3.14.A) in which the value of each feature is plotted on the corresponding radial axis.

After computing the connectivity profile of each node, in each network state and in each recording, we performed an unsupervised clustering (using K-means clustering) over all these six-dimensional connectivity profiles in order to identify categories of these profiles, which we call *connectivity styles*. With this approach we uncovered the existence of four general connectivity styles that a neuron can manifest within a network state:

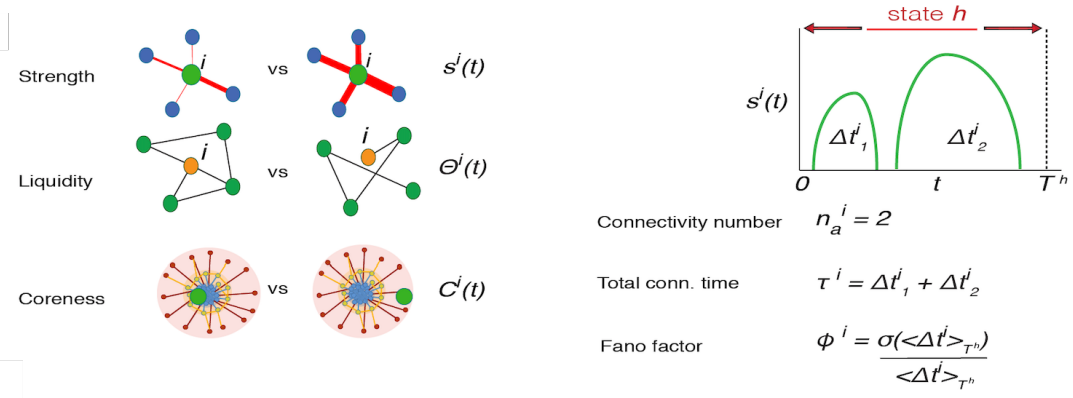

Figure 3.13. – **State-wise network features** Cartoons illustrating the features: the *strength* $s_i(t)$ of a node i at time t measures the global importance of node i's connections (the cartoon shows a comparison of low vs high values of $s^i(t)$); its liquidity; its coreness; the connectivity number n_a^i and total connectivity time τ^i of node i in a state; the Fano factor.

— *Core style (or "streamers")*, a class of nodes of high average coreness, average strength, average cosine-similarity, total connectivity time and low activation number n_a and Fano factor Φ: overall, a class of rather central neurons with numerous stable connections that are persistently connected within a state (blue representative polygone in Figure 3.14.A). A behavior similar to that of a speaker of an assembly, continuously conveying information to the same, and many, people: a *"streamer"* of information;

— *Peripheral style (or "callers")*, nodes with high activation number and total connectivity time but low strength, Fano factor and coreness: a class of peripheral nodes that are periodically connected in numerous events of similar connectivity durations and low weights within a state, whose connections are not completely liquid nor completely stable (red representative polygone in Figure 3.14.A). A behavior similar to a customer or guest regularly making short calls to trusted core members to be updated on the latest news: aka, a "caller".

— *Bursty core-skin style (or "free-lancer helpers")*, a class of connectivity profiles characterized by nodes with intermediate coreness and strength and high values of cosine similarity and total connectivity time (yellow representative polygone in Figure 3.14.A) displaying high values of Φ, therefore interpreted as a class of nodes that have stable connections, that are active for a long time yet with highly varying connectivity times.

— *Regular core-skin style (or "staff helpers")*, a classes of connectivity profile also characterized by nodes with intermediate coreness and strength and high values of cosine similarity and total connectivity time (purple representative polygone in Figure 3.14.A), but characterized, w.r.t. Bursty core-skin profiles, by low values

of the Fano factor, hence the connectivity durations of these nodes do not fluctuate much. The behaviors of these two connectivity styles, *Bursty* and *Regular core-skin*, can be assimilated to the one of external experts assisting core staff in a company, either with regular work schedules (the regular core-skin neurons could then be seen as *"staff helpers"*) or sporadically and irregularly (the bursty core-sking neurons could then be seen as *"free-lancer helpers"*).

Note that we also identified (and subsequently discarded) an additional "Junk" cluster with relatively fewer elements (9.7% of the total number of connectivity profiles computed for all neurons in all recordings) and small values of all features. We thus removed these cases, as usual in unsupervised clustering applications [63], to better discriminate the remaining "interesting" classes listed above.

Overall each connectivity profile (one for each neuron in each possible network state in the associated recording) was categorized as belonging to one of the above connectivity styles, according to the output cluster label assigned by the unsupervised clustering algorithm. However, a substantial diversity of connectivity profiles subsists within each of the clusters. We therefore considered as well a soft classification scheme, which quantifies the degree of relation of each individual connectivity profile with the tendencies identified by each of the different connectivity style clusters. Concretely, we trained a machine learning classifier to receive as input a connectivity profile and predict the connectivity style assigned to it by this unsupervised clustering. In this way, after training, the classifier assigned to each connectivity profile a four-dimensional vector whose elements represented the probabilities of belonging to any one of the four possible connectivity styles (see *Methods* for details). In Figure 3.14.B, each connectivity profile is represented as a dot with as coordinates the soft classification labels produced by the classifier, i.e., the probabilities that each given connectivity profile belongs to the periphery, core-skin (summing the probabilities for the bursty and regular subtypes) or core connectivity styles. This plot reveals, on the one hand, the existence of a gap between core (blue) and periphery (red) connectivity profiles: in other words, connectivity profiles that are likely to be classified as of the "streamer" type are very unlikely to be classified as being of the "caller" type, stressing the radical difference between these two connectivity styles. On the other hand, both the core and periphery connectivity styles display some mixing with the core-skin style, as made clear by the almost continuous paths of connectivity profiles from the core (blue) to the core-skin (yellow) and from the core-skin to the periphery (red). This means that there is a continuum spectrum of connectivity profiles interpolating between "streamers" and "helpers" on one side and "helpers" and "callers" on the other. The polygones shown in Figure 3.14.A are on the contrary *archetypal* (in the sense introduced by [27]). These archetype profiles manifest in an extreme manner the tendencies inherent to their connectivity style. This is reflected by the fact that they lie at the vertices of the bounded soft membership space represented in Figure 3.14.B. They display thus strong similarity to just one connectivity style, which they epitomize even better than the centroids of the associated connectivity style cluster, having near zero chance of being misclassified (cluster centroids are shown for comparison in Figure 3.15).

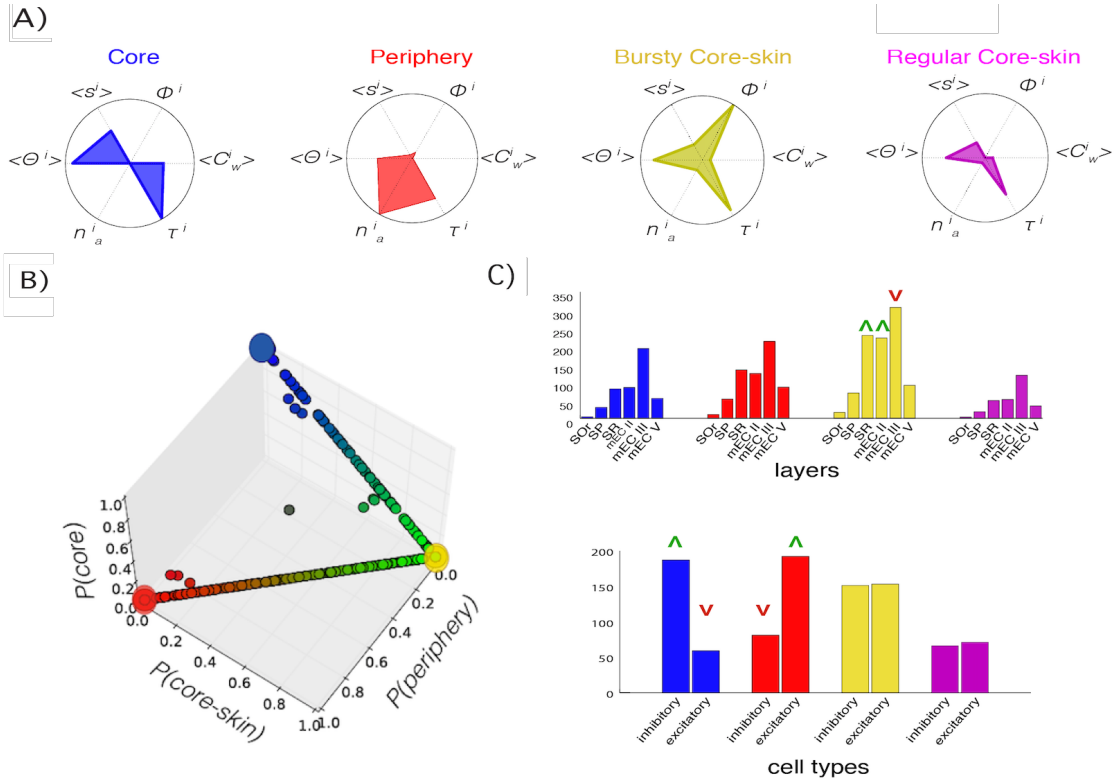

Figure 3.14. – **Connectivity profiles.** **A)** The connectivity profiles, i.e., 6-dimensional vectors whose components are its *state-averaged* features: average coreness $\langle C_w^i \rangle_h$, average liquidity $\langle \Theta^i \rangle_h$, average strength $\langle s^i \rangle_h$, connectivity number n_a^i, total connectivity time τ^i, Fano factor Φ^i. Clustering of all the connectivity profiles yields 4 *connectivity styles*: core (blue), periphery (red), bursty core-skin (yellow) and regular core-skin (magenta). **B)** 3D plot of the connectivity styles space. **C)** Histograms of the layer location (top plot) and of cell type (inhibitory and excitatory, bottom plot) populations per connectivity style. A green upward arrow means that the connectivity style of the corresponding color is statistically over-represented in the corresponding layer or cell type, whereas a red downward arrow means that the connectivity style is under-represented in that layer or cell type.

We also check whether the connectivity styles where indeed classes of neuron behaviours related to the network states. In order to do so we compute the *silhouette score* of a connectivity style as the difference between the distance of the centroid of the relative cluster of connectivity profiles from that of the nearest cluster, and the distance from that of the furthest cluster. We then compare the mean silhouette score averaged over all empirical connectivity styles in a recording to distributions obtained for each recording by the following null model: we first reshuffle randomly the network-state labels of the time-frames of the whole recording while conserving the total length of each network-state. We then compute the connectivity profiles on the randomized states, cluster them in order to retrieve the connectivity styles,

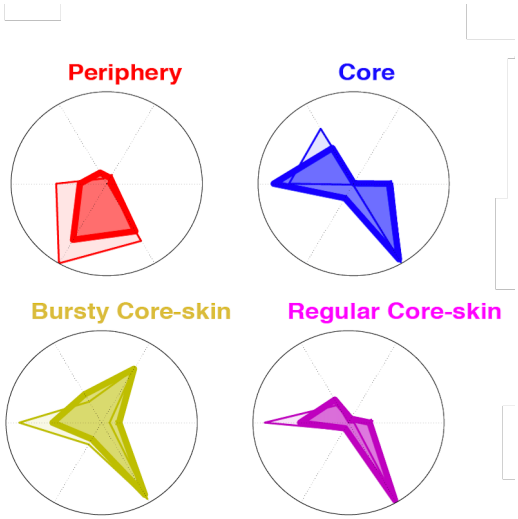

Figure 3.15. – Maximal connectivity profile of each connectivity style (lower opacity), as shown in Figure 3.14.A and connectivity profile of the centroid of the Kmeans clustering result (higher opacity).

and compute the new silhouette. Figure 3.16 shows indeed that clustering quality of empirical connectivity styles was in a large majority of cases well above chance level.

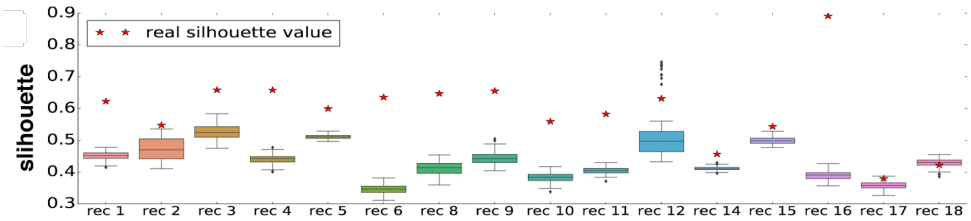

Figure 3.16. – Silhouette plot: the red stars give for each recording the silhouette value for the Kmeans clustering performed on the connectivity profiles to retrieve the connectivity styles. These values are compared to distributions (boxplots) obtained for each recording by the following null model. We first reshuffle randomly the network-state labels of the time-frames of the whole recording while conserving the total length of each network-state. We then compute the connectivity profiles on the randomized states, cluster them in order to retrieve the connectivity styles, and compute the new silhouette. The boxplots correspond to the distribution of these null model silhouette values, obtained for 200 realizations of the reshuffling.

We finally checked whether the different connectivity styles were adopted more or less frequently by neurons in specific anatomical locations or of specific types (excitatory or inhibitory). In Figure 3.14.C, we plot the number of connectivity profiles

assigned to each style (colors as in Figure 3.14.A), separating them by anatomical layer and brain region. However, since we recorded unequal number of cells in the different layers (see Figure 3.1), we also accounted for the different numbers of cells and recordings per layer and estimated chance-level expectations for the connectivity style counts in each layer: this allowed us to detect significant over- or under-representations of certain styles at different locations. The numbers of "streamers" (core), "staff helpers" (regular core-skin) and "callers" (periphery) profiles were compatible with chance levels at all the recorded locations. We only detected over-representations (green upward triangles) of "free-lancer helpers" (bursty core-skin) in Stratum Radiatum (SR) of CA1 and Layer II of medial Enthorinal Cortex, and an under-representation (red downward triangle) of this style in Layer III of medial Enthorinal Cortex (see section 3.6 for possible interpretations). These moderate deviations from chance levels suggest that the connectivity styles adopted by different neurons (and thus their centrality in the core-periphery architecture of information sharing networks) are only poorly affected by their anatomical location in the hippocampal formation circuit.

We found however a stronger inter-relation between cell type and connectivity styles (Figure 3.14.C, bottom). We still found representatives of any of the connectivity styles among both excitatory and inhibitory neurons. However we found that the fraction of inhibitory (resp., excitatory) neurons among the core neurons was significantly above (resp., below) chance level. Conversely, the fraction of inhibitory (resp., excitatory) neurons among the peripheral neurons was significantly below (resp., above) chance level.

3.4.1. Connectivity profiles are network-state dependent and not only node-dependent

We have computed connectivity profiles per neuron *and* per network state, in order to enable the detection of a possible network-state dependency of the temporal properties of the neurons connectivity. However, the state-specificity of this computation does not prevent a priori a neuron to always assume the same connectivity profile across all possible network states to which it participates. It is thus an open question, whether connectivity profiles are only node-dependent (for a given neuron, the same in every state) or, more generally, state-dependent (for a given neuron, possibly different across different network states).

To answer this question, we checked whether network state transitions are associated or not to connectivity style modifications at the level of individual neurons. We found that changes in the connectivity style of a neuron upon a change of state are the norm rather than the exception. We computed for every neuron the index η, quantifying the diversity of connectivity styles that a neuron assumes across the different network state transitions occurring during a recording. We named it cross-network-state connectivity profile transition rate η^i of neuron i and it is defined as:

$$\eta^i \equiv \frac{\#\, profile\ transitions\ of\ node\ i}{max(\#\, global\ classes, \#\, network-states)}. \tag{3.3}$$

It quantifies the tendency of neuron i to switch, often or rarely, between connectivity profiles belonging to different connectivity styles in different states as it is bounded in the range $0 \leq \eta \leq 1$ and assumes the null value if the neuron always remains in the same connectivity style (no style transitions); it takes the unit value if the neuron changes connectivity style every time that a network state transition occurs, and it assumes intermediate values if style transitions occur for some of the network state transitions but not for all. The distribution of the observed values of this η index is shown in Figure 3.17.A. This distribution is bimodal, with a first peak occurring around $\eta \sim 0.5$ and a second at $\eta \sim 1$ (computed according to either unweighted or weighed network state transitions). This means that almost no neuron was associated to a network state-independent, fixed connectivity style. On the contrary, a large number of neurons changed connectivity style in at least roughly half of the network state transitions (first mode of the distribution), and many changed style at almost each state transition (second mode of the distribution of η).

Figure 3.17.B is a graph-representation of the transition matrix between connectivity styles, computed over all the observed connectivity style transitions. We plot here a weighted, directed graph, in which the two connectivity styles "regular" and "bursty core-skin" have been merged for simplicity into a single category. The width of each colored edge corresponds to the value of the transition rate from the class of the same color. The transition rate is defined as the probability that a node characterized by one of the three connectivity styles in one network-state, switches to one of the other two connectivity styles in the successive network-state. Consistently with Figure 3.14.B, we find that edges of large weight connect the core-skin to the periphery and to the core

in both directions: high transition rates are found between these styles. The edges connecting core and periphery are sensibly smaller. We can thus conclude that it is largely more likely that neurons of a *core* connectivity profile switch to a *core-skin* profile in the following network state than to a *peripheral* profile, and vice versa: direct transitions between core profiles and periphery profiles are not very likely to occur, although they are not impossible.

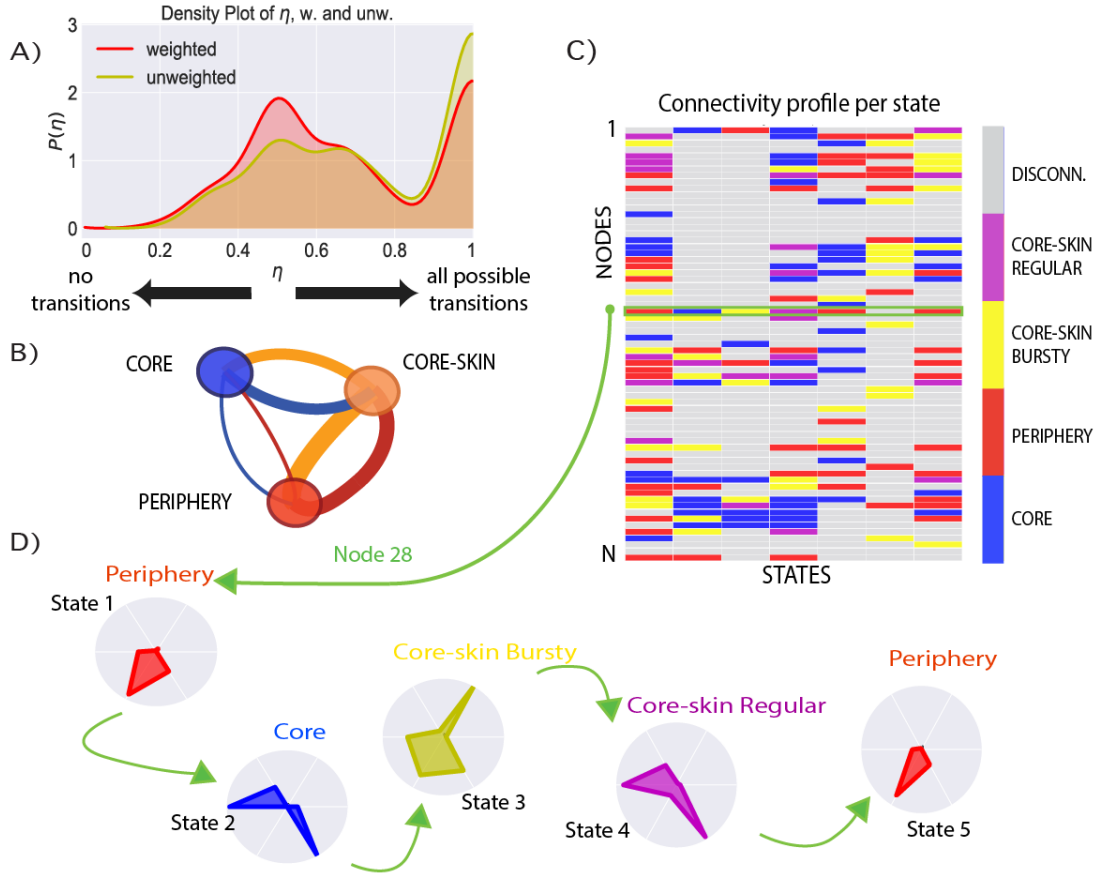

Figure 3.17. – **Network-state specificity of connectivity profiles.** **A)** Histogram of the connectivity-style-switching probability η of nodes, in the weighted (red) and unweighted (yellow) cases, computed for each neuron in each recording. **B)** Visualization as a weighted, directed graph of the cross-network-state connectivity style transition matrix. **C)** Matrix representation of the changes in connectivity styles of the neurons when the network changes state. Each element (s,n) of the matrix is coloured according to the connectivity style to which node n's connectivity profile belongs in state s. **D)** Connectivity profile transitions of node $n = 28$.

Individual neurons can thus float through the core-periphery architecture, descending from core towards periphery and ascending back into the core, via crossing the core-skin styles. The overall behavior of neurons switching styles between states is illustrated in Figures 3.17.C and 3.17.D for a specific recording. The former is a matrix

whose element (i, s) has the color of the connectivity style exhibited by node i in state s. In this plot we highlight the row corresponding to the state-wise evolution of a specific selected node, whose successive connectivity profiles in the successive network state ares shown in Figure 3.17.D.

More complete transition matrices (including as well the core-skin class separation into "bursty" and "regular", and the "junk" classes) are shown in Figure 3.18.

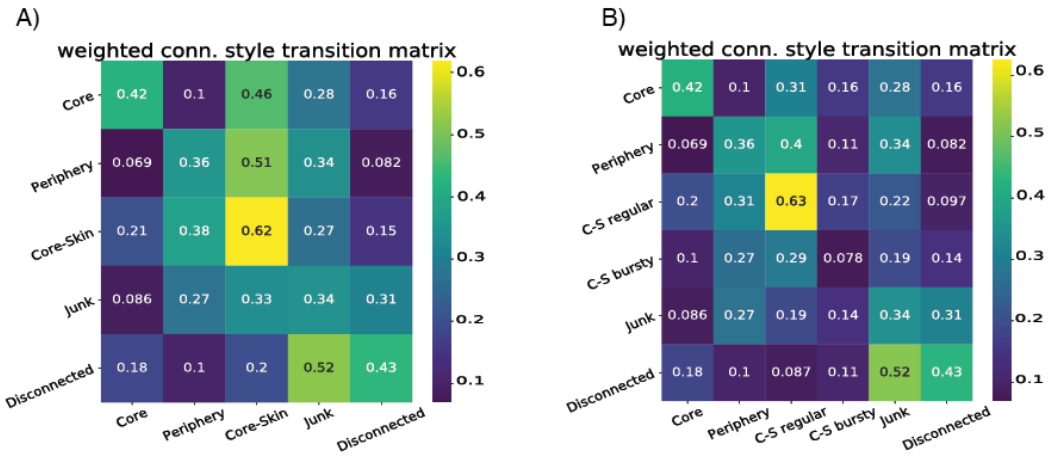

Figure 3.18. – **A)** Transition matrix T_{ij} between connectivity styles of a neuron in successive network states taking into account the core, periphery, core-skin and junk connectivity styles, as well as network states in which the neurons are not connected to the rest of the network. **B)** Transition matrix T_{ij} between connectivity styles of a neuron in successive network states, with separate core-skin regular, core-skin bursty styles. For both matrices, each diagonal element $T(i,i)$ represents the persistency rate of the corresponding connectivity style, i.e., the probability of a neuron to exhibit the same connectivity style in two successive global network states. The non-diagonal matrix elements are normalized on each row so that $\sum_{j\neq i} T(i,j) = 1$.

3.4.2. Connectivity profiles only poorly depend on firing rate

In our recordings we observed a diversity of firing rates between different single units. While the median firing rate was close to ~ 1 Hz, some neurons had, at specific moments, high rates approaching 40 Hz, despite the anesthesia conditions. Importantly, firing rates were also changing across the different network states. To check whether variations of temporal connectivity features compiled in the state-specific connectivity profiles of different neurons could simply be explained by these firing rate variations, we constructed scatterplots of state-specific coreness, liquidity, strength, number of activations, Fano factors and total time of activation for the different neurons against their firing rate, averaged over the corresponding state. These scatter plots are shown in Figure 3.19, where there is no evident relation between the average firing of a neuron in a network state and the network properties that we computed, showing that the various connectivity styles are not simply related to the neurons' activity.

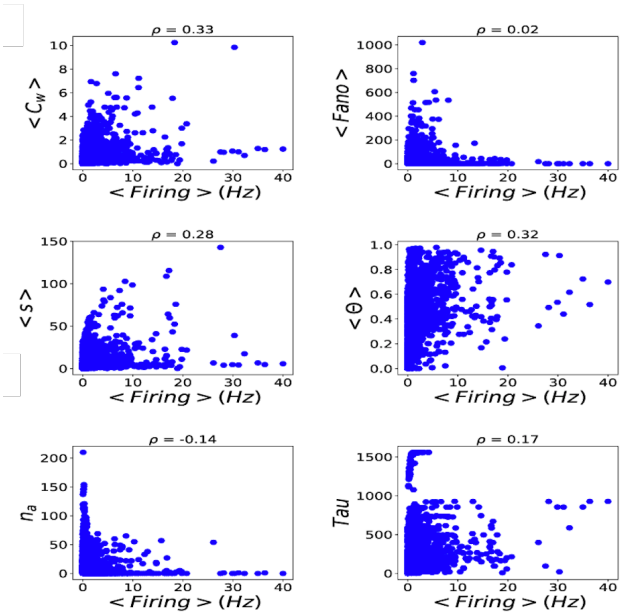

Figure 3.19. – Scatterplots between each one of the 6 features computed for each neuron in each network-state of each recording and the average firing rate of the same neuron in the same network state.

The degree of correlation between firing rate and connectivity features was at best mild. Cells with larger than median firing rate tended to have slightly less liquid neighborhoods on average, but the range of variation was broad and largely overlapping with the one of liquidity values for lower firing rate neurons. Other features, such as total time of activation, displayed an even weaker dependence on firing rate, while some others, such as the connectivity number, tended to be inversely correlated with firing, but, once again, in a rather weak manner (the correlation coefficient is $\rho = -0.14$).

Overall, the analyses of Figure 3.19 indicate that the structure of information sharing networks is shaped by the coordination of firing between units more than by the firing rates of individual cells.

3.4.3. Relations between connectivity styles and active information storage

As mentioned in Chapter 2, information sharing can be seen as a generalized form of cross-correlation where the time-lagged mutual information capture all types of linear and nonlinear correlations. Analogously, one can evaluate a generalized auto-correlation functional, known under the name of active information storage [110]. We evaluated active information storage of a given neuron, within a given time-window following [47], as defined in equation 2.4. While information sharing quantifies the amount of information in common between the present activity of a neuron and the past activity of another, information storage (see Chapter 2) is meant to capture the amount of information in the present activity of a neuron which was already conveyed by its past activity. In this sense, neurons with a large value of information storage would functionally act as "memory buffers" repeating in time the same information content. In [47] we found that information storage, as information sharing, is state-dependent and that some cells, that we called therein "storage hubs" display particularly large values of storage. We checked here whether high storage cells manifest some preferential connectivity style.

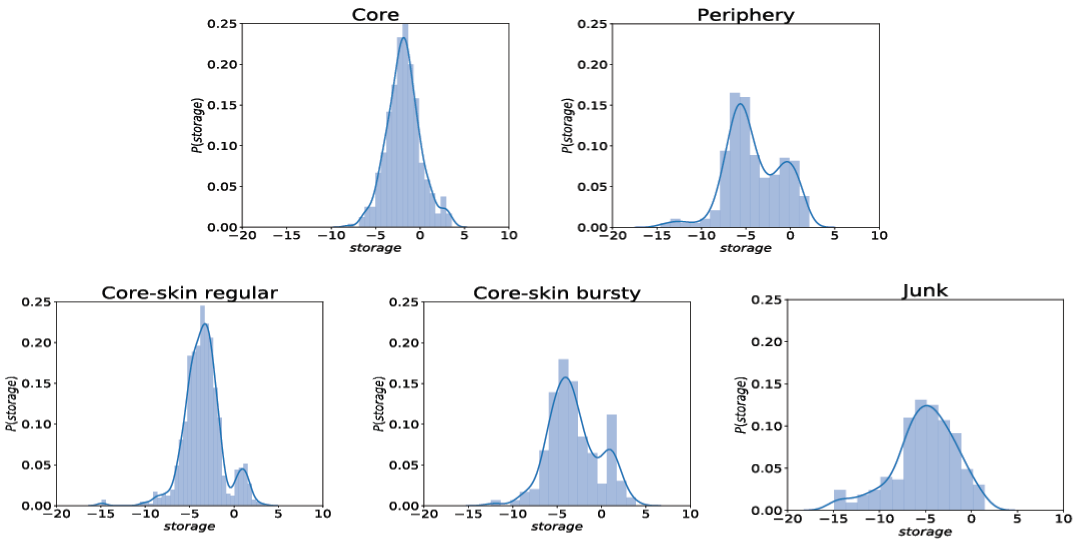

Figure 3.20. – Density plots of the logarithm of the network-state-aggregated storage (see 2.4) of connectivity profiles of each of the five (junk included) connectivity styles.

We show in Figure 3.20 distributions of information storage values, separated according to the connectivity style assumed by different neurons in each different network

state. We found that high storage is not associated exclusively to specific styles of connectivity. On the contrary, cells with high storage could be found for any of the connectivity styles. The overall larger storage values where found for core streamers cells. However, we could find high storage cells even among the core-skin helpers and the periphery callers. Interestingly, distributions of storage for core-skin and periphery styles were bimodal, including a peak at high-storage values.

3.5. Changes in epilepsy

As shown in [45] (see Chapter 2 for further details), epilepsy seems to induce the disruption of the organization in time of the firing, storage and sharing sub-states. Together with colleagues, I was interested in investigating whether repeating the analysis presented in the previous sections on recordings from epileptic rats would reveal substantial changes in the dynamic core-periphery structure of information sharing networks. We therefore measured the coreness and the liquidity (Jaccard index) for the extracted unweighted information sharing networks. Interestingly, we found that average coreness and the overall coreness distributions computed within a sub-state were not significantly different in epilepsy for either mEC or CA1 (Figure 3.21). Therefore, the core-periphery architecture of information sharing networks within every sub-state is preserved in epilepsy. However, during the SO state, the average Jaccard values in CA1 are significantly decreased in epilepsy as compared to control (Figure 3.22). Thus, in CA1 there is enhanced liquidity of the connectivity and more volatile recruitment of neurons in the core.

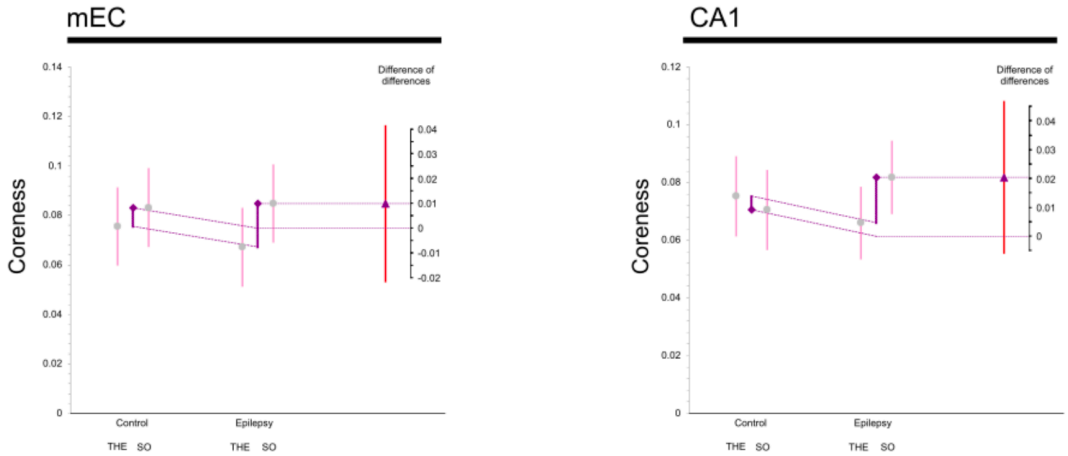

Figure 3.21. – **Coreness Values:** Average values and difference of differences graphs for data features taken from sharing networks, for both control and epileptic animals. Circles and triangles represent the mean, and all bars represent a 99% bootstrapped confidence interval. Significance is shown using the symbol (*) with their standard 1012 corresponding meaning (*, p<0.05; **, p<0.01; ***, p<0.001).

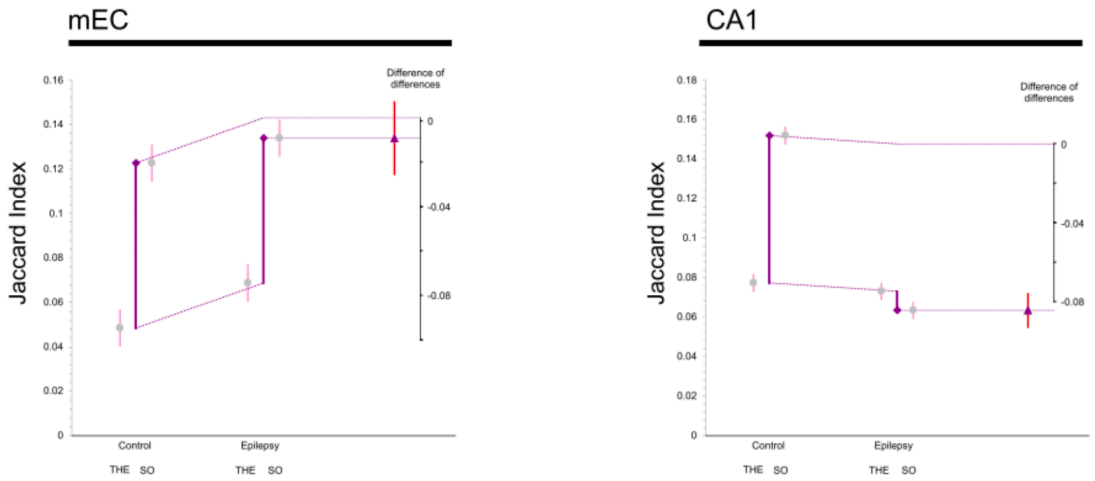

Figure 3.22. – **Jaccard Values:** Average values and difference of differences graphs as in Figure 3.21. Note the very large effect size in the decrease of the Jaccard index in CA1 during SO. Accordingly, the brain state specificity of connectivity variance is lost. Significance is shown using the symbol (*) with their standard corresponding meaning (*, p<0.05; **, p<0.01; ***, p<0.001).

3.6. Conclusion

We have here described the internal organization of assemblies of neurons dynamically exchanging information through time, using a temporal network framework and developing adequate tools for their analysis. In line with [46], we found a coexistence of organization, such as the existence of discrete network states, and freedom, such as the liquid continuous reorganization of network neighborhoods within each state. The rich information sharing dynamics we revealed in our anesthesia recordings in hippocampus and enthorinal cortex cannot be explained merely in terms of transitions between global brain states (here, alternations between "REM-sleep"-like THE epochs and SO epochs). On the contrary, we found that each of the global states gives access to wide repertoires of possible networks of information sharing between neurons. These network states repertoires are largely global state-specific and are robustly identified using both weighted and unweighted network characterizations.

We extracted here functional connectivity networks evaluating information sharing —i.e., time-lagged mutual information— between the firing of pairs of single units. This choice was motivated by the fact that mutual information is relatively simpler to evaluate than other more sophisticated and explicitly directed measures of information transfer [158], which require larger amounts of data to be properly estimated. Using a simpler measure was thus better compliant with our need to estimate connectivity within short windows, to give rise to a temporal network description. Although mutual information is a symmetric measure, the introduction of a time-lag makes our metric

"pseudo-directed" because information cannot causally propagate from the future to the past. Therefore, sharing of information between the past activity of a node i and the present activity of another node j could be indicative of a flow of information from i to j. When computing time-lagged mutual information between all directed pairs of single units in our recording, we found however only a very mild degree of asymmetry. As shown in Figure 3.23, most strong information sharing connections were very close to symmetric, indicative of time-lagged mutual information peaking near zero-lag for these connections. This finding corresponds to the early intuition that members of a cell assembly share information via their tightly synchronized firing [1, 84]. Figure 3.23 also shows that some of the more weakly connected pairs of neurons displayed a varying degree of directional asymmetry, with the strongest unbalance found for cells with a core connectivity style. However, the strengths of nodes with unbalanced pseudo-directed sharing were orders of magnitude smaller than for balanced nodes. Our choice to ignore asymmetries appears thus well justified, as well as the choice to use lagged mutual information rather than more complex directed metrics.

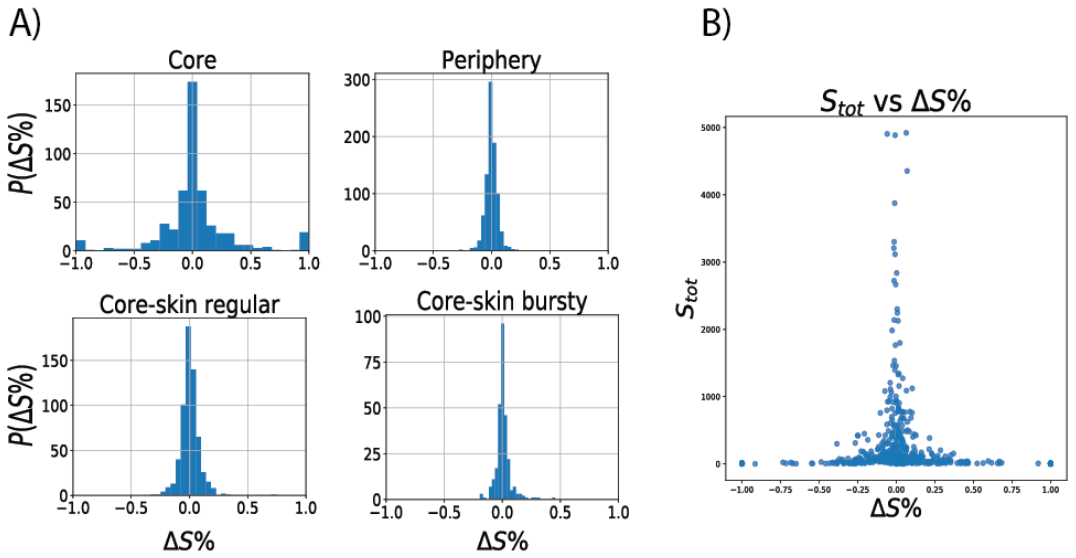

Figure 3.23. – **A)** Distribution of values of $\Delta S\%$ for the connectivity profiles of each connectivity style. All the distributions of are peaked around 0, with the extreme values (+1 and −1) reached only for *core* connectivity profiles. The corresponding population of perfect senders and receivers represents a small portion of the overall number of connectivity profiles. **B)** Scatterplot of the values of S_{tot} vs. $\Delta S\%$, the former representing the total aggregate strength of a neuron during a state: $S^{i,h}_{tot} = s^{i,h}_{in} + s^{i,h}_{out}$. The scatterplot shows that perfect sender/receiver neurons ($\Delta S\% = \pm 1$) correspond to very low values of S_{tot}, hence they correspond to very weakly connected neurons.

A striking architectural property of the measured information sharing networks was their core-periphery architecture. Such architecture was preserved at every timeframe (as shown in Figure 3.4.B), although the coreness of individual neurons changed smoothly through time even within states. This preservation of a global functional architecture despite the variation of the specific realizations and participant neurons is reminiscent of "functional homeostasis" observed in highly heterogeneous circuits that must nevertheless perform in a stable and efficient manner a crucial function [99, 115]. What is important is that, at any time, a functional separation between "streamers", "helpers" or "callers" exist, however which neurons specifically assume these roles and the exact location of these neurons within the anatomical circuit (cf. Figure 3.14.C) appear to be less important.

Core-periphery organizations have been found in many social, infrastructure, communication and information processing networks, with various types of coreness profiles, i.e., strong or gradual separations between the innermost core and the most peripheral nodes [56, 88, 102, 147]. The dynamics of this type of structures has however barely been tackled in temporal networks [68]. In neuroscience, such architecture has been identified in larger-scale networks of inter-regional functional connectivity, during both task and rest [10, 21, 28, 141], in line with the general idea that cognition requires the formation of integrated coalitions of regions, merging information streams first processed by segregated sub-systems [55, 166]. Here, we find that a similar architecture is prominent at the completely different scale of networks between single units within local micro-circuits in the hippocampal formation. The core-periphery architecture of information sharing thus reflects dynamic information integration and segregation. Cells belonging to the core form an integrated ensemble, within which strong flows of information are continually streamed and echoed. At the opposite end of the hierarchy of connectivity styles, peripheral neurons are segregated and perform transient "calls" toward "streamer" neurons in the core to get updated and share their specific information contents.

Following [39], a "syntax of information processing" would be enforced by the spatio-temporal organization of neuronal firing. Our dynamic core-periphery architecture is also ultimately determined by the coordinated firing patterns of many neurons. The fact that these coordinated firing patterns invariantly translate into networks with a core-periphery architecture can be seen as a proxy for the existence of a syntactic organization of information flows. In this self-organized syntax, peripheral neurons are in the ideal functional position to act as "readers" of the contents streamed by the integrated cell assembly formed by core neurons. Transitions between network states may act as the equivalent of bar lines, parsing the flow of information into "words" or longer sentence blocks, spelled with an irregular tempo. In the vision of [39], roles such as the one of reader or chunking into informational words would be a by-product of neuronal firing organization. We stress thus here once again that even in our case the real "stuff" out of which sharing functional networks are made are spiking patterns at the level of the assembly. The network representation provides however a natural and intuitive visualization of the dynamics of these patterns. Coordinated firing events —and not single neuron firing properties, cf. the poor correlations in Figure 3.19—

are mapped into network structures and changes of firing pattern into changes of connectivity style within the network. The logical syntax of assembly firing is thus translated into a dynamic topological architecture of sharing networks, which is easier to study and characterize.

In order to interpret the functional role of this emergent core-periphery organization, one should elucidate the information processing roles played by individual neurons within this network organization. An entire spectrum of possible roles may exist, mirroring the smooth separation subsisting between core and periphery. Communication between core and periphery can be helped by core-skin neurons, which sporadically connect to the core, transiently expanding its size. Speculatively, such breathing of the integrated core may be linked to fluctuating needs in terms of information processing bandwidth, analogous to dynamic memory allocation in artificial computing systems. The possible algorithmic role of neurons with different connectivity styles could be investigated using metrics from the partial information decomposition framework [175]. Beyond pseudo-directed sharing, it may be possible to identify: neurons acting as active memory buffers displaying large information storage [110]; neurons actively transfering information to others, associated to large transfer entropy [158]; or, yet, neurons combining received inputs into new original representations, associated to positive information modification values [111]. As previously said, we could at least quantify information storage. In particular, as shown in Figure 3.20, sub-groups of core-skin helpers and periphery callers existed with high storage values, approaching the ones of storage hubs within the core. Therefore, at least some of the core-skin or periphery cells transiently connected to the core may play the role of ancillary memory units, "flash drives" sporadically plugged-in when needed to write or read specific information snippets. Unfortunately, the number of coordinated firing events observed in our recordings was not sufficient for a reasonable estimation of transfer or modification, beyond storage. We can nevertheless hypothesize that core neurons are the work-horses of information modification, shaping novel informational constructs via their integrated firing.

We found that the bursty core-skin style —the "freelancer helper" role— was over-represented in SR of CA1 and Layer 2 of EC. SR receives inputs from hippocampus CA3 which are believed to be linked to retrieval of previously encoded associations [82, 157]. CA3, an associative memory module crucial for retrieval, receives inputs on its turn from layer 2 of EC. The over-representation of the bursty core-skin style in SR and layer 3 of EC may thus be compliant with our intuition of "helpers" as additional on-demand storage resources, plugged to the core when needed to read the specific contents buffered by their spiking. On the contrary, layer 3 of EC, which sends inputs to SLM of CA1, would rather mediate encoding than retrieval [59, 157]. Correspondingly, in layer 3 of EC the over-representation of freelancer helpers observed in layer 2 is replaced by an under-representation, consistently with the complementary functions that inputs from these EC layers are postulated to play.

We also found an excess of inhibitory interneurons among core style cells (Figure 3.14.C). Inteneurons tended to exhibit larger firing rates than excitatory cells, but we showed that coreness is not significantly affected by firing rate (Figure 3.19). Therefore,

this excess is rather to be linked to a key functional role of interneurons in mediating cell assembly formation. Their central position within the core of the information sharing network may allow them to efficiently control the recruitment of new neurons into the integrated core and orchestrate their coordinated firing, as already discussed in the literature [32, 149].

Remarkably, however, in a majority of cases, the connectivity style adopted by a neuron was only poorly affected by its anatomical localization or by its cell type. Apart from the few exceptions just discussed above, the distribution of the different styles through the different anatomical regions and layers was indeed close to chance levels. In particular, the fact of being localized within a specific layer of CA1 or EC did not affect in a significant way the probability of belonging to the core or to the periphery. Furthermore, a majority of neurons switched between different styles when network state changed (Figure 3.17), indicating that connectivity styles and, in particular, core membership are not hardwired. In contrast, it is often thought that the function that a neuron plays is affected by its individual firing and morphology properties, as well as by details of its synaptic connections within the circuit [33]. In this dominating view, functional hubness would thus be the garland reserved to a few elite cells, selected because of their extreme technical specialization, largely determined by their developmental lineage [51]. Here —further elaborating on [47]— we propose a more "democratic" view in which core membership and, more in general, connectivity style would be dynamically appointed, such that the total number of neurons that are elected into the core at least once is much larger than the currently active core members at specific times. The core composition can indeed be radically reorganized when the network state switch and can fluctuate between alternative majorities of hippocampal or enthorinal cortex neurons (Figure 3.5.B).

Such a democratic system implies a primacy of collective dynamics at the neuronal population level, flexibly shaping coordinated firing ensembles, on technical specialization and "blood" origins at the single neuron level. Switching network states may reflect transitions between alternative attractors of firing dynamics [7] implementing alternative firing correlations. Discrete state switching coexist however with more liquid fluctations of core attachment, which would rather suggest a complex but not random dynamics at the edge of instability [113, 119]. State transitions and flexible core-periphery reorganization are also poorly determined by global oscillations, despite the important role played by oscillations in information routing [38, 178]. Even if global oscillatory modes do not "freeze" information sharing patterns they nevertheless affect them, with different oscillatory states giving rise to alternative repertoires of possible information sharing networks (Figure 3.12.C). Computational modelling of spiking neural circuits may help in the future to reach a mechanistic understanding of how ongoing collective oscillations interact with discrete attractor switching, meta-stable transients and plasticity to give rise to liquid core-periphery architectures of information sharing.

We also partially extended out method to recordings in a specific pathological condition, epilepsy (in which intrinsic assembly dynamics is altered [133], see Chapter 2), where we showed that while the core-periphery organization persists even in epileptic

rats, w.r.t. control, the overall brain state specificity of the liquidity of connections is lost.

We have started here applying a temporal network language to describe the internal life of cell assemblies along their emergence, expansion and contraction and sudden transformations. We chose here to focus on an anesthesia condition in which intrinsic information processing is not suppressed but considerably "slowed-down" with respect to behavior, for methodological convenience (possibility to use long time windows for network estimation). In [47], colleagues performed related analyses of information dynamics in natural sleep as well, finding again discrete state switching not only in the hippocampal formation but also in the prefrontal cortex. It will be interesting to consider in the future comparisons with additional conditions, as well as more detailed investigations of relations between network state dynamics and oscillatory dynamics or, even, actual behavior.

To cope, however, with the much faster time-scales relevant for behavioral tasks, we should modify our network estimation approach to avoid the use of too short windows. Nevertheless, information sharing networks could be estimated first in a state-resolved manner, by pooling together firing events based on the similarity of the conditions in which they occur — e.g., transient phase relations and synchrony levels [139] or co-activation patterns [114, 127]— rather than strict temporal contiguity. State-specific network frames could then be reallocated to specific times, depending on which "state" the system is visiting at different times, reconstructing thus an effective temporal network with the same time-resolution as the original recordings (see e.g. [165] for an analogous approach used at the macro-scale of fMRI signals). In this way it would become possible to link temporal network reconfiguration events to actual behavior, probing hence their direct functional relevance.

4. Temporal networks in the brain: Dynamic large-scale multilayer networks in epileptic patients

In this chapter I describe the research carried out with my two supervisors and in collaboration with Dr. Agnès Trebuchon, from the neurology and epileptology department of the Timone Hospital in Marseille and Dr. Christian Bénar, as mentor for spectral analyses. This work is aimed at uncovering the relation between the dynamic re-configuration of the FC of epileptic human patients and the rising of aphasia (see Chapter 2) as a post-seizure symptom in some patients. While this work is still ongoing, and some aspects of this research are still under investigation, I present here our main findings, discussing what the future challenges and possible results of the continuation of this scientific effort in the last section.

Epilepsy is a neurological disorder in which brain activity becomes abnormally synchronous, first in localized regions then spreading to other zones. As an effect of propagating seizures, unusual behavior feeling and sometimes even loss of awareness can arise, with the order and nature of symptom appearance informing the neurologist about the possible pattern of propagation of the seizure. It is evident that epilepsy is a network pathology, both because the interest regions are distributed and interacting and because the mechanisms themselves of the pathology are associated to disrupted local and global coupling between neuronal populations. A fact whose impact on the quality of life is often underestimated is that epileptic patients may suffer of cognitive deficits even well beyond the seizures themselves, as if network function alterations were not limited to just the hypersynchronization events associated to the seizure but were present, in more limited or different form, also during "baseline" conditions [92]. While seizure-related changes may be more prominent, these changes in epochs preceding and following seizures may be transient, subtler and difficult to detect, thus requiring the development of suitable network analysis tools.

Here we analyze intracranial EEG (or stereotaxic EEG, sEEG) recordings in individual epileptic patients, hospitalized and implanted with electrodes in order to better localize the epileptic foci, in prevision of a potential surgery (only treatment available due to the pharmacoresistance of their specific epilepsy). It is important to stress that the considered recordings are actual clinical data and that no patient is identical to another. Therefore, analyses must necessarily be conducted in a personalized manner for individual patients, without assuming that different cases can be grouped. Despite differences between patients (and even, sometimes, between different seizures for a given patient) our analyses turn out to be able to identify some general traits of the

network dynamics associated to entering and leaving an epileptic seizure phase and gradually recovering a baseline-like level.

Specifically, we will adopt a time-resolved multiplex network approach, in which different network layers correspond to networks of inter-channel coherence in different frequency bands. Since epilepsy is linked to hypersynchronization, it is natural to adopt a measure of Functional Connectivity tracking oscillatory synchronization. Synchrony alterations, however, are observed over multiple different coordinated frequency bands, including high-frequency bands where power is overall lower (which requires a multiplex network description) and are transiently manifesting (which requires a temporal network description). Our methods of analysis thus will describe both temporal and multiplex aspects of the measured dynamic Functional Connectivity revealed by recorded signals. We will identify, within each network layer, and via an unsupervised approach, a variety of distinct functional connectivity states, which not only happen to relate to a rough staging of the seizure event (pre, during and post seizure), but, furthermore, predict epochs of time during the post-crisis recovery in which language disturbances such as aphasia are reported by the clinician assisting the patients. Beyond single-layer analyses, we will show that epilepsy affects the coupling between layers, loosening it in some cases but strengthening it in others. This is an interesting observation in relation to the emergence of language disturbances as language parsing requires the tight coupling between neural dynamics events paced by different frequencies (associated to different language time-scales such as the ones separating phonemes, syllables, words, sentences [75, 125], see Chapter 2).

An important novel aspect of our approach is that we will characterize dynamic network states not only in terms of their state-specific connectivity patterns (such as e.g. a distinct modular partition for each state) but also in terms of their "style" of reconfiguration of connectivity. Indeed, functionally connectivity is never frozen, but keeps constantly reorganizing even within each of the states. Fluctuations around the state-specific multiplex connectivity patterns can be more or less structured, and occur through larger or smaller network variation events. We characterize the properties of within-state network dynamics: i) inspecting whether fast connectivity fluctuations maintain or disrupt the *module allegiance* pattern of different network nodes; and ii) quantifying the instantaneous rate of variation of functional networks, via a suitably defined measure of *speed*. So, dynamic connectivity states may differ between them for genuinely dynamic traits: dynamics could be fast in certain states and slower in others, or be random-like in some states and preserving the association of certain region pairs despite module reconfiguration in others. Such capacity to directly describe dynamics will crucially allow us to identify baseline as a condition in which networks fluctuate swiftly and in a spatiotemporally ordered manner, while pathology is associated to a loss of this flexibility and organization, even if network fluctuations are never suppressed.

4.1. Data and Approach

Data

The data under observation are stereo-electroencephalography (SEEG, Figure 4.1.a,b) recordings from patients affected by pharmaco-resistant epilepsy, who suffered from aphasia as a post-seizure symptom. In particular, we analyse here four recordings from three patients. The choice of the locations of the multiple contact electrodes (10 to 15 contacts per electrode, $2mm$ of length and $0.8mm$ of diameter each) is based on previous clinical investigation and aimed at identifying the brain areas involved in the origin and spreading of seizures. Each recording is manually annotated by the physicians and include, notably, markers at specific time-stamps that indicate the visually-identified onset and offset of the seizure. Furthermore, the language capabilities of patients after a seizure are assessed by periodic testing, in order to identify moments in which a patient undergoes language impairments. The testing enables to detect aphasia events of either one of two main forms that may be observed before the full recovery of a patient, namely comprehension and production impairments (Figure 4.1.c). Comprehension troubles are detected when a patient is not responsive to any question asked by the tester: the physician could for example ask the patient to point at the picture of a lemon, randomly placed among other pictures of objects (Figure 4.1.c, left), and the non-responsiveness of the patient to any verbal communication would indicate an undergoing impairment of language comprehension. Language production impairments are instead detected, for instance, when the testing physician points at the picture of an object and asks the patient to name the object: failure to name the object is thus taken as indication of impaired language production (Figure 4.1.c, right). In our analysis, as a first step, we do not distinguish between the two types of aphasia, combining their respective markers as an indication of on-going language impairment in general.

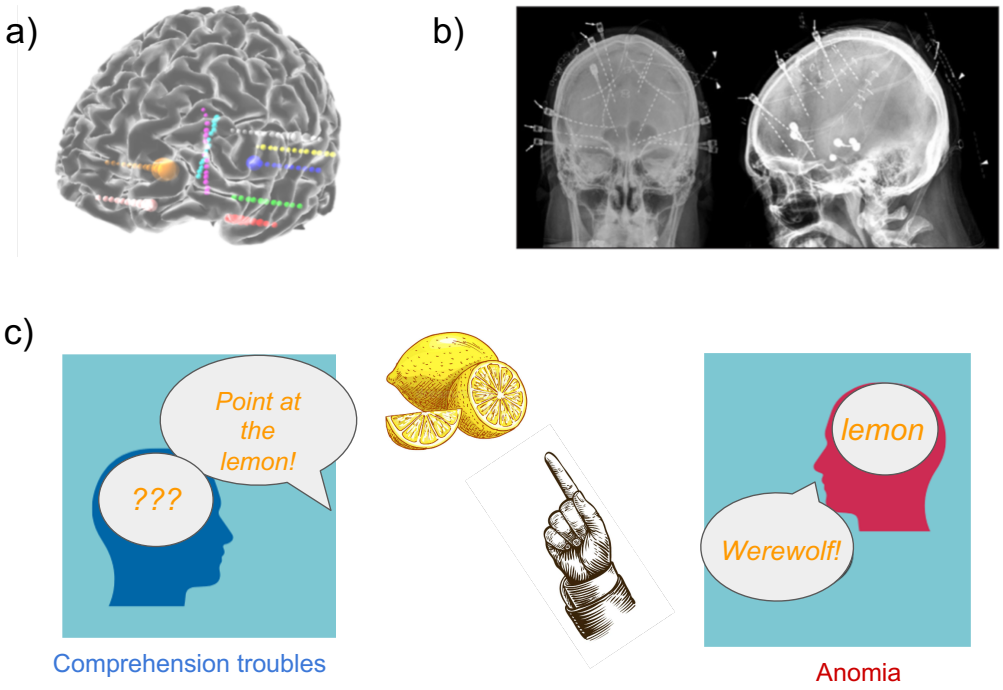

Figure 4.1. – **a)-b)** 3D reconstruction and imaging of intracranial electrodes in a patient. **c** example of testing of the language comprehension (left) and production (right) impairments.

Wavelet coherence and temporal multiplex

As previously mentioned, we are interested in studying the time-varying functional connectivity of these networks in different frequencies, as different frequency bands are thought to be responsible for different language processing operations [125]. For this reason, between each pair of signals recorded we compute the wavelet coherence in 5 different frequency bands. To do so, we decompose signals in the time-frequency domain along the Morlet wavelet family. The Morlet wavelet is defined for frequency f and time τ as:

$$\Psi_{\tau,f}(u) = \sqrt{f} e^{i2(u-\tau)} exp\left(-\frac{(u-\tau)^2}{\sigma^2}\right), \tag{4.1}$$

so that $\Psi_{\tau,f}(u)$ is the product of a sinusoidal wave at frequency f with a Gaussian function centered at time τ, with a standard deviation σ proportional to $1/f$. The wavelet transform of a signal $x(u)$ is a function of time τ and frequency f given by the convolution with the Morlet wavelet:

$$W_x(\tau, f) = \int_{-\infty}^{+\infty} x(u) \cdot \Psi^*_{\tau,f}(u) du. \tag{4.2}$$

From the wavelet transform of two signals x and y, we can define the wavelet cross-spectrum between x and y around time t and frequency f:

$$SW_{xy}(t,f) = \int_{t-\delta/2}^{t+\delta/2} W_x(\tau,f) \cdot W_y^*(\tau,f) d\tau \tag{4.3}$$

where δ is a scalar that depends on the frequency. The wavelet coherence $W.C.(t,f)$ is defined at time t and frequency f by:

$$W.C.(t,f) = \frac{|SW_{xy}(t,f)|}{[SW_{xx}(t,f) \cdot SW_{yy}(t,f)]^{1/2}} \tag{4.4}$$

where $W.C.(t,f)$ has values between 0 and 1. We compute the wavelet coherence $W.C(t,f)$ for each pair of signals in 5 frequency bands peaked around 1Hz, 5Hz, 10Hz, 20Hz and 40Hz, where the width of the time integration $\delta = 6/f$, and thus the width of each of the frequency bands equals 1/6 of the peak frequency. The coherence values computed for each of the 5 frequencies represent, for each pair of signals, 5 time series of temporal edges between the same nodes i and j representing the sources of the signals. We therefore represent these data as a time-varying multi-layer weighted network, where the weight of a temporal edge $(i,j,t)^l$ at time t, in layer l corresponds to the coherence in frequency l of nodes i and j at time t. Since the nodes in all layers are the same, we refer to this object as a *temporal multiplex network* (Chapter 1). We define a significance threshold for the coherence values by computing the coherence for pairs of randomly generated oscillating signals (500 iterations), and thus consider as significant values measured on empirical data only those that lie above the 95% confidence interval of the distribution of coherence of the random data. The sampling frequency of the recording is 1024Hz, and we down-sample the time series of the coherence between each pair of signals by a factor 12, with a resulting time resolution of the temporal-multiplex of $\tau = \frac{12}{1024}$s. A schematic representation of the extraction of the temporal multiplex from the raw data can be found in Figure 4.2. We note that there are two different approaches to analyse this kind of recordings:

— the monopolar montage: each signal measured by a contact in the electrode is considered and thus the coherence $W.C.(t,f)$ is computed between the time-series recorded by each contact. The size of the resulting network therefore corresponds to the total number of electrode contacts.

— the bipolar montage, in which one considers the difference between the signals recorded in contiguous contacts. So if x, y and z are the signals recorded by three contacts on the same electrode, the time series s_1 and s_2 used to compute the wavelet coherence would be $s_1 = x - y$ and $s_2 = y - z$. The size of the resulting network is therefore smaller than in the monopolar montage.

We note that qualitatively similar trends of what we will show in the next sections are observed when constructing networks in terms of time-series from monopolar and bipolar montages. We chose here however to focus on analyses in terms of a simpler monopolar montage, because the larger number of nodes, despite the larger noiseness and volume conduction, allows better emphasizing network structure in

the high frequency layers. Figures related to the analysis of the bipolar montage can be found in the appendix A.

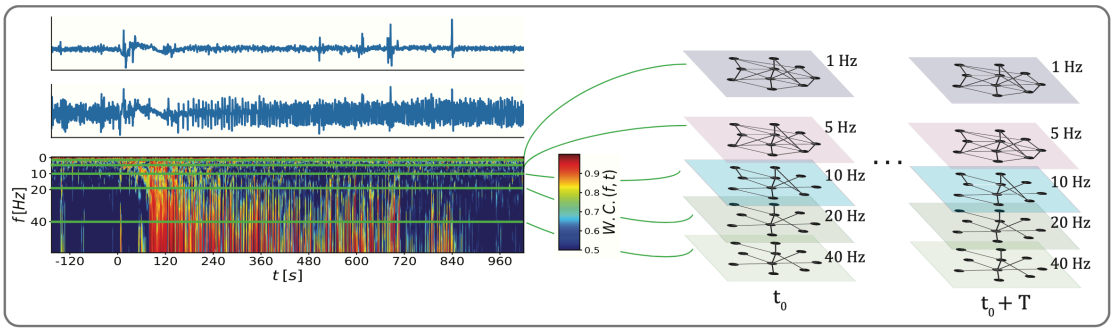

Figure 4.2. – **Analysis building blocks: a)** Schematic representation of a recording as a dynamic multiplex network; from each pair of signals A and B (blue curves on the top left) we compute the *Morlet wavelet coherence* at each time-stamp for a span of frequencies ranging from 1 to 80 Hz; we consider the 5 frequencies of interest, $1, 5, 10, 20$ and 40 Hz as the dynamics edges of the respective 5 layers (on the right) for the corresponding pair of regions. We therefore end up with an instantaneous network for each time-stamp in each of the 5 layers.

4.2. Layer-wise global network properties

We start our analysis by computing two global network measures on each layer as fast general indicators of connectivity fluctuations. Such measures are the instantaneous total network strength, namely the sum of edges' weights at each time point, and the layer's modularity, i.e., a quality function $Q(t) \in [0,1]$ which reflects the tendency of the network's layer to be organised into different modules (communities; in the literature $Q \geq 0.2$ for significant network partition into different modules/communities [64, 132]). See Chapter 1 for formal definitions of these quantities.

The five plots in Figures 4.3 and 4.4, each corresponding to a different frequency layer, are the time series of the layer-wise instantaneous total strength $s(t)$ (sum of all instant link weights) of the network (blue), and the instantaneous modularity $Q(t)$ (orange). We show here for the sake of conciseness analyses a representative seizure of one specific patient. However, unless otherwise specified, similar results are found for other seizures and patients as well (see A for the detailed analysis of other recordings). In Figure 4.3.(top left), corresponding to the 1Hz layer, the strength s is persistently close to $N = 117$ (the size of the network), meaning that, in average, each node is connected to almost the entirety of the rest of the network with high values of coherence. This layer of the network is therefore particularly dense, associated to global slow oscillations of the entire system, which causes the values of $Q(t)$ to be extremely low. This suggests that the 1Hz layer has no modules to be retrieved at any given time.

When increasing the frequency, a richer network dynamics start surfacing, also due to lower connection densities. The values of total strength in the 5Hz (Figure 4.3, top right) layer are lower than those of the 1Hz layer. The layer undergoes a sharp increase in total strength at seizure onset, which then rapidly decreases to baseline values, even before any of the reported clinical marker. The modularity values of the same layer are below $Q \sim 0.2$ for the entirety of the recording, yet a substantial drop of Q is observed in correspondence to seizure onset, thus coinciding with the increase in strength. The two time series of total strengths and modularity are anti-correlated for the other layers as well, as the emergence of additional transient links contribute to reduce the segregation between modules: for the 10Hz layer (Figure 4.3, bottom left) the trend of the two curves is very similar to the one of the 5Hz layer, with lower values of $s(t)$ and higher values of $Q(t)$; however, this layer resumes baseline strength and modularity values slightly later then the 5Hz one.

This tendency to have longer times for return to baseline values with increasing frequency is confirmed by the other higher frequency layers. For the 20Hz layer (Figure 4.3, bottom right) the return to baseline values is markedly slower, particularly for modularity, and even happens after the last clinical marker. The return to baseline values for the 40Hz layer, in Figure 4.4, is dramatically slower. For this layer, the perturbation induced by the seizure lasts the longest, as, in the considered example, baseline levels of network activity are resumed only in the last three minutes, well beyond the reported end of the seizure.

4.3. Allegiance states

As mentioned in the previous section, we carry on our layer-wise analysis by setting a time-window of length $L_w = 200$ time points ($L_w = 2.343$ seconds) and computing within this window the allegiance between each pair of regions. The result is a different *allegiance matrix* $A(w)$ for each time-window (see Chapter 1 for definition) whose matrix element $A_{ij}(w)$ corresponds to the probability of observing regions i and j in the same module (community) over the duration of the time window w (see Figure 4.5). We then slide the time window by a lag $\tau = 100$ pts. ($\tau = 1.171$ seconds), and compute the allegiance in the next window. Consecutive windows have therefore a 50% overlap. The result, for each layer, is a temporally-ordered series of allegiance matrices, each corresponding to the relative time window. Such construction allows us to study network dynamics on two different time-scales: the faster one of fluctuations within each time-window and the slower one of variations between windows of the within-window dynamics.

Allegiance analysis within each window captures the more or less marked tendency for different nodes to *move* in time across the different modules in a coordinated or independent manner. At each time-frame within the window a different network is estimated and could have different modular partitions. The fast network reconfiguration dynamics may affect modular structure differently. It may be that because of network reconfiguration, previous-time modules are dissolved and regenerated near-randomly

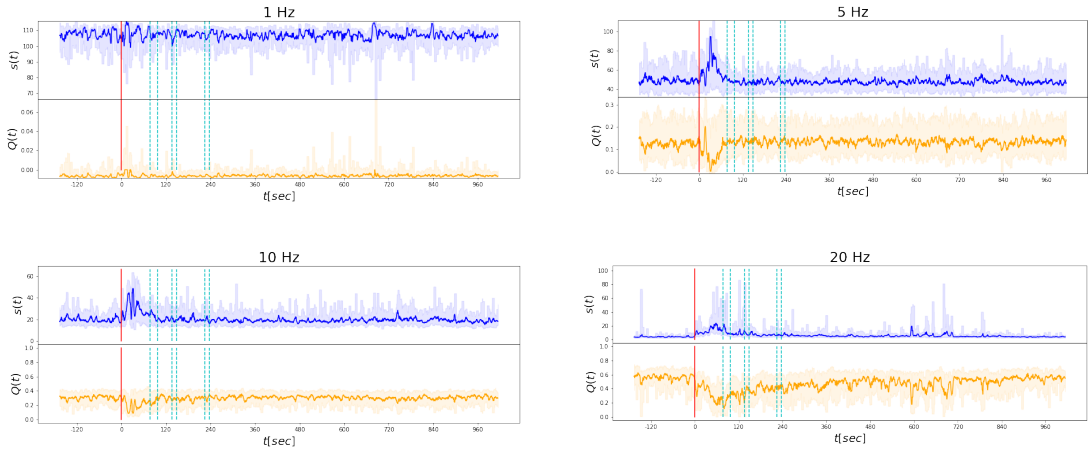

Figure 4.3. – **Strength and Modularity time series**: the blue curve in each of the plots corresponds to a windowed average of the instantaneous total strength computed for the corresponding layer, whereas the light blue shaded area represents the area between the 5th and 95th percentiles of the distribution of values of $\langle s(t) \rangle$ in the corresponding window. The orange line in each of the plots is the windowed average of the instantaneous modularity $Q(t)$ of the corresponding frequency layer, whereas the light orange shaded area corresponds to the portion of the distribution of values $Q(t)$ in the relative window included between the 5th and the 95th percentiles. The vertical lines in the plots represent the clinical markers: the seizure onset in red, and the language dysfunction markers are represented by the cyan dotted lines.

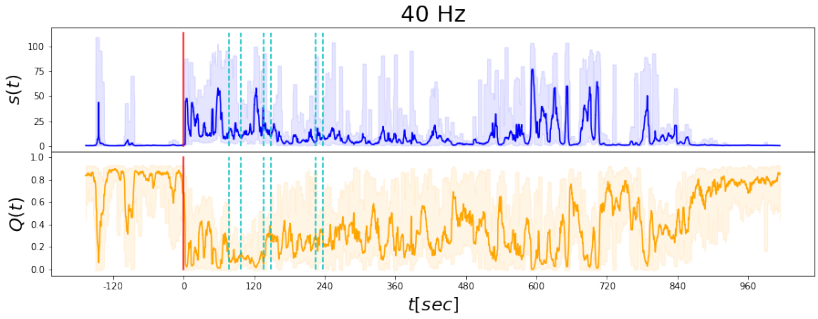

Figure 4.4. – **Strength and Modularity time series**: same as in 4.3, for the 40Hz layer.

without specific memory. In that case, the probability for any pair of network nodes to be systematically assigned to a same transient module (independently from which one this module is) would be low and at chance level, resulting in unstructured within-window allegiance matrices with small entries. However, the module reconfiguration could also occur in a more organized manner. Notably, regions may still be floating across modules but do it in coordinated groups, rather than independently one by

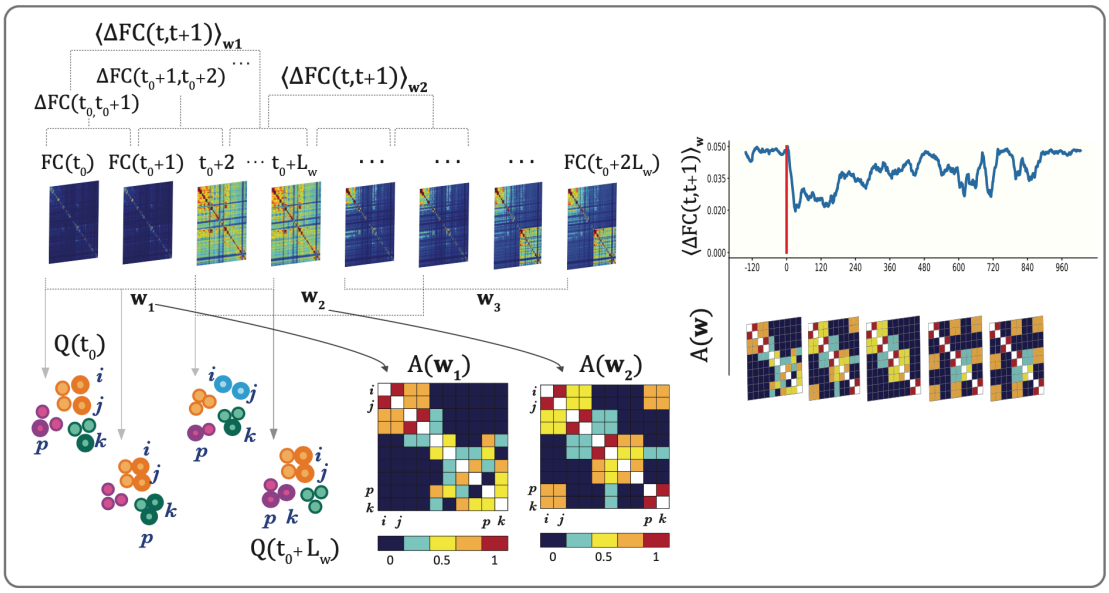

Figure 4.5. – **Analysis building blocks:** For each layer (frequency) we therefore have a series of instantaneous snapshots of the network, i.e., a stream of FC matrices (middle); from each pair of consecutive instantaneous FCs we compute the rate of change, cosine distance, $\Delta FC(t, t+1)$ from one to the other, which we then average over L_w (schematic representation on the top). At each time point we partition the network into its modules, while computing its modularity $Q(t)$ (bottom-left cartoon). Within each window w we compute the corresponding allegiance matrix $A(w)$, whose entries are 1 if the corresponding regions are assigned to the same modules throughout the whole window, as regions i and j in the cartoon, or 0 if they are never in the same module (nodes i and k in the cartoon). For each layer we therfore end up with a time series of $\langle \Delta FC(t, t+1) \rangle_w$ and a stream of allegiance matrices $A(w)$ (right).

one, so that entries with larger values can appear in the allegiance matrix. The average value of within-window module allegiance thus tell us whether module reconfiguration is more or less random and the block structure of the allegiance matrix tells us which are the nodes that tend to co-move across modules while module change and morph, as in a form of "liquid crystal" (to be opposed to the more "gas-like" random reconfigurations of low-allegiance time windows).

The style itself of module reconfiguration could change in time and become more or less "gaseous" vs "liquid". To detect these changes in dynamics style, one need to compare directly the dynamics. This can be done by computing the cosine similarity (see Chapter 3 for formal definition) between allegiance matrices computed within different time windows. These cosine similarities can then be compiled into a matrix, describing similarity between allegiance matrices observed at any possible pair of times, which we call the *dynamic allegiance matrix, dAM*. This construction is analogous to the so-called dFC matrix introduced to compare fMRI-based transient resting-state networks in [25, 112] or to the recurrence matrix probing the evolution

of sharing network topology in time, introduced by [46, 143] and already presented in chapter 3 of this thesis. However, we do not compare here connectivity but connectivity flows, whose internal spatio-temporal organization is epitomized by the time-resolved allegiance matrices. So, fast variations of network connectivity within each window are captured by time-resolved allegiance analysis and slower variations of network dynamics across windows are captured by the allegiance dynamics matrix.

The layer-wise Dynamic Allegiance Matrix, dAm^l, shown in Figure 4.6 for the 40Hz frequency band, is obtained by computing the cosine similarity (Chapter 3) between the upper triangular part (linearized into an $N*N-1/2$ vector $V^l(t)$) each allegiance matrix computed in the window $t^* \in [L_w, L_w+\tau, \ldots, T/\tau]$ (where τ is the 100 time points lag by which we slide the time window) and all of the other allegiance matrices,i.e. :

$$dAm^l(t,t^*) = \frac{\sum_{a=1}^{N*(N-1)/2} V^l(a,t)V^l(a,t^*)}{\sqrt{\sum_{a=1}^{N*(N-1)/2} V^l(a,t)^2}\sqrt{\sum_{b=1}^{N*(N-1)/2} V^l(b,t^*)^2}} \tag{4.5}$$

The matrix element $dAM^l(t,t*)$ therefore ranges from 0, when the two allegiance matrices in windows t and t^* are completely different, to 1, when the two are exactly identical. An example of dAM is shown in Figure 4.6, where we plot the dynamic allegiance matrix for the 40Hz layer (same recording as in Figure **??**). The block-wise structure of a layer's dAM suggests the existence of epochs, or states, in which the allegiance matrices computed in the corresponding time windows are similar: these are states in which the allegiance dynamics of regions is in a stable and persistent regime, that we refer to as *allegiance states*. We cluster the layer-wise tensor of allegiance matrices $\mathscr{A}_{ijt}$, whose element for $t = t^*$ corresponds to the allegiance matrix computed in the t^*th window, by means of a spectral clustering, using the dAm as precomputed distance matrix among the different windows along the time dimension.

In each recording we find 4 states that we now describe for one specific recording (same recording as in Figures 4.3, 4.4, 4.6). In Figures 4.7 and 4.8, in fact, we display the four allegiance states (clusters of time-windows in dAM) retrieved for the 40Hz band of a representative patient. Similar figures for the beta and alpha band and for another subject can be seen in A. The colormap in the top left matrix in Figure 4.7.a corresponds to the average Functional Connectivity matrix obtained by, first, computing the FC in the same time-windows defined to compute the allegiance matrices, and then by taking the average only on the windows that were assigned to a specific allegiance state, in this case, the *baseline* state. The matrix in the plot is characterized by overall low values for non-diagonal elements, whereas we see small clusters (blocks) of regions that are tightly interconnected lying on the diagonal. This suggests that within the baseline state, there are many subgroups of regions, of small size and involving neighbour regions, that are persistently tightly interconnected, hence the high values of modularity displayed before seizure onset and at the end of the recording in Figure 4.4. The top right colormap in Figure 4.7.a is the allegiance matrix averaged on all the time-windows labeled as *baseline*. The lattice-like structure of this matrix suggests the existence of several groups of nodes with high values of

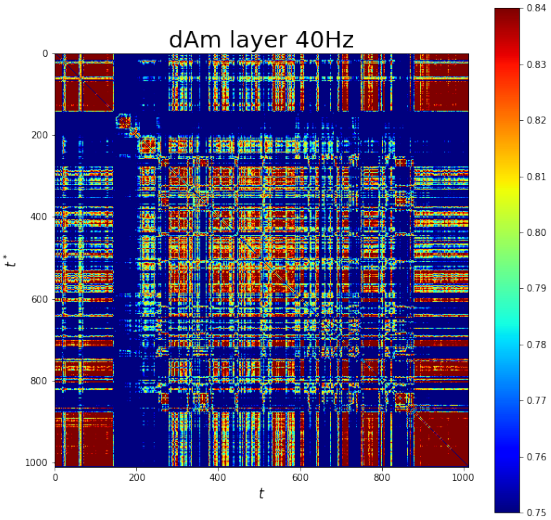

Figure 4.6. – **Dynamic Allegiance Matrix** of the 40Hz layer: the matrix element $dAM(t,t^*)$ is the cosine-similarity between the allegiance matrix computed in window t and that obtained in window t^*.

allegiance. Such groups are not exclusively composed of neighbouring regions as the out-of-diagonal blocks of high values of allegiance suggest. It is also evident from this plot how some groups of neighbor regions only share high values of allegiance within them, and their allegiance with the other regions is very low. For this patient, thus, the baseline state is associated to a structured allegiance matrix, indicating that the modular structure is not reconfigured in a random manner during the within-window fast network dynamics of baseline state windows. But... is this modular structure changing at all?

Indeed, high allegiance values may just indicate that modular structure is constant throughout the window. To discriminate between the cases of a "crystallized" modular partition, where nodes do not change at all their module membership and the one of a “liquid” reconfiguration where nodes do change module membership but do it in a non-completely random manner, dAM analysis is not enough and one must also evaluate whether the network is really changing on the fast time-scale within each window. This is done evaluating the rate of instantaneous change of networks within the windows. For each of the allegiance states, we thus also plot the distribution of the rate of change (cosine distance, i.e., 1−cosine similarity) of the instantaneous FC. At every time-stamp within the considered window, the instantaneous weighted FC is provided by the computation of the wavelet coherence between each pair of regions at the given time-stamp. Then, we compute the quantity $\Delta FC(t-1,t)$ which quantifies the variation of instantaneous FC from one time stamp to the next. We

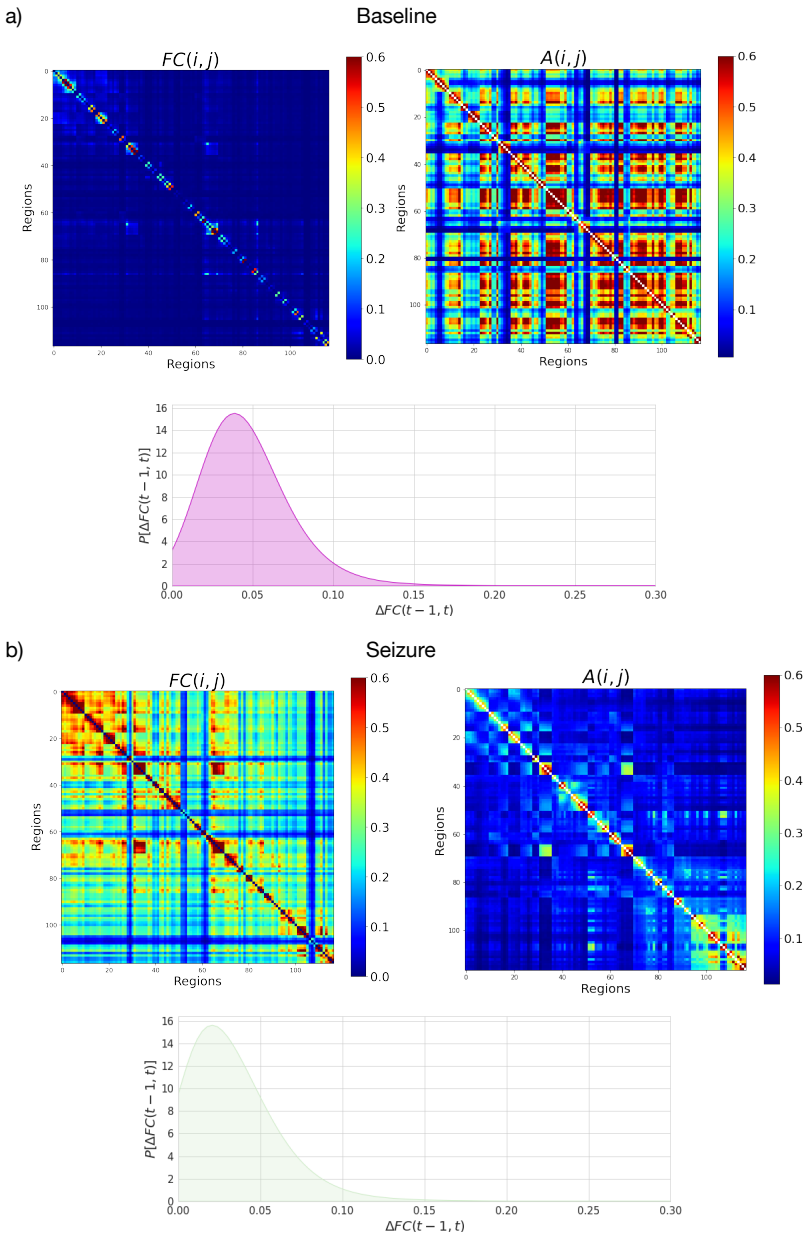

Figure 4.7. – **Allegiance States 40 Hz**: **a)** the top left colormap represents the state-wise average Functional Connectivity (FC) of the 40Hz layer, whose matrix element (i, j) corresponds to the average coherence between regions i and j during the time stamps labeled as state 1; the top right colormap is the allegiance matrix averaged over the time stamps assigned to state 1; the density plot on the bottom represents the distribution of instantaneous rate of change (cosine distance) of the FC, $\Delta FC(t-1,t)$ of the time points (1 time point = $\frac{12}{1024}$Hz) included in the time windows assigned to state 1. **b**) the same plots for state 2.

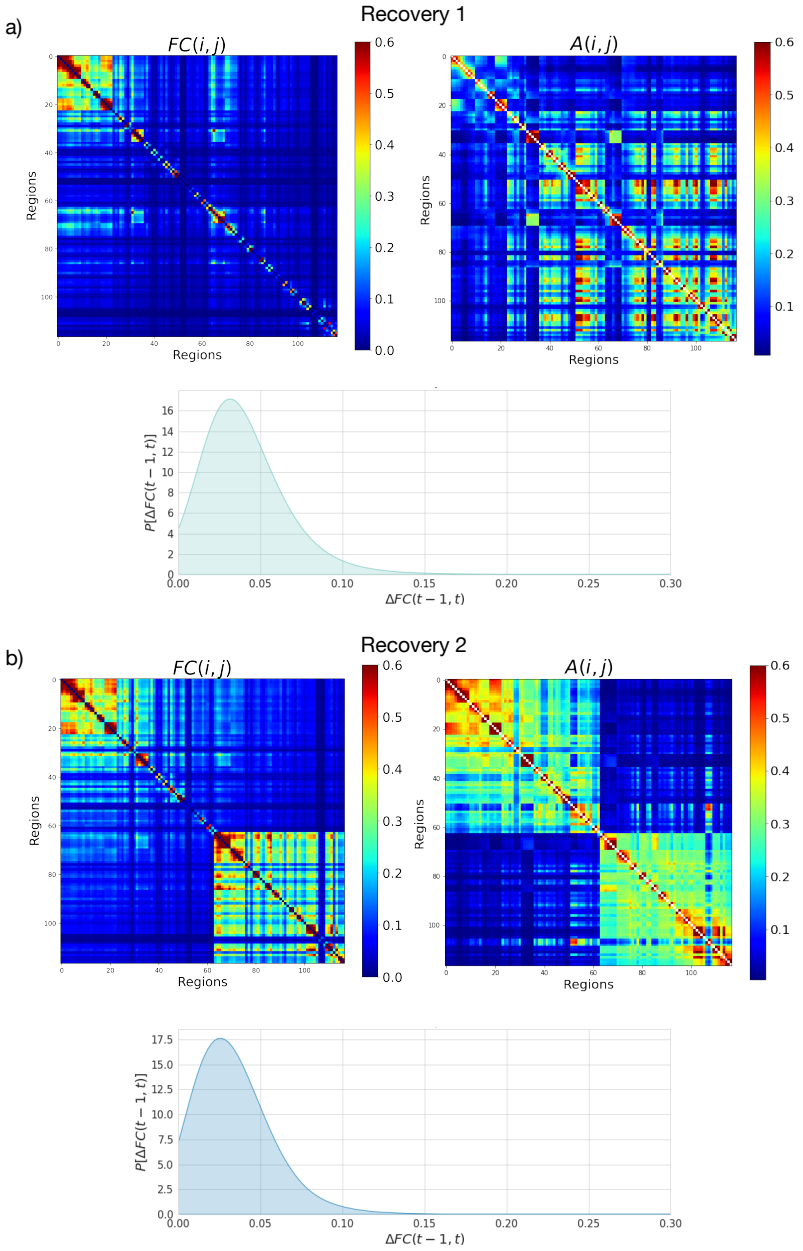

Figure 4.8. – **Allegiance States 40 Hz**: **a)**-**b)** the same plots as in Figure 4.7 for states 3 and 4, respectively.

compute this variation for all the contiguous time-points included in the considered window and we average it. In this way one can estimate the average rate of change —or speed— with the same time-resolution of the series of allegiance matrices out of which the dAM is computed (Figure 4.5). Overall, from Figure 4.7.a we conclude that the baseline allegiance state is not internally frozen, as windows within this state are associated to a distribution of speeds well above zero. On the contrary, as we will see, the baseline state is even the one with higher speed of internal reconfiguration.

This means that links do change in time but do it without leading to a fully random reconfiguration of modules, as the allegiance matrix is structured. For other patients, speed of baseline state is always high, however allegiance can be less structured (Figures in A). So baseline state is always very dynamic and can oscillate between more “gaseous” or “liquid crystal” styles of network reconfiguration.

This contrast between a connectivity matrix with weak entries and an allegiance matrix with strong entries is characteristically reverted for the *seizure* state in Figure 4.7.b. In fact, the state-wise average FC (top-left colormap) is overall characterised by higher values out-of-diagonal as well, indicative or a more global and network-widespread synchronization. Looking at the allegiance matrix, although persistently interconnected regions are still evidently present, especially in the top left corner of the matrix, there are fewer of these persistently connected pairs. Baseline state for the considered subject is associated to a marked distinction between regions that tend to be grouped together (red blocks in allegiance matrix) and regions that tend to be grouped apart (blue stripes), associated to a reconfiguration of within module connectivity. In the seizure state, instead, module identity is not as sharply maintained as in baseline, despite speed is substantially reduced. Thus a fast module-respecting dynamics is replaced by a slower module-mixing reconfiguration flow.

The average FC of the third state (top left matrix) in Figure 4.8.a has a block of persistently connected regions in the top-left corner, that are also connected to two smaller blocks that are visible along the diagonal. The average allegiance matrix in the top right block of Figure 4.8.a is characterised by few groups of nodes with high allegiance in its top left part: the matrix elements with higher values in this portion of the matrix correspond to the regions that are most connected in the FC matrix. We note the resemblance of this part of the allegiance matrix to that of the *seizure* state. The rest of the allegiance matrix in Figure 4.8.a appears to be more “crystallized”, in analogy with the corresponding part of the same matrix in Figure 4.7.a. We can therefore interpret this state as a transitional state, in terms of allegiance and connectivity, between the seizure and the baseline states. This is confirmed also in the density plot of the $\Delta FC(t-1,t)$ on the bottom, where the peak of the distribution lies between the two peaks of the same plots in the baseline and seizure states.

Both the FC and the allegiance matrices for the fourth state are different from the previous ones. In the top left plot of Figure 4.8.b, in the FC matrix, we note a separation into two subgraphs (a smaller block in the top left corner of the FC matrix, and a larger block in the bottom right corner) of the 40Hz layer of the network. The same tendency is underlined also in the allegiance matrix (top right plot), where the two separate diagonal blocks of the matrix correspond to two independent subsets of regions: two regions in the same sub-network have coordinated flow across the modules in the network (high allegiance), whereas two regions from different sub-networks have low allegiance, and thus move independently across the different modules. In other words, this state seems to be characterised by the emergence of two independent "crystal-like" allegiance dynamics of two large groups of regions.

Interestingly the two subnetworks are restricted respectively to temporal regions (top left block in the allegiance matrix) and parietal regions (bottom right block). In

the density plot of $\Delta FC(t-1,t)$ on the bottom we see how the peak of the distribution of values of $\Delta FC(t-1,t)$ is lower than that of the previous state shown in Figure 4.8.a, which suggests how these state could represent a transient slowing down of the overall connectivity dynamics, where the allegiance is momentarily restricted in a configuration which substantially differs both from the baseline and the seizure sates. This raises the question on whether this state, which cannot be seen as a transitional state from seizure back to baseline, could indeed be involved in the appearance of language impairments. It is worth indeed reminding that the language system involves interactions between regions belonging to both these subnetworks, forming two separate "crystals" in this fourth allegiance state. We can thus plausibly expect that the lack of dynamic coordination between these subnetworks may result in dysfunctions of the language system, notably different forms of aphasia.

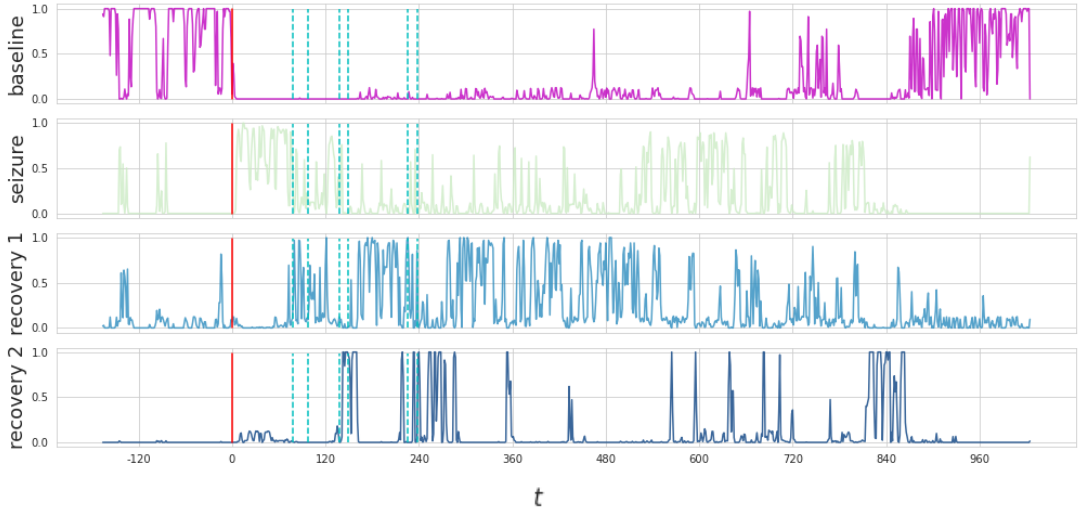

Figure 4.9. – **States of dynamics**: the four curves represent the probability $P(t) \in [0,1]$ of each time window t to belong to the baseline (magenta, top), seizure (light green, second plot), recovery-1 (light blue, $3rd$ plot) or recovery-2 (dark blue, bottom) states.

4.4. Relations between pathological manifestations and allegiance state dynamics

Verifying the validity of the latter hypothesis requires studying the time-courses of recruitment of the different allegiance states, in relation to the manifestation of language disruptions. In the previous section, we presented representative allegiance matrices for each of the identified allegiance states (in a representative patient, for the 40 Hz band). However, the exact allegiance matrices are changing time-window by

time-window and may be closer to or farther away from the typical allegiance structure. Given this internal variability of allegiance structure within each of the allegiance state, it may be useful to develop a soft classification approach, in which we evaluate, for every time-window the confidence with which we can attribute it to either one of the reference allegiance states. To do so, it is natural to generalize a procedure we previously used in chapter 3 to classify along time the changes of style of temporal connectivity of individual neurons. We then computed, through a classification procedure, the probability that the modular reconfiguration flow observed within each time-window correspond to the one of a considered allegiance state. The result are time-series of the confidence with which each given time-window could be assigned to either one of the allegiance states. Usually this probability peaks at every given time for one of the states, most often the one to which the considered time-window has been assigned by crisp clustering. However, we now have soft membership time-series whose evolution that can be more naturally correlated to external time-stamps (e.g. via a lagged-correlation analysis, see later).

In order to compute the state-wise probabilities presented in Figure 4.9 we run a K-nearest-neighbour classifier with the labels obtained by the spectral clustering as training data and the time series of allegiance matrices as target values. We therefore extract a four dimensional state-assignment probability vector for each allegiance matrix (time window): each of the four curves plotted in Figure 4.9 therefore corresponds to one of the four dimensions of all the time-windows. In Figure 4.9 we plot the time series of state-wise probabilities: for instance, the magenta curve on the top corresponds to the probability of each window, and corresponding allegiance matrix, to be labeled as *baseline*. We note how the curve is initially close to 1, except for two sudden low drops, and then drops to 0 in proximity of the seizure onset marker, to resume high values only in the last 240 seconds of the recording. On the contrary, the seizure state's probability curve (in green) starts off with null values, has two sudden peaks corresponding to the drops in the baseline's curve, and reaches its maximum in the period between seizure onset and the first appearance of aphasia. The rest of the curve undergoes sharp transitions from 0 or low values to higher values, and eventually goes persistently to zero when the baseline curve returns persistently high values, i.e, when the 40Hz layer of the network returns to its initial regime. The third curve reaches values close to one only starting in the vicinity of the first marker of language dysfunctions. The curve then undergoes frequent and sharp transitions from values close to 1 to values close to 0 until 540 seconds from seizure onset, the values of the curve at its peaks then start decreasing until it lays persistently at values close to 0. The fourth state is the rarest, as the peaks of the dark blue curve at the bottom of Figure 4.9 are unfrequent, yet they occur in the very proximity of the last three clinical markers, as well as in other later moments up to 860 seconds from seizure onset, when the curve drops to zero. This is a first hint suggesting that our hypothesis of a relation between the manifestation of the fourth state of allegiance and the emergence of language dysfunctions is true.

We further probe this hypothesis in Figure 4.10, where we plot the lagged cross correlation between the peaks of the probability curves of each state and the time-series

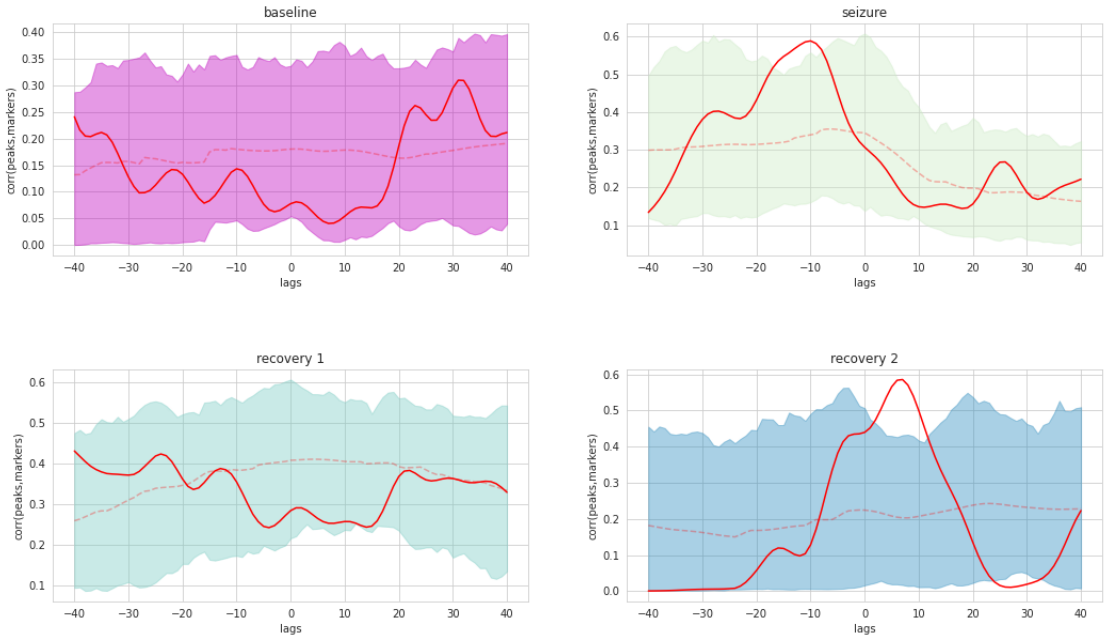

Figure 4.10. – **States of dynamics**: each of the four plots represents the lagged cross-correlation between the peaks of the curves in Figure 4.9 of each state (baseline, seizure, recovery-1 and recovery-2) with the language dysfunction markers (red line); the shaded areas are comprised between the 5th and 95th percentiles of the values of cross-correlation computed for the peaks of $P(t)$ of each state with a random permutation of the clinical markers in the $[60s, 260s]$ interval.

of the markers of language dysfunctions. To compute this lagged cross-correlation, we first convolve the train of clinical markers with a gaussian kernel of suitable width, so to convert them into a continuous time-series and then compute the lagged cross-correlation of this time-series with the time-series of probability of being in different states. The resulting cross-correlograms are shown in Figure 4.10 as thick and continuous red lines.

Non-zero lagged cross-correlations may however arise just as an effect of the limited number of clinical markers, matching by chance some of the peaks of probability of being in a state. We need then to estimate chance-level expectations for cross-correlation levels (by randomly reallocating the timing of clinical markers and recomputing the corresponding randomized marker densities and cross-correlations). Iterating this procedure 100 times allows estimating, the median chance-level cross-correlogram (dashed red lines in Figure 4.10) as well the 95th and 5th percentile (shaded area) of chance-level cross correlation curves. From these plots we see how only the seizure state and the fourth state have a significant value of correlation with the original time series of clinical markers. Interestingly, the fourth "two-crystals" allegiance state manifests a matching at close latency with clinical markers occurring even far away

the seizure ending, during the long recovery phase.

It is indeed important to stress that the analysis of the time-series of allegiance state membership in the 40 Hz band reveals the existence of an extended recovery period lasting well beyond the seizure offset (and also beyond the last reported clinical marker, 750s after seizure offset). Such finding is confirmed by analyses of other patients as well. When moving to other frequency bands, a similar tendency to the existence of a long recovery time before restoring baseline state can be observed even for the 20 Hz and the 10 Hz band. However, the lower is the considered frequency layer and the shorter lasts the recovery range. Thus, the 40 Hz layer is the one whose dynamic alterations bring the strongest evidence for the existence of a long-lasting recovery, whose existence is intuitively clear for the neurologist and neuropsychologist practitioner, without that neuroimaging biomarkers found until now a clear evidence for it. This recovery period is also highly dynamic, as the baseline, but sees an alternation of different states, notably, in this case, two different recovery-phase specific allegiance states, one of them more strongly associated with the reporting of language dysfunction.

Since a style of network dynamics is characterized both by the spatiotemporal organization of module reconfiguration (the allegiance matrix of the considered window) and the rate at which network reconfiguration occur (tracked by the dynamic Functional Connectivity speed within the considered window), we also related speed variations to clinical markers and seizure dynamics.

In Figure 4.11 we plot the average value of $\Delta FC(t-1,t)$ computed over each time window, and we assign each point with the corresponding allegiance state label. This analysis unveils how the baseline state is actually the state characterised by a faster dynamics, in terms of changes in the connectivity, which was also reflected in Figure 4.7. The seizure state has the lowest values of $\langle \Delta FC(t-1,t) \rangle_w$, or average *FC speed* at seizure onset and for the following seconds, except for the two pre-ictal spikes that occur at baseline and another highly perturbed period of the 40Hz layer occurring between 480 and 840 seconds from seizure onset. The two other states clearly alternate each other, with the former occurring in moments of increasing dynamics, whereas the latter is present in the sudden drops of FC speed, that also occur in the proximity of the language dysfunction markers. Going beyond the evaluation of an average state-specific speed of FC reconfiguration, the analyses of Figure 4.11 provide a continuous evaluation of speed variations along the recording, identifying a smooth time-course rather than discrete switching events. After the sudden drop of speed associated to seizure onset, speed slowly starts increasing until reaching baseline levels again at the end of the extended recovery period. However, the gradual increase of speed is interrupted by momentary slowing-down of dynamics, associated to the recruitment of the fourth allegiance state and, thus, a separation of the functional network into two independent sub networks and the arising of evident aphasia symptoms.

The same plots for the other three recordings can be found in the appendix A, in Figures A.3, A.5 and A.7 and reveal qualitatvely similar phenomenology with differences described in the next dedicated section. We also repeated this speed analysis for the other frequency bands. As in the case already of Figure 4.9, the time-course of

speed for the 20 and the 10 Hz layers are similar in their drop at seizure onset and existence of a gradual recovery. However, the return to baseline speed level occurs much earlier, with the 40 Hz layer being the one more strongly and distinctly manifesting the described dynamic phenomenology.

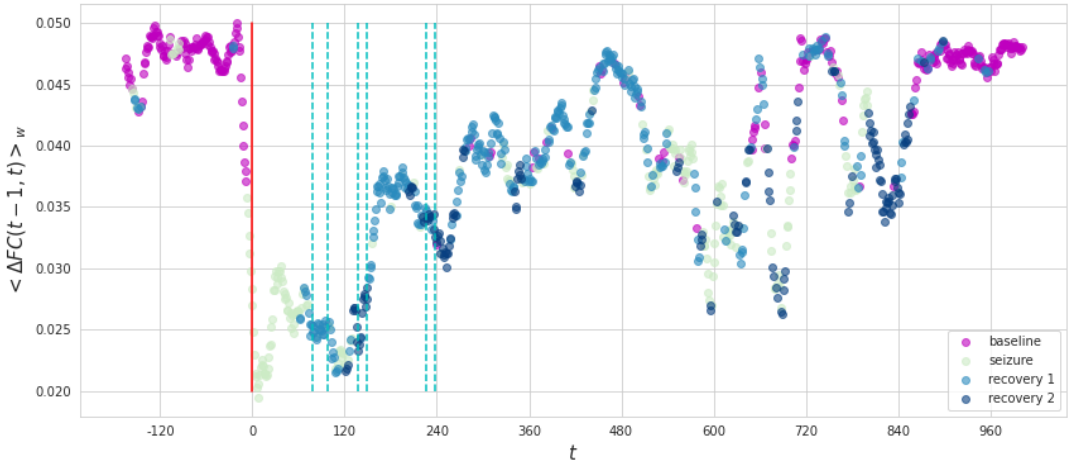

Figure 4.11. – **States of dynamics**: each of the colored dots corresponds to the average value of the instantaneous rate of change of the FC in a time window $\langle \Delta FC(t-1,t) \rangle_w$ and its color corresponds to the allegiance state label assigned to the corresponding time window.

Comparison of different recordings

A truth well known by any neurologist and neuropsychologist (and, probably, medical doctor in general) is that every patient is a "world apart". This is not the place where to generally comment on the importance of unique cases in neurology [144]. However, we should not be surprised that differences exist between the network analyses of recordings of seizures in different patients, as different patients have idiosyncrasies in their pathological profile and aetiology, despite the effort made by our neurologist collaborators to select similar cases. Yet, it is important to analyze comparatively the properties of different patients and seizures, so to extract qualitatively, if not quantitatively, common aspects and thus validate our description of seizure and recovery phases in terms of multiplex temporal network descriptors.

In order to capture the similarities and differences across different subjects and different recordings, in Figure 4.12 we graphically represent the four allegiance states, *baseline*, *seizure*, *recovery* 1 and *recovery 2*, found in all patients, as radar plots similar to what was done for network-state-wise connectivity profiles of neurons in Chapter 3, only this time on the three radial axis of each plot we plot allegiance-state quantities:

— the median value of the allegiance matrix computed over all the time points included in the relative allegiance state $\bar{A}$, as a first, rough indicator of how spatiotemporally-organized is module reconfiguration for each given state;

— the average value of the dFC-speed $\bar{v}$ within the relative allegiance state, quantifying how large is the rate of generic network reconfiguration for a state; we report this index for the recovery state for which it is the largest, as an indication of how allegiance state switching dynamics for a recording include a state related to the reporting of aphasia symptoms;

— the *symptom relation index* Θ defined as:

$$\Theta = \sum_{\tau \in \Gamma} \left(XC(\tau) - XC_{shuffled}(\tau) \right), \tag{4.6}$$

where $\Gamma = \left\{ \tau \| XC(\tau) \geq 95\%_{percentile \quad chance \quad level} \quad XC_{shuffled}(\tau) \right\}$. Thus Θ corresponds to the area comprised between the measured cross-correlation $XC(\tau)$ and the 95% confidence interval (upper bound of colored area in Figures 3.17, A.3, A.5 and A.7).

The values on the radial axes of the radar plots in Figure 4.12 are normalized in each row (each row corresponds to a different recording), whereas each column corresponds to a different allegiance state. Its is important to mention that the number of identified dynamic states could vary according to patients. Some of the patients, for instance, had two markedly distinct epilepsy states, with the initial fast spike-wave complex phase of the seizure showing up as a separate state. For the compilation of this comparative analyses we thus had to choose which state to include for comparison, trying to identify states with the highest qualitative matching. All information about each recording is, nevertheless, shown in the appendix A. The resulting selection of polygons in Figure 4.12 reveals a mixture of common traits and patient-specific (or even seizure-specific within a patient) traits.

We note how the baseline state is characterised in all analyzed seizure recordings by the highest values of $\bar{\nu}$, confirming that the baseline activity, in the 40Hz layer, is generally associated to a fast internal reconfiguration of functional connectivity (or, the rest baseline is a restless condition). This speed of network dynamics is in contrast slowed down the most during the seizure allegiance state, whereas for the two recovery states we note the tendency to have intermediate speeds progressively bridging between the seizure-state minimum and the baseline-state maximum. There is thus roughly a common speed ordering between the different allegiance states for all recordings. For the two recovery states, though, some differences exist between the patients. We chose here to name as "recovery state 2" the one among recovery states for a patient showing the largest symptom relation index Θ. With this convention, thus, the recovery state 2 has a slower speed than the recovery state 1 in the two seizure events studied for patient 1, but the relation is inverted in the recordings from patient 2 and 3. Yet, in general, recovery states are between seizure and baseline, associated to a ramping up speed along the whole recovery period (even if local minima of speed during recovery are not as precisely aligned with symptom appearance as for the reference patient). Furthermore, all recordings included a recovery state with a larger (and significant) symptom relation index, a non-trivial finding that is sufficient to confirm the relation existing between dynamic network reconfiguration, on one side, and aphasia symptoms manifestation, on the other.

The situation is more heterogeneous for the third considered feature, the median allegiance level $\bar{A}$. The state with maximal $\bar{A}$ varies from a recording to the other. For the reference recording of patient 1, chosen for display in the rest of the chapter, we found maximal internal allegiance level at baseline and minimum internal allegiance during seizure, but for the other recordings (including the second seizure of the same patient), the order is reverted. This finding is not necessarily surprising. We know that a large variety of connectivity states and modes is expected as well to exist during resting-state fluctuations at baseline as well [41, 94]. Thus, over the set of considered recordings, we find here a mix of baseline states, always fast-reconfiguring (cf. the systematically large $\bar{\nu}$) but with sometimes higher ("liquid" baseline)and sometimes lower ("gaseous" baseline) internal allegiance levels (cf. the heterogeneous $\bar{A}$). However, in all cases, transition to seizure change qualitatively the nature of the allegiance state, dissolving the internal allegiance structure, if seizure arise on a liquid/structured baseline state, or materializing one, if the seizure onsets on top of a more gaseous/unstructured baseline state.

We also note a general tendency of the fourth "recovery 2" state to have higher values of median allegiance with respect to the third "'recovery 1" state, except for the recording of patient 2 (third row): in this recording (see A) however, we stress that a true baseline state is never reached within the time-span of the recording; this could affect the quality of the clustering of the dAM and thus the retrieval of the states (particularly the proper identification and description of baseline properties, as we observe very short epochs only within a clear baseline) and generally suggests, together with the qualitative differences of the state-wise FC and allegiance matrices w.r.t to the other recordings, how each recording of each patient could display subtle

peculiarities. In all cases, there is a variety of states, whose internal style of dynamics can be described, in relation to symptoms, by the mix of markers we consider.

To conclude this fast comparison between recordings, we also remark that similar considerations could be made as well for the other layers, notably for the 20 and the 10 Hz ones. We have however, until now, completed our analyses only for the 40 Hz layer, which is the one generally showing the stronger pathology-related signal in all the other analyses we conducted.

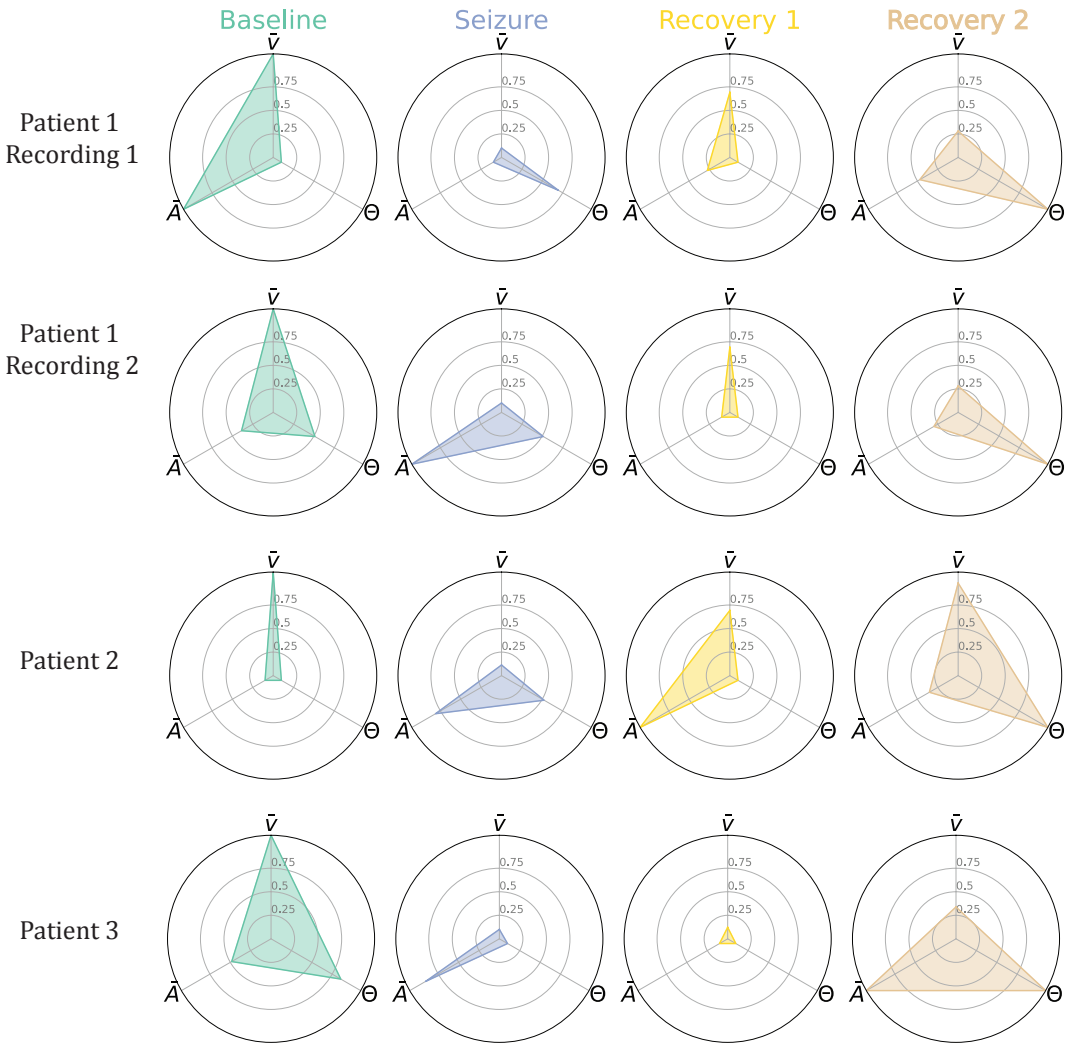

Figure 4.12. – **Allegiance states in the** 40 **Hz band:** for each recording (two recordings of patient 1 and one recording each for patients 2 and 3) we show here four allegiance states by plotting on a radar plot three quantities: the dFC speed averaged on the time points of the relative state, the average over the allegiance matrix computed on the time points assigned to the relative state as well as the Θ index of each state. The three quantities that give rise to each of the four radar plots of a recording are normalised over the recording: a value of 1 of a quantity in a radar plot means maximum value of that quantity with respect to radar plots in the same row. The light green radar-plots correspond to the baseline state; the blue plots correspond to seizure states, yellow and orange are recovery 1 and 2, respectively.

4.5. Interlayer co-allegiance

We have until now studied all layers in isolation, thus not fully exploiting the multiplex nature of our temporal network description. All layers at frequencies larger or equal than 10 Hz display a rich dynamics, but how coupled are the dynamics within different layers? Exactly as we studied modular allegiance within each layer, capturing how coordinated are modular partitions at different times, could we now define a form of *between-layer allegiance alignment*, to quantify, at each time, how similar are modular partitions over the same network nodes observed at different frequency layers?

To do so, we compute the cosine similarity between the allegiance matrix computed in a time window in a layer, with the allegiance matrices computed in the same window for each of the other layers, for all the time windows. We therefore end up with a time series of allegiance similarity for each pair of layers (Figure 4.13).

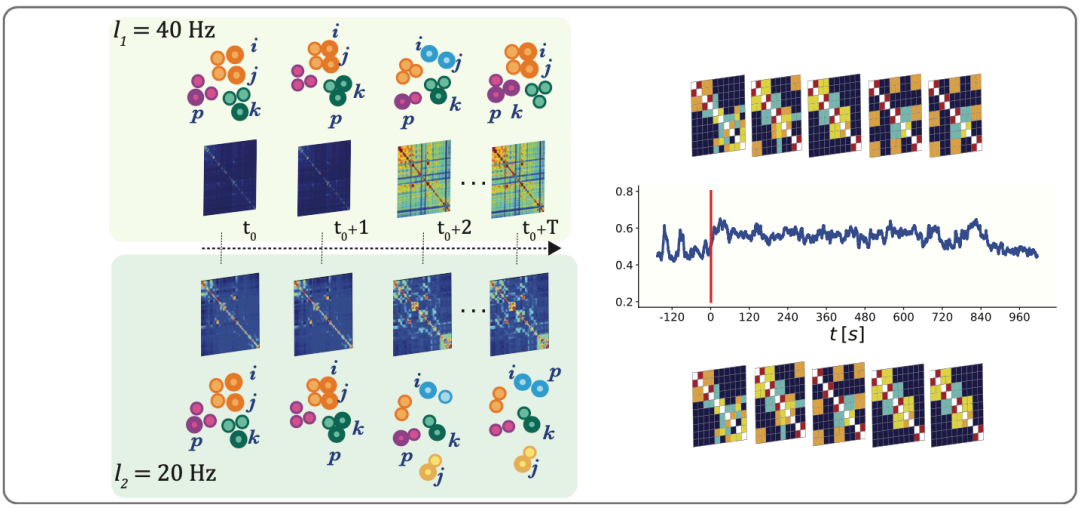

Figure 4.13. – **Analysis building blocks:** For each pair of layers (l_1 = 40Hz and l_2 = 20Hz in the cartoon) we compare the partition into modules at each time stamp by computing the cosine similarity of the relative module assignments (right).

This analysis reveals an increase, w.r.t. baseline, of the similarity between the allegiance matrices of the 40Hz and 20Hz layer (Figure 4.14.a, recording 1, patient 1). We choose to capture and better characterise the changes in the inter-layer allegiance similarity by segmenting the recording into four phases: pre-ictal, from the beginning of the recording to seizure onset; ictal, from seizure onset to offset; early-recovery, from seizure onset to the last clinical marker; late recovery, from the last marker to the end of the recording. We therefore observe the distribution of time-window-specific values of inter-layer allegiance similarity within each the four phases, and compare the distributions obtained for each recording in Figure 4.14.b. A distribution peaked around higher values of inter-layer allegiance of the ictal phase w.r.t pre-ictal is obtained in three out of four recording. The only exception is the last recording, for

which we already commented on the fact that baseline is ill-determined, as the final state we found at recording ending is not yet labeled again as the first state we find at beginning of recording, that is automatically labeled "baseline", but could already be, in reality, a transient within a pathological recovery-like state.

This finding seems to suggest that the dynamic re-organization of the nodes in the network in the 40Hz and 20Hz frequency bands become more similar, and coordinated (or, more trivially and possibly dysfunctionally, enslaved?), from seizure onset to offset. In Figure 4.14.c we plot analogous time series of inter-layer allegiance similarity between the 40Hz and 10Hz layers (top) and between the 20Hz and 10Hz layers (bottom). The corresponding phase-specific distributions for the four recordings are shown in Figure 4.14.d (40Hz vs 10Hz on the top, 20Hz vs. 10Hz on the bottom). We find no significant general trend across the different recordings from these analyses, noting overall fewer significant differences in the distribution of inter-layer similarity of the allegiance when comparing the allegiance dynamics in the 20 and 10 Hz layers (Figure 4.14.d, bottom). The strongest effect thus is an enslaving between fluctuations of network modular organization in the two faster 20 Hz and 40 Hz layers. As these frequency bands are believed to multiplex the routing of alternative information flows [126] or the implementation of distinct cognitive processes, particularly in language parsing and production [75], such loss of autonomy between the layers may be seen as a loss of complexity, associated to a reduced capability for rich information processing.

4.6. Discussion

The work introduced in the previous sections corresponds to an ongoing research, thus several findings need to be further investigated and therefore are not included in this chapter. However, the results that I described already raise several questions to discuss. First of all, we introduce a new approach to study multi-frequency time-varying data as a temporal multiplex network: such approach is relatively new and few studies have started using it [109], while no other data-driven studies with applications in systems neuroscience can be found in the literature. This representation of the data, in which each layer corresponds to the coherence between brain regions in a different frequency band, is potentially a powerful way to investigate parallel information dynamics unfolding on top of a brain network at different time-scales: a frequency in this context could indeed be viewed as a time-scale of the communication and exchange of information between different brain regions. Note that, usually, in systems neuroscience, functional interactions between different frequencies are studied through spectral metrics of cross-frequency coupling [42]. However, these cross-frequency interactions are difficult to detect directly from time-series analyses, as oscillatory power is usually already weak and heterogeneous between bands. Our multiplex network notion of alignement between the dynamics of different layer provides an alternative, network-based notion of cross-frequency coordination that may be more robust to track and less sensitive to power differences and fluctuations as already projected in an abstract connectivity domain.

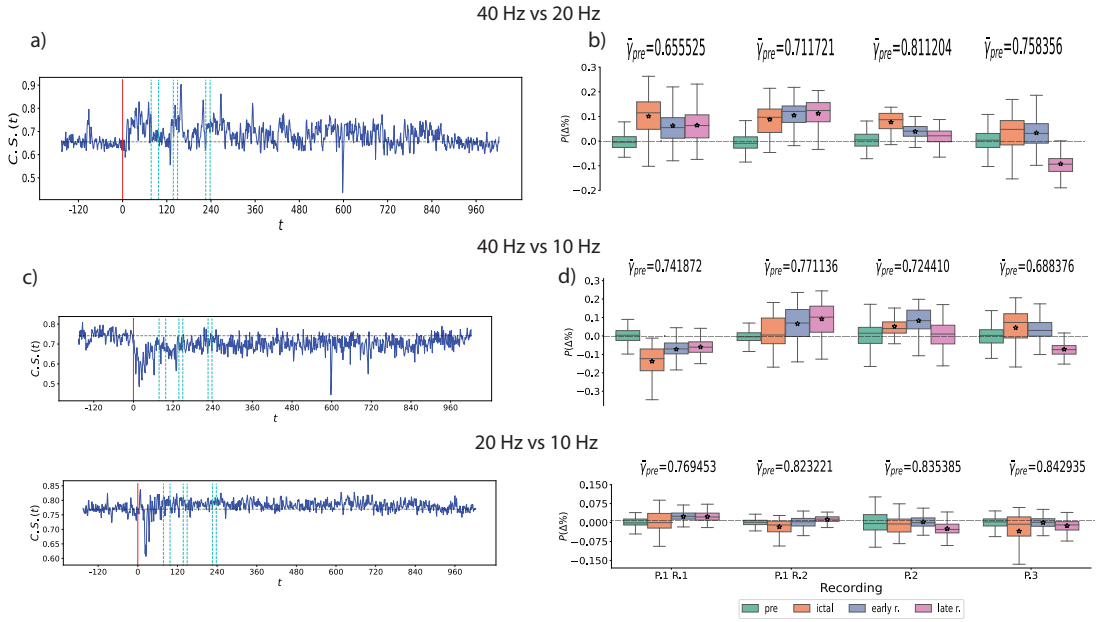

Figure 4.14. – **Multilayer allegiance: a)** the instantaneous inter-layer cosine similarity computed between the allegiance matrix of the 40Hz layer in a time window and the allegiance matrix of the 20Hz layer in the same window, recording 1. **b)** within each plot, the boxplots correspond to the distributions of the values of inter-layer similarity for the 40 and 20 Hz layers in recordings 1 to 4 in a specific moment of interest of the recording: the *pre-ichtal* (green boxplots) phase correspond to the baseline activity, from the start of the recording to seizure onset; the *ictal* (orange) phase goes from seizure onset to seizure offset; the *early r.*, i.e., early recovery (blue), phase goes from seizure offset to the last language-dysfunction marker; the *late recovery* (pink) phase goes from the last marker to the end of the recording. We subtract the mean value of the inter-layer allegiance similarity computed over the pre-ictal phase of a recording to the distributions of each phase (i.e., green boxplots centered around 0), indicating such value $\bar{\gamma}_{pre}$ above the four corresponding boxplots. **C)** the inter-layer similarity of allegiance matrices computed for the 40 and 10 Hz layers (top), and for the 20 and 10 Hz layers (bottom) in recording 1. **D)** the four phase-specific boxplots of the distribution of inter-layer similarity for the 40 and 10 Hz layers (top), and for the 20 and 10 Hz layers (bottom), for all four recordings.

The analysis shown in Figure 4.14 is a first attempt in the direction of studying inter-frequency interactions via a temporal multiplex network approach, and already serves us with some potentially useful information. In fact, it allows us to capture the heightened coordination of the allegiance dynamics of the 40 and 20 Hz layers, which in turn could cause a loss of independence of the different information processing

operations normally separately related to these two time-scales. Usually, different frequency layers should be able to have an independent dynamics as they subserve the needs of bottom-up and top-down information flows that should be independently modulated depending on task, behavior or brain state [126]. In the specific case of language, it has been proposed that modulations at θ/α and β/ low γ frequencies are associated respectively to syllable- and phoneme-related processing, while higher frequencies in the high-γ range are reserved for internal computations linked e.g. to lexical-semantic interpretation [75, 125]. If the between-layer articulation is disrupted and impoverished, therefore, we could expect that information about the syllabic and phonemic levels is not anymore properly fed into the interpretation system, which could be a functional mechanism leading to aphasia symptoms of different forms.
Another aspect of our analyses that we would like to highlight is the fact that we designed a framework to describe network reconfiguration traits, without direct reference to the traits of individual time-resolved networks. In other words, we focus on the moving flow, not on its stop-motion frames. In a similar fashion to what was described in Chapter 3, here we trace discrete states of the evolution of each of the layers of the multiplex: these states represent indeed different dynamical styles of the nodes of the network to flow across the different communities/modules of the network in a more coordinated or more random manner. The dynamical nature of these states is highlighted by the sensible differences in their dFC-speed, which is the property of those plotted on the radial axes in Figure 4.12 that most allows to identify similar allegiance states across different recordings and patients. States can be classified not only in virtue of how internally variable they are, but also on how this internal variability is organized, as tracked by the joint inspection of speed and modular allegiance level within time-windows of observations. We therefore note the general tendency of the baseline state, to be the more restless one; and also the one of seizure onset to cause an abrupt “phase transition” of the network reconfiguration dynamics with more structured (or unstructured) baseline dynamics getting suddenly unstructured (or frozen). The seizure indeed enforces a hyper-synchronization of the network, resulting in a slow reconfiguration of the network along with a general loss of community structure. In such a situation, network fluctuations are either strongly suppressed (which can artificially raise allegiance, but allegiance to a random-like uniform partition) or just reduced to an unstructured noise around a frozen dense network configuration (hence the allegiance decrease).

The seizure offset is then followed by a long recovery period whose impact on network dynamics is strikingly and unmistakably detected by our approach. Interestingly, we retrieve two allegiance states that only occur in the time period comprised between the offset of the seizure and the full recovery of the baseline state. Of these two, one state corresponds to an ongoing transition from a seizure-like regime to a baseline-like one, and occurs in moments in which the rate of reconfiguration of the functional network "speeds up". The second state, (the fourth state in Figure 4.12), occurs instead in local minima of the dFC-speed, and seems to correspond to moments in which the network is transiently "trapped" in a dysfunctional regime with substantial differences when compared to the other states: here the network is divided into two independent

sub-networks, whose nodes move across the existing modules in the network in a coordinated manner only with nodes from the same sub-network.

Importantly, one of the sub-networks includes temporal brain regions, whereas the other is composed of parietal regions. Our analysis thus seems to suggest the existence of a reoccurring state, which most correlates with the language impairment markers, in which the communication between the parietal and temporal regions seems to be disrupted. These results relate especially to the high-gamma (40Hz) frequency band. The layer-wise analysis of the other frequencies can be found in appendix A.

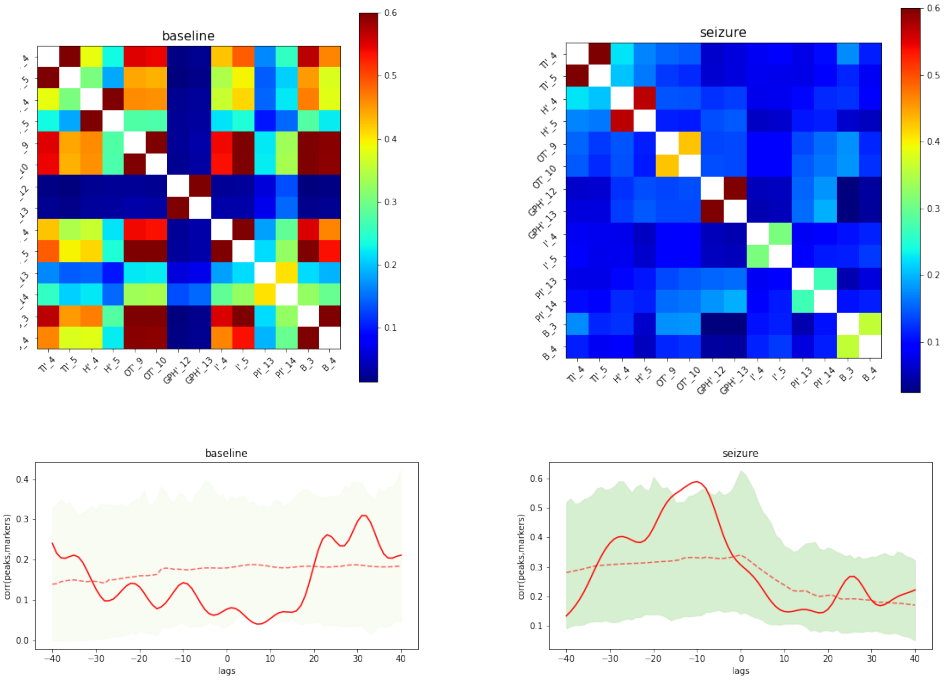

Figure 4.15. – **Language system-restricted analysis 1** baseline and seizure allegiance matrices (top); lagged cross correlation plots (bottom) for the two states.

This last finding opens questions that specifically relate to the language system, as this system involves both temporal and parietal nodes whih-ch are broken through the two split "crystals". The next step of our research should consist, in fact, on restricting the analysis of the allegiance states to network nodes in our recordings known to be relevant for the language system. This will allow further investigating whether the emergence of language impairments could be explained in terms of specific changes in the FC, allegiance and in the dFC of the language sub-network, that possibly hide more fine-grained explanations than those described so far in this chapter. An exploratory analysis in this direction has already revealed similarities with the FC and allegiance matrices of the language system with those of the overall network (Figures 4.15 and 4.16). These figures are the product of the extraction of allegiance states by clustering the time-windowed allegiance matrices of only the language-specific sub-network: interestingly we retrieve the same four states as in Figures 4.7 and 4.8. In particular we

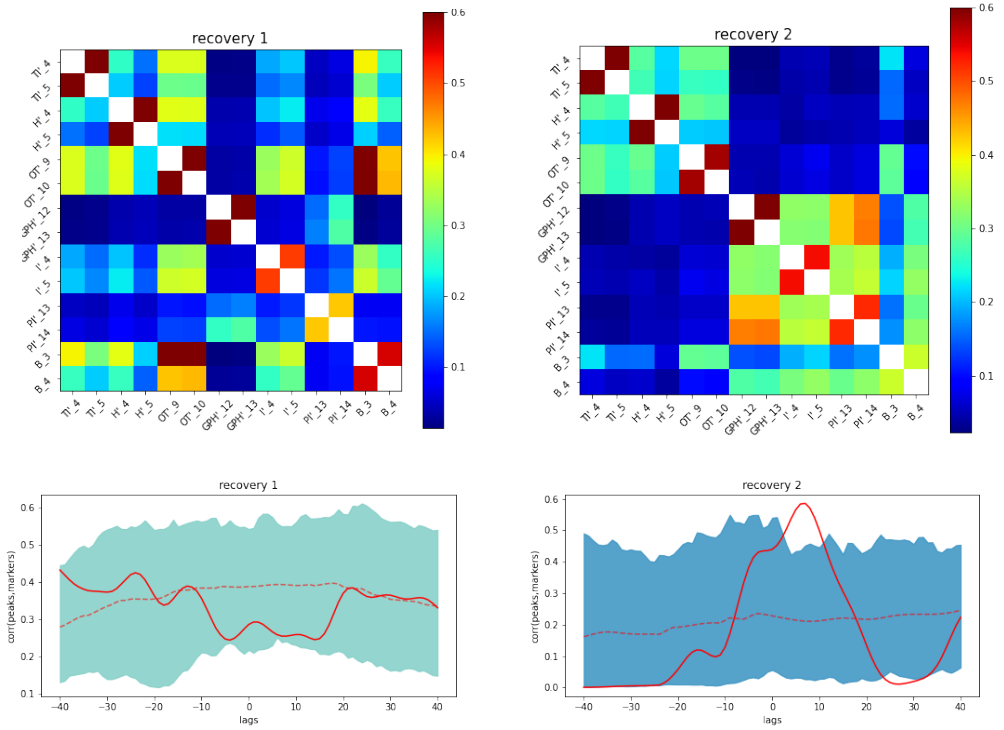

Figure 4.16. – **Language system-restricted analysis 2** recovery 1 and recovery 2 allegiance matrices (top); lagged cross correlation plots (bottom) for the two states.

find a separation into two groups of regions of higher allegiance in the second recovery state (Figure 4.16, right-plot) also when restricting the analysis to the language system. Also in this case, the recovery 2 state has the most significant correlation with the language-impairment markers. It would be therefore interesting in the future to study in greater detail the dynamical profile of this and along with the other states, possibly "zooming down" all the way to the node level. Such analysis could uncover the functional changes across the different allegiance states happening to language-related brain regions, that ultimately relate to the arising of aphasia. A hypothesis here is that nothing special is occurring to the language system, whose network dynamics seems to essentially mirror the one of the global networks which we previously described. However, the functional impact on the language system of the perturbations of this global network dynamics would be particularly strong and severe, as, because of its distributed localization, the language system's internal integration gets transiently lost.

A limitation in this study is represented by the number of recordings analysed. We note, however, how already the analyses carried out for four recordings of three patients highlight the peculiarity of each seizure, even in the same patient. Future research in this direction should involve larger cohorts of patients, which could result in a further generalization of our current findings. In addition, it could be interesting to take into account larger frequency bands when computing the wavelet coherence

between pairs of signals or to implement different denoising techniques that define a specific significance threshold for each individual layer of edges in the temporal multiplex, thus assuring the same density in each layer. This could lead to a better study of the allegiance dynamics unfolding at the lower frequencies (longer time-scales), which could not be captured by our current analysis.

5. Novel structures in temporal networks: the *Temporal rich club phenomenon*

As I have mentioned in Chapter 1, a common challenge in the study of networks consists in identifying relevant structures, and several complementary approaches have been put forward to characterize networked data sets and their more central elements. For instance, hubs, single nodes with very large numbers of connections (degrees), are known to influence spreading processes [5, 16]. A quantification of a core-periphery structure identifies a central core of well-connected nodes [151] (see Chapters 1 and 3). The k-core decomposition [6] decomposes the network into subgraphs of increasing connectedness, with correspondingly increasing influence in spreading processes [100]. The rich-club coefficient quantifies whether the nodes with large numbers of neighbors (the hubs) tend to form more tightly interconnected groups [48, 123, 138, 159, 179] that can, for instance, share the control of resources in social and collaboration networks [138], or shape the routing and integration of communication in brain networks [85, 137, 167] (see Chapter 2 for more details). While all these approaches are effective for static networks, an increasing number of data sets include temporal information about edges, which can appear and disappear on different time scales: static networks are often only aggregated representations of the resulting temporal networks [89–91] (see Chapter 1), in which the information about the temporality of interactions has been lost. Thus, any structure found in a static network obtained by temporal aggregation of data could in fact be formed by edges that were active at unrelated times. To investigate structures in temporal networks, it is thus crucial to take into account the complex temporal properties of the data. For instance, various types of hubs can be defined, and a given node can be central during a certain period and peripheral in the next one (as shown in our work, described in Chapter 3); Network modular structures can evolve (which can e.g. be a resource for cognitive processing [34]); Processes can only take causal, time respecting paths among the elements of a network [146, 156]; Concurrency, i.e., the simultaneity of connections of a given node with others, is key in epidemic propagation processes [122]; Temporal motifs are defined as the repetition of the connections in a small temporal subgraph in a given order[104]; Well connected structures such as cores are not static but are defined on specific time-intervals [44, 68].

Overall, structures and hierarchies in temporal networks need to be defined and investigated taking into account (i) the temporality and simultaneity of the interactions forming the structure, (ii) the time-span on which the structure exists.

Here, I describe a new way to investigate the cohesion of increasingly central nodes in a temporal network, namely, the *temporal rich club coefficient*: given a temporal network, our aim is to quantify whether nodes who interact with increasing numbers of other nodes (i.e., with increasing degree in the aggregate network) tend also to interact *with each other simultaneously and in a stable way* (i.e., during a certain time period). We thus first define the $\Delta-$*cohesion* of a group of nodes at each time t, as the density of links persistently connecting the nodes in the group during a time interval of length Δ starting at t. We then consider groups of nodes of increasing degree in the aggregated network, and measure the maximum value of their $\Delta-$cohesion over time: this quantifies whether these groups are tightly *and simultaneously* interconnected at least once *for a certain duration* Δ. Moreover, and as in the case of the static rich club coefficient ([48]), a natural question is whether these simultaneous connections could exist just by chance, so that we compare the result with adequate null models for temporal networks [70] (see Section 1.2.4 for details). To show the broad interest of this new analysis tool for temporal networks, we consider empirical temporal networks representing very different systems: an air transportation infrastructure, a face-to-face interaction network in a social context, and a neuronal assembly, i.e., one of the information-sharing networks presented and analysed in Chapter 3. In each case, we compute the temporal rich-club coefficient for the data and several null models, and highlight how it unveils interesting properties of the data. We show in particular how static and temporal rich clubs are independent phenomena, how a temporal rich club impacts spreading processes, and how a temporal network undergoing successive states [121] can present a distinct temporal rich club in each state. All together, these findings suggest that the temporal rich club coefficient provides a new tool in the complex analysis of temporal networks, shedding light on the role and connections of their most prominent elements and providing additional relevant information on the different periods of interest of the network.

5.1. Simultaneity and Cohesion

We consider a temporal network in discrete time on a time interval $[1, T]$ (Figure 5.1.a) represented as a snapshot-sequence network. We denote by *temporal edges* the interactions between pairs of nodes in each snapshot. The temporal aggregation over $[1, T]$ yields a static, aggregated network (see Chapter 1) $G = (V, E)$ with set of nodes V and set of edges E (Figure 5.1.b), in which an edge is drawn between two nodes i and j if they have at least shared one temporal edge, with a weight w_{ij} given by the number of temporal edges between i and j. The degree k of a node in G is the number of distinct other nodes with which it has interacted at least once in $[1, T]$, and its strength s the total number of temporal edges it has participated to.

As stated above, our goal is to quantify a temporal rich club effect, corresponding to the fact that nodes of increasing degree in G tend to be more connected than by chance *simultaneously and for a certain duration*. We first remind that the rich club coefficient $\phi(k)$ and the rich club ordering is detected by comparing $\phi(k)$ with the

value obtained for a random network with the same degree sequence as the original one, $\phi_{ran}(k)$ (see Chaoter 1 for formal definition). The ratio

$$\rho(k) = \frac{\phi(k)}{\phi_{ran}(k)} .$$

$\rho(k) > 1$ indicates indeed that the nodes with degree larger than k are more connected than by chance.

Here, to take into account temporality, we first define at each time t the $\Delta-$cohesion $\epsilon_{>k}(t,\Delta)$ (schematic representation in Figure 5.1.c-d) as the number of ties between nodes of $S_{>k}$ that remain stable over the time interval $[t, t+\Delta]$, normalized by the maximal possible value $N_{>k}(N_{>k}-1)/2$. We then define the temporal rich club coefficient as the maximal cohesion observed in the temporal network over time:

$$M(k,\Delta) \equiv \max_t \epsilon_{>k}(t,\Delta) \tag{5.1}$$

In other terms, $M(k,\Delta)$ is the maximal density of temporal edges observed in a stable way for a duration Δ among nodes of aggregated degree larger than k. While, by definition, $M(k,\Delta)$ is non-increasing as a function of Δ, a $M(k,\Delta)$ increasing with k denotes that the most connected nodes tend as well to be increasingly connected with each other in a simultaneous way for a duration at least Δ. However, such simultaneity might also be observed by chance. To detect a temporal rich club effect, one needs therefore to compare $M(k,\Delta)$ with the value $M_{ran}(k,\Delta)$ obtained in a suitable null model of the temporal network:

$$\mu(k,\Delta) \equiv \frac{M(k,\Delta)}{M_{ran}(k,\Delta)} \tag{5.2}$$

$\mu(k,\Delta) > 1$ indicates that the nodes of degree larger than k are more connected simultaneously on at least one time interval of duration Δ than expected by chance. Although there is a large variety of null models for temporal networks [70], we focus here on randomization procedures that preserve the overall activity timeline of the temporal network (number of temporal edges at each time) as well as the degree of each node in the aggregated graph: in particular, we will focus on the three randomization procedures presented in Chapter 1, Section 1.2.4, namely the *timestamps shuffling*, the *event shuffling* and the *degree-constrained link shuffling*.

Furthermore, as $M(k,\Delta)$ is defined as a maximum over time, it is also relevant to study the time evolution of the $\Delta-$cohesion $\epsilon_{>k}(t,\Delta)$, in order to find the moments of highest simultaneous connectivity of $S_{>k}$, and to check whether this cohesion is stable or fluctuates strongly. This allows for instance to distinguish between *stable or recurrent* and *transient* rich club effects: in the former case, $\epsilon_{>k}(t,\Delta)$ reaches its maximum $M(k,\Delta)$ repeatedly, or remains close to it, while in the latter, $M(k,\Delta)$ is reached only once or only at specific moments.

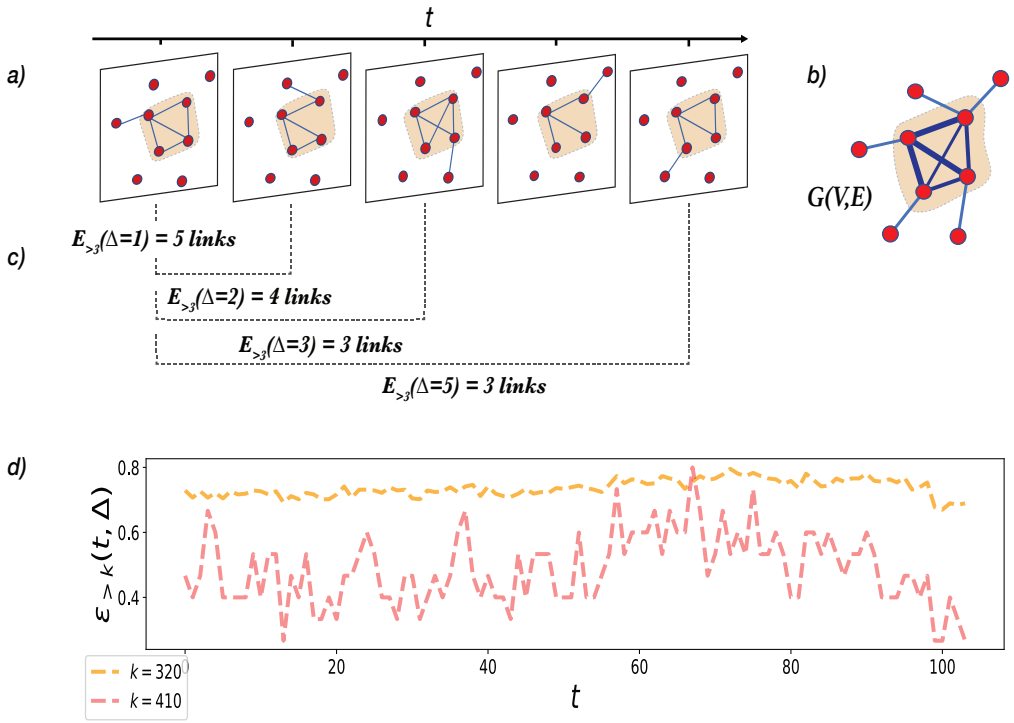

Figure 5.1. – **a)** Schematic representation of a temporal network as a sequence of instantaneous snapshots where nodes are connected by temporal edges. **b)** Time aggregated graph $G(V,E)$, where the weight of an edge corresponds to the number of occurrences of the corresponding temporal edge. The set $S_{>3}$ of nodes of degree larger than 3 in the aggregate graph G and its induced subgraph are included in the orange shaded area. **c)** Maximal number of edges among the nodes of $S_{>3}$ that are simultaneously stable over a duration Δ, $E_{>3}(\Delta)$, for different values of Δ. **d)** Two examples of time series of the $\Delta-$cohesion $\epsilon_{>k}(t,\Delta)$ computed for the U.S. Air Transportation Temporal Network, with $\Delta = 1$; for $k = 320$ (orange dotted line), $\epsilon_{>320}(t,\Delta = 1)$ remains persistently large, corresponding to a *stable* temporal rich club, while for $k = 410$ the cohesion values fluctuate strongly, suggesting the existence of a *transient* temporal rich club.

5.2. The temporal Rich Club: a study of air transportation networks

We first apply our measure on a data set describing the U.S. air transportation infrastructure from 2012 to 2020. This data set represents the connections between US airports, with temporal resolution of one month, from January 2012 to September 2020, for a total of 105 time stamps. The $N = 1920$ nodes of the temporal network represent the airports, and in each monthly snapshot a temporal edge is drawn between two

nodes if there was at least one direct flight between the corresponding airports during that month. The degree of a node in the aggregated network is thus the number of other airports to which it has been connected directly once, and its strength is its total number of temporal edges. The data is publicly available on the website of the Bureau of Transportation Statistics (https://www.transtats.bts.gov/, "Air Carrier Statistics (From 41 Traffic) - U.S. Carriers" data base).

The average number of temporal edges in a snapshot is 6126 and, in the aggregated network, the average degree is 44, with degrees ranging from 1 to 498.

Figure 5.2.a shows the $k-\Delta$ diagram of the temporal rich club coefficient $M(k,\Delta)$ as a color plot (the size of $S_{>k}$ being shown on top). At fixed k, $M(k,\Delta)$ decreases as Δ increases (by definition, as larger Δ is a stronger requirement in terms of stability of temporal edges). At fixed Δ, $M(k,\Delta)$ is small for small and intermediate k, and decreases rapidly as Δ increases: many small airports have fluctuating activity, sometimes seasonal, so that many temporal edges involving these airports are not very stable [69], leading to a small cohesion at the global level. The maximal cohesion however increases with k: airports with more connections tend also to be more interconnected and with increasingly stable connections (as found also in [69]). $M(k,\Delta)$ reaches very large values around $k\sim 315$, even at large Δ, indicating a stable and very cohesive structure. In fact, most of the 31 airports in $S_{>315}$ are hubs of the U.S. air transportation system, which are largely interconnected with very stable (and simultaneous) connections. For higher values of k, $M(k,\Delta)$ decreases again, especially at large Δ, with a final increase close to the maximum possible value of k (such that $|S_{>k}|\geq 2$). This pattern indicates that, when restricting to $k>380-390$, the interconnections of the nodes of $S_{>k}$ become actually less simultaneous and stable than in $S_{>315}$: this indicates that some airports with degree larger than $380-390$ have actually *less* stable connections than others with degree $315<k<380$, i.e., that some of the airports with very large aggregated degree have fluctuating connections. This is also clear from the timelines of $\Delta-$cohesion shown in Figure 5.1.d for $k=320$ and $k=410$, with lower and more fluctuating values for $k=410$.

We further investigate this point in Figure 5.2.c-d: Figure 5.2.c shows the 20 airports with largest aggregated degree, i.e., number of distinct other airports with which they share a direct connection (degree values ranging from 350 to 498). We highlight in red the airports that are as well among the 20 nodes with largest aggregated strength ($s>10,000$), and in light blue the others. While the red nodes are typically well-known hubs, we find among the nodes in light blue airports such as Burbank-Hollywood (BUR), Teterboro Airport (TEB) and Westchester County Airport (HPN). It turns out these airports serve as reliever airports for hubs such as LAX (Los Angeles) and JFK (New York), respectively: they are therefore extremely well connected in the aggregated network but have fluctuating connections, depending on the needs of the neighbouring hubs. Figure 5.2.d highlights the differences between the two types of nodes, i.e. the "real" hubs and the reliever airports, by displaying the Jaccard index between the connections of O'Hare International Airport (ORD, top plot) and Westchester County Airport (HPN, bottom) in successive months. ORD ($k=421$) has a very stable neighborhood while HPN (reliever airport for JFK), despite having the largest aggregated

degree value $k = 498$, undergoes changes of up to 80% of its neighborhood from a month to the next.

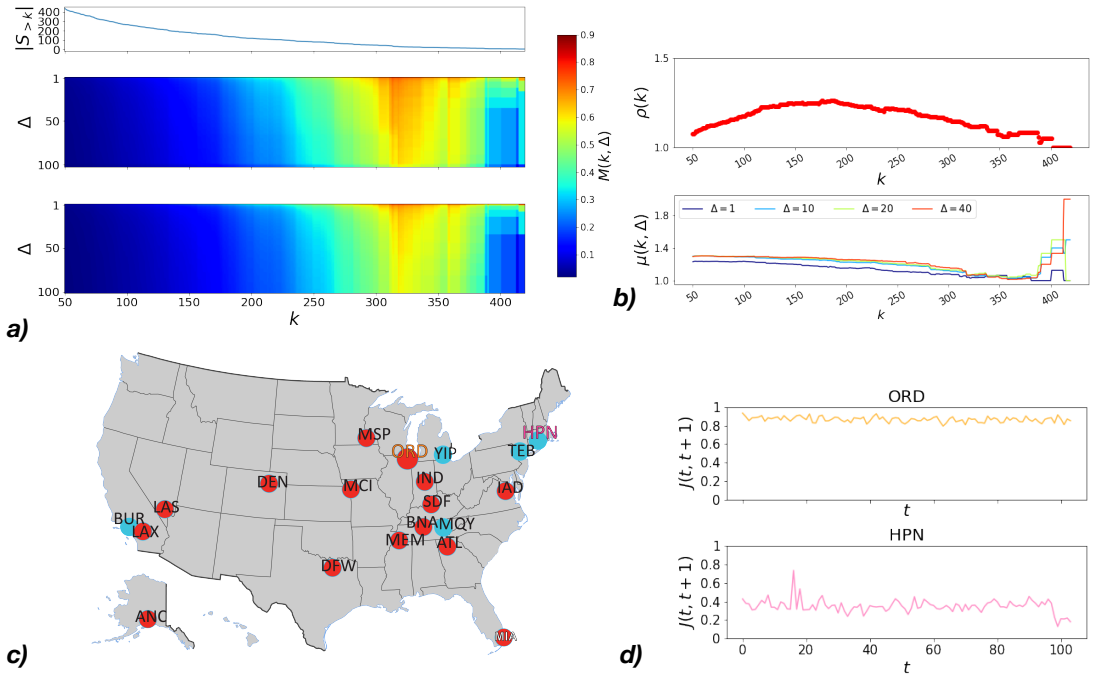

Figure 5.2. – **U.S. air transportation temporal network. a)** (top) Size $N_{>k} = |S_{>k}|$ of the sub-network of nodes of aggregate degree larger than k as a function of k; (middle) temporal rich club coefficient $M(k,\Delta)$ as a color plot as a function of k and Δ, for the U.S. air transportation temporal network; (bottom) $M_{ran}(k,\Delta)$ obtained for a randomized version of the temporal network that preserves the activity timeline and the structure of the aggregated network. **b)** (top) Static rich club coefficient $\rho(k)$ of the aggregated graph, as a function of the aggregate degree k; $\rho(k) > 1$ indicates that a rich club ordering is present [48], i.e., that the set of nodes $S_{>k}$ has more connections than expected by chance; (bottom) ratio $\mu(k,\Delta)$ between $M(k,\Delta)$ and $M_{ran}(k,\Delta)$ as a function of k for specific values of Δ. $\mu(k,\Delta) > 1$ indicates that a temporal rich club ordering is present, i.e., that the interactions within $S_{>k}$ are more simultaneous than expected by chance. **c)** Geographic locations of the 20 airports with largest aggregate degree ($S_{>350}$); airports that are also in the group of 20 nodes with highest strength ($s > 10,000$, i.e., at least about 100 different connections each month on average) in the aggregated network are depicted in red, whereas the light blue nodes have low strength. **d)** Jaccard index of the neighborhood of a node between times t and $t+1$ as a function of time, computed for O'Hare International Airport (ORD, top), and Westcherster County Aiport (HPN, bottom): both airports are in the top 20 nodes for aggregate degree, yet ORD is also in the set of 20 nodes with largest aggregate strength, whereas HPN is not.

Figure 5.2.a (bottom) displays for comparison the maximal cohesion $M_{ran}(k,\Delta)$ for the time-stamp reshuffling of the data, with conserved activity timeline and aggregated network, obtained by reshuffling the timestamps of the temporal edges. $M_{ran}(k,\Delta)$ shows similar patterns but smaller values than $M(k,\Delta)$ for all (k,Δ), showing that a temporal rich club ordering is present: for any $S_{>k}$, the interactions tend to be more simultaneously cohesive than expected by chance. This is the case even at very large k: even when the reliever airports lead to a smaller $M(k,\Delta)$, its value is still larger than by chance.

Differences with chance expectations are further investigated in Figure 5.2.b, which also highlights that the static and temporal rich club orderings show different patterns. The top plot of the figure displays the normalized static rich club coefficient $\rho(k)$ (see also [48]): $\rho(k) > 1$ indicates the presence of a static rich club ordering, which becomes stronger as k increases from 50 to ~ 250. At large aggregated degree ($k \gtrsim 250$), $\rho(k)$ decreases, indicating that the density of links among the hubs tends to be closer to the one of a null model: these hubs have such large degree that, even in a null model, they tend to be largely interconnected. The bottom plot of Figure 5.2.b shows that the ratio $\mu(k,\Delta)$ vs. k for various Δ exhibits a different trend: $\mu(k,\Delta)$ is above 1 and almost constant over a large range of k values, and decreases for $320 \lesssim k \lesssim 380$: in this range of k values, $S_{>k}$ is a mix of hubs and reliever airports, with both very stable connections and others much less stable. The randomization by time stamp reshuffling does not perturb the most stable connections, so that M and M_{ran} are closer. Finally for the largest aggregated degree values, $\mu(k,\Delta)$ reaches again very large values, especially for large Δ: here many of the remaining connections are to reliever airports, which are not necessarily very stable nor simultaneous, yet much more so than by chance. For completeness, the comparison of the $k-\Delta$ diagram of the maximal cohesion $M(k,\Delta)$ of the original data with the three randomized reference models presented in Figure 1.2.4 is displayed in 5.3.

The analysis of the US air transportation network under the lens of the temporal rich club can thus shed light on the different roles of well-connected nodes, and highlights how temporal and static rich clubs can co-exist albeit with different patterns.

5.3. Temporal rich clubs and spreading processes

The second dataset we consider is a temporal network of face-to-face close proximity contacts between 232 children and 10 teachers in a Primary School of Lyon, France, during two days in 2009, as collected by the SocioPatterns collaboration using wearable devices. The original data is publicly available from the SocioPatterns website (http://www.sociopatterns.org/datasets/primary-school-temporal-network-data/)The temporal edges between two nodes at a specific time stamp correspond to the detection by wearable sensors of a face-to-face interaction between the two corresponding individuals at that time [43, 162].

The original time resolution of the dataset is 20s for two schooldays, and, in order to smoothen the short time noisy dynamics, we perform a temporal coarse-graining

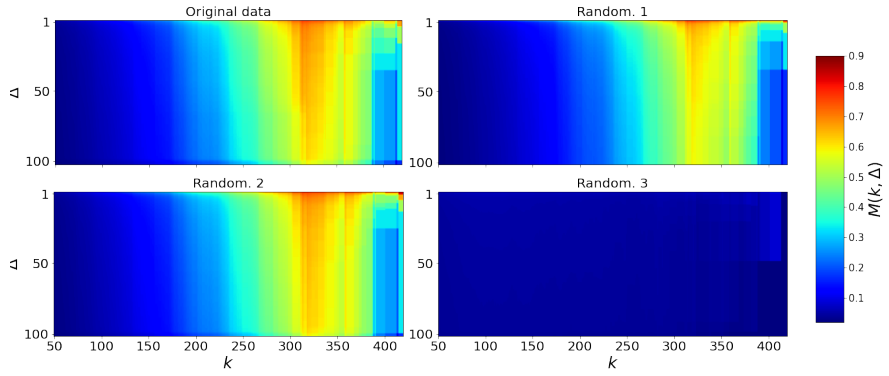

Figure 5.3. – **Air transportation temporal network:** the four plots correspond to the $k-\Delta$ diagrams of the maximal cohesion $M(k,\Delta)$ of the original data set (top left, shown also in Figure 2.a), the *Timestamps reshuffling* (top right, shown also in Figure 2.a) randomization of the temporal network and the *Event* (bottom left) and *Degree-constrained link* reshuffling (bottom right).

on successive time-windows of 5 minutes. We first consider the first school day only, i.e., a temporal network of $N = 242$ nodes and duration $T = 103$ time stamps (each representing a 5-minutes time window). The maximal degree in the aggregated network is $k_{max} = 98$, the minimum and average degrees are $k_{min} = 1$ and $\langle k \rangle = 49$, respectively,

Figure 5.4.a displays the $k-\Delta$ diagrams of $M(k,\Delta)$ for the original temporal network (middle) and its randomized version ($M_{ran}(k,\Delta)$, bottom), with the size of $S_{>k}$ (top panel), as for Fig. 5.2a. At fixed Δ, $M(k,\Delta)$ tends to increase with k; moreover, $M(k,\Delta)$ decreases more slowly with Δ when k increases: nodes with higher degree in the aggregated network tends to be more tightly interconnected, and in a more stable way. For instance, the 7 nodes of $S_{>87}$ keep a maximal cohesion $M(k,\Delta) \gtrsim 0.06$ up to $\Delta = 25$. Notably, these structures disappear in the randomized version of the temporal network, with much lower cohesion values on the whole $k-\Delta$ domain, indicating a temporal rich club ordering in the data. This is confirmed in Figure 5.4.b, which also highlights the differences between static and temporal rich clubs. The top plot displays the normalized static rich club coefficient $\rho(k)$, which is larger than 1 and tends to slightly increase, as with other social networks [48]: the children with a larger diversity of contacts (the degree in the aggregated network is the number of distinct other individuals contacted) tend also to be more interconnected than expected by chance alone. For the temporal rich club coefficient, the ratio $\mu(k,\Delta)$ quantifies moreover the difference in simultaneous interactions with respect to the randomized version: it is higher for larger Δ, as stable simultaneous interactions are disrupted in the null model, remains stable on a broad range of k values, and tends to decrease at larger k. This indicates that the nodes of the temporal network are connected in a much more simultaneous way than expected by chance, especially when considering stable interactions.

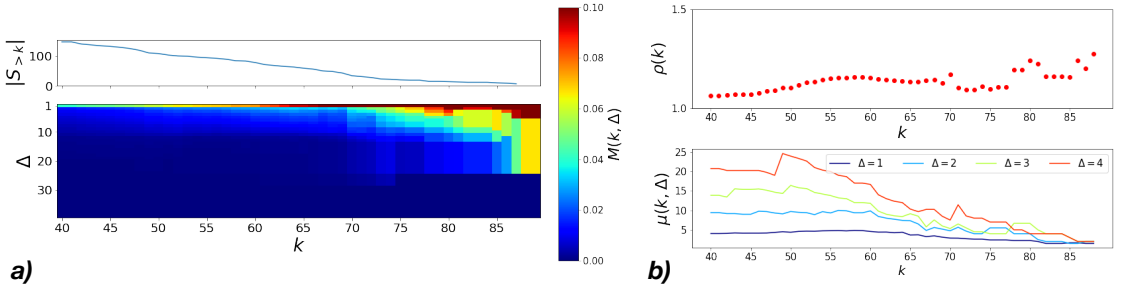

Figure 5.4. – **Primary school temporal network. a)**(top) Size $|S_{>k}|$ of the sub-network of nodes of aggregate degree larger than k as a function of k of the Primary School temporal network; (bottom) Maximal cohesion $M(k,\Delta)$ as a function of k and Δ. **b)** (top) Static rich club coefficient $\rho(k)$ computed for the aggregated graph as a function of the aggregate degree k; (bottom) ratio $\mu(k,\Delta)$ between $M(k,\Delta)$, computed for the data, and $M_{ran}(k,\Delta)$, for different values of Δ.

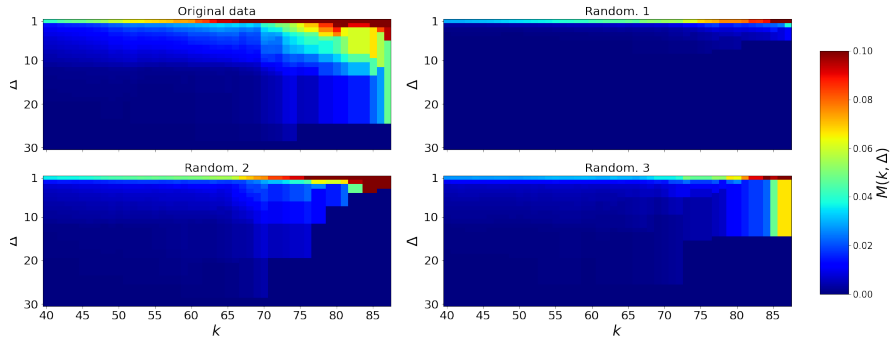

Figure 5.5. – **Primary School temporal network:** the four plots correspond to the $k-\Delta$ diagrams of the maximal cohesion $M(k,\Delta)$ of the original data set (top left), the *Timestamps reshuffling* randomization of the temporal network and the *Event* (bottom left) and *Degree-constrained link* (bottom right) shufflings as described in Chapter 1, section 1.2.4.

In Figure 5.5 we plot the comparison of the k diagrams computed for the empirical data and all of the three randomizations. Furthermore, we compare the results obtained by partially aggregating the original network with a 5 minutes time-resolution (Figure 5.4), taking only into account the first school day, to the $k-\Delta$ diagrams obtained for different values of the parameters of the partial aggregation of the same network: in Figure 5.6 are the $k-\Delta$ diagrams of the empirical network, limited to the first school day, but with 1 minute time-resolution, whereas in Figure 5.7 we analyze the maximal cohesion over 2 school days, with a 5 minutes partial aggregation. These plots highlight the differences in maximal cohesion between the empirical and randomized networks.

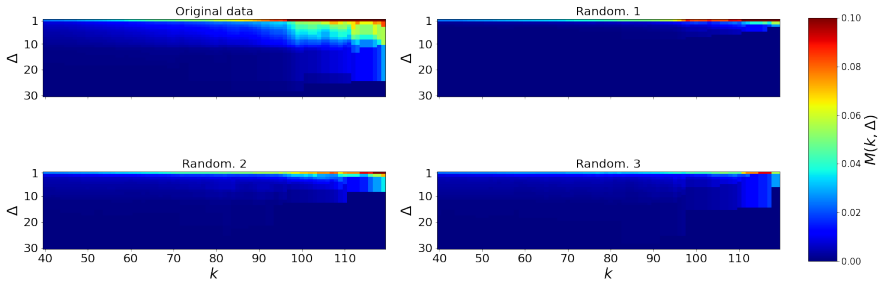

Figure 5.6. – **Primary School temporal network,** 2 **days:** the top left plot corresponds to the $k-\Delta$ diagram of the maximal cohesion $M(k,\Delta)$ of the original data set computed over two school days. The other three plots are the $k-\Delta$ diagram of the maximal cohesion $M(k,\Delta)$ of the *Timestamps reshuffling* (top right) randomization of the temporal network and the *Event* (bottom left) and *Degree-constrained link* (bottom right) shufflings.

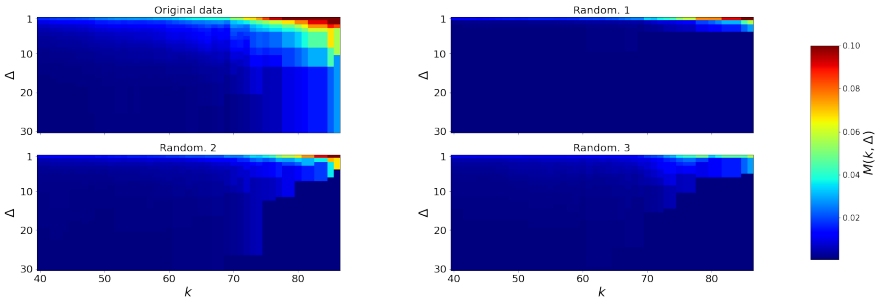

Figure 5.7. – **Primary School temporal network,** 1*st* **day,** 1 **minute time resolution:** the top left plot corresponds to the $k-\Delta$ diagram of the maximal cohesion $M(k,\Delta)$ of the original data set computed over one school day, with a partial time aggregation of 1 minute (3 successive 20s-snapshots). The other three plots are the $k-\Delta$ diagram of the maximal cohesion $M(k,\Delta)$ of the *Timestamps reshuffling* (top right) randomization of the temporal network and the *Event* (bottom left) and *Degree-constrained link* (bottom right) reshufflings.

We investigate the dynamics of the temporal rich club in Figure 5.8.a through the evolution of the instantaneous $\Delta-$cohesion $\epsilon_{>k}(t,\Delta)$ of the 7 nodes with aggregated degree $k>87$ for several values of Δ. We show also for reference the activity timeline of the network: the simultaneous cohesion of these nodes fluctuates strongly, is 0 in many snapshots and reaches its maximum in the periods of high overall activity (namely recess and lunch break [162]), forming a transient but repeated temporal rich club. We have verified that these students actually belong to different school classes, which explains why the moments of highest cohesion of this group can only happen during the breaks.

The temporal network under scrutiny represents interactions among individuals, which can be the support of many processes, and in particular of the spread of information or infectious diseases. It is thus relevant to investigate whether the temporal

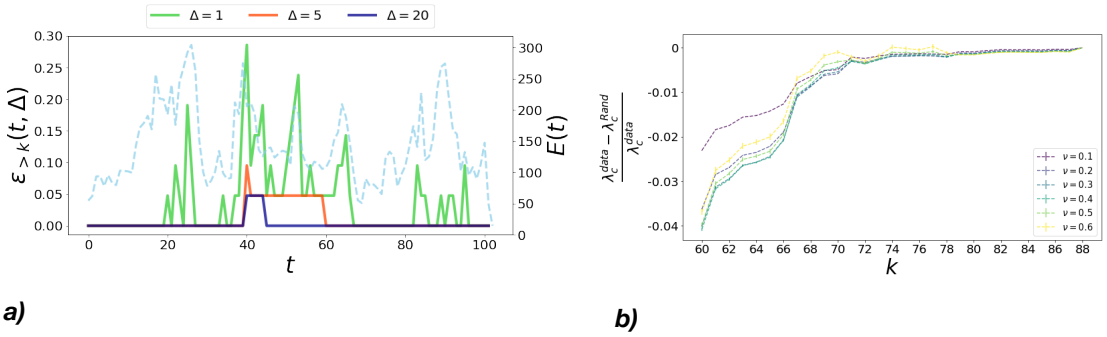

Figure 5.8. – **Primary school temporal network. a)** Instantaneous values of the cohesion $\epsilon_{>87}(t,\Delta)$ of $S_{>k}$ for various values of the temporal resolution Δ, together with the instantaneous number of edges of the network $E(t)$ (dashed blue line). **b)** Relative difference between the epidemic threshold λ_c^{data}, computed for the original dataset, and λ_c^{rand}, computed after the randomization of the interactions between the nodes of $S_{>k}$.

rich club ordering plays a role in the unfolding of such processes, as with other temporal structures [44]. We therefore consider the paradigmatic susceptible-infected-susceptible (SIS) model of spreading processes (see Chapter 1), in which nodes can be either susceptible (S) or infectious (I): a susceptible can become infectious upon contact with an infectious, with probability λ per time step; infectious individuals recover with probability ν at each time step and become susceptible again. We quantify the interplay between the temporal network and the spread by the epidemic threshold λ_c at given ν: it separates a phase at $\lambda < \lambda_c$ in which the epidemic dies out from a phase at $\lambda > \lambda_c$ where it reaches a non-zero fraction of the population. We compute the epidemic threshold, using the method of [168], in (i) the original data set (λ_c^{data}) and (ii) versions of the data set in which the temporal edges connecting the nodes in $S_{>k}$ are randomized (λ_c^{rand}), thus disrupting their simultaneity. Specifically, we apply the timestamps shuffling to these in $S_{>k}$, while keeping all the other temporal edges fixed. The activity timelines of both the whole temporal network and of the nodes of $S_{>k}$ are thus preserved, as well as the structure of the aggregate edges of the subgraph induced by $S_{>k}$. However, the simultaneity of the connections between the nodes of $S_{>k}$ is disrupted (note however that such temporal randomization leaves the static rich club unaltered). Figure 5.8.b displays the relative difference between the two obtained values as a function of k. This difference takes higher absolute values for lower values of k, which can be expected as the randomization affects then a larger number of temporal edges; most importantly, λ_c^{data} is systematically lower than λ_c^{rand}: this indicates that the spreading process is favoured by the temporal rich club of the data, i.e., by the stronger simultaneity of connections than in the randomized versions [122]. The effect is also larger for larger ν, i.e., for faster processes. Cohesive simultaneous structures of prominent nodes in a temporal network, as revealed by the temporal rich club ordering, can thus affect spreading dynamics unfolding on top of the network.

5.4. Temporal rich clubs and network states

We finally investigate the temporal rich club patterns in the information-sharing networks initially analysed in [46], as presented in Chapter 2, and further investigated as described in Chapter 3. We focus our analysis of the information-sharing network extracted for one particular recording (the same recording for which the results shown in Figures 3.4, 3.5, 3.6A-C). Thus, the network analysed here is made of $N = 67$ nodes. Each temporal edge represents a "functional connection", i.e. the existence of a significant mutual information (equation 2.2) between the firing patterns of the corresponding pair of neurons computed in a sliding window of 10 seconds. Successive time windows are shifted of 1 second: this is the temporal resolution of the network, which lasts 2284 seconds. We first note that the aggregated network is very dense: the average degree is $\langle k \rangle = 54$ (whereas the minimal value of k is $k_{min} = 14$) and the maximal degree is equal to $N - 1 = 66$. In such a dense network, the static rich club ordering cannot be assessed as randomization of the links of the high degree nodes cannot be achieved. Taking into account temporality reveals a much richer picture. Figure 5.9 shows that the temporal rich club coefficient $M(k, \Delta)$ increases with k for each value of Δ, and that higher values of k are needed to reach a given cohesion when Δ increases: groups of nodes with increasing aggregated degree are simultaneously interconnected for increasing durations. The group of 8 neurons with largest degree (which are each connected at least once over the temporal network duration to each of the other nodes) are in particular very strongly interconnected in a simultaneous way, with $M(k, \Delta) \geq 0.5$ up to $\Delta = 140$. We show in Figure 5.10 that $M_{ran}(k, \Delta)$ takes much smaller values and do not exhibit any relevant structure, indicating the existence of a temporal rich club in this data set.

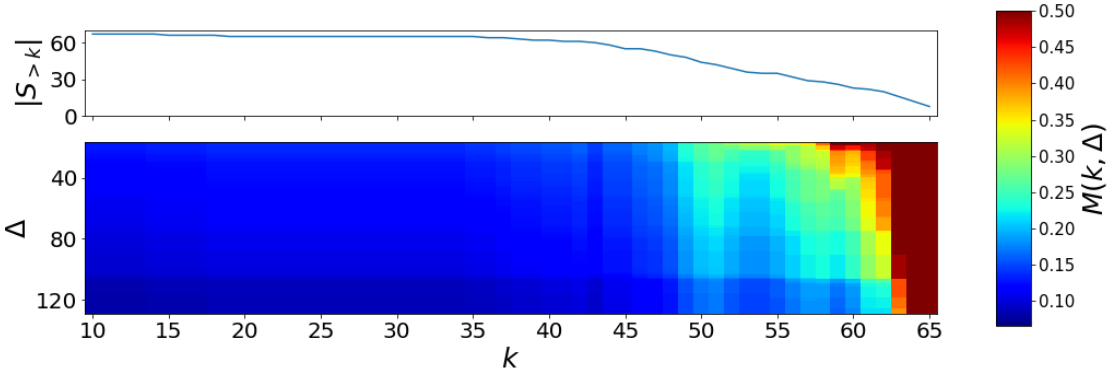

Figure 5.9. – **Temporal network of information sharing neurons.** (top) Size $|S_{>k}|$ of the subnetwork of nodes of aggregate degree larger than k as a function of k; (bottom) Maximal cohesion $M(k, \Delta)$ as a function of k and Δ.

As investigated in Chapter 3, the temporal network of functional connectivity actually goes through several "states", found through the hierarchical clustering of the network similarity matrix shown in Figure 5.11.a [121]: each element (t, t^*) of this matrix gives the similarity between the snapshots of the network at times t and t^*, and

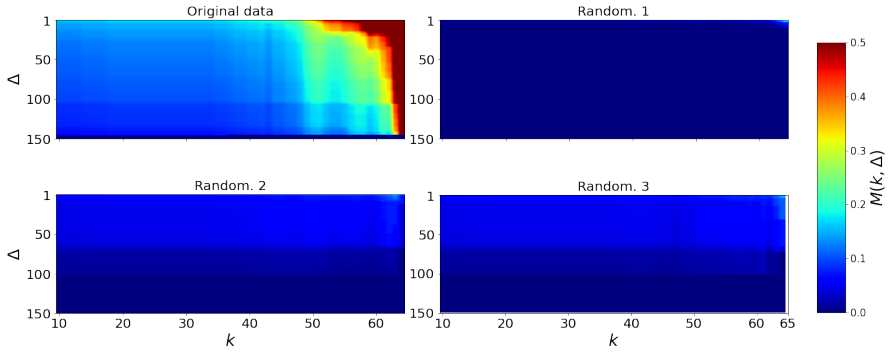

Figure 5.10. – **Neuronal assembly:** the four plots correspond to the $k-\Delta$ diagrams of the maximal cohesion $M(k,\Delta)$ of the original data set (top left, shown also in Figure 4.a), the *Timestamps reshuffling* (top right) randomization of the temporal network and the *Event* (bottom left) and *Degree-constrained link* (bottom right) shufflings.

periods of stability of the network ("states") are found as periods of large similarity values (red blocks along the diagonal). The timeline of successive states is shown in Figure 5.11.b, and Figure 5.11.c shows the instantaneous cohesion $\epsilon_{>65}(t,\Delta=1)$ of the nodes with highest degree in the network aggregated on the whole recording: the cohesion among these nodes changes strongly from one state to another, and actually reach very large values only during one specific state. We thus investigate separately these different states, computing an aggregated network G^s for each state s by aggregating the temporal edges in the snapshots belonging to s, and defining $S^s_{>k}$ as the set of nodes with degree larger than s in G^s: nodes are not similarly active in each state and have thus different degrees in the different G^s. This leads us to measure the state-specific temporal rich club coefficients $M^s(k,\Delta)$.

Figure 5.12.a-b show that the corresponding $k-\Delta$ diagrams for states 1, 3 and 5 have similar but distinct patterns, with in each case more stable simultaneously interconnected sets of nodes as k increases, i.e., a temporal rich club structure (we show in the SI that the randomized data sets yield much lower values of M).

Furthermore, Figure 5.11.d displays the $\Delta-$cohesion over time of the sets of nodes with largest degree in each of these states: notably, this instantaneous cohesion is maximal (and reaches the maximal possible value $\epsilon_{>k}(t,\Delta)=1$) precisely in the time stamps of the corresponding state. Note that the sizes of $|S^1_{>44}|=5$, $|S^3_{>56}|=7$, $|S^5_{>39}|=6$ in the three states are comparable, but that the nodes belonging to these three sets are mostly different: of the nodes in $S^1_{>44}$ only one is also in $S^3_{>56}$, and $S^5_{>39}$ has an empty intersection with the other sets.

Overall, the analysis of this temporal network highlights how a temporal rich club phenomenon can be present even when a static rich club cannot be identified. Moreover, it shows that distinct temporal rich clubs can be found when a temporal network goes through different states. Further investigation of the mutual relations of the state-wise temporal rich clubs could help shed light on the function of the different states of the system, adding to the analysis outlined in Chapter 3.

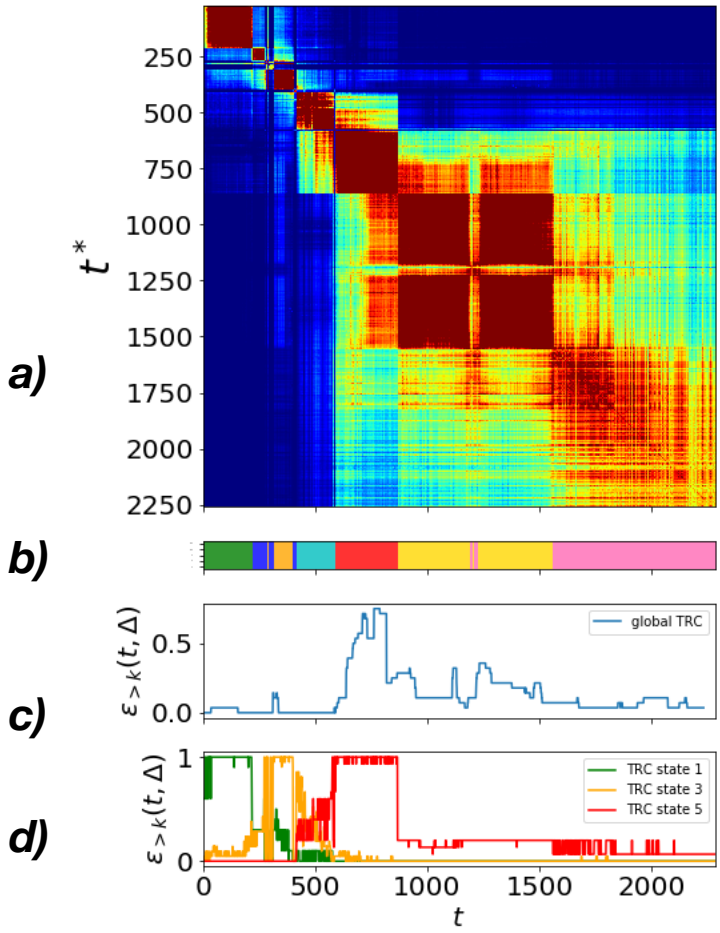

Figure 5.11. – **Temporal network of information sharing neurons.** **a)** Temporal network similarity matrix: the (t, t^*) matrix entry is given by the similarity between the instantaneous snapshots of the network at times t and t^*. The red blocks around the diagonal indicate periods in which the network remains similar to itself, i.e., "states" of the network [122]. **b)** Timeline of the states of the network, represented as a colored barcode (each color represents a different state), as extracted by clustering of the similarity matrix in Chapter 3. **c)** Instantaneous cohesion $\epsilon_{>65}(t,\Delta)$ of the $N_{>65} = 8$ nodes of aggregate degree larger than $k = 65$. **d)** Instantaneous cohesion $\epsilon_{>k}(t,\Delta)$ of the nodes with highest degree in the aggregate graphs of states 1, 3 and 5, as a function of time during the whole recording (respective largest degree values: 45, 57 and 40, same color code as in panel c)); the sets have sizes $|S^1_{>44}| = 5$ (cohesion in green), $|S^3_{>56}| = 7$ (orange) and $|S^5_{>39}| = 7$ (red); $S^1_{>44}$ has 1 node in common with $S^3_{>56}$, and $S^5_{>39}$ has no node in common with $S^1_{>44}$ nor with $S^3_{>56}$.

5.5. Conclusion

In this Chapter I have presented the definition of a novel concept to investigate temporal networks and quantify the patterns of simultaneous interconnectedness

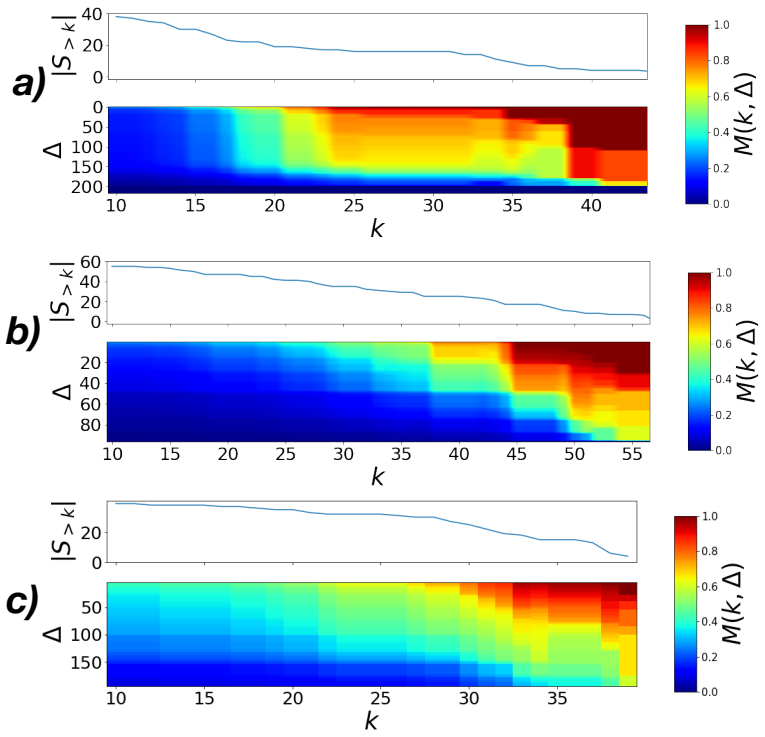

Figure 5.12. – **Temporal network of information sharing neurons. a-b)** For each of the states 1, 3 and 5, size $|S_{>k}|$ as a function of k in the aggregate network of the state, and color-plot of the temporal rich club coefficient $M^s(k,\Delta)$ for the temporal network restricted to the same state.

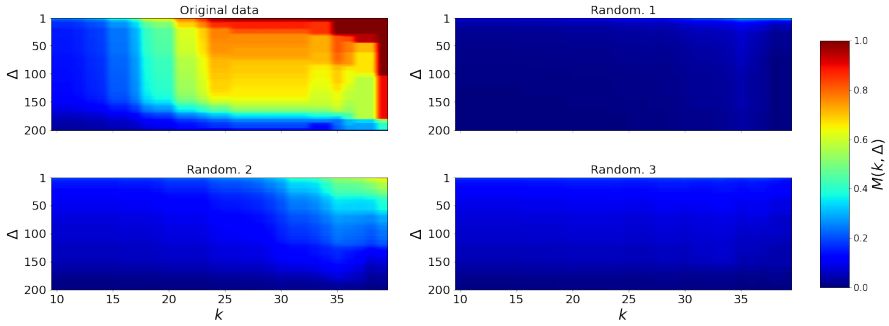

Figure 5.13. – **Network state** 1 **of neuronal assembly:** the four plots correspond to the $k-\Delta$ diagrams of the maximal cohesion $M(k,\Delta)$ computed within network state 1 of the original data set (top left, shown also in Figure 4.f), the *Timestamps reshuffling* (top right) randomization of the state-wise temporal network and the *Event* (bottom left) and *Degree-constrained link* (bottom right) shufflings.

of nodes, namely the Temporal Rich Club. We have defined the temporal rich club

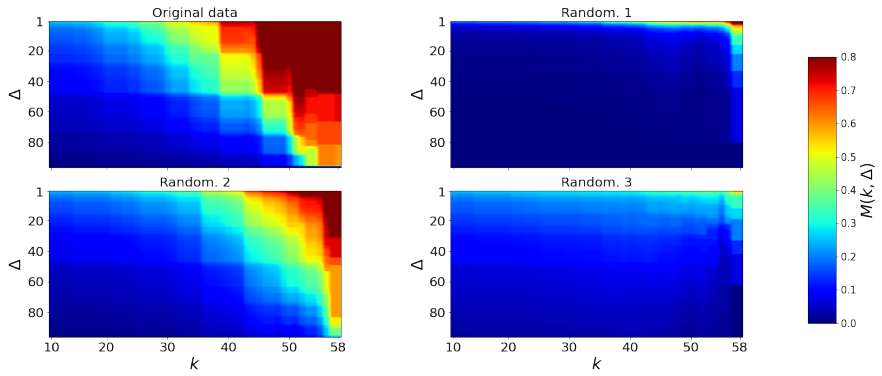

Figure 5.14. – **Network state** 3 **of neuronal assembly:** the four plots correspond to the $k-\Delta$ diagrams of the maximal cohesion $M(k,\Delta)$ computed within network state 3 of the original data set (top left, shown also in Figure 4.g), the *Timestamps reshuffling* (top right) randomization of the state-wise temporal network and the *Event* (bottom left) and *Degree-constrained link* (bottom right) shufflings.

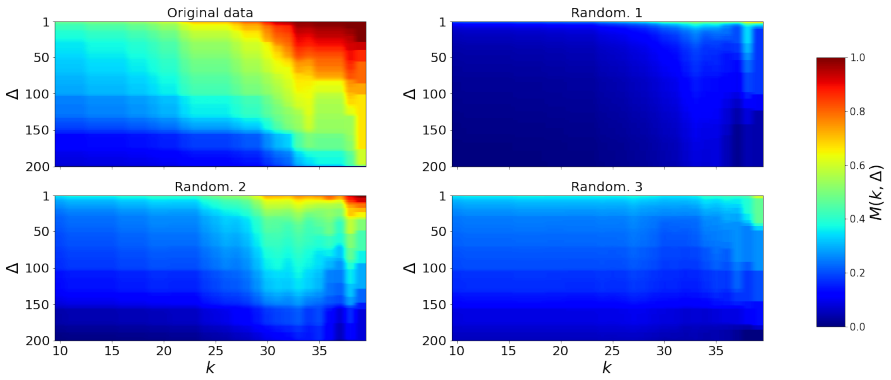

Figure 5.15. – **Network state** 5 **of neuronal assembly:** the four plots correspond to the $k-\Delta$ diagrams of the maximal cohesion $M(k,\Delta)$ computed within network state 5 of the original data set (top left, shown also in Figure 4.h), the *Timestamps reshuffling* (top right) randomization of the state-wise temporal network and the *Event* (bottom left) and *Degree-constrained link* (bottom right) shufflings.

coefficient as the maximal value of the density of links stable during at least a duration Δ between nodes having aggregated degree at least k. For each data set, we compare the empirical values to those reached in randomized versions of the data, in which the activity timeline as well as the properties of the aggregated network (and potentially its whole structure) are preserved, in order to measure whether the simultaneity and stability of the connections of groups of nodes is higher than expected: a temporal rich club ordering corresponds indeed to higher simultaneous cohesion than expected by chance. Note here a delicate point: many randomization procedures are possible

for a temporal network [70], so the comparison with randomized data could be done in several ways. As the focus is on the simultaneity of connections, we have limited ourselves to reshuffling procedures that maintain the network activity timeline and the aggregated properties of the nodes. Other reshuffling methods could however be considered.

In two of the data sets we have explored, both static and temporal rich club ordering were present. In general however, a static rich club in the aggregated graph could exist with or without a temporal rich club, as the links of the static network could correspond to interactions occurring at different times. Vice-versa, interactions could be more simultaneous than expected by chance, with a temporal rich club ordering, without forming a static rich club. This is the case for the network of information-sharing neurons, where the large density of the aggregated network makes the static rich club concept irrelevant, while taking into account temporality reveals a more interesting picture with a temporal rich club ordering.

A limit of our analysis comes from the fact that we have considered the degree of nodes in the aggregate network as the reference for centrality in the aggregate network. A natural extension of our work would be to consider instead the strength of the nodes in the aggregate network, i.e., the number of temporal edges to which they have participated during the span of the temporal network: in this case, the focus would be to investigate the simultaneity of the connections within the set $S_{>s}$ of nodes having participated to more than s temporal edges. As strength and degree are generally correlated, the results are expected to be similar, but some significant and interesting differences might emerge, as in the example of the air transportation temporal network where the reliever airports have a very high degree but relatively low strength.

Overall, the temporal rich club perspective provides a new tool to study temporal networks and in particular to unveil the relevance of simultaneous interactions of increasingly connected nodes in processes unfolding on top of the temporal network: we have shown for instance that a temporal rich club pattern favours spreading dynamics, similarly to other static or temporal cohesive structures [44, 100, 122], suggesting to add such new measure to the repertoire of methods to study contagion processes in networks. Moreover, we have shown how distinct temporal rich club patterns can be found when a temporal network evolves through different states, and provide thus an additional way to characterize such states and, possibly, investigate their function. For instance, I introduced in Chapter 2 how key processes in neural information processing, such as synaptic plasticity, are critically affected by the timing of neuronal interactions [117] and different temporal rich clubs in different states may thus enable flexible computations within a same circuit (in line with [46], as seen in Chapter 2 and with my previous work explored in detail in Chapter 3). In conclusion, this work provides a new procedure to detect relevant temporal and structural patterns in a general temporal network, enabling a new quantitative perspective on the temporal patterns of data sets coming from very different fields, from highlighting the role of simultaneous connections between central nodes in spreading on a temporal network of social interactions to that of hubs in air transportation infrastructures or in neuronal

assemblies.

6. Conclusions and perspectives

This thesis is an attempt to move forward in the hypothesis that the *missing link* between the physical *structure* of brain networks and their *function* lies in the *dynamics* of these systems. We explore this hypothesis with a data-driven, temporal networks approach, through which we find that not only the transient configurations of FC can represent a meaningful observable that relates to brain state and health condition changes: In fact, we show in this work that it is possible to extract discrete epochs of the evolution of a brain temporal network that represent different *dynamical regimes* of the system and thus that dynamics constitutes in itself an informative biomarker.

This is the case for the *network-states* introduced in Chapter 3, identified by the rate of change, the *liquidity*, of the network. Analogously, the *allegiance-states* that we define in Chapter 4 correspond to different regimes in which pairs of nodes *move*, more or less coherently, around the different communities in time. Furthermore, the states are characterised by clearly different values of the rate of change of the FC, the *dFC-speed*, which in turn suggests that we are not dealing with a set of different "frozen" structures, but that each state could instead be seen as a different way of the system to explore the ensemble of the possible configurations of FCs. The rate of the variability of the temporal network itself is what we conceive as the fundamental criterion to identify a network- or allegiance-state: this variability can resemble the motion of a viscous fluid, as we see in the *seizure* state in Chapter 4, where the overall dynamics is slowed down, or it could be more like the motion of free particles in a gas, as it seems to be the case in the baseline allegiance state, which has faster dynamics. Thus network dynamics is not noise on top of static functional architectures but a functional mechanism by itself (what matters is not only how networks are but also how networks change): this implies that alterations of dynamics may lead to dysfunction. This is what we start seeing when looking at epilepsy, in Chapter 4, where two of the identified allegiance states coincide with the language impairments of aphasic epileptic patients. This evidence opens promising avenues for the design of novel, sensitive biomarkers that capture the different dynamical styles displayed by brain networks during their evolution. This will be possible only having the right tools to decsribe not only the spatial organization networks but also the spatiotemporal organization of their flow of reconfiguration.

Beyond the detection of these dynamical regimes that a time-varying functional network *visits* throughout its evolution we also show how one can dig deeper and further characterise a state by "zooming in" at the network node level. Interestingly, in Chapter 3 we find that common behaviors, *connectivity styles*, of nodes can be

found across different states. Even though the quantities that we measure and use to define a *connectivity profile* are indeed the result of a temporal aggregation over the time-stamps belonging to a network-state, they represent statistics that inform about the dynamics of a node: the number of times that it was active throughout a state, along with the burstiness of its activity as well as the rate of change of its neighborhood. Therefore the connectivity styles also represent different common *dynamical* profiles of a node. Nodes in the case of Chapter 3 are neurons, and the temporal network in which they are involved is what we take as a proxy of the ongoing exchange of information between them. Therefore it is reasonable to interpret the connectivity styles as different typical ways in which a neuron can be involved in the processing of a specific information. The finding that a neuron can display what we define a *core* connectivity profile within a state, only to then result as a *peripheral* node in another state, and that all connectivity styles are distributed equally across morphologically and anatomically different groups, is another hint that, possibly, the anatomy and physiology are not sufficient to explain the *function* of a node. Instead the function of a node could be the transient result of an emerging (and evolving) need of the collective, the overall network, to "assign" that function to one of its elements.

In Chapter 5 I have described our work aimed at investigating the dynamics of the connections of a temporal network, and the emergence of temporally cohesive structure. We have introduced the novel definition of the *Temporal Rich Club* and shown that our definition enables to discern groups of highly connected nodes in the time-aggregated representation of the network from a purely temporal structure, that can only be detected when taking into account the simultaneity of the connections of its members. We have shown the efficacy of this measure to distinguish between transient and persistent temporal rich clubs, in the context of an air transportation network. We have described how the existence of a temporal rich club can be important in the spreading of a disease in a network of social contacts and, in continuity with the studies described in Chapters 3 and 4, we have found that the emergence of transient temporal rich clubs is also related to the different states of its evolution. In particular, the two studies in chapters 3 and 5 seem to converge on a specific point: the emergence of temporally cohesive groups of highly connected nodes that only last throughout a specific network-state that have almost zero overlap from one state to the other, seems to reinforce that indeed *important* nodes, neurons, change from state to state. As a future perspective it would be interesting to further investigate the relation between temporal rich clubs and cell assemblies in neuronal networks. Future research in this direction could be aimed at modeling the exchange of information among spiking neurons as a diffusion process on a temporal network, and it would be interesting to see what could be the role, function of such a structure in this process. At a larger scale, it could be important to relate the rich-club organization of connectomes to the temporal rich club analysis of the corresponding time-varying functional connectivity. Another interesting research line could investigate the emergence of temporal rich clubs to the *dynamical style* of the network: can we detect a cohesive and persistent temporal rich club in a network with a high rate of change

of its connections? Could there be a slow dynamical regime of the network where nevertheless no temporal rich club can be identified?

To summarize, in systems neuroscience theories have often supposed static functional architectures and the use of static network theoretic tools has confirmed these theories in a partially limited way, as such tools could not capture more complex dynamics. A data-driven approach that takes into account not only space but also time can capture underlying properties going beyond these static theories and thus introduce a paradigm shift: dynamics ceases to be noise on top of static entities, to become a functional structure and resource. This thesis proposes a few important steps in this direction, describing how temporal networks represent a suitable methodological framework to this aim.

Data driven approaches that study the functional connectivity in the brain encounter nonetheless some fundamental issues: the choice of a metric for the estimation of the FC and the extraction of windowed streams of FCs is the first step of the analysis, but one then needs to discern the *significance* of the measured functional edges, also with respect to the length of the chosen time-window. Studies showed the need for great amounts of data to properly estimate information-theoretic measures of, for instance, directed functional connectivity (Transfer Entropy, TE) [172, 177]. In neuroimaging rigorous approaches have been introduced to quantify the minimal amount of data needed for network identification, such as to recognize that two network measurements are a measurement of the same functional network (for instance, resting-state FC of a given subject). This test-retest reliability for static networks was studied e.g. systematically in [164], where it was shown that global and local graph metrics were variably reliable, depending on the duration of the fMRI scan of patients (time-window length for the computation of the FC) and the sample size (number of patients). For the estimation of temporal networks little is known and we do not have rules of thumb yet. We have used pseudo-directed lagged MI (Chapter 3), rather than genuinely directed TE, because it should require less data given the smaller dimensionality of joint probability densities to sample. For the coherence (Chapter 4), windows are way shorter than classical long windows, however by averaging on broad bands and windows rather than using exact time-frequency points we make some form of denoising. Overall, in our work, we do not pay particular attention to the actual values of FC links, but rather we study their inter-relations (cosine-distance/similarity is insensitive to global rescaling and global fluctuations of average weights), so, if the bias is not link specific, wrong quantititative estimation do not affect the assessment of the relative strengths of different links. Furthermore, when studying temporal networks one needs many instantaneous snap-shots. To improve network reliability one needs longer windows, but this reduces the number of windows. So there must be an optimal tradeoff when doing space-time estimation, rather than just space estimation. Future studies will have to clarify this important point. In both chapters 3 and 4 we don't commit on the values of time-resolved FC being measures of some information flow in exact quantitative units, rather we evaluate these numbers pretty much as

"machine-learning features", i.e. operationally well-defined quantities that still serve as numeric markers of a state of interaction.

In my personal opinion, the future challenges of the application of temporal networks approaches in systems neuroscience lie in the needed effort to integrate into a common, broader picture the intensive research that has been dedicated to describe the connectivity, structural and functional, in the brain. I believe a possible step forward in this direction could be achieved by representing the different types of networks, from the genetic networks "all the way up" to whole-brain functional networks, as time-varying multilayer networks. Furthermore, one could think of networks of social interactions as the ultimate, largest possible scale (layer) related to human behavior. Aiming at such formidable task could at the very least motivate attempted answers to complex questions, that could in turn help us rethink even some fundamental concepts in network science: for instance, "can we define a multi-layer, temporal community in a network where each layer represents a different spatial or temporal scale?", "if so, what is its meaning?". I therefore conclude this manuscript stressing how data driven approaches can represent not only a powerful way to describe real complex systems, but can help to develop new theoretical tools to further investigate the world where we live in and, possibly, to have a clearer vision of how we want it to be.

Bibliography

[1] Moshe Abeles. *Local Cortical Circuits, An Electrophysiological Study*. Berlin: Springer, 1982 (cit. on pp. 58, 59, 102).

[2] Sophie Achard and Ed Bullmore. "Efficiency and Cost of Economical Brain Functional Networks". In: *PLOS Computational Biology* 3.2 (Feb. 2007), pp. 1–10. DOI: 10.1371/journal.pcbi.0030017. URL: https://doi.org/10.1371/journal.pcbi.0030017 (cit. on pp. 47, 48).

[3] Sophie Achard, Chantal Delon-Martin, Petra E. Vértes, et al. "Hubs of brain functional networks are radically reorganized in comatose patients". In: *Proceedings of the National Academy of Sciences* 109.50 (2012), pp. 20608–20613. ISSN: 0027-8424. DOI: 10.1073/pnas.1208933109. eprint: https://www.pnas.org/content/109/50/20608.full.pdf. URL: https://www.pnas.org/content/109/50/20608 (cit. on p. 48).

[4] Sophie Achard, Raymond Salvador, Brandon Whitcher, et al. "A Resilient, Low-Frequency, Small-World Human Brain Functional Network with Highly Connected Association Cortical Hubs". In: *Journal of Neuroscience* 26.1 (2006), pp. 63–72. ISSN: 0270-6474. DOI: 10.1523/JNEUROSCI.3874-05.2006. eprint: https://www.jneurosci.org/content/26/1/63.full.pdf. URL: https://www.jneurosci.org/content/26/1/63 (cit. on pp. 46, 47).

[5] Réka Albert and Albert-László Barabási. "Statistical mechanics of complex networks". In: *Rev. Mod. Phys.* 74 (1 Jan. 2002), pp. 47–97. DOI: 10.1103/RevModPhys.74.47. URL: https://link.aps.org/doi/10.1103/RevModPhys.74.47 (cit. on p. 137).

[6] José Ignacio Alvarez-Hamelin, Luca Dall'Asta, Alain Barrat, et al. "K-core decomposition of Internet graphs: hierarchies, self-similarity and measurement biases". In: *Networks and Heterogeneous Media* 3 (Apr. 2008), p. 371. URL: https://hal.archives-ouvertes.fr/hal-00012974 (cit. on pp. 24, 25, 137).

[7] Daniel J. Amit. *Modeling Brain Function&Mdash;the World of Attractor Neural Networks*. New York, NY, USA: Cambridge University Press, 1989. ISBN: 0-521-36100-1 (cit. on p. 105).

[8] Alessandra Angelucci, Jonathan B. Levitt, Emma J. S. Walton, et al. "Circuits for Local and Global Signal Integration in Primary Visual Cortex". In: *Journal of Neuroscience* 22.19 (2002), pp. 8633–8646. ISSN: 0270-6474. DOI: 10.1523/JNEUROSCI.22-19-08633.2002. eprint: https://www.jneurosci.org/

content/22/19/8633.full.pdf. URL: https://www.jneurosci.org/content/22/19/8633 (cit. on p. 42).

[9] Lucas Arbabyazd, Kelly Shen, Zheng Wang, et al. "Virtual Connectomic Datasets in Alzheimer's Disease and Aging Using Whole-Brain Network Dynamics Modelling". In: *eNeuro* 8.4 (2021). DOI: 10.1523/ENEURO.0475-20.2021. eprint: https://www.eneuro.org/content/8/4/ENEURO.0475-20.2021.full.pdf. URL: https://www.eneuro.org/content/8/4/ENEURO.0475-20.2021 (cit. on p. 52).

[10] Andrea Avena-Koenigsberger, Bratislav Misic, and Olaf Sporns. "Communication dynamics in complex brain networks." In: *Nature reviews. Neuroscience* 19.1 (2017), pp. 17–33. ISSN: 1471-003X. DOI: 10.1038/nrn.2017.149 (cit. on p. 103).

[11] S. Kathleen Bandt, Pierre Besson, Ben Ridley, et al. "Connectivity strength, time lag structure and the epilepsy network in resting-state fMRI". In: *NeuroImage: Clinical* 24 (2019), p. 102035. ISSN: 2213-1582. DOI: https://doi.org/10.1016/j.nicl.2019.102035. URL: https://www.sciencedirect.com/science/article/pii/S2213158219303833 (cit. on p. 68).

[12] Albert-László Barabási and Márton Pósfai. *Network science*. Cambridge: Cambridge University Press, 2016. ISBN: 9781107076266 1107076269. URL: http://barabasi.com/networksciencebook/ (cit. on p. 23).

[13] Pascal Barone, Alexandre Batardiere, Kenneth Knoblauch, et al. "Laminar Distribution of Neurons in Extrastriate Areas Projecting to Visual Areas V1 and V4 Correlates with the Hierarchical Rank and Indicates the Operation of a Distance Rule". In: *Journal of Neuroscience* 20.9 (2000), pp. 3263–3281. ISSN: 0270-6474. DOI: 10.1523/JNEUROSCI.20-09-03263.2000. eprint: https://www.jneurosci.org/content/20/9/3263.full.pdf. URL: https://www.jneurosci.org/content/20/9/3263 (cit. on p. 42).

[14] Fabiano Baroni, Benjamin Morillon, AgnÃšs TrÃ©buchon, et al. "Converging intracortical signatures of two separated processing timescales in human early auditory cortex". In: *NeuroImage* 218 (2020), p. 116882. ISSN: 1053-8119. DOI: https://doi.org/10.1016/j.neuroimage.2020.116882. URL: https://www.sciencedirect.com/science/article/pii/S1053811920303682 (cit. on p. 70).

[15] A. Barrat, M. Barthélemy, R. Pastor-Satorras, et al. "The architecture of complex weighted networks". In: *Proceedings of the National Academy of Sciences* 101.11 (2004), pp. 3747–3752. ISSN: 0027-8424. DOI: 10.1073/pnas.0400087101. eprint: https://www.pnas.org/content/101/11/3747.full.pdf. URL: https://www.pnas.org/content/101/11/3747 (cit. on p. 20).

[16] Alain Barrat, Marc Barthelemy, and Alessandro Vespignani. *Dynamical processes on complex networks*. Cambridge university press, 2008 (cit. on pp. 36, 137).

[17] Fabrice Bartolomei, Maxime Guye, and Fabrice Wendling. "Abnormal binding and disruption in large scale networks involved in human partial seizures". In: *EPJ Nonlinear Biomedical Physics* 1.1 (2013), p. 4 (cit. on p. 67).

[18] Fabrice Bartolomei, Stanislas Lagarde, Fabrice Wendling, et al. "Defining epileptogenic networks: Contribution of SEEG and signal analysis". In: *Epilepsia* 58.7 (2017), pp. 1131–1147. DOI: https://doi.org/10.1111/epi.13791. eprint: https://onlinelibrary.wiley.com/doi/pdf/10.1111/epi.13791. URL: https://onlinelibrary.wiley.com/doi/abs/10.1111/epi.13791 (cit. on pp. 67, 68).

[19] Danielle S Bassett and Marcelo G Mattar. "A network neuroscience of human learning: potential to inform quantitative theories of brain and behavior". In: *Trends in cognitive sciences* 21.4 (2017), pp. 250–264 (cit. on p. 35).

[20] Danielle S Bassett, Nicholas F Wymbs, Mason A Porter, et al. "Dynamic reconfiguration of human brain networks during learning". In: *Proceedings of the National Academy of Sciences* 108.18 (2011), pp. 7641–7646 (cit. on pp. 46, 55).

[21] Danielle S Bassett, Nicholas F Wymbs, M Puck Rombach, et al. "Task-based core-periphery organization of human brain dynamics". In: *PLoS Computational Biology* 9.9 (2013), e1003171 (cit. on p. 103).

[22] Danielle S. Bassett, Mason A. Porter, Nicholas F. Wymbs, et al. "Robust detection of dynamic community structure in networks". In: *Chaos: An Interdisciplinary Journal of Nonlinear Science* 23.1 (2013), p. 013142. DOI: 10.1063/1.4790830. eprint: https://doi.org/10.1063/1.4790830. URL: https://doi.org/10.1063/1.4790830 (cit. on pp. 35, 36).

[23] Danielle Smith Bassett and Ed Bullmore. "Small-World Brain Networks". In: *The Neuroscientist* 12.6 (2006). PMID: 17079517, pp. 512–523. DOI: 10.1177/1073858406293182. eprint: https://doi.org/10.1177/1073858406293182. URL: https://doi.org/10.1177/1073858406293182 (cit. on p. 43).

[24] Demian Battaglia. "Function Follows Dynamics: State-Dependency of Directed Functional Influences". In: *Directed Information Measures in Neuroscience*. Ed. by Michael Wibral, Raul Vicente, and Joseph T. Lizier. Berlin, Heidelberg: Springer Berlin Heidelberg, 2014, pp. 111–135. ISBN: 978-3-642-54474-3. DOI: 10.1007/978-3-642-54474-3_5 (cit. on p. 50).

[25] Demian Battaglia, Thomas Boudou, Enrique C.A. Hansen, et al. "Dynamic Functional Connectivity between order and randomness and its evolution across the human adult lifespan". In: *NeuroImage* 222 (2020), p. 117156. ISSN: 1053-8119. DOI: https://doi.org/10.1016/j.neuroimage.2020.117156. URL: https://www.sciencedirect.com/science/article/pii/S105381192030642X (cit. on pp. 53, 56, 58, 115).

[26] Demian Battaglia and Andrea Brovelli. "Functional connectivity and neuronal dynamics: insights from computational methods". In: *The Cognitive Neurosciences, Sixth Edition*. Ed. by George R. Mangun David Poeppel and Michael S. Gazzaniga. May 2020. URL: https://hal.archives-ouvertes.fr/hal-02304918 (cit. on pp. 50, 51).

[27] Demian Battaglia, Anastassios Karagiannis, Thierry Gallopin, et al. "Beyond the frontiers of neuronal types." In: *Frontiers in Neural Circuits* 7 (2013), p. 13. DOI: 10.3389/fncir.2013.00013 (cit. on p. 91).

[28] Federico Battiston, Jeremy Guillon, Mario Chavez, et al. "Multiplex core-periphery organization of the human connectome". In: *Journal of The Royal Society Interface* 15.146 (2018), p. 20180514. ISSN: 1742-5689. DOI: 10.1098/rsif.2018.0514. eprint: 1801.01913 (cit. on p. 103).

[29] Vincent D Blondel, Jean-Loup Guillaume, Renaud Lambiotte, et al. "Fast unfolding of communities in large networks". In: *Journal of Statistical Mechanics: Theory and Experiment* 2008.10 (Oct. 2008), P10008. DOI: 10.1088/1742-5468/2008/10/p10008. URL: https://doi.org/10.1088/1742-5468/2008/10/p10008 (cit. on p. 25).

[30] Marco Bocchio, Claire Gouny, David Angulo-Garcia, et al. "Hippocampal hub neurons maintain distinct connectivity throughout their lifetime". In: *Nature communications* 11.1 (2020), pp. 1–19 (cit. on p. 62).

[31] Davi D. Bock, Wei-Chung Allen Lee, Aaron M. Kerlin, et al. "Network anatomy and in vivo physiology of visual cortical neurons". In: *Nature* 471.7337 (2011), pp. 177–182 (cit. on p. 42).

[32] P Bonifazi, M Goldin, M A Picardo, et al. "GABAergic hub neurons orchestrate synchrony in developing hippocampal networks." In: *Science* 326.5958 (2009), p. 1419 1424. ISSN: 0036-8075. DOI: 10.1126/science.1175509 (cit. on pp. 61, 105).

[33] Sam A. Booker and Imre Vida. "Morphological diversity and connectivity of hippocampal interneurons". In: *Cell and Tissue Research* 373.3 (2018), pp. 619–641. ISSN: 0302-766X. DOI: 10.1007/s00441-018-2882-2 (cit. on p. 105).

[34] Urs Braun, Axel Schäfer, Henrik Walter, et al. "Dynamic reconfiguration of frontal brain networks during executive cognition in humans." In: *PNAS* 112.37 (2015), pp. 11678–11683 (cit. on pp. 55, 56, 137).

[35] Andrea Brovelli, Mingzhou Ding, Anders Ledberg, et al. "Beta oscillations in a large-scale sensorimotor cortical network: Directional influences revealed by Granger causality". In: *Proceedings of the National Academy of Sciences* 101.26 (2004), pp. 9849–9854. ISSN: 0027-8424. DOI: 10.1073/pnas.0308538101. eprint: https://www.pnas.org/content/101/26/9849.full.pdf. URL: https://www.pnas.org/content/101/26/9849 (cit. on p. 49).

[36] Nicolas Brunel and Xiao-Jing Wang. "What Determines the Frequency of Fast Network Oscillations With Irregular Neural Discharges? I. Synaptic Dynamics and Excitation-Inhibition Balance". In: *Journal of Neurophysiology* 90.1 (2003). PMID: 12611969, pp. 415–430. DOI: 10.1152/jn.01095.2002. eprint: https://doi.org/10.1152/jn.01095.2002. URL: https://doi.org/10.1152/jn.01095.2002 (cit. on p. 45).

[37] Ed Bullmore and Olaf Sporns. "Complex brain networks: graph theoretical analysis of structural and functional systems". In: *Nature Reviews Neuroscience* 10.3 (2009), pp. 186–198 (cit. on p. 43).

[38] György Buzsáki. *Rhythms of the Brain*. New York, NY, USA: Oxf University Press, 2006 (cit. on pp. 45, 61, 105).

[39] György Buzsáki. "Neural Syntax: Cell Assemblies, Synapsembles, and Readers". In: *Neuron* 68.3 (2010), pp. 362–385. ISSN: 0896-6273. DOI: 10.1016/j.neuron.2010.09.023 (cit. on p. 103).

[40] György Buzsáki and Edvard I Moser. "Memory, navigation and theta rhythm in the hippocampal-entorhinal system." In: *Nature Neuroscience* 16.2 (2013), p. 130 138. ISSN: 1546-1726. DOI: 10.1038/nn.3304 (cit. on p. 61).

[41] Vince D Calhoun, Robyn Miller, Godfrey Pearlson, et al. "The chronnectome: time-varying connectivity networks as the next frontier in fMRI data discovery". In: *Neuron* 84.2 (2014), pp. 262–274 (cit. on pp. 54, 127).

[42] Ryan T Canolty and Robert T Knight. "The functional role of cross-frequency coupling." In: *Trends in cognitive sciences* 14.11 (Nov. 2010), pp. 506–515 (cit. on p. 131).

[43] Ciro Cattuto, Wouter Van den Broeck, Alain Barrat, et al. "Dynamics of Person-to-Person Interactions from Distributed RFID Sensor Networks". In: *PLOS ONE* 5.7 (July 2010), pp. 1–9. DOI: 10.1371/journal.pone.0011596. URL: https://doi.org/10.1371/journal.pone.0011596 (cit. on p. 143).

[44] Martino Ciaperoni, Edoardo Galimberti, Francesco Bonchi, et al. "Relevance of temporal cores for epidemic spread in temporal networks". In: *Scientific Reports* 10.1 (2020), p. 12529. DOI: 10.1038/s41598-020-69464-3. URL: https://doi.org/10.1038/s41598-020-69464-3 (cit. on pp. 33, 137, 147, 153).

[45] Wesley Clawson, Tanguy Madec, Antoine Ghestem, et al. "Disordered information processing dynamics in experimental epilepsy". In: *bioRxiv* (2021). DOI: 10.1101/2021.02.11.430768. eprint: https://www.biorxiv.org/content/early/2021/02/12/2021.02.11.430768.full.pdf. URL: https://www.biorxiv.org/content/early/2021/02/12/2021.02.11.430768 (cit. on pp. 73, 74, 100).

[46] Wesley Clawson, Ana F Vicente, Maëva Ferraris, et al. "Computing hubs in the hippocampus and cortex." In: *Science advances* 5.6 (June 2019), eaax4843 (cit. on pp. 61–67, 74, 101, 116, 148, 153).

[47] Wesley Clawson, Ana F. Vicente, Maëva Ferraris, et al. “Computing hubs in the hippocampus and cortex”. In: *Science Advances* 5.6 (2019) (cit. on pp. 99, 105, 106).

[48] V. Colizza, A. Flammini, M. A. Serrano, et al. “Detecting rich-club ordering in complex networks”. In: *Nature Physics* 2.2 (2006), pp. 110–115 (cit. on pp. 26–29, 137, 138, 142–144).

[49] Michele Coscia. *The Atlas for the Aspiring Network Scientist*. 2021. arXiv: 2101.00863 [cs.CY] (cit. on pp. 22, 23, 27).

[50] Michele Coscia, Fosca Giannotti, and Dino Pedreschi. “A classification for community discovery methods in complex networks”. In: *Statistical Analysis and Data Mining: The ASA Data Science Journal* 4.5 (2011), pp. 512–546. DOI: https://doi.org/10.1002/sam.10133. eprint: https://onlinelibrary.wiley.com/doi/pdf/10.1002/sam.10133. URL: https://onlinelibrary.wiley.com/doi/abs/10.1002/sam.10133 (cit. on p. 26).

[51] Rosa Cossart. “Operational hub cells: a morpho-physiologically diverse class of GABAergic neurons united by a common function.” In: *Current opinion in neurobiology* 26 (2014), p. 51 56. ISSN: 0959-4388. DOI: 10.1016/j.conb.2013.12.002 (cit. on pp. 62, 105).

[52] Sandra Courtens, Bruno Colombet, AgnÃšs TrÃ©buchon, et al. “Graph Measures of Node Strength for Characterizing Preictal Synchrony in Partial Epilepsy”. In: *Brain Connectivity* 6.7 (2016). PMID: 27140287, pp. 530–539. DOI: 10.1089/brain.2015.0397. eprint: https://doi.org/10.1089/brain.2015.0397. URL: https://doi.org/10.1089/brain.2015.0397 (cit. on p. 68).

[53] Peter Csermely, András London, Ling-Yun Wu, et al. “Structure and dynamics of core/periphery networks”. In: *Journal of Complex Networks* 1.2 (Oct. 2013), pp. 93–123 (cit. on p. 26).

[54] Gustavo Deco, Viktor K. Jirsa, and Anthony R. McIntosh. “Emerging concepts for the dynamical organization of resting-state activity in the brain”. In: *Nature Reviews Neuroscience* 12.1 (2011), pp. 43–56 (cit. on p. 51).

[55] Gustavo Deco, Giulio Tononi, Melanie Boly, et al. “Rethinking segregation and integration: contributions of whole-brain modelling.” In: *Nature Reviews Neuroscience* 16.7 (2015), p. 430 439. ISSN: 1471-003x. DOI: 10.1038/nrn3963 (cit. on p. 103).

[56] Fabio Della Rossa, Fabio Dercole, and Carlo Piccardi. “Profiling core-periphery network structure by random walkers”. In: *Scientific reports* 3 (Mar. 2013), p. 1467 (cit. on pp. 77, 79, 103).

[57] S. N. Dorogovtsev, A. V. Goltsev, and J. F. F. Mendes. “k-Core Organization of Complex Networks”. In: *Phys. Rev. Lett.* 96 (4 Feb. 2006), p. 040601. DOI: 10.1103/PhysRevLett.96.040601. URL: https://link.aps.org/doi/10.1103/PhysRevLett.96.040601 (cit. on p. 24).

[58] S. N. Dorogovtsev and J. F. F. Mendes. *Evolution of networks: From biological nets to the Internet and WWW*. Oxford: Oxford University Press, 2003 (cit. on p. 19).

[59] Vincent Douchamps, Ali Jeewajee, Pam Blundell, et al. "Evidence for encoding versus retrieval scheduling in the hippocampus by theta phase and acetylcholine." In: *The Journal of neuroscience : the official journal of the Society for Neuroscience* 33.20 (2013), pp. 8689–704. ISSN: 0270-6474. DOI: 10.1523/jneurosci.4483-12.2013 (cit. on p. 104).

[60] Vıctor M. Eguluz and Konstantin Klemm. "Epidemic Threshold in Structured Scale-Free Networks". In: *Phys. Rev. Lett.* 89 (10 Aug. 2002), p. 108701. DOI: 10.1103/PhysRevLett.89.108701. URL: https://link.aps.org/doi/10.1103/PhysRevLett.89.108701 (cit. on p. 38).

[61] P. Erdos and A. Rènyi. "On the evolution of random graphs:" in: *The Structure and Dynamics of Networks*. Princeton University Press, 1960, pp. 38–82. DOI: doi:10.1515/9781400841356.38. URL: https://doi.org/10.1515/9781400841356.38 (cit. on p. 23).

[62] Alexia Fasola, F.-Xavier Alario, Marion Tellier, et al. "A description of verbal and gestural communication during postictal aphasia". In: *Epilepsy Behavior* 102 (2020), p. 106646. ISSN: 1525-5050. DOI: https://doi.org/10.1016/j.yebeh.2019.106646. URL: https://www.sciencedirect.com/science/article/pii/S1525505019305906 (cit. on p. 71).

[63] David Forsyth. *Probability and statistics for computer science*. Berlin: Springer, 2018 (cit. on p. 91).

[64] Santo Fortunato. "Community detection in graphs". In: *Physics Reports* 486.3 (2010), pp. 75–174. ISSN: 0370-1573. DOI: https://doi.org/10.1016/j.physrep.2009.11.002. URL: http://www.sciencedirect.com/science/article/pii/S0370157309002841 (cit. on pp. 24, 25, 112).

[65] Angela D. Friederici. "The Brain Basis of Language Processing: From Structure to Function". In: *Physiological Reviews* 91.4 (2011). PMID: 22013214, pp. 1357–1392. DOI: 10.1152/physrev.00006.2011. eprint: https://doi.org/10.1152/physrev.00006.2011. URL: https://doi.org/10.1152/physrev.00006.2011 (cit. on p. 69).

[66] Pascal Fries. "Rhythms for Cognition: Communication through Coherence". In: *Neuron* 88.1 (2015), pp. 220–235. ISSN: 0896-6273. DOI: https://doi.org/10.1016/j.neuron.2015.09.034. URL: https://www.sciencedirect.com/science/article/pii/S0896627315008235 (cit. on p. 45).

[67] Karl J. Friston. "Functional and Effective Connectivity: A Review". In: *Brain Connectivity* 1.1 (2011). PMID: 22432952, pp. 13–36. DOI: 10.1089/brain.2011.0008. eprint: https://doi.org/10.1089/brain.2011.0008. URL: https://doi.org/10.1089/brain.2011.0008 (cit. on p. 49).

[68] Edoardo Galimberti, Alain Barrat, Francesco Bonchi, et al. “Mining (maximal) span-cores from temporal networks”. In: *Proceedings of the 27th ACM International Conference on Information and Knowledge Management*. ACM. 2018, pp. 107–116 (cit. on pp. 33, 103, 137).

[69] Aurelien Gautreau, Alain Barrat, and Marc Barthélemy. “Microdynamics in stationary complex networks”. In: *Proceedings of the National Academy of Sciences* 106.22 (2009), pp. 8847–8852. ISSN: 0027-8424. DOI: 10.1073/pnas.0811113106. eprint: https://www.pnas.org/content/106/22/8847.full.pdf. URL: https://www.pnas.org/content/106/22/8847 (cit. on p. 141).

[70] Laetitia Gauvin, Mathieu Génois, Márton Karsai, et al. *Randomized reference models for temporal networks*. 2018. arXiv: 1806.04032 [physics.soc-ph] (cit. on pp. 34, 138, 139, 153).

[71] Valeria Gelardi, Joël Fagot, Alain Barrat, et al. “Detecting social (in)stability in primates from their temporal co-presence network”. In: *Animal Behaviour* 139 (2019), p. 239 (cit. on p. 76).

[72] Amir Ghasemian, Pan Zhang, Aaron Clauset, et al. “Detectability Thresholds and Optimal Algorithms for Community Structure in Dynamic Networks”. In: *Phys. Rev. X* 6 (3 July 2016), p. 031005. DOI: 10.1103/PhysRevX.6.031005. URL: https://link.aps.org/doi/10.1103/PhysRevX.6.031005 (cit. on p. 35).

[73] Anandamohan Ghosh, Y. Rho, A. R. McIntosh, et al. “Noise during Rest Enables the Exploration of the Brain’s Dynamic Repertoire”. In: *PLOS Computational Biology* 4.10 (Oct. 2008), pp. 1–12. DOI: 10.1371/journal.pcbi.1000196. URL: https://doi.org/10.1371/journal.pcbi.1000196 (cit. on p. 50).

[74] E. N. Gilbert. “Random Graphs”. In: *The Annals of Mathematical Statistics* 30.4 (1959), pp. 1141–1144 (cit. on p. 23).

[75] Anne-Lise Giraud and David Poeppel. “Cortical oscillations and speech processing: emerging computational principles and operations”. In: *Nature Neuroscience* 15.4 (2012), pp. 511–517 (cit. on pp. 70, 108, 131, 133).

[76] M. Girvan and M. E. J. Newman. “Community structure in social and biological networks”. In: *Proceedings of the National Academy of Sciences* 99.12 (2002), pp. 7821–7826. ISSN: 0027-8424. DOI: 10.1073/pnas.122653799. eprint: https://www.pnas.org/content/99/12/7821.full.pdf. URL: https://www.pnas.org/content/99/12/7821 (cit. on p. 25).

[77] S. Gómez, A. Arenas, J. Borge-Holthoefer, et al. “Discrete-time Markov chain approach to contact-based disease spreading in complex networks”. In: *EPL (Europhysics Letters)* 89.3 (Feb. 2010), p. 38009. DOI: 10.1209/0295-5075/89/38009. URL: https://doi.org/10.1209/0295-5075/89/38009 (cit. on p. 38).

[78] Georgia G. Gregoriou, Stephen J. Gotts, Huihui Zhou, et al. "High-Frequency, Long-Range Coupling Between Prefrontal and Visual Cortex During Attention". In: *Science* 324.5931 (2009), pp. 1207–1210. DOI: 10.1126/science.1171402 (cit. on p. 49).

[79] Patric Hagmann, Leila Cammoun, Xavier Gigandet, et al. "Mapping the Structural Core of Human Cerebral Cortex". In: *PLOS Biology* 6.7 (July 2008), pp. 1–15. DOI: 10.1371/journal.pbio.0060159. URL: https://doi.org/10.1371/journal.pbio.0060159 (cit. on pp. 42, 43).

[80] Enrique CA Hansen, Demian Battaglia, Andreas Spiegler, et al. "Functional connectivity dynamics: Modeling the switching behavior of the resting state". In: *NeuroImage* 105 (2015), pp. 525–535 (cit. on pp. 51–54).

[81] Leland H. Hartwell, John J. Hopfield, Stanislas Leibler, et al. "From molecular to modular cell biology". In: *Nature* 402.6761 (1999), pp. C47–C52 (cit. on p. 24).

[82] Michael E Hasselmo and Chantal E Stern. "Theta rhythm and the encoding and retrieval of space and time." In: *NeuroImage* 85 Pt 2 (2013), pp. 656–66. ISSN: 1053-8119. DOI: 10.1016/j.neuroimage.2013.06.022 (cit. on p. 104).

[83] Xiaosong He, Danielle S Bassett, Ganne Chaitanya, et al. "Disrupted dynamic network reconfiguration of the language system in temporal lobe epilepsy". In: *Brain* 141.5 (Mar. 2018), pp. 1375–1389 (cit. on pp. 71, 72).

[84] Donald Hebb. *The Organization of Behavior: a Neuropsychological Theory*. New York: Wiley, 1949 (cit. on pp. 58, 59, 102).

[85] Martijn P. van den Heuvel and Olaf Sporns. "Rich-Club Organization of the Human Connectome". In: *Journal of Neuroscience* 31.44 (2011), pp. 15775–15786. ISSN: 0270-6474. DOI: 10.1523/JNEUROSCI.3539-11.2011. eprint: https://www.jneurosci.org/content/31/44/15775.full.pdf. URL: https://www.jneurosci.org/content/31/44/15775 (cit. on pp. 43, 44, 137).

[86] Gregory Hickok and David Poeppel. "The cortical organization of speech processing". In: *Nature Reviews Neuroscience* 8.5 (2007), pp. 393–402 (cit. on p. 69).

[87] Petter Holme. "Core-periphery organization of complex networks". In: *Phys. Rev. E* 72 (4 Oct. 2005), p. 046111. DOI: 10.1103/PhysRevE.72.046111. URL: https://link.aps.org/doi/10.1103/PhysRevE.72.046111 (cit. on p. 26).

[88] Petter Holme. "Core-periphery organization of complex networks". In: *Phys. Rev. E* 72 (4 Oct. 2005), p. 046111. DOI: 10.1103/PhysRevE.72.046111. URL: https://link.aps.org/doi/10.1103/PhysRevE.72.046111 (cit. on p. 103).

[89] Petter Holme. "Modern temporal network theory: a colloquium". In: *The European Physical Journal B* 88.9 (2015), p. 234 (cit. on pp. 34, 137).

[90] Petter Holme and Jari Saramäki. "Temporal networks". In: *Physics Reports* 519 (2012), pp. 97–125 (cit. on pp. 31, 38, 137).

[91] Petter Holme and Jari Saramäki, eds. *Temporal Network theory*. Springer, Singapore, 2019 (cit. on p. 137).

[92] Gregory L Holmes. "Cognitive impairment in epilepsy: the role of network abnormalities." In: *Epileptic disorders : international epilepsy journal with videotape* 17.2 (June 2015), pp. 101–116 (cit. on p. 107).

[93] Christopher J Honey, Rolf Kötter, Michael Breakspear, et al. "Network structure of cerebral cortex shapes functional connectivity on multiple time scales". In: *Proceedings of the National Academy of Sciences USA* 104.24 (2007), pp. 10240–10245 (cit. on p. 51).

[94] R Matthew Hutchison, Thilo Womelsdorf, Elena A Allen, et al. "Dynamic functional connectivity: promise, issues, and interpretations". In: *Neuroimage* 80 (2013), pp. 360–378 (cit. on p. 127).

[95] Yuji Ikegaya, Gloster Aaron, Rosa Cossart, et al. "Synfire chains and cortical songs: temporal modules of cortical activity." In: *Science (New York, N.Y.)* 304.5670 (2004), p. 559 564. ISSN: 0036-8075. DOI: 10.1126/science.1093173 (cit. on p. 59).

[96] Lorenzo Isella, Juliette StehlÃ©, Alain Barrat, et al. "What's in a crowd? Analysis of face-to-face behavioral networks". In: *Journal of Theoretical Biology* 271.1 (2011), pp. 166–180. ISSN: 0022-5193. DOI: https://doi.org/10.1016/j.jtbi.2010.11.033. URL: https://www.sciencedirect.com/science/article/pii/S0022519310006284 (cit. on p. 39).

[97] Emily M. Jin, Michelle Girvan, and M. E. J. Newman. "Structure of growing social networks". In: *Phys. Rev. E* 64 (4 Sept. 2001), p. 046132. DOI: 10.1103/PhysRevE.64.046132. URL: https://link.aps.org/doi/10.1103/PhysRevE.64.046132 (cit. on p. 43).

[98] M. Karsai, M. Kivelä, R. K. Pan, et al. "Small but slow world: How network topology and burstiness slow down spreading". In: *Phys. Rev. E* 83 (2011), 025102(R) (cit. on p. 39).

[99] Tilman Kispersky, Gabrielle J Gutierrez, and Eve Marder. "Functional connectivity in a rhythmic inhibitory circuit using Granger causality." In: *Neural systems & circuits* 1.1 (2011), p. 9. ISSN: 2042-1001. DOI: 10.1186/2042-1001-1-9 (cit. on p. 103).

[100] Maksim Kitsak, Lazaros K. Gallos, Shlomo Havlin, et al. "Identification of influential spreaders in complex networks". In: *Nature Physics* 6.11 (2010), pp. 888–893 (cit. on pp. 137, 153).

[101] Mikko Kivelä, Alex Arenas, Marc Barthelemy, et al. "Multilayer networks". In: *Journal of Complex Networks* 2.3 (July 2014), pp. 203–271 (cit. on pp. 29, 30).

[102] Sadamori Kojaku and Naoki Masuda. "Core-periphery structure requires something else in the network". In: *New Journal of Physics* 20.4 (Apr. 2018), p. 043012. DOI: 10.1088/1367-2630/aab547 (cit. on p. 103).

[103] Nancy J Kopell, Howard J Gritton, Miles A Whittington, et al. "Beyond the connectome: the dynome". In: *Neuron* 83.6 (2014), pp. 1319–1328 (cit. on p. 50).

[104] Lauri Kovanen, Márton Karsai, Kimmo Kaski, et al. "Temporal motifs in time-dependent networks". In: *Journal of Statistical Mechanics: Theory and Experiment* 2011.11 (2011), P11005 (cit. on p. 137).

[105] Jean-Philippe Lachaux, Antoine Lutz, David Rudrauf, et al. "Estimating the time-course of coherence between single-trial brain signals: an introduction to wavelet coherence". In: *Neurophysiologie Clinique/Clinical Neurophysiology* 32.3 (2002), pp. 157–174. ISSN: 0987-7053. DOI: https://doi.org/10.1016/S0987-7053(02)00301-5. URL: https://www.sciencedirect.com/science/article/pii/S0987705302003015 (cit. on p. 68).

[106] Jean-Philippe Lachaux, Eugenio Rodriguez, Jacques Martinerie, et al. "Measuring phase synchrony in brain signals". In: *Human Brain Mapping* 8.4 (1999), pp. 194–208. DOI: https://doi.org/10.1002/(SICI)1097-0193(1999)8:4<194::AID-HBM4>3.0.CO;2-C (cit. on p. 45).

[107] Stanislas Lagarde, Nicolas Roehri, Isabelle Lambert, et al. "Interictal stereotactic-EEG functional connectivity in refractory focal epilepsies". In: *Brain* 141.10 (Aug. 2018), pp. 2966–2980 (cit. on p. 68).

[108] Lichan Liu and Andreas A. Ioannides. "Spatiotemporal dynamics and connectivity pattern differences between centrally and peripherally presented faces". In: *NeuroImage* 31.4 (2006), pp. 1726–1740. ISSN: 1053-8119. DOI: https://doi.org/10.1016/j.neuroimage.2006.02.009. URL: https://www.sciencedirect.com/science/article/pii/S105381190600108X (cit. on p. 49).

[109] Quan-Hui Liu, Xinyue Xiong, Qian Zhang, et al. "Epidemic spreading on time-varying multiplex networks". In: *Phys. Rev. E* 98 (6 Dec. 2018), p. 062303. DOI: 10.1103/PhysRevE.98.062303. URL: https://link.aps.org/doi/10.1103/PhysRevE.98.062303 (cit. on p. 131).

[110] Joseph T Lizier, Fatihcan M Atay, and Jºrgen Jost. "Information storage, loop motifs, and clustered structure in complex networks." In: *Physical Review E* 86.2-2 (2012), p. 026110. ISSN: 1539-3755. DOI: 10.1103/physreve.86.026110 (cit. on pp. 63, 99, 104).

[111] Joseph T Lizier, Benjamin Flecker, and Paul L Williams. "Towards a synergy-based approach to measuring information modification". In: 2013 IEEE Symposium on Artificial Life (ALife. 2013, p. 43 51. ISBN: New-2005_Electronic_978-1-4673-5863-7. DOI: 10.1109/alife.2013.6602430 (cit. on p. 104).

[112] Diego Lombardo, Catherine CassÃ©-Perrot, Jean-Philippe Ranjeva, et al. "Modular slowing of resting-state dynamic functional connectivity as a marker of cognitive dysfunction induced by sleep deprivation". In: *NeuroImage* 222 (2020), p. 117155. ISSN: 1053-8119. DOI: https://doi.org/10.1016/j.neuroimage.2020.117155. URL: https://www.sciencedirect.com/science/article/pii/S1053811920306418 (cit. on pp. 58, 115).

[113] Wolfgang Maass, Thomas Natschlager, and Henry Markram. "Real-time computing without stable states: a new framework for neural computation based on perturbations." In: *Neural Computation* 14.11 (2002), p. 2531 2560. ISSN: 0899-7667. DOI: 10.1162/089976602760407955 (cit. on p. 105).

[114] Arnaud Malvache, Susanne Reichinnek, Vincent Villette, et al. "Awake hippocampal reactivations project onto orthogonal neuronal assemblies." In: *Science (New York, N.Y.)* 353.6305 (2016), p. 1280 1283. ISSN: 0036-8075. DOI: 10.1126/science.aaf3319 (cit. on pp. 59, 106).

[115] Eve Marder and Jean-Marc Goaillard. "Variability, compensation and homeostasis in neuron and network function." In: *Nature Reviews Neuroscience* 7.7 (2006), p. 563 574. ISSN: 1471-0048. DOI: 10.1038/nrn1949 (cit. on pp. 50, 103).

[116] N. T. Markov, M. M. Ercsey-Ravasz, A. R. Ribeiro Gomes, et al. "A Weighted and Directed Interareal Connectivity Matrix for Macaque Cerebral Cortex". In: *Cerebral Cortex* 24.1 (Sept. 2012), pp. 17–36 (cit. on p. 42).

[117] H Markram, W Gerstner, and P J Sjöström. "Spike-timing-dependent plasticity: a comprehensive overview." In: *Frontiers in synaptic neuroscience* 4 (2012), p. 2 (cit. on p. 153).

[118] Henry Markram, Eilif Muller, Srikanth Ramaswamy, et al. "Reconstruction and Simulation of Neocortical Microcircuitry". In: *Cell* 163.2 (2015), pp. 456–492. ISSN: 0092-8674. DOI: https://doi.org/10.1016/j.cell.2015.09.029. URL: https://www.sciencedirect.com/science/article/pii/S0092867415011915 (cit. on p. 43).

[119] Olivier Marre, Pierre Yger, Andrew P Davison, et al. "Reliable recall of spontaneous activity patterns in cortical networks". In: *The Journal of neuroscience : the official journal of the Society for Neuroscience* 29.46 (2009), p. 14596 14606. ISSN: 0270-6474. DOI: 10.1523/jneurosci.0753-09.2009 (cit. on p. 105).

[120] Sergei Maslov and Kim Sneppen. "Specificity and Stability in Topology of Protein Networks". In: *Science* 296.5569 (2002), pp. 910–913. DOI: 10.1126/science.1065103. eprint: http://www.sciencemag.org/content/296/5569/910.full.pdf. URL: http://www.sciencemag.org/content/296/5569/910.abstract (cit. on pp. 82, 84).

[121] Naoki Masuda and Petter Holme. "Detecting sequences of system states in temporal networks". In: *Scientific Reports* 9.1 (2019), p. 795 (cit. on pp. 138, 148).

[122] Miller Joel C. Masuda Naoki and Holme Petter. "Concurrency measures in the era of temporal network". In: *J. R. Soc. Interface.182021001920210019* (2021) (cit. on pp. 33, 38, 137, 147, 150, 153).

[123] Julian J. McAuley, Luciano da Fontoura Costa, and TibÃ©rio S. Caetano. "Rich-club phenomenon across complex network hierarchies". In: *Applied Physics Letters* 91.8 (2007), p. 084103. DOI: 10.1063/1.2773951. eprint: https://doi.org/10.1063/1.2773951. URL: https://doi.org/10.1063/1.2773951 (cit. on p. 137).

[124] Leenoy Meshulam, Jeffrey L. Gauthier, Carlos D. Brody, et al. "Collective Behavior of Place and Non-place Neurons in the Hippocampal Network". In: *Neuron* 96.5 (2017), 1178–1191.e4. ISSN: 0896-6273. DOI: https://doi.org/10.1016/j.neuron.2017.10.027. URL: https://www.sciencedirect.com/science/article/pii/S0896627317309960 (cit. on p. 59).

[125] Lars Meyer. "The neural oscillations of speech processing and language comprehension: state of the art and emerging mechanisms". In: *European Journal of Neuroscience* 48.7 (2018), pp. 2609–2621. DOI: https://doi.org/10.1111/ejn.13748. eprint: https://onlinelibrary.wiley.com/doi/pdf/10.1111/ejn.13748. URL: https://onlinelibrary.wiley.com/doi/abs/10.1111/ejn.13748 (cit. on pp. 70, 108, 110, 133).

[126] Georgios Michalareas, Julien Vezoli, Stan van Pelt, et al. "Alpha-Beta and Gamma Rhythms Subserve Feedback and Feedforward Influences among Human Visual Cortical Areas." In: *Neuron* 89.2 (Jan. 2016), pp. 384–397 (cit. on pp. 131, 133).

[127] Jae-eun Kang Miller, Inbal Ayzenshtat, Luis Carrillo-Reid, et al. "Visual stimuli recruit intrinsically generated cortical ensembles." In: *Proceedings of the National Academy of Sciences of the United States of America* 111.38 (2014), E4053 61. ISSN: 0027-8424. DOI: 10.1073/pnas.1406077111 (cit. on pp. 59, 106).

[128] Giovanna Miritello, Rubén Lara, Manuel Cebrian, et al. "Limited communication capacity unveils strategies for human interaction". In: *Scientific Reports* 3.1 (2013), p. 1950. DOI: 10.1038/srep01950 (cit. on p. 76).

[129] Laura Mòdol, Vitor Hugo Sousa, Arnaud Malvache, et al. "Spatial Embryonic Origin Delineates GABAergic Hub Neurons Driving Network Dynamics in the Developing Entorhinal Cortex". In: *Cerebral Cortex* 27.9 (July 2017), pp. 4649–4661 (cit. on p. 62).

[130] Laura Mòdol, Vitor Hugo Sousa, Arnaud Malvache, et al. "Spatial embryonic origin delineates GABAergic hub neurons driving network dynamics in the developing entorhinal cortex". In: *Cerebral Cortex* 27.9 (2017), pp. 4649–4661 (cit. on p. 62).

[131] Remi Monasson and Simona Cocco. "Fast inference of interactions in assemblies of stochastic integrate-and-fire neurons from spike recordings". In: *Journal of Computational Neuroscience* 31.2 (2011), pp. 199–227 (cit. on p. 59).

[132] Peter J. Mucha, Thomas Richardson, Kevin Macon, et al. "Community Structure in Time-Dependent, Multiscale, and Multiplex Networks". In: *Science* 328.5980 (2010), pp. 876–878. DOI: 10.1126/science.1184819. eprint: https://www.science.org/doi/pdf/10.1126/science.1184819. URL: https://www.science.org/doi/abs/10.1126/science.1184819 (cit. on pp. 35, 112).

[133] Sarah Feldt Muldoon, Ivan Soltesz, and Rosa Cossart. "Spatially clustered neuronal assemblies comprise the microstructure of synchrony in chronically epileptic networks." In: *Proceedings of the National Academy of Sciences of the United States of America* 110.9 (2013), p. 3567 3572. ISSN: 0027-8424. DOI: 10.1073/pnas.1216958110 (cit. on pp. 73, 105).

[134] Sarah Feldt Muldoon, Vincent Villette, Thomas Tressard, et al. "GABAergic inhibition shapes interictal dynamics in awake epileptic mice". In: *Brain* 138.10 (Aug. 2015), pp. 2875–2890 (cit. on p. 72).

[135] M. E. J. Newman. "The Structure and Function of Complex Networks". In: *SIAM Review* 45.2 (2003), pp. 167–256. DOI: 10.1137/S003614450342480. eprint: https://doi.org/10.1137/S003614450342480. URL: https://doi.org/10.1137/S003614450342480 (cit. on p. 19).

[136] M. E. J. Newman. "Analysis of weighted networks". In: *Phys. Rev. E* 70 (5 Nov. 2004), p. 056131. DOI: 10.1103/PhysRevE.70.056131. URL: https://link.aps.org/doi/10.1103/PhysRevE.70.056131 (cit. on p. 20).

[137] Sunny Nigam, Masanori Shimono, Shinya Ito, et al. "Rich-Club Organization in Effective Connectivity among Cortical Neurons." In: *The Journal of Neuroscience* 36.3 (Jan. 2016), pp. 670–684 (cit. on p. 137).

[138] Tore Opsahl, Vittoria Colizza, Pietro Panzarasa, et al. "Prominence and Control: The Weighted Rich-Club Effect". In: *Phys. Rev. Lett.* 101 (16 Oct. 2008), p. 168702. DOI: 10.1103/PhysRevLett.101.168702. URL: https://link.aps.org/doi/10.1103/PhysRevLett.101.168702 (cit. on pp. 26, 137).

[139] Agostina Palmigiano, Theo Geisel, Fred Wolf, et al. "Flexible information routing by transient synchrony." In: *Nature Neuroscience* 20.7 (2017), p. 1014 1022. ISSN: 1097-6256. DOI: 10.1038/nn.4569 (cit. on p. 106).

[140] Hae-Jeong Park and Karl Friston. "Structural and Functional Brain Networks: From Connections to Cognition". In: *Science* 342.6158 (2013), p. 1238411. DOI: 10.1126/science.1238411 (cit. on p. 41).

[141] F. de Pasquale, M. Corbetta, V. Betti, et al. "Cortical cores in network dynamics". In: *NeuroImage* 180.J.¬†Neurosci. 26 2006 (2018), pp. 370–382. ISSN: 1053-8119. DOI: 10.1016/j.neuroimage.2017.09.063 (cit. on p. 103).

[142] Nicola Pedreschi, Demian Battaglia, and Alain Barrat. "The Temporal Rich Club Phenomenon". In: *arXiv preprint arXiv:2108.12170* (2021) (cit. on p. 18).

[143] Nicola Pedreschi, Christophe Bernard, Wesley Clawson, et al. "Dynamic core-periphery structure of information sharing networks in entorhinal cortex and hippocampus". In: *Network Neuroscience* 4.3 (Sept. 2020), pp. 946–975 (cit. on pp. 16, 74, 116).

[144] Sarah T Pendlebury, Philip Anslow, and Peter M Rothwell. *Neurological Case HistoriesCase Histories in Acute Neurology and the Neurology of General Medicine: Case Histories in Acute Neurology and the Neurology of General Medicine*. Oxford, UK: Oxford University Press, Nov. 2012 (cit. on p. 126).

[145] Rodrigo Perin, Thomas K. Berger, and Henry Markram. "A synaptic organizing principle for cortical neuronal groups". In: *Proceedings of the National Academy of Sciences* 108.13 (2011), pp. 5419–5424. ISSN: 0027-8424. DOI: 10.1073/pnas.1016051108. eprint: https://www.pnas.org/content/108/13/5419.full.pdf. URL: https://www.pnas.org/content/108/13/5419 (cit. on pp. 42, 43).

[146] René Pfitzner, Ingo Scholtes, Antonios Garas, et al. "Betweenness Preference: Quantifying Correlations in the Topological Dynamics of Temporal Networks". In: *Phys. Rev. Lett.* 110 (19 May 2013), p. 198701. DOI: 10.1103/PhysRevLett.110.198701. URL: https://link.aps.org/doi/10.1103/PhysRevLett.110.198701 (cit. on p. 137).

[147] M. Puck Rombach, M. Porter, J.H. Fowler, et al. "Core-Periphery Structure in Networks". In: *SIAM J. Appl. Math.* 74 (2014), p. 167 (cit. on p. 103).

[148] Pascale Quilichini, Anton Sirota, and György Buzsáki. "Intrinsic circuit organization and theta-gamma oscillation dynamics in the entorhinal cortex of the rat." In: *The Journal of neuroscience : the official journal of the Society for Neuroscience* 30.33 (2010), p. 11128 11142. ISSN: 0270-6474. DOI: 10.1523/jneurosci.1327-10.2010 (cit. on p. 74).

[149] Pascale¬†P. Quilichini, Michel Le¬†Van¬†Quyen, Anton Ivanov, et al. "Hub GABA Neurons Mediate Gamma-Frequency Oscillations at Ictal-like Event Onset in the Immature Hippocampus". In: *Neuron* 74.1 (2012), pp. 57–64. ISSN: 0896-6273. DOI: 10.1016/j.neuron.2012.01.026 (cit. on p. 105).

[150] Ben Gendon Yeshe Ridley, Celia Rousseau, Jonathan Wirsich, et al. "Nodal approach reveals differential impact of lateralized focal epilepsies on hub reorganization". In: *NeuroImage* 118 (2015), pp. 39–48. ISSN: 1053-8119. DOI: https://doi.org/10.1016/j.neuroimage.2015.05.096. URL: https://www.sciencedirect.com/science/article/pii/S1053811915005212 (cit. on p. 68).

[151] M. Puck Rombach, Mason A. Porter, James H. Fowler, et al. "Core-Periphery Structure in Networks". In: *SIAM Journal on Applied Mathematics* 74.1 (2014), pp. 167–190. DOI: 10.1137/120881683. eprint: https://doi.org/10.1137/120881683. URL: https://doi.org/10.1137/120881683 (cit. on p. 137).

[152] Michael G. Rosenblum, Arkady S. Pikovsky, and Jürgen Kurths. “Phase Synchronization of Chaotic Oscillators”. In: *Phys. Rev. Lett.* 76 (11 Mar. 1996), pp. 1804–1807. DOI: 10.1103/PhysRevLett.76.1804. URL: https://link.aps.org/doi/10.1103/PhysRevLett.76.1804 (cit. on p. 45).

[153] Giulio Rossetti and Rémy Cazabet. “Community Discovery in Dynamic Networks: A Survey”. In: *ACM Comput. Surv.* 51.2 (Feb. 2018). ISSN: 0360-0300. DOI: 10.1145/3172867. URL: https://doi.org/10.1145/3172867 (cit. on p. 35).

[154] Yoshio Sakurai. “Population coding by cell assembliesâwhat it really is in the brain”. In: *Neuroscience Research* 26.1 (1996), pp. 1–16. ISSN: 0168-0102. DOI: https://doi.org/10.1016/0168-0102(96)01075-9. URL: https://www.sciencedirect.com/science/article/pii/0168010296010759 (cit. on p. 59).

[155] Elad Schneidman, Michael J. Berry, Ronen Segev, et al. “Weak pairwise correlations imply strongly correlated network states in a neural population”. In: *Nature* 440.7087 (2006), pp. 1007–1012 (cit. on pp. 59, 60).

[156] I. Scholtes, N. Wider, and A. Garas. “Higher-order aggregate networks in the analysis of temporal networks: path structures and centralities”. In: *Eur. Phys. J. B* 89 (2015), pp. 1–15 (cit. on p. 137).

[157] Erik W. Schomburg, Antonio Fernandez-Ruiz, Kenji Mizuseki, et al. “Theta Phase Segregation of Input-Specific Gamma Patterns in Entorhinal-Hippocampal Networks”. In: *Neuron* 84.2 (2014), pp. 470–485. ISSN: 0896-6273. DOI: 10.1016/j.neuron.2014.08.051 (cit. on p. 104).

[158] Thomas Schreiber. “Measuring Information Transfer”. In: *Physical Review Letters* 85.2 (2000), pp. 461–464. ISSN: 0031-9007. DOI: 10.1103/physrevlett.85.461 (cit. on pp. 101, 104).

[159] M. Ángeles Serrano. “Rich-club vs rich-multipolarization phenomena in weighted networks”. In: *Phys. Rev. E* 78 (2 Aug. 2008), p. 026101. DOI: 10.1103/PhysRevE.78.026101. URL: https://link.aps.org/doi/10.1103/PhysRevE.78.026101 (cit. on p. 137).

[160] Olaf Sporns, Giulio Tononi, and Rolf KÃ¶tter. “The Human Connectome: A Structural Description of the Human Brain”. In: *PLOS Computational Biology* 1.4 (Sept. 2005), null. DOI: 10.1371/journal.pcbi.0010042. URL: https://doi.org/10.1371/journal.pcbi.0010042 (cit. on p. 42).

[161] Juliette Stehlé, François Charbonnier, Tristan Picard, et al. “Gender homophily from spatial behavior in a primary school: A sociometric study”. In: *Social Networks* 35.4 (2013), pp. 604–613. ISSN: 0378-8733. DOI: https://doi.org/10.1016/j.socnet.2013.08.003. URL: http://www.sciencedirect.com/science/article/pii/S0378873313000737 (cit. on p. 76).

[162] Juliette Stehlé, Nicolas Voirin, Alain Barrat, et al. "High-Resolution Measurements of Face-to-Face Contact Patterns in a Primary School". In: *PLOS ONE* 6.8 (Aug. 2011), pp. 1–13. DOI: 10.1371/journal.pone.0023176. URL: https://doi.org/10.1371/journal.pone.0023176 (cit. on pp. 143, 146).

[163] Gaia Tavoni, Ulisse Ferrari, Francesco P. Battaglia, et al. "Functional coupling networks inferred from prefrontal cortex activity show experience-related effective plasticity". In: *Network Neuroscience* 1.3 (Oct. 2017), pp. 275–301 (cit. on p. 61).

[164] M. Termenon, A. Jaillard, C. Delon-Martin, et al. "Reliability of graph analysis of resting state fMRI using test-retest dataset from the Human Connectome Project". In: *NeuroImage* 142 (2016), pp. 172–187. ISSN: 1053-8119. DOI: https://doi.org/10.1016/j.neuroimage.2016.05.062. URL: https://www.sciencedirect.com/science/article/pii/S1053811916301823 (cit. on p. 157).

[165] William Hedley Thompson, Per Brantefors, and Peter Fransson. "From static to temporal network theory: Applications to functional brain connectivity". In: *Network Neuroscience* 1 (2017), p. 69 (cit. on p. 106).

[166] Giulio Tononi, Gerald M. Edelman, and Olaf Sporns. "Complexity and coherency: integrating information in the brain". In: *Trends in Cognitive Sciences* 2.12 (1998), pp. 474–484. ISSN: 1364-6613. DOI: 10.1016/s1364-6613(98)01259-5 (cit. on p. 103).

[167] Emma K. Towlson, Petra E. Vértes, Sebastian E. Ahnert, et al. "The Rich Club of the C. elegans Neuronal Connectome". In: *Journal of Neuroscience* 33.15 (2013), pp. 6380–6387. ISSN: 0270-6474. DOI: 10.1523/JNEUROSCI.3784-12.2013. eprint: https://www.jneurosci.org/content/33/15/6380.full.pdf. URL: https://www.jneurosci.org/content/33/15/6380 (cit. on pp. 43, 44, 137).

[168] Eugenio Valdano, Luca Ferreri, Chiara Poletto, et al. "Analytical Computation of the Epidemic Threshold on Temporal Networks". In: *Phys. Rev. X* 5 (2 Apr. 2015), p. 021005. DOI: 10.1103/PhysRevX.5.021005. URL: https://link.aps.org/doi/10.1103/PhysRevX.5.021005 (cit. on p. 147).

[169] Eugenio Valdano, Chiara Poletto, Armando Giovannini, et al. "Predicting Epidemic Risk from Past Temporal Contact Data". In: *PLOS Computational Biology* 11.3 (Mar. 2015), pp. 1–19. DOI: 10.1371/journal.pcbi.1004152 (cit. on pp. 39, 76, 77).

[170] Laurens Van der Maaten and Geoffrey Hinton. "Visualizing data using t-SNE." In: *Journal of machine learning research* 9.11 (2008) (cit. on p. 57).

[171] Francisco Varela, Jean-Philippe Lachaux, Eugenio Rodriguez, et al. "The brainweb: phase synchronization and large-scale integration". In: *Nature Reviews Neuroscience* 2.4 (2001), p. 229 239. ISSN: 1471-0048. DOI: 10.1038/35067550 (cit. on pp. 45, 59).

[172] Raul Vicente, Michael Wibral, Michael Lindner, et al. "Transfer entropy—a model-free measure of effective connectivity for the neurosciences". In: *Journal of Computational Neuroscience* 30.1 (2011), pp. 45–67 (cit. on p. 157).

[173] Vincent Villette, Arnaud Malvache, Thomas Tressard, et al. "Internally Recurring Hippocampal Sequences as a Population Template of Spatiotemporal Information". In: *Neuron* 88.2 (2015), pp. 357–366. ISSN: 0896-6273. DOI: https://doi.org/10.1016/j.neuron.2015.09.052. URL: https://www.sciencedirect.com/science/article/pii/S0896627315008417 (cit. on pp. 59, 61).

[174] Xiao-Jing Wang. "Neurophysiological and Computational Principles of Cortical Rhythms in Cognition". In: *Physiological Reviews* 90.3 (2010). PMID: 20664082, pp. 1195–1268. DOI: 10.1152/physrev.00035.2008. eprint: https://doi.org/10.1152/physrev.00035.2008. URL: https://doi.org/10.1152/physrev.00035.2008 (cit. on p. 45).

[175] Michael Wibral, Viola Priesemann, Jim W Kay, et al. "Partial information decomposition as a unified approach to the specification of neural goal functions." In: *Brain and cognition* 112 (2017), p. 25 38. ISSN: 0278-2626. DOI: 10.1016/j.bandc.2015.09.004. eprint: 1510.00831 (cit. on p. 104).

[176] Jonathan Wirsich, Alistair Perry, Ben Ridley, et al. "Whole-brain analytic measures of network communication reveal increased structure-function correlation in right temporal lobe epilepsy". In: *NeuroImage: Clinical* 11 (2016), pp. 707–718. ISSN: 2213-1582. DOI: https://doi.org/10.1016/j.nicl.2016.05.010. URL: https://www.sciencedirect.com/science/article/pii/S2213158216300869 (cit. on p. 68).

[177] Patricia Wollstadt, Mario MartÃnez-Zarzuela, Raul Vicente, et al. "Efficient Transfer Entropy Analysis of Non-Stationary Neural Time Series". In: *PLOS ONE* 9.7 (July 2014), pp. 1–21. DOI: 10.1371/journal.pone.0102833. URL: https://doi.org/10.1371/journal.pone.0102833 (cit. on p. 157).

[178] Thilo Womelsdorf, Jan-Mathijs Schoffelen, Robert Oostenveld, et al. "Modulation of neuronal interactions through neuronal synchronization". In: *Science* 316.5831 (2007), p. 1609 1612. ISSN: 0036-8075. DOI: 10.1126/science.1139597 (cit. on p. 105).

[179] S. Zhou and R.J. Mondragon. "The rich-club phenomenon in the Internet topology". In: *IEEE Communications Letters* 8 (2004), pp. 180–182 (cit. on pp. 27, 137).

A. APPENDIX

A. Supporting Information of Chapter 4

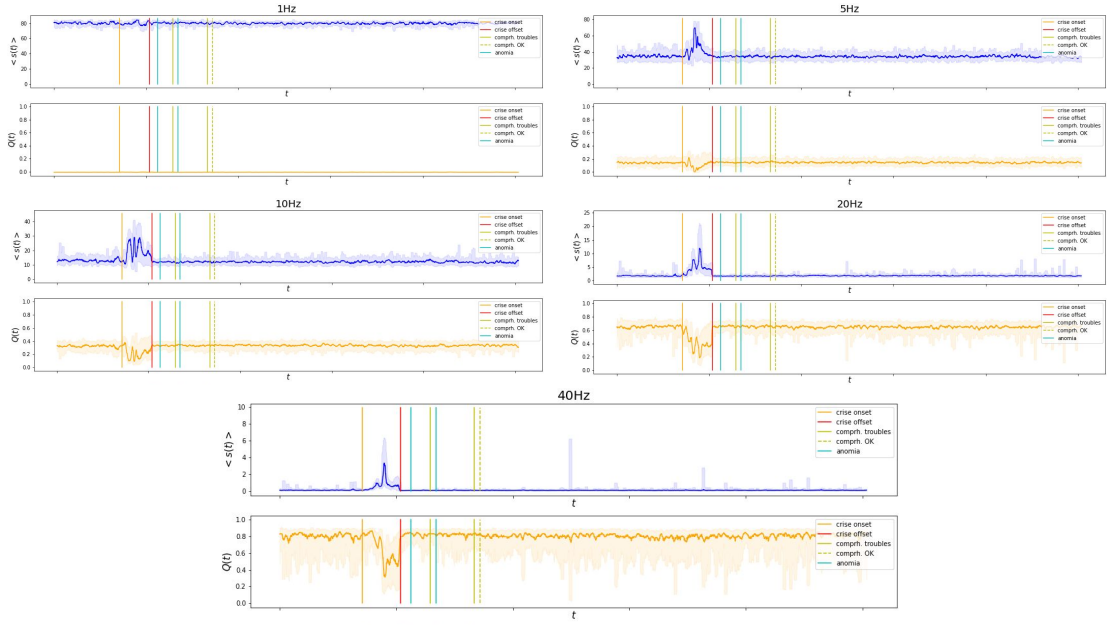

Figure A.1. – **Global network measures for bipolar montage**: plots of the instantaneous average strength $s(t)\rangle$ of nodes in the network (blue curve) and instantaneous modularity $Q(t)$ (orange) for the 1Hz, 5Hz, 10Hz, 20Hz and 40Hz layers for the bipolar montage. Same recording as in main text of Chapter 4.-

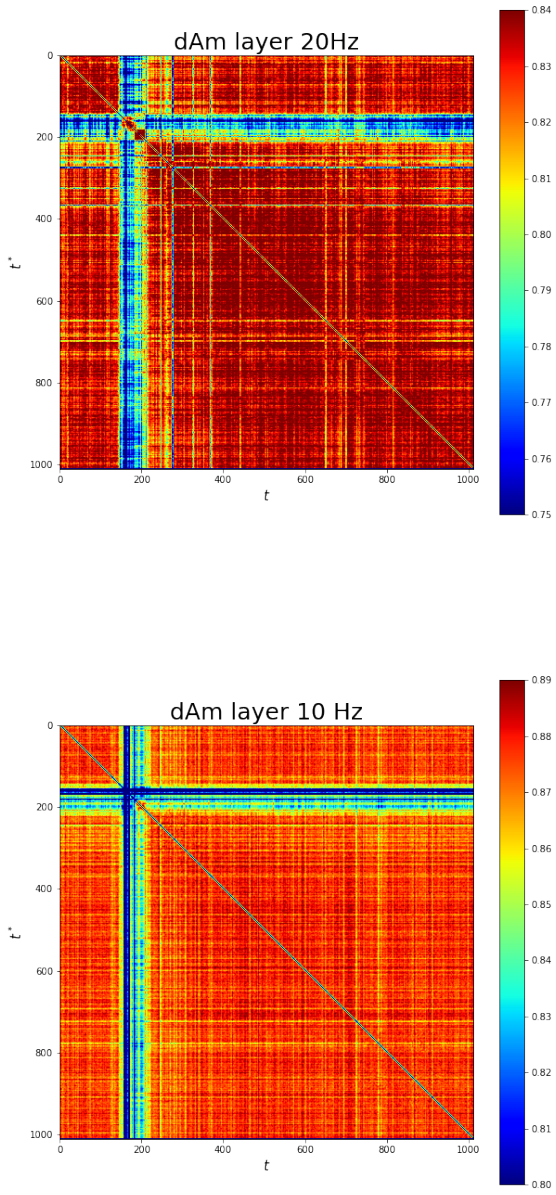

Figure A.2. – **Dynamic Allegiance Matrix:** The two plots are the Dynamic Allegiance Matrices, as explained in the main text, for the 20Hz (top) and 10Hz (bottom) frequency layers of the same recording whose 40Hz layer's dAM is shown in Figure 4.6

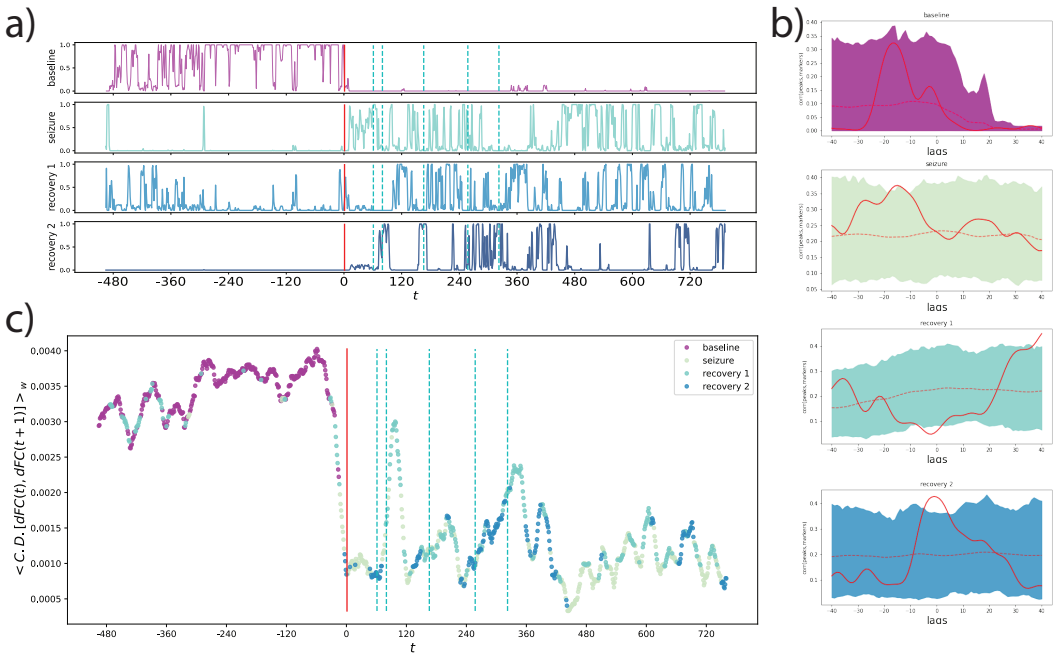

Figure A.3. – **Recording 2 - States of dynamics**: each of the four plots represents the cross-correlation between the peaks of the curves in **a)** of each state (baseline, seizure, recovery-1 and recovery-2 from top to bottom) with the language dysfunction markers (red line); the shaded areas are comprised between the 5th and 95th percentiles of the values of lagged cross-correlation computed for the peaks of $P(t)$ of each state with a random permutation of the clinical markers in the $[60s, 260s]$ interval. **c)** each of the colored dots corresponds to the average value of the instantaneous rate of change of the FC in a time window $\langle \Delta FC(t-1,t) \rangle_w$ and its color corresponds to the allegiance state label assigned to the corresponding time window.

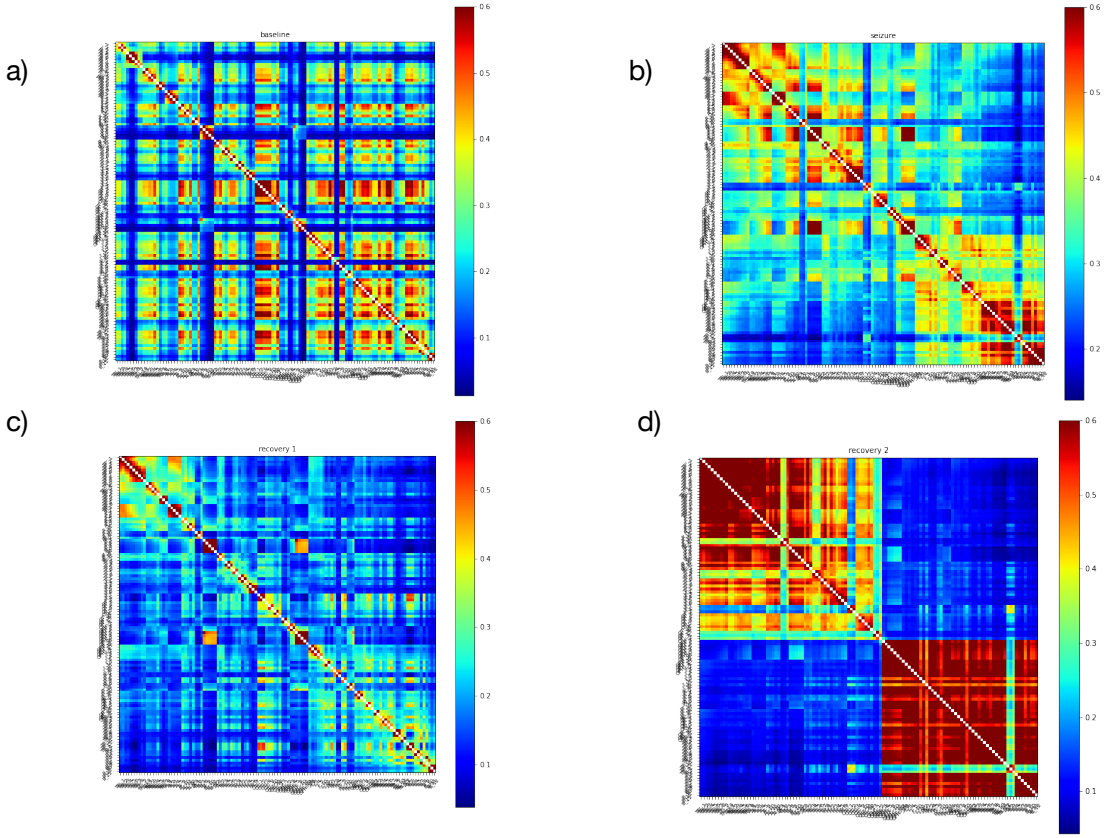

Figure A.4. – **Recording 2 - Allegiance matrices**: the state-wise allegiance matrices computed by averaging over the allegiance matrices measured in time windows assigned to the relative allegiance state. The four allegiance matrices in this plot correspond to the baseline state (**a)**), the seizure state (**b)**), the recovery 1 and 2 states (**c)**,**d)**) used to compute the state-wise radar plots in Figure 4.12 for recording 2.

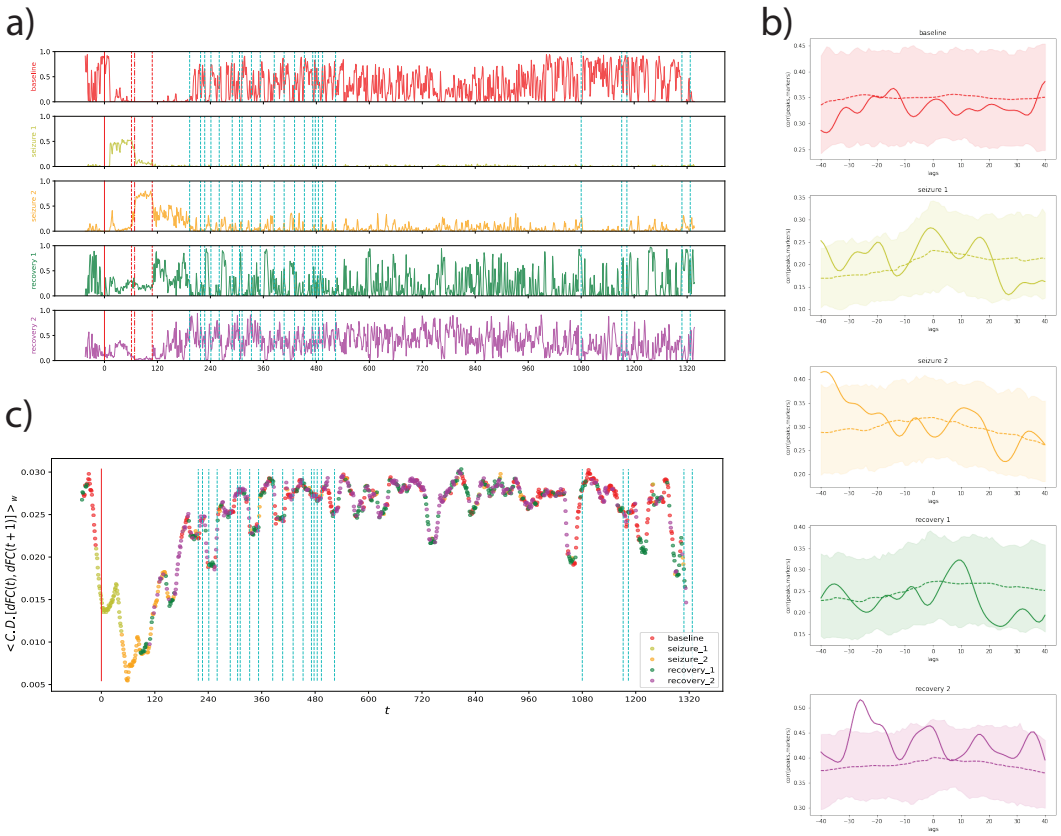

Figure A.5. – **Recording 3 - States of dynamics**: **a)** the five curves represent the probability $P(t) \in [0,1]$ of each time window t to belong to the baseline (red, top), seizure (two states, yellow and orange curves), recovery-1 (green, $4th$ plot) or recovery-2 (magenta, bottom) states. **b)** each of the five plots represents the lagged cross-correlation between the peaks of the curves in **a)** of each state (baseline, seizure-1 and 2, recovery-1 and recovery-2 from top to bottom) with the language dysfunction markers (red line); the shaded areas are comprised between the 5th and 95th percentiles of the values of cross-correlation computed for the peaks of $P(t)$ of each state with a random permutation of the clinical markers in the $[60s, 260s]$ interval. **c)** each of the colored dots corresponds to the average value of the instantaneous rate of change of the FC in a time window $\langle \Delta FC(t-1,t) \rangle_w$ and its color corresponds to the allegiance state label assigned to the corresponding time window.

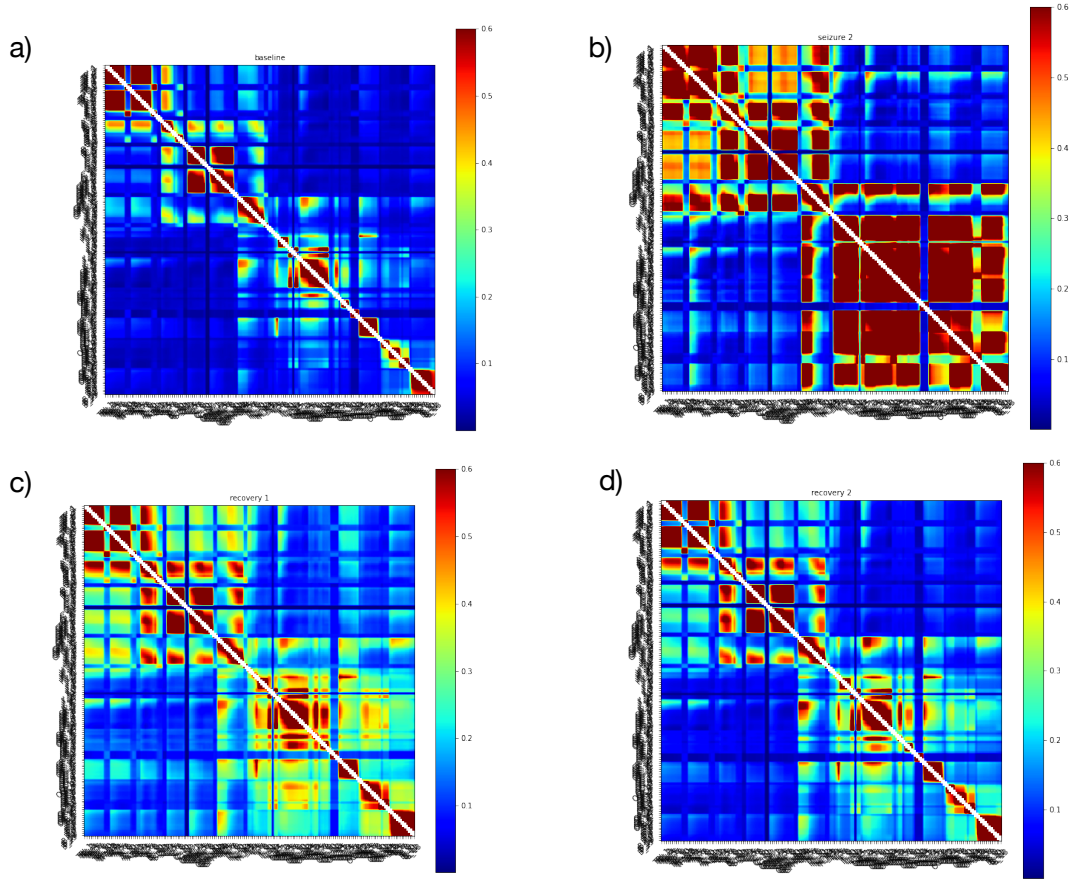

Figure A.6. – **Recording 3 - Allegiance matrices**: the state-wise allegiance matrices computed by averaging over the allegiance matrices measured in time windows assigned to the relative allegiance state. The four allegiance matrices in this plot correspond to the baseline state (**a)**), the seizure state (**b)**), the recovery 1 and 2 states (**c)**,**d)**) used to compute the state-wise radar plots in Figure 4.12 for recording 3.

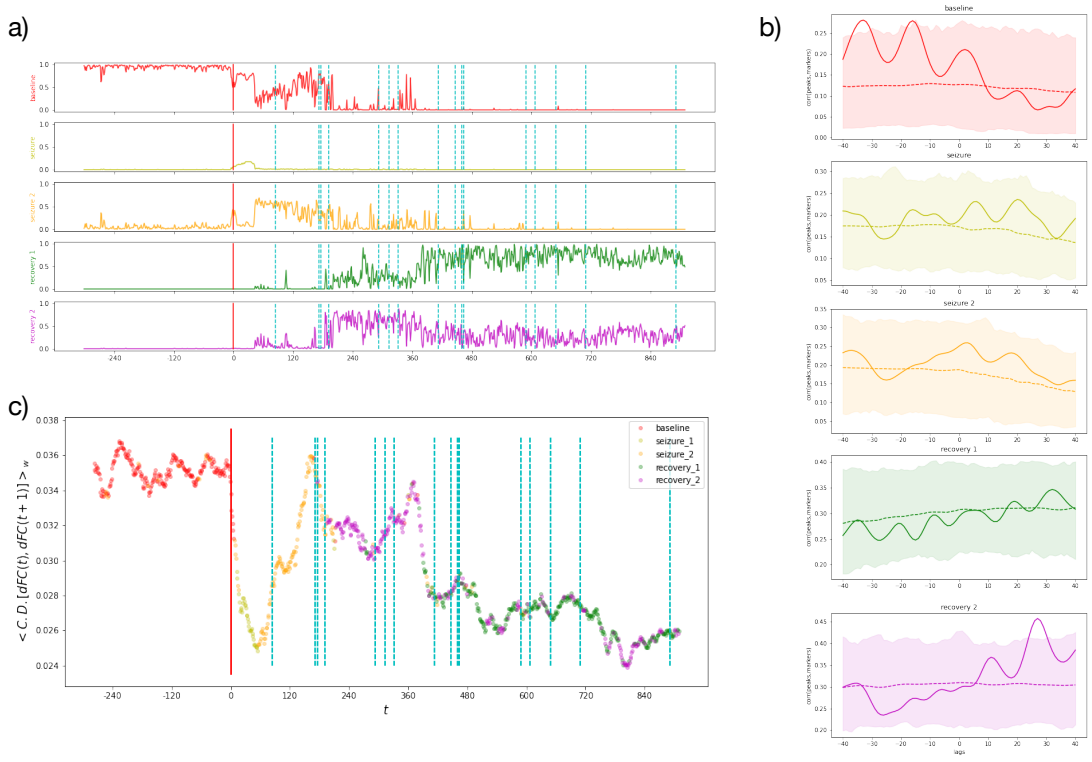

Figure A.7. – **Recording 4 - States of dynamics**: **a)** the five curves represent the probability $P(t) \in [0,1]$ of each time window t to belong to the baseline (red, top), seizure (two states, yellow and orange curves), recovery-1 (green, $4th$ plot) or recovery-2 (magenta, bottom) states. **b)** each of the five plots represents the lagged cross-correlation between the peaks of the curves in **a)** of each state (baseline, seizure-1 and 2, recovery-1 and recovery-2 from top to bottom) with the language dysfunction markers (red line); the shaded areas are comprised between the 5th and 95th percentiles of the values of cross-correlation computed for the peaks of $P(t)$ of each state with a random permutation of the clinical markers in the $[60s, 260s]$ interval. **c)** each of the colored dots corresponds to the average value of the instantaneous rate of change of the FC in a time window $\langle \Delta FC(t-1,t) \rangle_w$ and its color corresponds to the allegiance state label assigned to the corresponding time window.

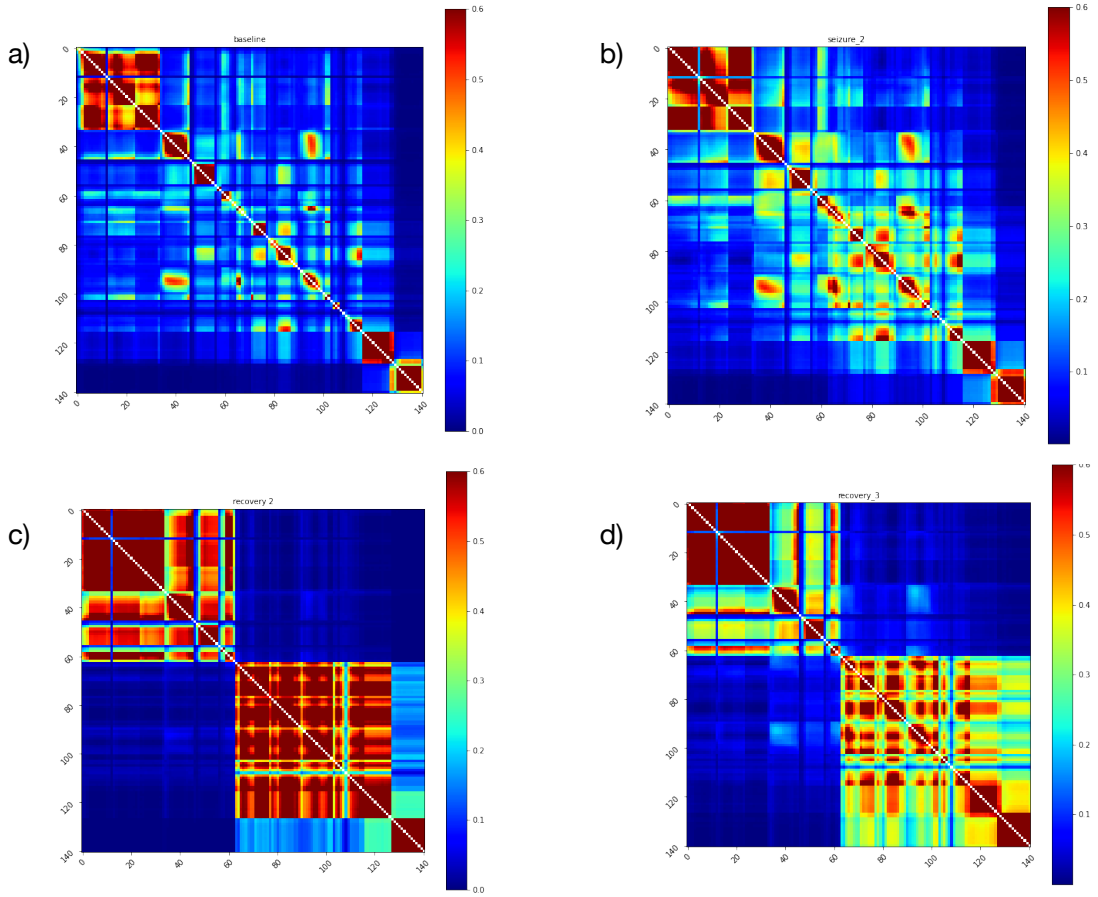

Figure A.8. – **Recording 4 - Allegiance matrices**: the state-wise allegiance matrices computed by averaging over the allegiance matrices measured in time windows assigned to the relative allegiance state. The four allegiance matrices in this plot correspond to the baseline state (**a)**), the seizure state (**b)**), the recovery 1 and 2 states (**c)**,**d)**) used to compute the state-wise radar plots in Figure 4.12 for recording 4.